UNIVERSITY OF SOUTHAMPTON

FACULTY OF ENGINEERING, SCIENCE & MATHEMATICS
Optoelectronics Research Centre

# New optical fibre based technologies and their application in highly nonlinear systems

by
Angela Camerlingo

Thesis for the degree of Doctor of Philosophy

April 2011

UNIVERSITY OF SOUTHAMPTON

ABSTRACT

FACULTY OF ENGINEERING, SCIENCE & MATHEMATICS
OPTOELECTRONICS RESEARCH CENTRE

Doctor of Philosophy

# NEW OPTICAL FIBRE BASED TECHNOLOGIES AND THEIR APPLICATION IN HIGHLY NONLINEAR SYSTEMS

by Angela Camerlingo

This thesis investigates new fibre technologies and their application in nonlinear optical systems, designed mainly for telecommunications. The thesis includes a study of two different directions in achieving a high nonlinearity in a fibre system, namely holey fibres filled with nonlinear liquids and soft glass, small core microstructured fibres. The challenges arising from the development of liquid-filled structures have made soft glass microstructured fibres the technology of choice for the realisation of highly nonlinear systems.

Amongst the various soft glasses, commercially available lead-silicate glasses are identified as the material for the development of highly nonlinear fibres. Small-core, lead-silicate fibres with different designs are considered within this thesis. A solid core holey fibre design as well as two all-solid designs, a multi-ring cladding and a simpler W-index profile, are characterised. The measurements confirm the advantages of the all-solid designs over the holey structures and reveal the possibility to achieve simultaneously a high nonlinear coefficient and a novel dispersion profile in such fibres. Some of the presented fibres are employed in all-optical wavelength conversion schemes based on four-wave-mixing. Numerical simulations and experimental results are combined to study the performance of the fibres and demonstrate their use in wavelength conversion devices. In particular, a lead-silicate W-index profile fibre, showing a high nonlinear coefficient of $820\mathrm{W}^{-1}\mathrm{km}^{-1}$ with a near zero dispersion profile at telecoms wavelengths, is employed to demonstrate a flat conversion gain in the whole C-band. The same fibre is then employed in FWM-based systems to demonstrate multi-channel wavelength conversion, generation of high repetition rate pulses and all-optical demultiplexing. The experiments presented in this thesis clearly reveal the potential of small-core soft-glass fibres for nonlinear applications.

The use of soft glass microstructured fibres in the mid-IR is also investigated. Tellurite holey fibres with different core sizes and hole arrangements are employed in a supercontinuum generation scheme.

# Contents

# List of Figures

# List of Tables

# List of acronyms

| | |
|---|---|
| **ASE** | Amplified Spontaneous Emission |
| **CVD** | Chemical Vapour Deposition |
| **CW** | Continous Wavelength |
| **DPSK** | Differential Phase Shift Keying |
| **EDFA** | Erbium Doped Fibre Amplifier |
| **EFRL** | Erbium Fibre Ring Laser |
| **FSM** | Fundamental Space filling Mode |
| **FWHM** | Full Width at Half Maximum |
| **FWM** | Four Wave Mixing |
| **GVD** | Group Velocity Dispersion |
| **HF** | Holey Fibres |
| **HMO** | Heavy Metal Oxide |
| **HNLF** | Highly Nonlinear Fibre |
| **HP EDFA** | High Power EDFA |
| **IR** | Infra-Red |
| **LMA** | Large Mode Area |
| **MOF** | Microstructured Optical Fibres |
| **MTIR** | Modified Total Internal Reflection |
| **NA** | Numerical Aperture |
| **NLF** | Non Linear Fibre |
| **NLSE** | Non Linear Schroedinger Equation |
| **NRZ** | Non Return to Zero |
| **OCT** | Optical Coherence Tomography |
| **OFCG** | Optical Frequency Comb Generation |
| **OOK** | On Off Keyed |
| **OPO** | Optical Parametric Oscillator |
| **OSA** | Optical Spectrum Analyser |
| **OSO** | Optical Sampling Oscilloscope |
| **PBF** | Photonic Bandgap Fibre |
| **PCF** | Photonic Crystal Fibre |
| **PRBS** | Pseudo Random Bit Sequence |
| **SBS** | Stimulated Brillouin Scattering |
| **SCG** | Super Continuum Generation |
| **SCW** | Surface Capillary Wave |
| **SEM** | Scanning Electron Microscope |
| **SEST** | Structured Element Stacking Technique |
| **SMF** | Single Mode Fibre |
| **SPM** | Self Phase Modulation |

| | |
|---|---|
| **SRS** | Stimulated Raman Scattering |
| **TIR** | Total Internal Reflection |
| **UV** | Ultra Violet |
| **WDM** | Wavelength Division Multiplexing |
| **XPM** | Cross Phase Modulation |
| **ZDW** | Zero Dispersion Wavelength |

# Declaration of Authorship

I, Angela Camerlingo, declare that the thesis entitled *New optical fibre based technologies and their application in highly nonlinear systems* and the work presented in the thesis are both my own, and have been generated by me as the result of my own original research. I confirm that:

- This work was done wholly or mainly while in candidature for a research degree at this University;
- Where any part of this thesis has previously been submitted for a degree or any other qualification at this University or any other institution, this has been clearly stated;
- Where I have consulted the published work of others, this is always clearly attributed;
- Where I have quoted from the work of others, the source is always given. With the exception of such quotations, this thesis is entirely my own work;
- I have acknowledged all main sources of help;
- Where the thesis is based on work done by myself jointly with others, I have made clear exactly what was done by others and what I have contributed myself;
- Parts of this work have been published in the journal articles and conference proceedings reported in the List of Publications at the end of this thesis.

Signed: _____

Date: _____

# *Acknowledgements*

The last four years have certainly been full of challenges and if I have managed to face them is thanks to the help and the encouragement of a number of people I would like to mention here.

First of all I would like to acknowledge my supervisor, Dr. Periklis Petropoulos, for giving me the possibility to work at the ORC. His help and support have been invaluable. He has taught me how to move the first steps in the lab and has never left me alone. He has also always been there when I felt low and confused, giving me advice and encouragement to go on. I would also like to thanks my co-supervisor, Prof. Dave Richardson, for always finding some time to dedicate to me whenever I needed it, despite being always incredibly busy.

I would also like to say thank you to all the people at the ORC I have worked with in the last few years. A big thank you has to go to Dr. Francesca Parmigiani for all her help with the equipment in the lab, for her precious advice and support when I needed it the most. A special thanks goes to Dr. Xian Feng for fabricating the fibres I used for my experiments and his help in the FAST lab. Also, I would like to thank Dr. Radan Slavik for the help with the experiment on the pulse generation and Dr. Francesco Poletti for the support with the numerical models. Many thanks to Dr. Peter Horak, Dr. Wei Loh and Dr. Marco Petrovich for the fruitful discussions. An immense thank you goes to Kevin Sumner and Dave Oliver for saving my files from my computer-related accidents! I would also like to thank the rest of the ORC staff, and in particular Eve Smith for her precious help throughout these years.

At the ORC I have found not only valuable colleagues but also very good friends. A big thank you goes to Francesca for always finding the right words to cheer me up in my dark moments, and there have been quite a few of them. I could never forget to thank Trina and Laura for all the moments we have shared on our tea and coffee breaks and also for all the happy time we have spent together outside the ORC. Many thanks goes to the ORC lunch crowd for the laugh and the fun before the small meeting room was taken away from us. Also, I would like to thank the OSA committee and in particular Nikita Daga and Mridu Kalita: without their help I could have never run the chapter for the whole year! It has been hard at times, but also a very valuable experience that has taught me a lot!

Life in Southampton outside the ORC would not have been as much fun without some of the people I have met here and that have become very good friends. Some of them have been here only for a short time, some others have been here with me throughout

my entire stay in Southampton, and some I have met only in my last period. No matter how long for, I would just like to say thank you for having been here! A big thank you to the first person I met in Southampton, Rossana, my housemate, who became a very good friend. Also, a special thank you goes to Nazila and Lindsay, for the cheerful lunch breaks and all the time spent together.

I could have not done it without the help of my friends at home. Whenever I felt discouraged, whenever I needed to hear a friendly voice, I knew that at the other side of the phone I would have always found you! Antonella, Floriana and Giusy thank you very much for your love and support!

I consider myself very lucky to have such a big and loving family. A big thank you has to go to my grandmother, my great aunties, my uncles and aunties, my cousins, in particular Carmen, for always believing in me.

Of course a big thank you goes to my parents, Carmine and Filomena, and my wonderful sisters, Melania and Annarita. You have always supported me, always encouraged me, always believed in me, even when I did not. I could never thank you enough for all you have done for me!

Finally, the biggest thank you goes to Mark. Thanks for all your loving support during the last few years, for putting up with me during the busy periods, and for taking such good care of me, especially in the last few months.

# Chapter 1

# Introduction

In recent years we have witnessed a rapidly increasing demand for data capacity in fibre optics-based communication systems. Everyday activities such as internet video and TV, voice communication, voice over IP, on-line video conferencing, on line chatting to on-line gaming have driven the development of high capacity transmission systems. Currently, the fiber optic data rate record is held by Nippon Telegraph and Telephone Corporation who have achieved 69.1Tbit/s over 240km of standard fiber [Sano *et al.*, 2010].

A communication network is based not only on a high speed transmission system, but also relies on an efficient switching system. The switching itself can be implemented in either the electrical or the optical domain. Switching in the electrical domain is very efficient and the technology is mature. The combination of optical transmission and electrical switching also works very well, as proven by today's commercial reality. However, because of the fast development of transmission systems mentioned above, the necessary Optical-Electronic-Optical conversion limits the transmission rate of each channel to the electronic speed. Therefore, in order to exploit the high transmission capacity of fibres within a network, the use of ultra fast all-optical signal processing techniques is highly desirable.

Many advanced all-optical applications for telecommunication signals, such as wavelength conversion or time demultiplexing, are based on nonlinear effects. A very promising medium for the realisation of all optical processing devices is represented by the optical fibre itself, in which the nonlinear behaviour derives from the dependence of the

refractive index on the intensity of light propagating in the fibre [Agrawal, 2006]. The use of an optical fibre for the realisation of nonlinear devices offers some important advantages: an optical fibre can support very high power density, show a long interaction length and reach high bit rate operation, while allowing ready integration into existing fibre systems [Yoo, 1996].

However, standard optical fibres are made of silica, an intrinsically low nonlinearity material and therefore high values of optical power and/or long lengths of fibre are required for nonlinear applications in silica-based fibres [Bogoni *et al.*, 2004a; Tanemura *et al.*, 2004]. Enhancing the fibre nonlinear coefficient with the addition of a dopant in the core, such as germaniun, has reduced the required length to a few kilometers [Hirano *et al.*, 2005; Yu *et al.*, 2001]. Despite the reduction in the fibre length, such lengths are impractical for real applications, due to issues of compactness and stability. Moreover, the accumulated dispersion associated with long propagation lengths can also compromise the performance of fibre-based nonlinear devices. Finally, in a nonlinear fibre the optical power needed to induce a nonlinear change in its refractive index is related to the power consumption of the device, which therefore becomes, together with the processing speed, a crucial factor in a processing system [Tucker *et al.*, 2007]. It is therefore necessary to achieve a medium that shows higher values of nonlinearity, while keeping the advantages offered by optical fibres.

In order to develop fibres exhibiting an enhanced value of effective nonlinearity as compared to standard fibres, silica has been replaced with highly nonlinear glasses, which show nonlinear refractive indices up to three orders of magnitude higher than silica. The development of small core non-silica step-index fibres has allowed for the fabrication of fibres with a high nonlinear coefficient [Kikuchi *et al.*, 2002; Sugimoto *et al.*, 2004; Troles *et al.*, 2006]. However, the zero dispersion wavelength of such glasses usually lies far from the C-band and therefore tailoring the dispersion properties of these fibres is not straightforward, thus resulting in fibres with large dispersion values at telecoms wavelengths.

An alternative approach that exploits the advantages of the use of soft glasses and overcomes the limitations of the step-index design, is represented by microstructured optical fibre (MOF) technology. MOFs consist of a core, which can be either solid or hollow, surrounded by a microstructured cladding, which can be based on either holes or

solid features running along the whole length of the fibre. Some of the most important properties of MOFs are the endlessly single- mode guidance [Birks *et al.*, 1997], the high values of numerical aperture (NA) [Monro and Richardson, 2003] and the high fibre nonlinearity [Monro *et al.*, 2002]. MOF technology is highly attractive also because of the flexibility it offers in terms of tailoring the waveguide dispersion properties. Handling the dispersion is an important issue in high speed optical devices, and therefore MOFs can be seen as a promising candidate for the realisation of compact nonlinear devices with enhanced performance [Ferrando *et al.*, 2001; Reeves *et al.*, 2002].

The presence of the micron-scale features in the cladding results in an effective refractive index of the cladding region strongly dependent on the operational wavelength. In particular holey fibres (HFs) with a small core surrounded by large holes allow for high values of NA which result in light to be effectively confined in the core, and therefore a fibre with an enhanced effective nonlinear coefficient. For pure silica MOFs, a maximum value of $70\mathrm{W}^{-1}\mathrm{km}^{-1}$ has been reported [Belardi *et al.*, 2002].

Therefore, while it is possible to engineer the cladding structure of a MOF in order to achieve the desired dispersion profile, the highest possible value of nonlinearity is limited by the properties of the material of which the fibre is made. In this sense, there are essentially two ways to increase the nonlinear coefficient in a MOF: replacing silica with a highly nonlinear glass, as mentioned earlier, or guiding light in a highly nonlinear medium, such as a liquid impregnated in the core region of a hollow core MOF.

## 1.1 Main objectives and results achieved within this thesis

The aim of this project is to investigate the features and feasibility of two fibre-based technologies for the realisation of highly nonlinear, dispersion tailored waveguides: nonlinear liquid filled fibres and soft glass fibres. The possibility to replace silica with glasses showing a higher nonlinear coefficient has been already investigated and several remarkable results have been obtained in the fabrication and characterisation of this class of fibres [Brilland *et al.*, 2006; Kiang *et al.*, 2002; Kumar *et al.*, 2003; Petropoulos *et al.*, 2003; Qin *et al.*, 2010]. Although these non-silica fibres exhibit a high nonlinear coefficient, their dispersion profile has not been optimised. On the other hand, liquid filling technology represents quite a new and largely unexplored topic and the primary steps

of this technology, such as the choice of the liquids or the development of a technique to fill a fibre, will be investigated. This thesis describes the advantages offered by both technologies towards the realisation of compact nonlinear devices and discusses the main issues related to the two.

The possibility to use soft glass fibres for the generation of a broad supercontinuum spectrum in the mid-infrared (mid-IR) is also investigated. Two tellurite-based HF structures showing a zero dispersion wavelength beyond 2$\mu$m are employed to investigate the generation of a broad spectrum. The main results achieved within this project are summarised below.

- The feasibility of liquid-filled nonlinear optical fibres is investigated. A capillary infusion model is numerically investigated and experimentally verified using various liquids. Also a selective filling technique is discussed.
- The advantages of soft glass-based all-solid structures over holey structures in terms of fabrication accuracy are demonstrated through optical characterisation of fibre samples.
- A short sample, 1.5m in length, of an all solid dispersion-shifted highly nonlinear soft glass fibre showing one of the lowest values of propagation loss reported so far in a non-silica fibre, (0.8dB/m) is successfully employed in a FWM-based wavelength conversion scheme with low BER power penalty (0.5dB at error free operation).
- The characterisation of an all-solid W-type fibre with a high nonlinear coefficient of 820W$^{-1}$km$^{-1}$ which shows low dispersion D=-3$\pm$1 ps/nm/km at 1550nm and an overall flat dispersion profile in the C-band is reported. Based on a 2m sample of this fibre, a flat FWM gain of 0dB across the whole C-band is demonstrated.
- FWM-based systems in a solid W-type dispersion flattened lead silicate fibre, such as multi-channel wavelength conversion of 40Gbit/s signals, high repetition rate (>160GHz) pulse generation and all-optical 160Gbit/s to 40Gbit/s signal demultiplexing are demonstrated to prove the potential of soft glass fibres for the development of highly nonlinear systems.
- The potential of tellurite microstructured fibres for supercontinuum generation in the mid-infrared (mid-IR) is explored. A broad spectrum covering the wavelength

range from 0.9$\mu$m up to 2.5$\mu$m is achieved in a 9cm sample of a large mode area tellurite holey fibre.

## 1.2 Thesis outline

The thesis is organised as follows.

Chapter 2 introduces the fundamentals of MOFs starting with an overview of the fabrication techniques. Particular attention is given to index guiding fibres, since most of the fibres used in the experiments carried out within this thesis belong to this group. Properties such as endlessly single mode guidance, propagation and bending loss, birefringence and dispersion properties are discussed for index guiding fibres. Photonic bandgap fibres are then introduced. For this class of fibres, single mode operation and propagation loss mechanisms are illustrated.

Chapter 3 start with a description of the main nonlinear phenomena taking place in a fibre. This Chapter then discusses the possibility to fill a MOF with a nonlinear liquid and presents the main results achieved in this direction. The physical mechanisms involved in the capillary filling of a MOF are discussed; a numerical model is presented and validated with experimental results for a range of liquids. This Chapter highlights the various issues related to the development of the nonlinear liquid filling technique. The challenges arising from the development of nonlinear liquid filled fibre systems led us to focus our time on the prospect of combining highly nonlinear glasses with MOF technology. The soft glass MOF technology is then introduced and an overview of the main results achieved so far is presented.

Chapter 4 illustrates the results of the characterisation of the small core MOFs fabricated within the ORC. Three different designs including both HFs and all-solid fibres based on commercial lead-silicate Schott glasses are presented. The potential of each design towards the realisation of highly nonlinear devices are illustrated. Moreover, the advantages of the all-solid designs are presented.

Chapter 5 presents a study of the four-wave-mixing (FWM) process in the all-solid lead-silicate fibres presented in Chapter 4. In particular FWM-based wavelength conversion

is explored in a dispersion shifted all-solid fibre and in tailored dispersion profile W-type fibres with different values of propagation loss and dispersion profile.

In Chapter 6, several applications based on the FWM process in a short length of the dispersion optimised W-type fibre are proposed and demonstrated. A multi-wavelength conversion scheme is proposed and experimentally demonstrated. The generation of high repetition rate pulses in such a fibre is investigated and the experimental results are supported with numerical simulations. Finally, an all-optical demultiplexing scheme from 160Gbit/s to 40Gbit/s is experimentally demonstrated.

Chapter 7 discusses the potential of soft glass fibres for supercontinuum generation in the mid-IR. The results achieved in two different holey fibres made of tellurite are illustrated.

The thesis closes with some general conclusions drawn in Chapter 8 where I summarise the results and discuss the future work.

The work reported in this thesis has resulted in a number of original publications, listed at the end of the thesis.

# Chapter 2

# Fundamentals of microstructured optical fibres

## Historical background

Optical fibres have found applications in many fields in science and technology as diverse as telecommunications, laser science, sensing, medical imaging, and material processing. These advancements have been made possible mainly because of the dramatic reduction of the glass attenuation. In 1966 Charles Kao suggested the fundamental limit of glass transparency to be just below 20dB/km [Kao and Hocham, 1966], but only a few years later Shultz, Keck and Maurer proposed a process known as chemical vapour deposition (CVD) to reduce the propagation losses down to 16dB/km for a single mode fibre [Kapron *et al.*, 1970]. Further improvement in the technology allowed just a few years later to achieve loss values as low as 0.2dB/km at the specific wavelength of 1550nm [Miya *et al.*, 1979].

Already since the early 1970s, when the technology for core-cladding fibres was not mature yet, Kaiser and co-workers proposed an alternative structure to obtain low loss fibres. Their idea involved guiding light in undoped silica simply by surrounding it by air. They proposed and fabricated the structure reported in Figure 2.1: the small fibre core was suspended in air within and protected by a robust jacket [Kaiser *et al.*, 1973]. These novel fibre structures were proven to guide light by total internal reflection, supporting only the fundamental mode and were therefore regarded as a new promising

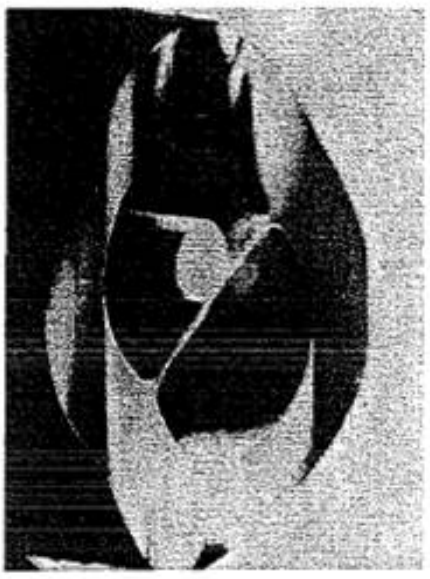

FIGURE 2.1: Single material fibre fabricated by Kaiser in 1973 [Kaiser *et al.*, 1973].

class of fibres. However, the contemporary improvement of the CVD technique allowed the fabrication of very low loss core-cladding fibres and therefore the research towards the development of silica-air fibre was abandoned.

The interest in this alternative class of fibre was renewed in the 1980s, after the invention of photonic crystals in 1987. In his work [Yablonovitch, 1987] the author developed three dimensional photonic crystals identifying the structures at a micron scale as a powerful means to modify the optical characteristics of the microstructured material. He suggested that in a dielectric medium, arranged in a periodic structure at the scale of the wavelength of light, destructive interference phenomena can occur, thus preventing light from propagating at certain wavelengths. Following this publication, a lot of work was focused on the fabrication of photonic crystals to produce photonic bandgaps in which the propagation of certain wavelengths was forbidden.

In 1995 Birks and co-workers extended the concept of photonic crystals to optical fibres by proposing to exploit a two-dimensional (2D) photonic bandgap for out-of-plane propagation that would allow the light to be confined in a defect and to be guided along the third direction [Birks *et al.*, 1995]. They introduced a new fibre structure: a single-material (silica) fibre showing a periodic arrangement of holes running along its entire length. One year later, in 1996, Knight and co-workers fabricated the first silica-air microstructured fibre [Knight *et al.*, 1996] using the stack and draw technique, a fabrication process that is described in more detail in Section 2.1.

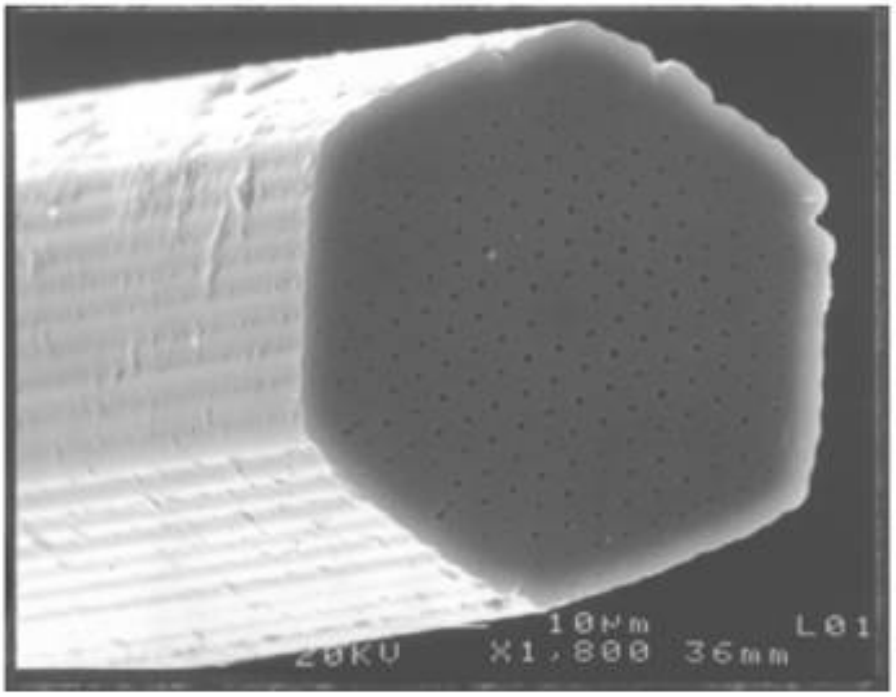


FIGURE 2.2: First reported single mode microstructured fibre by Knight and co-workers [Knight *et al.*, 1996].

Figure 2.2 shows a scanning electron microscope (SEM) image of the fibre: the structure presents an hexagonal arrangement of air holes surrounding a small solid silica core. Numerical simulations performed on this structure suggested that the fabricated fibre could not guide light by photonic bandgap as the air holes were too small to allow the formation of photonic bandgaps. However Knight and co-workers demonstrated that it was indeed possible to guide light in the fabricated fibre [Knight *et al.*, 1996]. This was due to the fact that the air holes were reducing the average refractive index of the holey silica cladding below that of the silica core leading to light guidance by a mechanism denoted as *modified total internal reflection* (MTIR).

This class of fibres attracted a great interest both in the academic and the industrial world as it can exhibit novel optical properties that cannot be achieved in a conventional core-cladding fibre. The main optical properties of this class of fibres will be outlined in Section 2.2.

In 1998 Knight and co-workers [Knight *et al.*, 1998] demonstrated guidance of light by photonic bandgap in a fibre whose structure followed the one previously proposed by Broeng and co-workers [Broeng *et al.*, 1998]: a new honeycomb silica-air structure that would allow achieving larger out-of-plane bandgaps making therefore plausible the

guidance by photonic bandgap. However, the fundamental mode of light in this fibre was not guided in the central hole representing the fibre core, but it was localised in the solid region around it. This would not allow a good overlapping of the guided mode with the Gaussian mode generated by most lasers and therefore the proposed structure was identified as not suitable for practical uses. Another important step towards the fabrication of what would be later known as photonic bandgap fibres was taken in 1999 by Cregan et al. [Cregan *et al.*, 1999]. They proposed a hexagonal hole arrangement of the cladding in order to increase the air-filling fraction and make guidance possible for propagation constants around the vacuum wavenumber, leading to the first fibre ever fabricated guiding in air through the photonic bandgap effect. The cross section of this fibre is shown in the SEM of Figure 2.3.

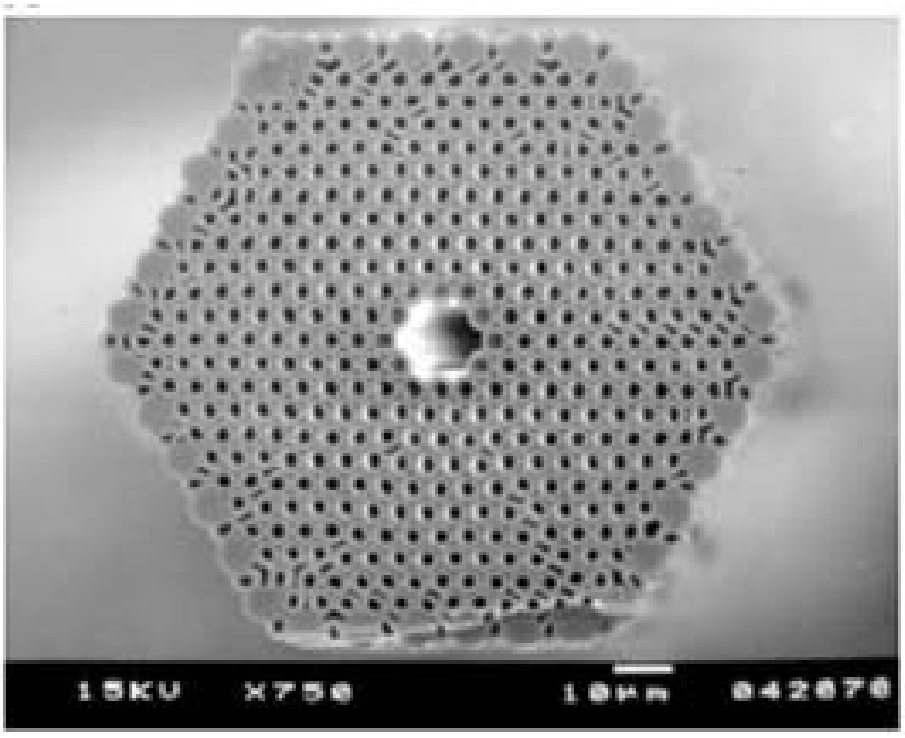

FIGURE 2.3: First fabricated single mode photonic bandgap fibre [Cregan *et al.*, 1999].

Since the fabrication of the first silica-air fibre, an intense research work has been carried out on this new class of fibres and many different structures have been proposed for different purposes. Undoped silica has been the main choice for the fabrication of such fibres for various reasons, namely the very low absorption of silica in the near IR wavelengths, its relatively low cost and the existence of well established techniques for handling the well known material. However silica does not represent the optimum choice

for a variety of applications. The relatively low intrinsic nonlinearity of silica and its transmission window limited to a range of wavelengths below $2\mu$m make silica a non suitable candidate for applications that require a high nonlinearity or a transmission range extended to the mid-IR. These limitations can be overcome by replacing silica with more suitable glasses. A group of glasses usually referred to as *soft glasses*, due to the fact that they show lower melting temperature than that of silica and usually contain a combination of different heavy metals, have proven to be an excellent choice. Many of the soft glasses indeed present a transmission window that extends beyond that of silica up in the mid-IR and show an intrinsic nonlinearity up to 1000 times higher than that of silica, allowing the fabrication of fibres with extremely high nonlinearity. Figure 2.4 illustrates SEM images of highly nonlinear holey fibres that have been fabricated using (a) lead silicate [Leong *et al.*, 2006], (b) tellurite [Liao *et al.*, 2009a], (c) bismuth [Ebendorff-Heidepriem *et al.*, 2004a] or (d) chalcogenide glasses [Brilland *et al.*, 2006].

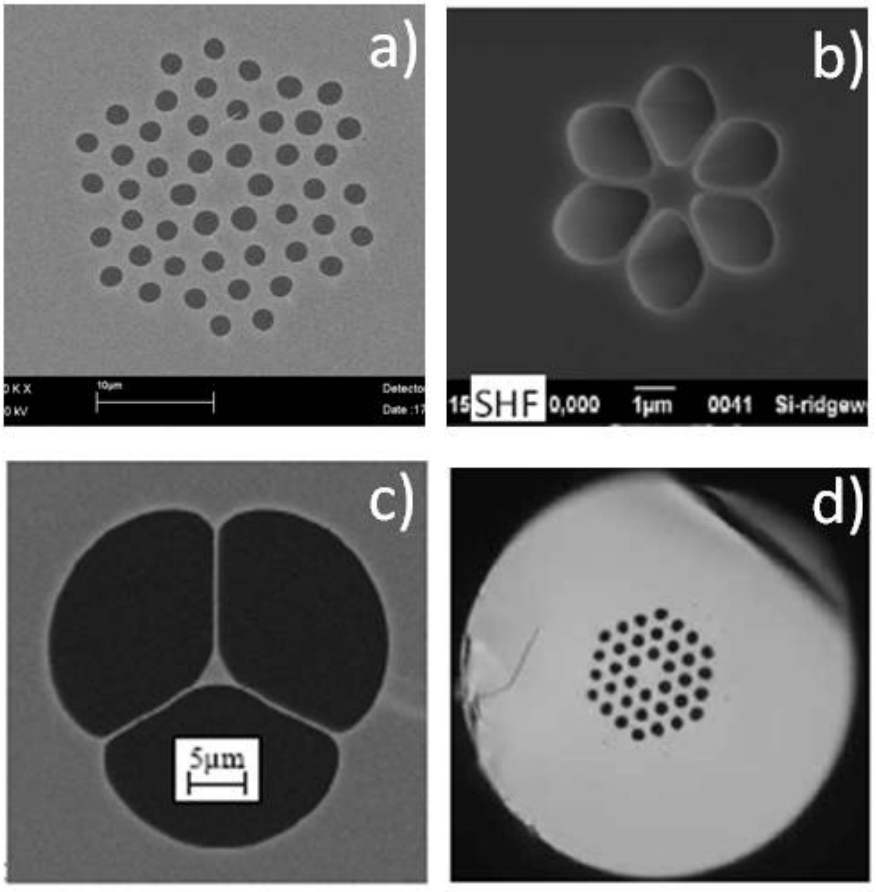


FIGURE 2.4: Examples of soft glass HF: (a) lead-silicate [Leong *et al.*, 2006], (b) tellurite [Liao *et al.*, 2009a], (c) bismuth [Ebendorff-Heidepriem *et al.*, 2004a], and chalcogenide [Brilland *et al.*, 2006].

The last few years have seen the development of all-solid HFs, where the holes are filled with a glass that is compatible with that of the main structure. These structures were first proposed and fabricated at the ORC in 2003 [Feng *et al.*, 2003b], [Feng *et al.*, 2005c]. The two glasses making the all-solid MOFs can in fact be arranged in various ways, not necessarily following the conventional hexagonal symmetry design of many HFs. This means that the holes can be replaced with any micron-scale solid regions of a second compatible glass [Feng *et al.*, 2009]. Figure 2.5(a) shows an SEM image of the first solid holey (SOHO) fibre, while Figure 2.5(b) illustrates a solid core fibre where the cladding is formed by alternative rings of glasses of various thicknesses. The advantages of an all-solid fibre over a HF are of great interest for this thesis and will be discussed in more detail in the following Chapters.

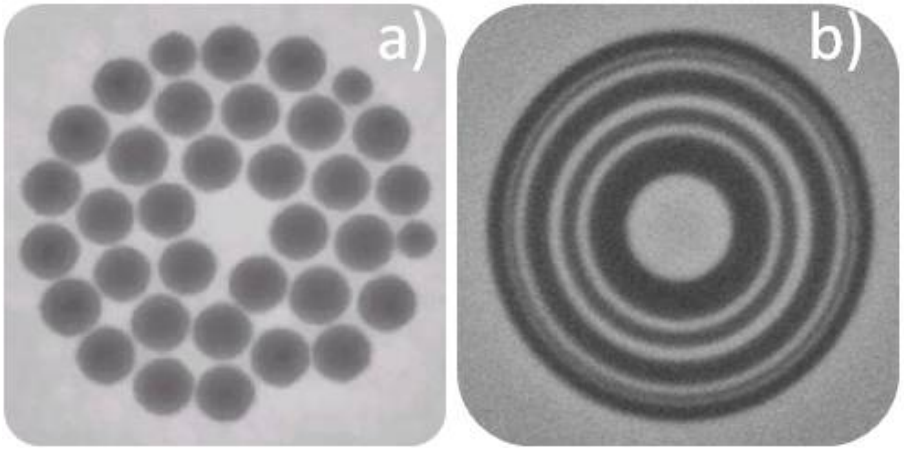


FIGURE 2.5: Examples of all-solid fibre where (a) the holes are filled with a compatible glass [Feng *et al.*, 2003b], (b) the glasses are organised in a multi-ring structure [Feng *et al.*, 2005c].

The great variety of fabricated fibres and the variety of names used to refer to them can sometimes lead to some confusion. It seems therefore worth to briefly clarify the nomenclature that is going to be used in this thesis. The first name given to the new class of fibres was *photonic crystal fibres* (PCFs) in reference to the periodic structures which are typical of photonic crystals. However, the cladding does not always have to be a periodic structure and therefore the term *microstructured optical fibres* (MOFs) will be used to indicate any fibre that presents micron scale features. In order to distinguish the two guidance mechanisms, fibres guiding by MTIR are generally referred to as *index guiding fibres* and whenever they present a holey structure they are referred to by the term *holey fibres* (HFs), while those guiding by the bandgap effect are referred to as *photonic bandgap fibres* (PBFs). In most of the experiments carried out for this thesis,

light propagates in the microstructured fibre relying on the MTIR process. For this reason, this Chapter illustrates the main properties of index-guiding fibres, in terms of the waveguiding mechanism, propagation and bending loss, birefringence and dispersion. This Chapter will also present a short description of the single mode operation conditions and of the causes of the propagation loss for a fibre guiding by the photonic bandgap effect.

## 2.1 Fabrication techniques

Standard optical fibres are produced in many laboratories worldwide using what is nowadays a very well established technique. The first step towards the fabrication of a standard optical fibre involves the fabrication of a preform, which represents a macroscopic version of the final fibre. A preform, which is usually fabricated using the CVD technique, consists in a glass rod of a few centimetres in diameter and of a length which may be up to a few meters. The glass rod shows a region of high refractive index to form the fibre core. In standard silica fibres this is achieved by doping the glass with germanium (Ge). The adoption of the CVD technique for the fabrication of preforms has allowed the deposition of high purity materials, resulting in what is the lowest value of loss reported so far for a standard silica optical fibre: 0.2dB/km. The preform is then heated up to the melting point in a furnace placed on top of a drawing tower and, with the aid of the force of gravity, a very thin and several kilometres long fibre can be drawn. The fibre is then coated with a polymer coating that provides mechanical protection and is usually wrapped around a spool.

The fabrication of a preform as outlined above gives the possibility to achieve a very small difference in the refractive index, usually around a percent, between the core and the cladding, which is typical of standard optical fibres. The CVD technique is clearly not suitable for the fabrication of MOFs, which can show a substantial difference in the refractive indices of the core and cladding, and therefore alternative techniques have been proposed.

Knight and co-workers have demonstrated that silica capillaries can be stacked together in an hexagonal configuration, then fused and finally drawn into a MOF [Knight *et al.*, 1998]. This procedure has been developed by Russell and co-workers [Russell, 2003] and

is known as the *stack and draw technique*. Although it has become the main technique currently used to fabricate silica MOFs [Russell, 2003], non-silica fibres can also be drawn using this approach as demonstrated by Monro and co-workers who successfully drew a Ge-La-sulphide fibre using capillary stacking [Monro *et al.*, 2000]. The stack and draw technique is very versatile and allows the fabrication of complex structures starting from elements of the appropriate shape and size. The first stage of the technique requires, in analogy with the drawing of a conventional fibre, the fabrication of a preform. This is done by stacking capillary silica tubes and rods together. If the fibre to be drawn is an index guiding HF, then the central capillary is generally replaced by a solid rod, which will form the fibre core at the end of the process. If, on the other hand, the fibre to be drawn is a PBF, a number of capillaries are removed to produce the central air-core. The fabrication of such a preform gives high flexibility in designing the final structure since it is possible to control both the shape and size of the core and the cladding, as well as their refractive index profile in the preform by properly arranging the capillaries together. Depending on the fibre structure, it might be necessary to add an additional step between the preform fabrication and the fibre drawing, usually known as *caning*. If the fibre to be drawn presents small features, the preform is reduced in scale into a smaller preform, usually referred to as a *cane*. The cane is then jacketed into another tube and the fibre is drawn. This approach has proven to be very effective for fibre with features smaller than $2\mu$m [Kiang *et al.*, 2002]. Once the required preform is ready, it is then drawn into the final fibre using a conventional fibre-drawing tower. After the drawing stage, the fibre is covered by a protective jacket that gives it the same robustness as a standard fibre. This process is schematically presented in Figure 2.6.

MOFs can also be fabricated by ultrasonic assisted mechanical *drilling* of glass rods [Mukasa *et al.*, 2006]. Using this technique, a variety of preforms of arbitrary hole sizes and shapes can be fabricated. The position of the holes can be accurately determined by using a micrometer in order to obtain a precise alignment [Feng *et al.*, 2005a]. This straightforward technique is however extremely time consuming for the fabrication of complex structures and is usually associated to a large contamination of the preform material that is responsible for an increase in the final value of propagation loss of the fibre.

The recent development of MOFs based on non-silica glasses has opened the possibility to explore different fabrication techniques. Non-silica glasses exhibit lower melting

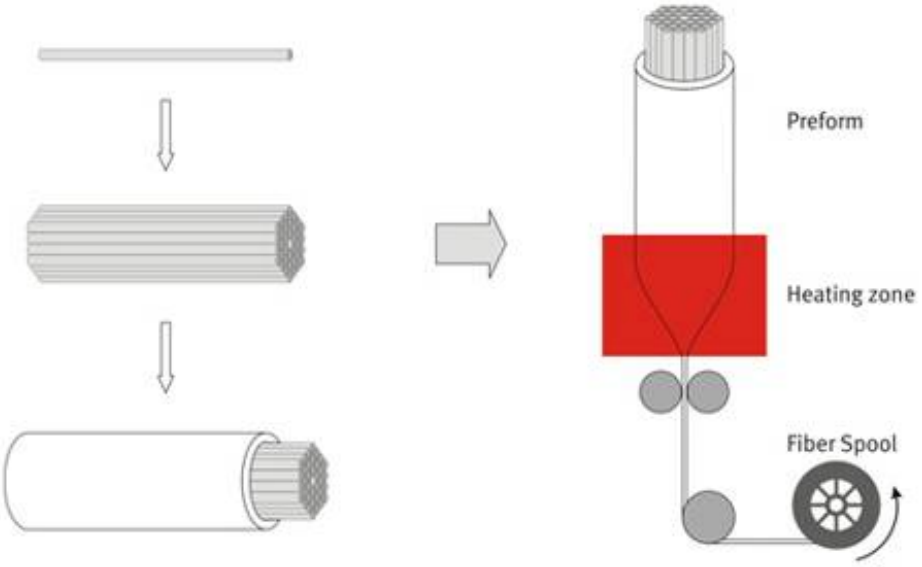


FIGURE 2.6: Schematic representation of the *stack and draw* technique, taken from [www.nktphotonics.com].

temperature values with respect to silica: this enables the preform to be fabricated with a technique widely known as *extrusion*. The process starts by heating the chosen bulk glass up to the softening point and then forcing it trough a die containing the desired preform element. A schematic representation of the process is shown in Figure 2.7. Once the preform has been extruded, the final fibre can be drawn in a conventional drawing tower.

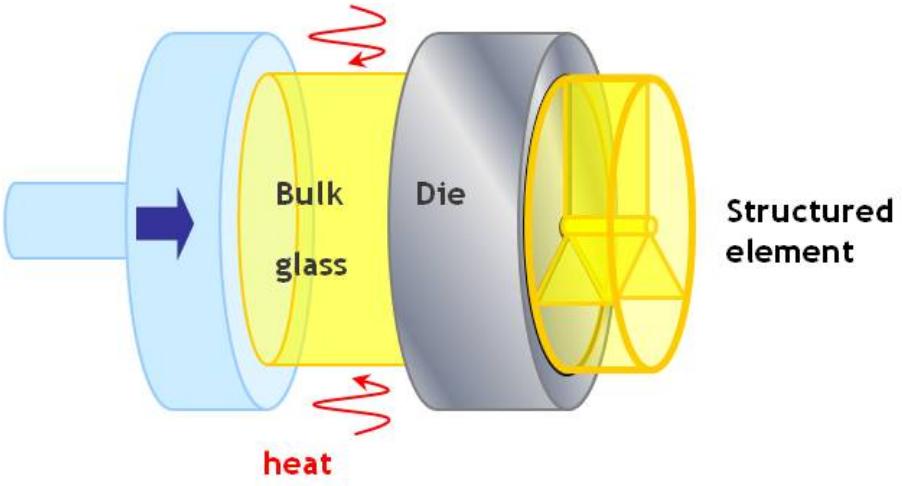


FIGURE 2.7: Schematic representation of the extrusion technique (taken from [Baggett, 2006]).

The extrusion technique presents several advantages over the stack and draw technique. First of all, the preform can be produced in this single step, thus avoiding the long

times required to stack the several capillary tubes together, typical of the stack and draw technique. Also, the low melting temperature of these materials allows little contamination of the glasses during the fabrication of the preform. This is a critical point for this class of material as they exhibit very high bulk losses. In order to improve the quality of the process, an additional step is required before the glasses are extruded. This consists in accurately polishing the glasses in order to improve the interface quality and reduce the roughness of the surfaces. This step allows reducing, or in the best case eliminating, the excess losses introduced by the fabrication process. A large number of materials can be extruded using this technique, including telluride, lead-silicate and chalcogenide glasses as well as polymers and the result is usually highly reproducible [Ebendorff-Heidepriem *et al.*, 2004a], [Kiang *et al.*, 2002], [Feng *et al.*, 2005a], [Monro *et al.*, 2002],[Ebendorff-Heidepriem *et al.*, 2004b], [Petropoulos *et al.*, 2003], [Feng *et al.*, 2003a], [Kumar *et al.*, 2003], [Ebendorff-Heidepriem *et al.*, 2005]. Finally, the extrusion technique allows a wider range of cladding structures when compared to the stack and draw technique as the holes are not restricted to a hexagonal arrangement.

Another technique that was already well known for the fabrication of core-cladding fibre [Ohishi *et al.*, 1986], [Mori *et al.*, 1998] has been successfully applied for fabrication of MOF preforms and is known as *casting*. In 2004 the first tellurite HF was drawn with this technique [Mori *et al.*, 2004]. Similarly to the drilling technique mentioned previously, casting is characterised by an accurate dimensional precision and allows the fabrication of fibres with large air-filling fractions.

The last few years have seen the combination of different techniques to improve the fabrication of MOF by exploiting the advantages that each technique can offer. The design flexibility of the stacking technique and the simplicity of the extrusion process has led to the development of the *structured element stacking technique* (SEST) [Leong *et al.*, 2005a]. This technique allows the fabrication of complex structures and to achieve good dispersion control in HFs, as this property is greatly influenced by the holes distribution in the cladding, as it will be explained in detail later in this thesis. The SEST technique looks at dividing a complex structure in structured elements that are easier to fabricate. The structured elements are first fabricated by extrusion and then stacked together to form the fibre preform. HFs made of a lead silicate glass (Schott SF57) have been fabricated within the ORC using the SEST technique and have been employed within

this thesis. The characterisation of these fibres and the issues related to this structure design are reported in Chapter 4.

The idea of combining the advantages of both the stack and draw and extrusion techniques has been extended from the fabrication of HFs to that of all-solid fibres, such as the multi-ring structure presented in Figure 2.5. This structure has been fabricated by Feng and co-workers [Feng *et al.*, 2005b] and involves the fabrication of a preform by extruding alternatively stacked high and low index glass disks through a circular aperture. Figure 2.8 illustrates a schematic of the fabrication of the preform for such a structure.

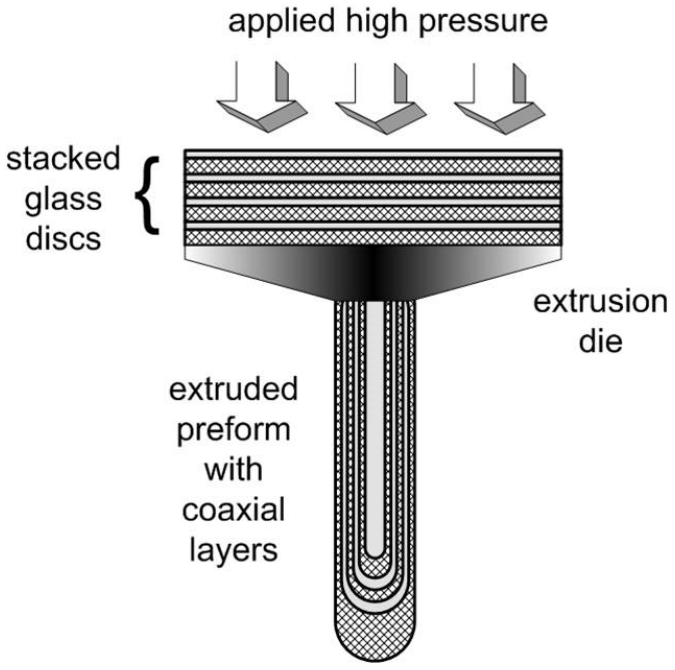


FIGURE 2.8: Schematic of the fabrication of a preform with coaxial ring structures by extrusion of alternately stacked high and low index glass discs, taken from [Feng *et al.*, 2005c].

Since the drawing of the first SOHO fibre [Feng *et al.*, 2003b], it has been clear that an all-solid structure presents many advantages over a holey one. One of the most challenging aspects of the development of the HF technology is indeed represented by the fibre fabrication. During the drawing of the fibre, the microstructured profile can change due to factors such as the internal pressure in the holes or the surface tension of the glass [Feng *et al.*, 2003a]. This results in variations in the cladding structure along the length of the fibre that are responsible for the sometimes substantial deviation of the optical properties of the fibre from the targeted ones. In an all-solid fibre, instead, the structure features of the preform are maintained with high accuracy during the fibre

drawing, allowing for a more reliable and predictable control of the microstructure of the fibre [Feng *et al.*, 2009].

Although the fabrication of an all-solid fibre might seem just a straightforward extension of the concept of a glass-air fibre, the fabrication of such a fibre is still quite challenging as it is necessary to find two (or more) thermally and chemically compatible glasses with different refractive indices. However, soft-glass all-solid fibres have been fabricated within the ORC and I have employed them in telecoms applications, proving the benefits of all-solid designs over HFs, as it will be illustrated in Chapter 5.

## 2.2 Index guiding fibres

As mentioned previously in this Chapter, index guiding MOFs are fibres with a high index core surrounded by a microstructured cladding that guides light by a process known as MTIR. This waveguiding mechanism, although very similar to the one occurring in standard step-index fibres, leads to a number of unique and novel properties. Since the introduction of the first silica HF [Birks *et al.*, 1995], many structures have been proposed. The most typical HF exhibits an hexagonal hole arrangement surrounding a solid core, such as the one shown in Figure 2.9. The main parameters that describe the properties of the fibre are the hole diameter (denoted with d) and the pitch from hole to hole ($\Lambda$). It is also very common to refer to the ratio $d/\Lambda$, the *air filling fraction*, to describe the properties of a holey fibre.

The solid fibre core usually occupies the size of three [Mortensen *et al.*, 2003b], seven [Limpert *et al.*, 2006] or even more holes. The air holes in the cladding reduce its refractive index, ($n_{clad}$<$n_{glass}$) and therefore the light can be guided in the solid core ($n_{core}$=$n_{glass}$) by MTIR. The effective cladding index can be evaluated by estimating the fundamental mode of the cladding, which can be approximated to that of an infinitely periodic structure with the same cladding parameter, also known as *fundamental space filling mode*, (FSM), defined as follows:

$$n_{clad} \approx n_{FSM} = \frac{\beta_{FSM}}{k} \tag{2.1}$$

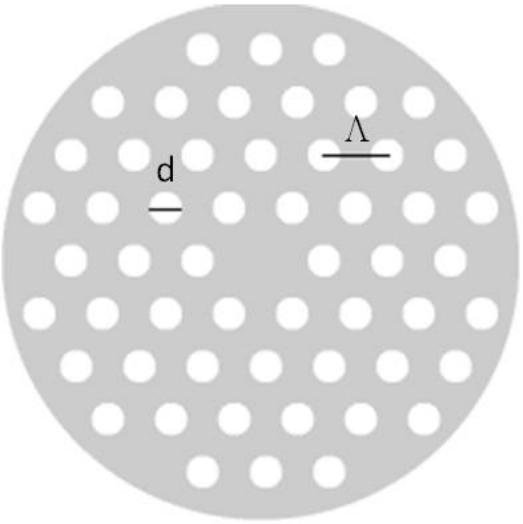


FIGURE 2.9: Schematic example of a photonic crystal fibre: d is the hole diameter and Λ the hole to hole pitch.

where $\beta_{FSM}$ is the propagation constant of the fundamental cladding mode and k=$2\pi/\lambda$ is the free space wave number. For short wavelengths the FSM is confined in the silica region, therefore for shorter wavelengths the effective index of the cladding ($n_{clad}$) tends to the value of the glass ($n_{glass}$). On the other hand, when the wavelength becomes comparable or greater than the pitch Λ part of the field will extend significantly into the holes [Riishede *et al.*, 2001], thus lowering the effective index to a value that is a weighted average of the refractive index of glass and air. Figure 2.10 shows the evolution of the FSM intensity for increasing values of wavelength, for the air-hole structure shown on the left with a d/Λ=0.6. The field intensity has been evaluated for increasing value of λ, normalized over the value of the pitch Λ.

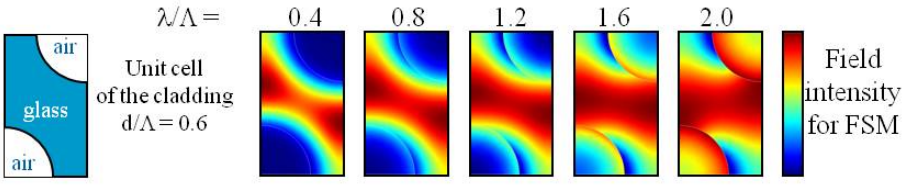


FIGURE 2.10: Simulated field intensity for FSM of a structure with d/Λ=0.6 and different values of wavelength [courtesy of Dr. J. Baggett].

The wavelength dependence of the refractive index of the holey cladding is responsible for the unique and novel properties of this class of fibres.

### 2.2.1 Endlessly single mode guidance

The dependence of the effective cladding index on the wavelength has an immediate consequence on the single mode propagation condition of a HF. In order to evaluate the single mode behaviour of a HF, it is useful to refer to a conventional fibre. A standard step index fibre is said to be single mode if the V number is less then 2.405. The V number is defined as:

$$V = \frac{2\pi a NA}{\lambda} \tag{2.2}$$

where $a$ is the core diameter and NA, the *numerical aperture*, is defined as follows:

$$NA = \sqrt{n_{core}^2 - n_{clad}^2} \tag{2.3}$$

where $n_{core}$ and $n_{clad}$ are the refractive indices of core and cladding respectively.

In analogy with a step index fibre, Mortensen and co-workers proposed that the V-number for a HF can be rewritten as follows [Mortensen *et al.*, 2003a]:

$$V_{HF} = k_{\perp}\Lambda = \frac{2\pi\Lambda}{\lambda}\sqrt{n_{core}^2 - n_{FSM}^2} \tag{2.4}$$

where $k_{\perp}$=ksin$\theta$ is the free space transverse wave number and $\theta$ is the divergence angle. Mortensen and co-workers showed that the fibre's central defect (the core) can support a higher order mode only when the effective transverse wavelength $\lambda_{\perp}=2\pi/k_{\perp}$ can fit in the defect region, i. e. $\lambda_{\perp} < 2\Lambda$. Given this condition, it is easy to conclude that a HF is endlessly single mode as long as $V_{HF}=2\pi\Lambda/\lambda_{\perp}<\pi$.

In order to achieve single mode guidance in a fibre, it is possible to rely on the difference in the *confinement loss*, see Section 2.2.2, between the fundamental mode and the higher order modes. Since higher order modes extend further into the fibre cladding, the material constituting the cladding is chosen to exhibit a refractive index higher than the effective index of the higher order modes. The difference in the confinement loss of the fundamental and higher order modes allows the latter to be neglected in a few meters of fibre, making the fibre *effectively single mode*. This approach has been adopted in

the multi-ring all solid design presented within this thesis. In such a structure, which will be presented in Section 4.2.2, the periodic cladding with rings of various thicknesses imposes losses of the order of a few tens of dB/m for any higher order modes [Feng *et al.*, 2009].

### 2.2.2 Propagation loss

The current value of loss for a silica step index fibre, 0.2dB/km, is mainly limited by Rayleigh scattering and IR absorption. However, it has been found that both Rayleigh scattering and IR absorption are lower in pure silica than in germanium-doped silica. This means that in theory lower values of loss are possible in pure silica fibres rather than in conventional germanium-doped silica standard fibres [Ohashi *et al.*, 1992]. Silica HFs, made by only one material, have therefore the potential to show improved values of losses when compared to standard fibres. In reality, silica HFs still exhibit relatively high loss and the lowest value reported so far is ∼0.3dB/km [Tajima *et al.*, 2003]. The main reason for the inconsistency is related to the increase in the Rayleigh scattering in a HF due to the roughness of the surface between the core and the holes [Zhou *et al.*, 2005]. In addition to this, the imperfections and inhomogeneities occurring during the fabrication process itself also contribute to an increase in the final loss [Zhou *et al.*, 2005].

Another factor contributing to the final loss in a HF is represented by the confinement loss [White *et al.*, 2001]. In a single material fibre, such as a HF, the cladding microstructure only extends for a finite region and is surrounded by an external region, the jacket, with the same refractive index as the fibre core. The cladding cannot therefore isolate the core form the jacket and part of the light leaks out of the core generating radiative losses. This kind of loss is strictly related to the cladding parameters and therefore a careful design is necessary to ensure that it is maintained at sufficiently low levels [White *et al.*, 2001]. A common route to reducing the confinement loss is to increase the number of rings in a HF, although this makes the fabrication process more challenging. Numerical studies have predicted that the confinement loss can be reduced down to an acceptable value of 0.2dB/km for a HF with a relatively large number of rings (greater than 5) and large air-filling fraction ($d/\Lambda > 0.9$) [Finazzi *et al.*, 2003].

When silica is replaced by highly nonlinear glasses, such as the soft glasses used to fabricate the fibres reported in this thesis, then the propagation losses are significantly increased, becoming up to four orders of magnitude higher than those reported in a silica HF. Soft glasses, indeed, show higher values of material losses when compared to silica, usually in the range of a few dB/m at telecom wavelengths and therefore MOFs made of soft glasses usually present values of loss of the order of 1-5dB/m in this wavelength range [Feng *et al.*, 2005a]. Apart from the high bulk loss of the glasses, the main contribution to the loss in a soft glass HF, is due to the impurities and the defects introduced during the fabrication process. Recent developments of the fabrication technique have led to the fabrication of fibres that exhibit propagation loss values very close to those of the bulk glass [Mori *et al.*, 2004].

The challenges that arise during the fabrication of a structure with microscale features are due to the complex interactions between the temperature, surface tension and internal pressure within the holes of the structure itself. In order to solve this problem it is possible to think of all-solid fibre designs based on two or more soft glasses arranged in a specific way [Feng *et al.*, 2009]. The properties and the advantages of an all-solid MOF over a HF will be discussed later in this thesis. Here it seems important to stress that an all-solid fibre presents additional issues in terms of loss. The unmatched viscosity between the core and the cladding can lead to imperfection losses, making the compatibility of the glasses in terms of viscosity a determining factor. Recent improvements in the fabrication processes have limited the losses introduced by the viscosity compatibility and all-solid lead-silicate fibres with propagation losses close to the bulk value of the soft glass used as a core, 0.8dB/m [Mukasa *et al.*, 2006], have been successfully fabricated [Feng *et al.*, 2005a].

Although the loss of soft glass MOFs are considerably higher than silica MOFs, it is worth noticing that this class of fibres is mainly targeted to the development of meter-long highly nonlinear devices and therefore propagation loss of a few dB/m can be tolerated.

### 2.2.3 Bending loss

One of the most important issues related to the practical use of a MOF regards the bending losses. A great number of applications require the fibre to be coiled at a certain radius and therefore bending losses can play an important role in determining the properties of the fibre.

When light propagating in a fibre encounters a bend, the field distorts to a degree that is related to the degree of the bend and as a result of this process some of the power can be lost. In order to understand the bending loss of a MOF, it is possible to refer to the bending loss experienced in a standard optical fibre. In such a fibre, the bending losses are strictly related to the *effective mode area*, defined by:

$$A_{eff} = \pi w^2 \tag{2.5}$$

where $w$ is the mode radius and for single mode fibres it can be estimated using Marcuse's formula [Marcuse, 1977]:

$$\frac{w}{a} \approx 0.65 + \frac{1.619}{V^{3/2}} + \frac{2.879}{V^6} \tag{2.6}$$

In any fibre, both conventional fibres and MOFs, bending loss increases when the effective area increases and when the NA decreases [Marcuse, 1976]. For this reason, bending loss is typically an important issue in MOFs with a large mode area. Such fibres can be employed in high power systems, when a large mode area is required to increase the damage threshold. The fibres developed for this thesis are mostly small core fibres and therefore the bending losses do not represent an issue.

### 2.2.4 Birefringence properties

Any single mode fibre is in reality not truly single mode, but supports indeed, two degenerate modes that are polarised in two orthogonal directions. In an ideal fibre, with a perfect cylindrical symmetry along its entire length, a mode that is excited with the polarisation on the x-axis would not be coupled to the mode excited with the polarisation on the orthogonal y-axis. However, in reality, there exist a number of inevitable factors that contribute to break this ideal symmetry. They can be due to both internal factors,

such as the random variations in the core dimension that can occur along the length of the fibre, and external factors, such as the unavoidable bending of the fibre. As a result, the propagation constant becomes slightly different for the two polarisation axes, i. e. the two polarisation modes travel with two different phase velocities. This property is referred to as *modal birefringence* and it is defined by using the following adimensional parameter [Kaminow, 1981]:

$$B_m = \frac{|\beta_x - \beta_y|}{k} = |n_x - n_y| \tag{2.7}$$

where $n_x$ and $n_y$ are the modal refractive indices of the two polarisation states. For a given value of $B_m$, the two excited polarisation modes exchange their power in a periodic way while they propagate along the length of the fibre. The variation in the polarisation state is often quantified by introducing another parameter, known as the *beat length*:

$$L_B = \frac{2\pi}{|\beta_x - \beta_y|} = \frac{\lambda}{B_m} \tag{2.8}$$

The unavoidable changes in the polarisation state can be solved by employing fibres with a considerable amount of birefringence, usually known as *polarisation maintaining fibres*. When the light is launched on one of the polarisation axes of this class of fibres, this polarization state will be preserved even if the fibre is bent.

The above discussion can be applied to a standard fibre as well as to a MOF. In the latter indeed, even in the presence of a structure with a greater than 2-fold symmetry, such as a holey cladding, an ideally perfect cross-section profile leads to absence of birefringence [Steel *et al.*, 2001]. However, when any structural defect is combined with the small feature size and the large index contrast that characterises MOFs, then even a small asymmetry can be translated in large values of birefringence. The degree of flexibility offered by the MOF design allows achieving higher values of birefringence in these fibres when compared to standard fibres. Highly birefringent MOFs can be fabricated by introducing an asymmetry to the fibre profile either in the core [Hansen *et al.*, 2001] or in the cladding structure [Ortigosa-Blanch *et al.*, 2000]. Using the latter solution, MOFs with an exceptionally short beat length of only 0.3mm have been fabricated [Furusawa *et al.*, 2001].

### 2.2.5 Dispersion properties

The cladding features in a MOF are responsible not only for determining the number of modes supported by the fibre, but also for its dispersive properties. Analogously to a standard optical fibre, the effect of the dispersion can be quantitatively analysed by expanding the propagation constant $\beta$ in a Taylor series around the frequency $\omega_0$ at which the pulse is centred:

$$\beta(\omega) = n(\omega)\frac{\omega}{c} = \beta_0 + \beta_1(\omega - \omega_0) + \frac{1}{2}\beta_2(\omega - \omega_0)^2 + ... \tag{2.9}$$

where $\beta_j = \left(\frac{d^j\beta}{d\omega^j}\right)_{\omega=\omega_0}$. The first derivative $\beta_1$ is inversely proportional to the *group velocity* ($v_g$), $\beta_1 = 1/v_g$, while $\beta_2$ is a measure of the variation of $v_g$ with the frequency, usually referred to as the *group velocity dispersion*. The group velocity dispersion is usually quantified by the *dispersion parameter* D:

$$D = \frac{d\beta_1}{d\lambda} = \frac{-2\pi c}{\lambda^2}\beta_2 = \frac{-\lambda}{c}\frac{d^2n}{d\lambda^2} \tag{2.10}$$

usually expressed in units of ps/nm/km. The dispersion gives an indication of the difference in the group velocity between two waves of slightly different wavelengths travelling in the material.

The chromatic dispersion parameter D is actually the sum of two contributions: the *material dispersion* $D_m$ and the *waveguide dispersion* $D_w$. The material dispersion is caused by the wavelength dependence of the refractive index of the medium in which light is propagating. Figure 2.11 shows the material dispersion for some of the glasses mentioned in Section 2.1: silica, lead-silicate glasses (SF6 and SF57) and bismuth oxide glasses. Pure silica shows a zero-dispersion-wavelength (ZDW) at 1.28$\mu$m. Above this value, the material dispersion is *anomalous* (D>0), while below the ZDW the material dispersion is *normal* (D<0). For higher-index glasses the ZDW is shifted towards longer wavelengths, resulting in a large amount of normal dispersion at telecom wavelengths.

The material dispersion can be compensated for with the waveguide dispersion, even if this is not a straightforward task. The waveguide dispersion mainly depends on the structure of the fibre and therefore MOFs represent a very attractive class of fibre as they

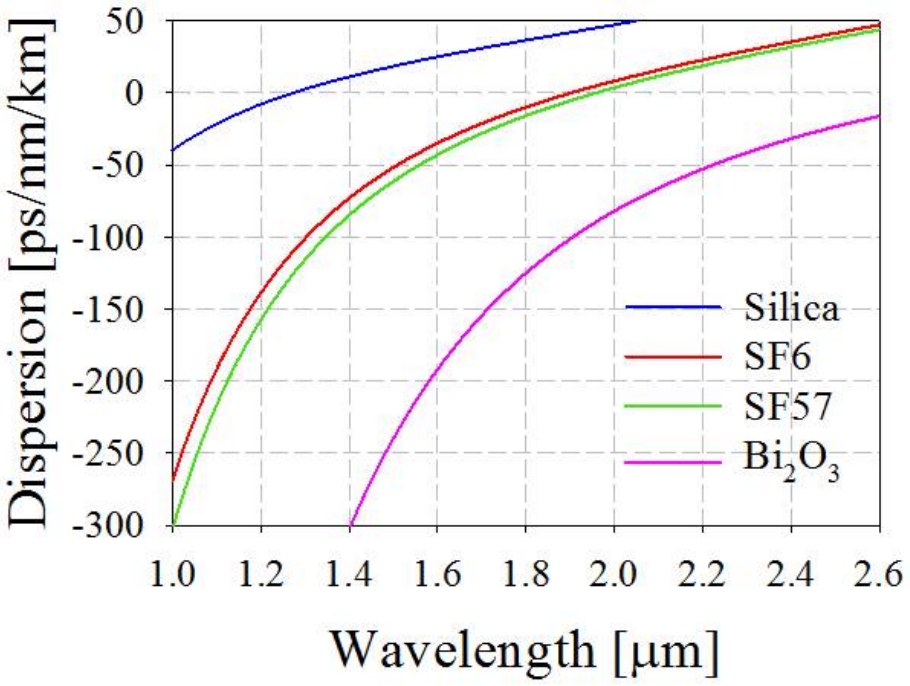


FIGURE 2.11: Material dispersion curves for silica [Agrawal, 2006], lead-silicate Schott SF6 and SF57 [Schott, 2003], and bismuth oxide glasses [Gopinath *et al.*, 2005].

allow for flexible engineering of the micron-scale features of the cladding parameters. In particular, the possibility to design a structure with a near-zero and flat dispersion profile at telecom wavelengths is highly desirable for many applications based on nonlinear effects, as it will be outlined in the following Chapters. In order to achieve zero or nearly-zero ultra-flattened chromatic dispersion in MOFs, several different designs have been proposed so far. Among them it is possible to distinguish the HF designs with uniform optimized air-holes [Ferrando *et al.*, 2000], [Ferrando *et al.*, 2001], MOFs with two-defected air-hole rings [Wu and Chao, 2005], or MOFs with air-hole diameters of variable size [Saitoh and Koshiba, 2004]. In particular, Saitoh and Koshiba have proposed a systematic study of the effect of the cladding parameters on the dispersion of a silica HF [Saitoh and Koshiba, 2005]. Figure 2.12 shows how a flat dispersion profile can be achieved over a range of wavelengths for a certain value of $\Lambda$ and as a function of the $d/\Lambda$ parameter.

An example of silica HFs designed and fabricated to target a low and flat dispersion profile is reported in Figure 2.13(a), [Reeves *et al.*, 2002]. The fibre shows a hole diameter $d=0.57\mu$m and a pitch $\Lambda=2.47\mu$m. The corresponding measured dispersion profile is represented by the blue curve in Figure 2.13(b). Figure 2.13(b) also shows (in red) the

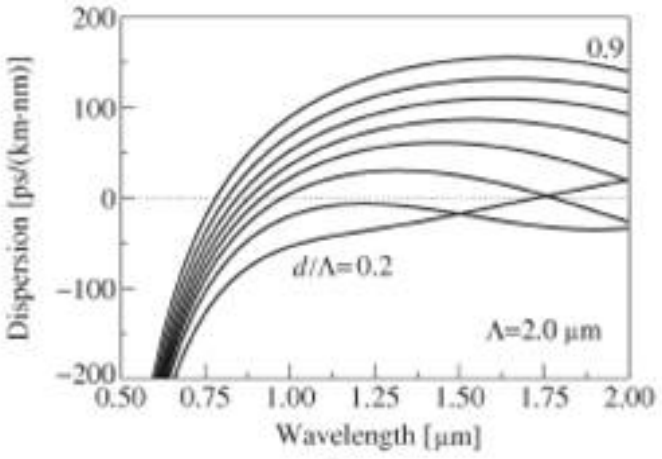


FIGURE 2.12: Dispersion properties of a solid core HF for various values of d/Λ, taken from [Saitoh and Koshiba, 2005].

measured dispersion profile of a HF with a similar structure to that reported in Figure 2.13(a) with a hole diameter d=0.58$\mu$m and a pitch Λ=2.59$\mu$m.

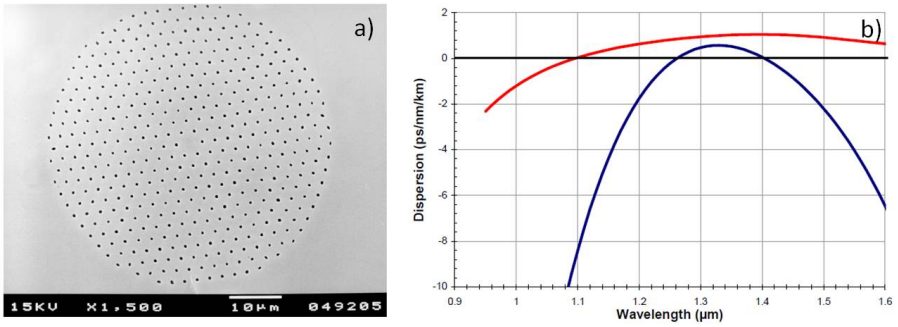


FIGURE 2.13: (a): Example of silica- based MOF with a flat dispersion profile; (b): Measured dispersion profiles for ultra flattened dispersion MOFs similar to the fibre structure shown in (a). Red curve: d=0.58$\mu$m, Λ=2.59$\mu$m, blue curve: d=0.57$\mu$m, Λ=2.47$\mu$m, taken from [Reeves *et al.*, 2002].

From Figure 2.13(b) it is clear that by increasing the hole diameter from 0.57$\mu$m to 0.58$\mu$m and the pitch Λ from 2.47$\mu$m to 2.59$\mu$m a dispersion $|D|$ <1.2ps/nm/km can be achieved over a wavelength range from 1$\mu$m to 1.6$\mu$m.

An alternative design has been proposed by Hansen and co-workers [Hansen *et al.*, 2003]. The fibre features a doped core surrounded by three regions arranged symmetrically around the core and surrounded in turn by twelve rings of holes. By varying the pitch and the hole size, Hansen and co-workers have demonstrated that a zero dispersion and a flat profiles can be obtained over a wide range of wavelengths. The fabricated fibres show holes size in the range of 0.47-0.5$\mu$m and a pitch in the range 1.48-1.51$\mu$m.

Despite the remarkable results obtained by Reeves and co-workers and Hansen and co-workers, it is evident that a highly accurate and precise control of the cladding hole shape and size is necessary when targeting a fibre with ultra-low dispersion. Moreover, the fabrication of this type of PCF is non-trivial because the hole diameters required for a flat dispersion profile are of sub-micron dimensions. In such a case, any small fluctuation in the holey structure that occur unavoidably during the fibre drawing step have a stronger effect on the fibre dispersive properties.

The effect of the variation of a holey structure on the dispersive properties of the final fibre has been investigated in this thesis and is presented in Chapter 4. As a possible solution to this problem, all-solid fibres have been proposed as these structures allow for a better control of the cladding features during the fibre drawing.

## 2.3 Photonic bandgap fibres

The possibility to exploit light guidance in air has attracted a lot of attention in the last few decades. From a practical point of view, air-guidance eliminates the problem of back reflection whenever the fibre is used in a free-space system. Moreover, the low nonlinearity and high surface damage threshold make this class of fibre advantageous for applications that require high power levels: a hollow core fibre is indeed able to withstand higher optical intensities values than silica and, even more, soft glass fibres. High energy ($370\mu$J) nanosecond pulses have been delivered in a hollow core PBF at $1.06\mu$m, increasing the damage threshold of this fibre by 25 times when compared to standard fibres [Shephard *et al.*, 2004]. Moving from the nanosecond to the femtosecond pulse regime, it has been recently demonstrated that a record value of peak intensity of $1.6{\cdot}10^{14}$W/cm$^2$ for a 40fs pulse with an average energy of $1.8\mu$J has been successfully coupled into a hollow core PBF [Ishaaya *et al.*, 2009]. In both works mentioned above, the propagation of light in the hollow core is multi-moded.

The photonic bandgap effect in an optical fibre requires the existence of a 2D periodic pattern of holes that runs along the fibre length perpendicularly to the fibre axis [Russell, 2003],[Broeng *et al.*, 1999], [Broeng *et al.*, 2000]. The existence of a periodic structure in the fibre cross-section results in the formation of *photonic bandgaps*: the frequencies lying inside the bandgap are unable to propagate within the cladding. By breaking the

periodicity of the structure with the introduction of a structural defect, it is possible to confine and propagate light through the defect. In the proximity of the defect light at frequencies inside the bandgap is allowed to propagate, while far from the defect the periodicity of the periodic structure forbids the propagation through it [Broeng *et al.*, 2000].

A typical PBF exhibits a hollow core surrounded by a holey cladding as shown in Figure 2.14.

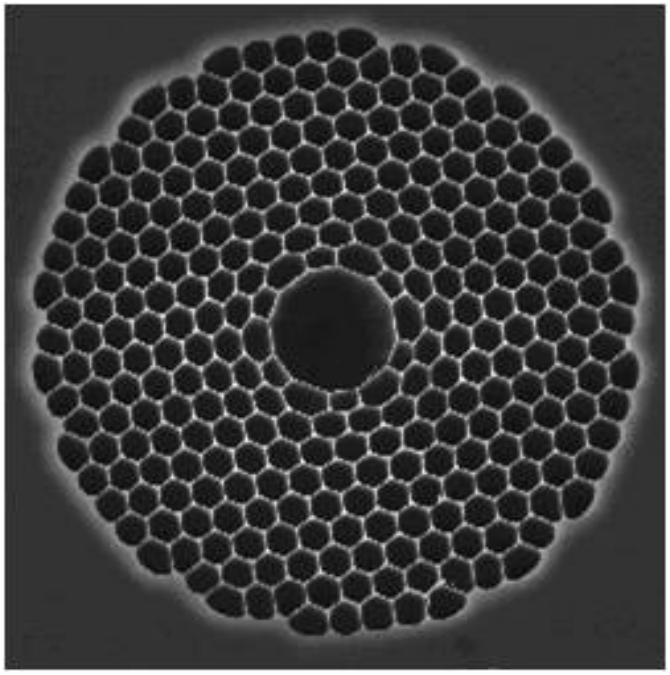

FIGURE 2.14: A SEM image of a photonic bandgap fibre fabricated at the ORC.

Hollow-core MOFs can indeed be regarded as 2D photonic crystals with a defect in the centre, referring to the periodic cladding and the hollow core respectively, thus enabling guidance of light in air by the photonic bandgap effect. The following paragraph discusses the main properties of a PBF that are more relevant to the work carried out in this project: single mode operation and loss properties.

### 2.3.1 Single mode operation

Several applications of hollow core PBFs would benefit from single mode propagation through a short length of fibre. A possible example is represented by the use of a PBF filled with a gas or a liquid for wavelength conversion, where coupling the pump into higher order modes can lead to a reduced conversion efficiency. The use of a PBF filled

with a liquid is of particular importance in the work presented in Chapter 3 of this thesis where the selective filling of a fibre sample with a liquid is investigated in order to exploit the properties of this medium.

The two most common structures of a hollow core PBFs are formed by omitting 7 or 19 cells to form the core as shown in Figure 2.15.

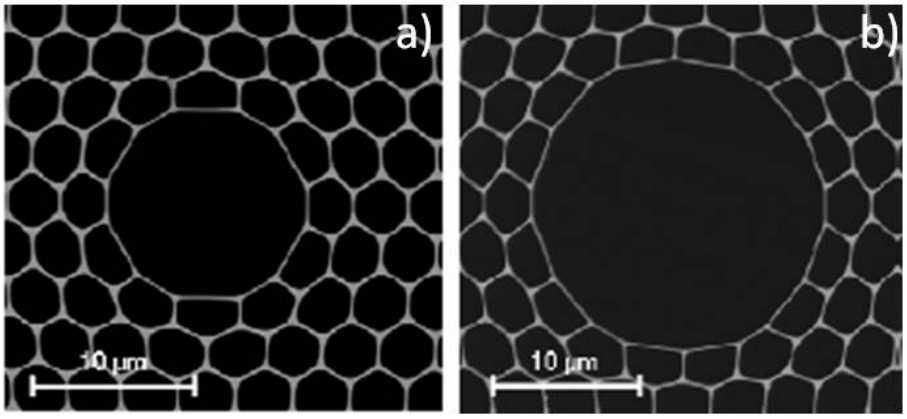


FIGURE 2.15: Two common PBF structures: 7-cell core (a) and 19-cell core (b) fabricated within the ORC.

The number of modes supported by a hollow core PBF has been proven to be directly proportional to the core diameter. [Cregan *et al.*, 1999]. For a 7-cell structure such as that presented in Figure 2.15(a), numerical simulations have shown that not only the fundamental mode can be guided, but also an additional group of 4 higher order modes can propagate [Broeng *et al.*, 2000]. A bigger core structure, such as the 19-cell fibre shown in Figure 2.15(b), will support an even higher number of modes within the bandgap, as reported in [Smith *et al.*, 2003]. Higher order modes usually show higher confinement and scattering loss when compared to the fundamental mode: this difference can be exploited by using a sufficiently long sample of the fibre in order to obtain effectively single-mode operation at the required wavelength. However, the idea of having single mode propagation also over a short sample of photonic bandgap fibre is very attractive for several applications such as high power delivery, when the undesired higher order modes can lead to a non uniform intensity distribution at the output of the fibre. Other applications, that will be discussed in more detail in Chapter 3 of this thesis, of a single mode PBF includes the selective filling of a fibre sample with a gas or a liquid, in order to exploit the properties of these media. Recently, the first steps towards the fabrication of a single mode PBF have been taken by Petrovich and co-workers [Petrovich *et al.*, 2008]: they have demonstrated that robust single mode

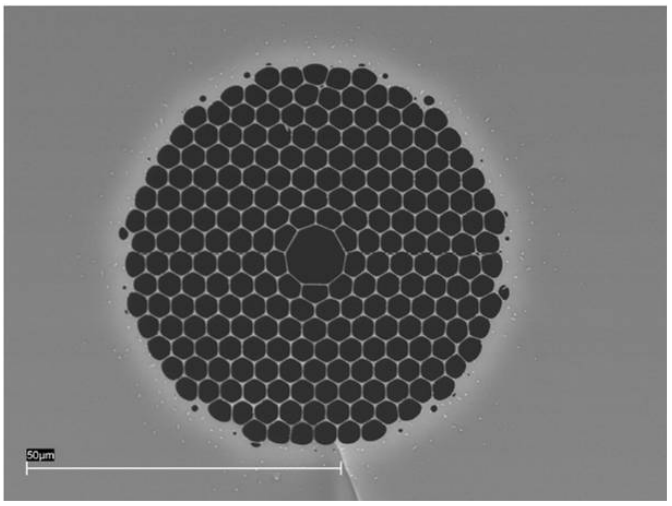


FIGURE 2.16: SEM image of the 3-cell core PBF taken from [Petrovich *et al.*, 2008].

propagation is possible in a fibre the core of which has been formed by omitting only 3 cells in the original preform. A SEM image of the fabricated fibre is shown in Figure 2.16. Numerical simulations indeed show that such a structure supports only the fundamental mode in the range of wavelengths between 1300nm and 1560nm, while a 7-cell and a 19-cell fibre with the same cladding parameters supports 12 and 40 modes respectively in the same wavelength range.

### 2.3.2 Loss in a photonic bandgap fibre

As mentioned in Section 2.2.2, any fibre with a high refractive index outer jacket shows leaky modes and PBFs are not an exception, as they also exhibit a finite number of hole rings. Saitoh and co-workers demonstrated how the confinement loss can be reduced to a negligible value by a careful design: by including a sufficient, but practical from a fabrication point of view, number of rings in the fibre and by increasing the air-filling fraction [Saitoh and Koshiba, 2003].

Since light propagates in air for a hollow core PBF, it is reasonable to think that the confinement loss of the fibre plays the most determinant role in the overall fibre loss, as the air shows negligible absorption and suffers from lower scattering than any solid material. However, the presence of an air-glass interface introduces new contributions to the overall fibre loss in addition to the confinement loss. During the fabrication step, some impurities can be found on the interfaces, thus increasing the loss due to absorption or can act as a centre of formation of crystallites, microscopic crystals that constitute a

solid, which are responsible for an additional component of scattering loss. While these two contributions can be neglected by improving the fibre fabrication processes, there is another phenomenon that cannot be neglected: the scattering at the air-glass interface, which has indeed been found to be the main limitation to the achievement of a low loss PBF [Roberts *et al.*, 2005]. Such scattering derives from surface capillary waves (SCWs) that are frozen into the fibre during the drawing process and are inevitable because of their thermodynamic origin [Jackle and Kawasaki, 1995]. A systematic study on surface roughness has been conducted by Roberts and co-workers [Roberts *et al.*, 2005]. Since the roughness due to SCWs cannot be easily reduced by improving the fabrication processes, they have proposed to act on the structure of the fibre instead and have demonstrated that, with a careful design of the fibre parameters and the right choice of wavelength, the lowest value that is possible to achieve are 0.2dB/km at 1620nm and 0.13dB/km at 1900nm.

Apart from acting on the reduction of SCWs, a further way to reduce the loss in a hollow core PBF is to reduce the overlap between air and glass. This can be done by enlarging the core size from 7 to 19 cell, leading to a loss reduction from 13dB/km [Smith *et al.*, 2003] down to 1.2dB/km [Roberts *et al.*, 2005] and the value could be further reduced by enlarging the core size even more. However, as illustrated in the previous paragraph, enlarging the core means that a larger number of higher order modes will be propagated, limiting the practical use of the fibre.

## 2.4 Conclusions

The aim of this Chapter was to illustrate the main properties of two classes of MOFs, namely index guiding HFs and PBFs, and to provide an overview of the potential optical properties that can be achieved in a MOF and that cannot be otherwise attained in a conventional fibre. After having illustrated the fabrication techniques common to the two types of MOFs, an overview of the main properties of the two classes of fibres was given. The waveguiding mechanism of holey fibres based on modified total internal reflection was discussed together with the main properties they can offer. Holey fibres can be designed to achieve novel properties like single mode guidance at all wavelengths or unusual dispersion properties, opening up the way for many interesting and novel applications, as it will be discussed further in the Thesis. Most of the experiments

carried out in this project involve the use of a microstructured fibre that guides light by modified total internal reflection, and therefore more attention was given to this class of fibres over PBFs. However, for the latter class of fibre, the conditions for single mode guidance and the main causes of the losses these fibres can show were illustrated, as these are the main features that will be taken into account during the experiments that will be presented in the next Chapters.

# Chapter 3

# Enhancing nonlinear effects in microstructured optical fibres

The possibility to exploit MOF technology for the realisation of highly nonlinear fibres is discussed in this Chapter. First, a description of the nonlinear phenomena that occur in an optical fibre that are most relevant to this work is presented. This Chapter then introduces the main parameters that affect the nonlinear behaviour of an optical fibre, such as the effective area and the nonlinear refractive index. In order to enhance the nonlinear coefficient of a fibre, two routes are explored: the possibility to fill the holes of the fibre with a highly nonlinear liquid and the combination of MOF technology with highly nonlinear glasses. The most suitable liquids are presented and the main steps taken towards the development of this technique are illustrated. A review of the main applications that have been demonstrated using liquid filled fibres is also included. Finally, an overview of the main compound glasses that can be used for the fabrication of highly nonlinear fibres is given.

## 3.1 Nonlinear effects in optical fibres

The most important nonlinear effects that be observed in an optical fibre are third harmonic generation, four wave mixing (FWM) and nonlinear refraction. The first two are highly inefficient processes in an optical fibre, unless special efforts are made to satisfy the phase matching conditions. This thesis will not consider the third harmonic

generation process, whereas FWM-based applications will be investigated extensively and therefore more attention will be given to this phenomenon in the following Chapters.

Most nonlinear effects originate from nonlinear refraction, a phenomenon that results from the electric field intensity dependence on the refractive index of the fibre core and that is known as *Kerr effect*. The most studied nonlinear effects induced by the Kerr effect are self-phase modulation (SPM) and cross-phase modulation (XPM). This class of nonlinear effects, together with FWM, are *elastic*, which means that there is no exchange of energy between the propagating electric field and the dielectric medium. There is also a second class of nonlinear effects that result from stimulated *inelastic* scattering, during which some of the energy of the propagating field is transferred to the dielectric medium. Stimulated Raman scattering (SRS) and Stimulated Brillouin scattering (SBS) belong to this class and are both related to the vibrational excitation modes of the dielectric medium. The main difference between these two is the participation of optical phonons in SRS and acoustic phonons in SBS as will be explained in detail in this Chapter. In the following paragraphs, a brief introduction of the most important nonlinear phenomena in optical fibres is presented. Both elastic and inelastic scattering processes are considered.

### 3.1.1 Elastic nonlinear processes

The propagation of an electromagnetic field in a nonlinear dispersive medium, such as an optical fibre, is governed by the general wave equation

$$\nabla^2 E - \frac{1}{c^2}\frac{\partial^2 E}{\partial t^2} - \mu_0 \frac{\partial^2 P}{\partial t^2} = 0 \tag{3.1}$$

where c is the speed of light, and E and P are the electric field and the induced polarisation respectively. Eq. 3.1 can be derived from the well-known Maxwell's equations [Hecht, 1998]. In order to solve Eq. 3.1, it is necessary to find a relation between P and E. In the case of a dielectric medium the induced polarisation P can be written as follows [Agrawal, 2006]:

$$P(r,t) = P_L(r,t) + P_{NL}(r,t) \tag{3.2}$$

where the linear polarisation term $P_L$ is related to the first order susceptibility $\chi_1$ through the relation:

$$P_L(r,t) = \int_{-\infty}^{+\infty} \epsilon_0 \chi_1(t-t')E(r,t')dt' \tag{3.3}$$

and the nonlinear polarisation term $P_{NL}$ can be written in terms of the third order susceptibility [Agrawal, 2006]:

$$P_{NL}(r,t) = \int\int\int_{-\infty}^{+\infty} \epsilon_0 \chi_3(t-t_3, t-t_2, t-t_1)E(r,t_3)E(r,t_2)E(r,t_1)dt_3dt_2dt_1 \tag{3.4}$$

Eqs. 3.1 - 3.4 provide a general set of equations to study the nonlinear effects in an optical fibre, that in order to be solved need a few approximations to be considered. As a first approximation, it is possible to assume that the electric field maintains its polarisation along the whole length of the fibre. Also, the pulse envelope is assumed to be varying slowly. Moreover, for a pulse centred at the angular frequency of $\omega_0$, the spectral width $\Delta\omega$ is considered to be much smaller than the central frequency $\omega_0$ i.e., $\Delta\omega \ll \omega_0$. This assumption allows the electric field E to be written as follows:

$$E(r,t) = \frac{1}{2}(E(r,t)e^{-i\omega t} + c.c.)\widehat{x} \tag{3.5}$$

Where $\widehat{x}$ is the polarisation vector and E(r,t) is a function that varies slowly with time. In a similar way, the polarisation components $P_L$ and $P_{NL}$ can be expressed as follows:

$$P_L(r,t) = \frac{1}{2}(P_L(r,t)e^{-i\omega t} + c.c.)\widehat{x} \tag{3.6}$$

$$P_{NL}(r,t) = \frac{1}{2}(P_NL(r,t)e^{-i\omega t} + c.c.)\widehat{x} \tag{3.7}$$

Finally, in an optical fibre the response of the electrons to an applied field occurs over a scale time of ∼60-70fs [Agrawal, 2006]. Therefore, for a field with a pulse duration $T_p$>1ps, it is possible to consider the nonlinear response as being instantaneous.

When substituting Eq. 3.5 into Eq. 3.4, $P_{NL}$ is found to have a term oscillating at $\omega_0$ and an additional term at $3\omega_0$. The third-harmonic frequency term can be neglected because in optical fibres the phase matching conditions are not met, unless particular effort is made.

The component $P_{NL}$ can therefore be written as

$$P_{NL}(r,t) = \epsilon_0 \epsilon_{NL} E(r,t) \tag{3.8}$$

where $\epsilon_{NL}$ is given by [Agrawal, 2006]:

$$\epsilon_{NL} = \frac{3}{4}\chi_3 \left|E(r,t)\right|^3 \tag{3.9}$$

where $\chi_3$ is the third order susceptibility. Under the approximation of a slowly varying envelope and considering the perturbative nature of $P_{NL}$, it is possible to assume a solution of the electric field in the form:

$$E(r, \omega - \omega_0) = F(x,y)A(z, \omega - \omega_0)e^{i\beta_0 z} \tag{3.10}$$

where F(x,y) is the modal distribution, $\beta_0$ is the propagation constant at $\omega$=$\omega_0$ and A(z,$\omega$) is a slowly varying function of z. Substituting Eq. 3.10 into Eq. 3.5, the expression for the electric field becomes:

$$E(r,t) = \frac{1}{2}(F(x,y)A(z,t)e^{-i\omega t + i\beta_0 z}) + c.c. \tag{3.11}$$

where A(z,t) is the inverse Fourier transform of A(z, $\omega - \omega_0$) and represents the slowly varying pulse envelope. After some algebraic manipulations of the precedent expressions, the equation that governs the propagation of A(z,t) is:

$$\frac{\partial A}{\partial z} + \beta_1 \frac{\partial A}{\partial t} + i\frac{\beta_2}{2}\frac{\partial^2 A}{\partial t^2} - \frac{\beta_3}{6}\frac{\partial^3 A}{\partial t^3} + \frac{\alpha A}{2} - i\gamma A \left|A\right|^2 = 0 \tag{3.12}$$

where $\beta_1$, $\beta_2$, $\beta_3$ are the first, second and third derivatives respectively of the propagation constant $\beta$ with respect to $\omega$ evaluated for $\omega = \omega_0$. The parameter $\gamma$ expresses the nonlinear coefficient of the fibre and is defined as:

$$\gamma = \frac{2\pi n_2^E}{A_{eff}\lambda} \tag{3.13}$$

where $n_2^E$ is the *nonlinear refractive index coefficient*, related to the third-order susceptibility and the linear refractive index $n(\omega)$ through the expression [Agrawal, 2006]:

$$n_2^E = \frac{3}{8n(\omega)} Re(\chi_3) \tag{3.14}$$

The parameter $A_{eff}$ is the *effective mode area* and is defined as [Agrawal, 2006]:

$$A_{eff} = \frac{\left(\int\int_{-\infty}^{+\infty} |F(x,y)|^2 \, dxdy\right)^2}{\int\int_{-\infty}^{+\infty} |F(x,y)|^4 \, dxdy} \tag{3.15}$$

In order to evaluate the effective area, it is necessary to know the modal distribution F(x,y) for the fundamental fibre mode. If F(x,y) is approximated to a Gaussian distribution, the effective area can be expressed by the relation [Agrawal, 2006] $A_{eff} = \pi w^2$ as given in Eq. 2.5.

Eq. 3.12 can be found in a different form, when the following transformation is applied:

$$T = t - z/v_g = t - \beta_1 z \tag{3.16}$$

The term $\beta_1$ is related to the group-velocity $v_g$, allowing to study the pulse evolution in a frame of reference moving with the pulse group velocity. Eq. 3.12 can be written as:

$$\frac{\partial A}{\partial z} + i\frac{\beta_2}{2}\frac{\partial^2 A}{\partial T^2} - \frac{\beta_3}{6}\frac{\partial^3 A}{\partial T^3} + \frac{\alpha A}{2} - i\gamma A\,|A|^2 = 0 \tag{3.17}$$

This equation is usually referred to as the nonlinear Schrödinger equation (NLSE), as it is the analogue of the Schrödinger equation with the addition of a nonlinear term and the third-order dispersion term. [Agrawal, 2006]

It is common to define a time scale normalized to the input pulse width $T_0$:

$$\tau = \frac{T}{T_0} = \frac{t - \beta_1 z}{T_0} \tag{3.18}$$

and a normalized amplitude U(z,$\tau$):

$$A(z,\tau) = \sqrt{P_0} e^{-\alpha z/2} U(z,\tau) \tag{3.19}$$

where $P_0$ is the peak power of the incident pulse. Using these parameters and ignoring the third order dispersion term, Eq. 3.17 takes the following form:

$$\frac{\partial U}{\partial z} + i\frac{sign(\beta_2)}{2L_D}\frac{\partial^2 U}{\partial \tau^2} - \frac{iU\left|U\right|^2 e^{-\alpha z}}{L_{NL}} = 0 \tag{3.20}$$

where sign($\beta_2$)=$\pm$1 is the sign of the second order derivative and

$$L_D = \frac{T_0^2}{|\beta_2|} \tag{3.21}$$

$$L_{NL} = \frac{1}{\gamma P_0} \tag{3.22}$$

are known as the *dispersion length* and the *nonlinear length* respectively. Eq. 3.21 and Eq. 3.22 express the length scales over which the effects of dispersion and nonlinearity respectively start to become significant.

Eq. 3.20 needs to be modified if the effect of inelastic stimulated scattering processes has to be taken into account. During an experiment, the input peak power of the incident pulse may be above the SBS or SRS threshold, thus transferring energy to a new pulse that propagates in the same or in the opposite direction as the incident one, as it will be explained in more detail later in this Chapter. When the peak power is above the SBS or SRS threshold, the interaction between the newly generated pulse and the input pulse can be considered through XPM.

#### 3.1.1.1 Self phase modulation

SPM effects occur when an intense beam propagates in a nonlinear medium. The intense beam results in a change of the nonlinear refractive index of the medium which is responsible for an intensity dependent phase change on the propagating beam. In order to study the temporal and spectral evolution of a pulse under the effects of SPM, it is possible to start from the normalised NLSE. Eq. 3.20 can be solved by using a solution in the form:

$$U(z,T) = V(z,T)e^{i\Phi_{NL}(z,T)} \tag{3.23}$$

As a first approach, it is possible to consider negligible the effect of dispersion, so that in Eq. 3.20 $\beta_2$=0. Eq. 3.23 can be substituted in Eq. 3.20, and after some algebraic manipulations, the real and imaginary part can be equated together:

$$\frac{\partial V(z,T)}{\partial z} = 0 \tag{3.24}$$

$$\frac{\partial \Phi_{NL}(z,T)}{\partial z} = \frac{e^{-\alpha z}}{L_{NL}} V(z,T) \tag{3.25}$$

Eq. 3.24 shows that the amplitude of V(z,t) does not change along the length of the fibre, while Eq. 3.25 can be integrated to give the general solution:

$$U(L,T) = U(0,T)e^{i\Phi_{NL}(L,T)} \tag{3.26}$$

where U(0,T) is the amplitude of the field at z=0 and $\Phi_{NL}$ can be expressed in the form [Agrawal, 2006]:

$$\Phi_{NL}(L,T) = |U(0,T)|^2 \frac{L_{eff}}{L_{NL}} \tag{3.27}$$

where the parameter $L_{eff}$ is known as the effective length and is expressed by the relation:

$$L_{eff} = \frac{1 - e^{-\alpha L}}{\alpha} \tag{3.28}$$

The effective length takes into account the loss of the fibre and it is always shorter than the actual fibre length, L, because of the propagation loss. In the ideal case of the loss parameter $\alpha$ being reduced to zero, the effective length coincides with the actual fibre length.

Eq. 3.27 means that SPM does not affect the pulse shape in the time domain, while it is responsible for an intensity dependent phase shift. The maximum phase shift occurs at the pulse centre, i.e. T=0, where U is a function that has been normalised so that $\|U(0,0)\|$=1, and is given by:

$$\Phi_{max} = \frac{L_{eff}}{L_{NL}} \tag{3.29}$$

The SPM induced phase shift increases with the fibre length and depends on the fibre nonlinear parameter $\gamma$ and the power of the applied electromagnetic wave. The time dependence of the phase shift indicates that, along the pulse, the instantaneous frequency differs from its central value, $\omega_0$. This frequency change is usually referred to as *frequency chirp* and can be expressed as:

$$\delta\omega(T) = -\frac{L_{eff}}{L_{NL}} \frac{\partial}{\partial t} |U(0,T)|^2 \tag{3.30}$$

The chirp induced by SPM increases with the fibre length, generating new frequency components while the pulse propagates along the fibre.

The above analysis is valid when the dispersion can be neglected. An analogous analysis can be applied in the case of negligible nonlinear effects, i.e. when the dispersion plays the most determining role in the pulse broadening. In order to explain the pulse evolution in this case, an initially unchirped Gaussian pulse propagating through a fibre is considered. As shown in [Agrawal, 2006], a Gaussian pulse maintain its shape during the propagation, while at any point along the fibre its width is given by:

$$T_1(z) = -T_0 \left[1 + (z/L_D)^2\right]^{1/2} \tag{3.31}$$

Eq. 3.31 shows how the dispersion broadens the pulse and that the dispersion-induced broadening does not depend on the sign of the dispersion. Analogously to the previous case, the phase shift is time dependent and is responsible for a frequency chirp which can be expressed as:

$$\delta\omega(T) = \frac{sign(\beta_2)(z/L_D)}{1+(z/L_D)^2}\frac{T}{T_0^2} \tag{3.32}$$

where the chirp depends on the sign of the dispersion.

When the contribution of dispersive and nonlinear effects need to be considered at the same time, Eq. 3.20 can be written as follows:

$$\frac{\partial U}{\partial z} + i\frac{sign(\beta_2)}{2}\frac{\partial^2 U}{\partial \tau^2} - Ni\,|U|^2\,e^{-\alpha z} = 0 \tag{3.33}$$

where N is expressed as:

$$N = \frac{L_D}{L_{NL}} = \frac{\gamma P_0 T_0^2}{|\beta_2|} \tag{3.34}$$

and is a non-dimensional parameter which defines the relative effect of the dispersion and SPM during the pulse propagation. It is clear that the dispersion is more relevant if N$\ll$1, while SPM dominates when N$\gg$1. When N$\sim$1 both SPM and dispersion contribute to the pulse evolution along the fibre. In order to understand the evolution of the pulse, it is possible to refer to a Gaussian pulse in a fibre with parameters chosen so that N=1, as reported in [Agrawal, 2006]. Under this condition, a pulse in the normal regime, broadens faster than when only the effect of dispersion is taken into account, i.e. the SPM effect enhances the broadening otherwise due only to dispersion. The pulse broadening leads to a reduced spectral broadening compared to the case when the effect of GVD is ignored. On the other hand, in the anomalous dispersion regime the pulse broadens while propagating in the fibre and it then becomes stable at a length imposed by the dispersion length. At the same time the spectrum becomes narrower rather than broader as expected as a consequence of SPM. This behaviour is due to the fact that in the anomalous dispersion regime $\beta_2$>0, and therefore the SPM induced chirp and the dispersion induced chirp (Eq. 3.30 and Eq. 3.32 respectively) have opposite signs.

#### 3.1.1.2 Cross phase modulation

When two or more fields are concurrently propagating in a nonlinear medium, they interact with each other inducing a phase change in each of the beams. This effect is known as XPM.

Similarly to the case of SPM, it is possible to start from the NLSE to analyse the effect of XPM. It is assumed that two waves are propagating simultaneously in the nonlinear medium, on the same polarisation axis of a fibre. Following an analysis analogous to the one described in Section 3.1.1.1, and under the same assumptions, the following set of two coupled NLSEs is reached [Agrawal, 2006]:

$$\frac{\partial A_1}{\partial z} + \frac{1}{v_{g1}}\frac{\partial A_1}{\partial z} + i\frac{\beta_{21}}{2}\frac{\partial^2 A_1}{\partial t^2}\frac{\alpha_1}{2}A_1 - i\gamma A_1(|A_1|^2 + 2\,|A_2|^2) = 0 \tag{3.35}$$

$$\frac{\partial A_2}{\partial z} + \frac{1}{v_{g2}}\frac{\partial A_2}{\partial z} + i\frac{\beta_{22}}{2}\frac{\partial^2 A_2}{\partial t^2}\frac{\alpha_2}{2}A_2 - i\gamma A_2(|A_2|^2 + 2\,|A_1|^2) = 0 \tag{3.36}$$

where

$$v_{g1} = \frac{1}{\beta_{11}} \qquad v_{g2} = \frac{1}{\beta_{12}} \tag{3.37}$$

and $A_j$ is the slowly varying field, $\alpha_j$ is the propagation loss, $\gamma_j$ is the nonlinear parameter, $\beta_{1j}$ and $\beta_{2j}$ are the first and second order derivatives of the propagation constant $\beta_{0j}$ and the index j=1,2 indicates the $j^{th}$ field. Looking at the last term of Eq. 3.35 and 3.36 and comparing it with the same term in Eq. 3.17 it can be seen that for two simultaneously propagating beams with the same polarisation, the phase change induced by XPM is twice as effective as the phase change induced by SPM for the same intensity.

Eq. 3.35 and 3.36 are often written as:

$$\frac{\partial A_1}{\partial z} + i\frac{\beta_{21}}{2}\frac{\partial^2 A_1}{\partial T^2}\frac{\alpha_1}{2}A_1 - i\gamma A_1(|A_1|^2 + 2\,|A_2|^2) = 0 \tag{3.38}$$

$$\frac{\partial A_2}{\partial z} + i\frac{\beta_{22}}{2}\frac{\partial^2 A_2}{\partial T^2}\frac{\alpha_2}{2}A_2 - i\gamma A_2(|A_2|^2 + 2\,|A_1|^2) = 0 \tag{3.39}$$

where the two parameters T and $d$ represent a reference time frame with the pulse travelling at the speed $v_{g1}$ and an indication of the group velocity mismatch respectively and are defined as:

$$T = \frac{t - z}{v_{g1}} \qquad d = \frac{v_{g1} - v_{g2}}{v_{g1} v_{g2}} \tag{3.40}$$

The parameter d plays a determinant role in the XPM process, as pulses with different group velocities tend to walk off from each other, thus leading to a reduced XPM interaction. In order to quantify this concept, it is possible to introduce the walk-off length, defined as:

$$L_w = \frac{T_0}{d} \tag{3.41}$$

which represents a measure of the fibre length over which two overlapping pulses separate from each other as a consequence of the difference in their respective group velocities. The longer the walk-off length, the more effective the XPM interaction.

#### 3.1.1.3 Four wave mixing

Another process deriving from the third-order nonlinear susceptibility is FWM. It occurs when two photons from one or more waves are annihilated, creating new photons at different frequencies, so that the energy is conserved in the process:

$$\omega_3 + \omega_4 = \omega_1 + \omega_2 \tag{3.42}$$

where $\omega_j$ is the frequency of the $j^{th}$ field.

FWM is a nonlinear process that occurs when the phase-matching condition between the interacting waves is satisfied:

$$\Delta\beta = \beta(\omega_3) + \beta(\omega_4) - \beta(\omega_2) - \beta(\omega_1) \tag{3.43}$$

where $\beta(\omega_j)$ is the propagation constant of the $j^{th}$ field.

In the most common configuration for FWM-based applications, a strong pump at a frequency $\omega_p$ is launched in the medium together with a weak signal at $\omega_s$, generating a new *idler* wave at a frequency $\omega_f$, as well amplifying the weak signal at $\omega_s$. Many of the applications presented in this thesis have relied on FWM, therefore a more detailed analysis of this effect will be presented in Chapter 5.

### 3.1.2 Inelastic nonlinear processes

#### 3.1.2.1 Stimulated Raman scattering

Raman scattering in a molecular medium is responsible for the transfer of a small portion of the power ($\sim 10^{-6}$) from the incident field to a new field. When the molecules absorb energy the resulting photon show a lower energy and are shifted to the red side of the incident spectrum (Stokes scattering). When the molecules lose energy, the resulting photon are shifted to the blue side of the spectrum (Anti-Stokes scattering). In a quantum mechanical description, this kind of scattering takes place as one photon of certain energy is excited to a virtual state and creates a photon of reduced energy when transiting to a vibrational state. One of the most interesting features of Raman scattering consists in the fact that it is a process that extends over a broad range of frequencies. For fused silica, the Raman gain extends over $\sim$40THz, with a peak located at around 13THz [Agrawal, 2006]. The reason for this peculiar behaviour is found in the non-crystalline nature of glasses, where the molecular vibrational states are not well defined as in crystalline structures, but spread into overlapping bands, generating a continuum [Shuker and Gammon, 1970]. The frequency range over which the scattered photons are shifted is referred to as the *Raman gain bandwidth*.

#### 3.1.2.2 Stimulated Brillouin scattering

SBS involves the interaction of a photon with the material in which the wave is propagating, resulting in the generation of a new photon that is downshifted in frequency from the incident wave.

This phenomenon has its origins in the process of electrostriction [Boyd, 2003]. The incident pump field generates an acoustic wave that modulates the refractive index

of the medium, and the induced index grating is responsible for the scattering of the incident pump. The scattered pump gives rise to the generation of a new photon that is downshifted in frequency, because of the shift associated to the grating moving at a certain acoustic velocity. The frequency shift of the scattered photon, compared to the incident photon, is known as the *Brillouin shift*. SBS can be described quantum mechanically by the annihilation of a photon from the pump and the generation of a Stokes photon and an acoustic phonon at the same time.

It is possible to define the *Brillouin power threshold* as the input pump power for which the generated Stokes power is equal to the pump power at the fibre output. In conditions of steady-state regime, i.e. when only a single frequency CW pump is considered to be incident on the nonlinear medium, the power threshold can be expressed as [Agrawal, 2006]:

$$P_{thr} = 21\frac{A_{eff}}{g_B L_{eff}} \tag{3.44}$$

where $P_{thr}$ is the threshold pump power and $g_B$ is the Brillouin gain coefficient, related to the Brillouin scattering cross-section.

## 3.2 Obtaining a high nonlinear coefficient in microstructured optical fibres

### 3.2.1 Nonlinear coefficient

The nonlinear refractive index $n_2^E$ is the coefficient of proportionality between an applied electric field and the induced variation of the refractive index. The refractive index can be written as:

$$n(\omega, E) = n(\omega) + n_2^E \, |E|^2 \tag{3.45}$$

where $n(\omega)$ is the linear part given by:

$$n(\omega) = 1 + \sum_{j=1}^{m} \frac{B_j \omega_j^2}{\omega_j^2 - \omega^2} \tag{3.46}$$

where $\omega_j$ is the resonance frequency and $B_j$ is the strength of the j$^{th}$ resonance. In Eq. 3.45 E is the electric field, and $n_2^E$ is the nonlinear refractive index as defined in Eq. 3.14. In the standard metric system, the electric field E has units of V/m and $n$ is a dimensionless parameter. According to Eq. 3.14, $n_2^E$ can therefore be expressed in units of $m^2/V^2$. However it is quite common to express the nonlinear refractive index in $m^2/W$. In this case, the refractive index is defined as:

$$n(\omega, I) = n(\omega) + n_2 I \tag{3.47}$$

where I is the intensity of the optical field E related to it by the following relationship:

$$I = \frac{1}{2} \epsilon_0 c n \left| E \right|^2 \tag{3.48}$$

where $\epsilon_0$ is the *vacuum permittivity*, c is the speed of light in vacuum and n is the linear part of the refractive index.

It is possible to convert the value from one domain to the other using the following relationship [Agrawal, 2006]:

$$n_2 = \frac{2}{\epsilon_0 c n} n_2^E \tag{3.49}$$

The nonlinear refractive index $n_2$ represents the dependence of the refractive index on the optical intensity and in an optical fibre it depends only on the material chosen as the fibre core. In order to quantify the nonlinearity in a fibre, it is possible to refer to the *effective nonlinear coefficient*, previously defined as:

$$\gamma = \frac{2\pi n_2}{\lambda A_{eff}} \tag{3.50}$$

The effective nonlinear coefficient is expressed in units of $W^{-1}m^{-1}$ or $V^{-1}m^{-1}$, or more commonly $W^{-1}km^{-1}$ or $V^{-1}km^{-1}$, where $n_2$ is expressed in terms of the intensity I or

the electric field E respectively. The value of $n_2$ for silica is $\sim 2 \cdot 10^{-20} m^2/W$ and the effective nonlinear coefficient of a conventional fibre is $\sim 1 W^{-1} km^{-1}$. This low value is mainly limited by the intrinsically low value of $n_2$ for silica.

Eq. 3.50 shows that there are essentially two ways of obtaining a high effective nonlinear coefficient in a fibre. One way is to manipulate the fibre structure so as to decrease the $A_{eff}$; alternatively a different material can be employed with the scope of increasing the $n_2$. These two possibilities are considered separately in the following sections.

### 3.2.2 Effective area

The effective area represents a measure of the area occupied by the fundamental mode when it propagates along the fibre. Eq. 2.5 shows that $A_{eff}$ is directly proportional to the mode radius which is in turn, dependent on the core size and the V-number of the fibre, [Mortensen, 2002]. An arbitrary reduction on the core size is not feasible, as there is a limit beyond which it is not possible to reduce the core size without compromising the confinement of the incident light in the core [Finazzi *et al.*, 2003] and therefore the remaining possibility lies in acting on the NA.

As expressed in 2.2.1 the NA of a fibre is related to the difference in refractive indices of core and cladding. A large value of NA allows the light to be more tightly confined in the core resulting in a reduction in the value of $A_{eff}$. In the case of a Ge-doped optical fibre, the maximum NA achievable is dictated by the amount of germanium doping that can be achieved in the silica core. However, a high concentration of germanium results in high Rayleigh scattering, which results in higher values of fibre attenuation [Ghatak and Thyagarajan, 1998]. This means that a trade-off exists between the highest achievable $\gamma$ and the lowest $\alpha$ in a fibre. The highest value of nonlinear coefficient that has been achieved in a standard Ge-doped fibre is $\sim 26\ W^{-1} km^{-1}$ for a fibre with an $A_{eff}$ of $8 \mu m^2$ and a core diameter of $2.4 \mu m$, [Okuno *et al.*, 1999].

In a MOF the difference between the refractive indices of core and cladding can be much higher than in a standard Ge-doped optical fibre. For a silica HF for example, the air holes reduce the refractive index of the cladding to the value of air (n=1), which is $\sim 30\%$ lower than the refractive index of silica (n=1.45). The consequent large values of NA that can be achieved in a MOF offer a tight confinement of the light in the core, thus

reducing its effective area [Mortensen, 2002]. Moreover, in a silica-air HF, the core size can be reduced down to a few microns, leading to the minimum value of $A_{eff}$ of $1.5\mu m^2$, [Finazzi *et al.*, 2003]. Based on this result, a small core silica HF showing a record nonlinearity of $\sim 70 W^{-1}km^{-1}$ has been fabricated by Belardi and co-workers, [Belardi *et al.*, 2002].

#### 3.2.2.1 Increasing the nonlinear coefficient in an optical fibre

The value of $\gamma$ reported in [Belardi *et al.*, 2002], despite being 70 times higher than that of a standard Ge-doped optical fibre can be dramatically improved by guiding light in a material with a higher $n_2$ than that of silica. There are essentially two ways of achieving this in a fibre: either by filling a hole in a glass fibre with a nonlinear medium and then forcing light to travel in it or by fabricating a fibre using a more nonlinear material than silica. Both of these approaches have been considered in this project. The following sections present a feasibility study on filling optical MOFs with nonlinear liquids, and also provide an overview of compound glass optical fibres, which is the technology of choice for the remainder of this thesis.

## 3.3 Liquid filled microstructured fibres

The first attempt to fill a fibre with a liquid was conducted in the 1970s, [Gambling and Payne, 1972] when it was demonstrated that a liquid filled fibre could support propagation of light. The core of the fibre used for the experiment was filled with a liquid (hexachlorobuta 1-3-diene) whose refractive index (n=1.5563) was higher than the one of the solid silica cladding (n=1.444) and the light was therefore guided in the liquid core by TIR.

In the same period, Chandrasekhar started investigating the properties of liquid crystals, [Chandrasekhar, 1977]. He found out that the refractive index of such liquids is strongly influenced by the molecular alignment which in turn is strongly dependent on the temperature at which the liquid is kept. The dependence of the refractive index on the temperature suggested that liquid crystals would be an ideal candidate for the realisation of tunable devices. The recent years have seen a development in the fabrication of PBFs where the light propagation relies on the photonic bandgap effect. The

position and the width of the photonic bandgap are strongly dependent on the refractive index of the fibre. Therefore, the possibility to fill a PBF with liquid crystals has been investigated for the realisation of tunable photonic bandgap fibres, [Larsen and Bjarklev, 2003, 2004].

The air holes in a MOF open up new opportunities to exploit the interaction of light with a medium through the evanescent field in the air holes. Monro and co-workers, [Monro *et al.*, 1999] have demonstrated that a significant part (up to 30%) of the modal power can overlap with the air holes for a solid core fibre with a cladding showing a $d/\lambda \sim 0.7$. The evanescent field in the holes benefits from a long interaction length, as the holes run along the entire fibre length, and has been successfully exploited for the realisation of gas and liquid sensors, [Fini, 2004; Hoo *et al.*, 2001; Jensen *et al.*, 2004; Martelli *et al.*, 2005].

The prospect of filling the holes of a MOF with a highly nonlinear liquid has attracted a great attention in the last few years and it has been viewed as an effective way to enhance the nonlinear effect in a fibre, otherwise limited by the intrinsically low nonlinear value of the refractive index of silica.

One of the first attempts to use nonlinear liquids to enhance the nonlinear properties of a MOF was performed in 2005. Yiou and co-workers investigated the possibility to achieve SRS in a MOF with a hollow core filled with ethanol, [Yiou *et al.*, 2005]. Ethanol has a nonlinear refractive index ~6 times higher than silica but a lower linear refractive index (n=1.36), which makes it impossible to guide light by TIR in a silica capillary tube and therefore a hollow core PBF was chosen for the demonstration. Using this fibre it has been possible to demonstrate SRS; however, the propagation in the core was multimoded. Lebrun and co-workers proposed a solution to solve this issue: a completely filled ethanol PBF, [Lebrun *et al.*, 2007]. This choice resulted in single mode SRS process that was 25% more efficient than the one obtained in [Yiou *et al.*, 2005].

$CS_2$ has been used to theoretically demonstrate supercontinuum generation [Zhang *et al.*, 2006]. Filling the core of a PBF with such a liquid, an output spectrum spanning from 500nm to 2000nm has been theoretically demonstrated. Figure 3.1(a) shows the structure proposed in [Zhang *et al.*, 2006], where the hollow core ($a$=4$\mu$m) has been filled with $CS_2$, while the cladding ($d/\Lambda$=0.66) is left unfilled. Figure 3.1(b) shows the corresponding dispersion profile of the proposed fibre.

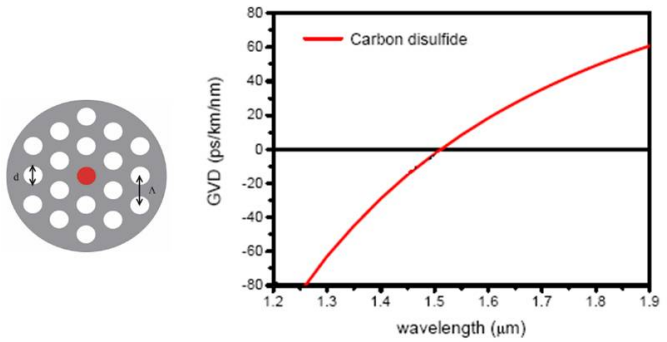


FIGURE 3.1: Schematic fibre structure (a) and corresponding dispersion profile (b) of the $CS_2$ filled core fibre, (adapted from [Zhang *et al.*, 2006]).

The proposed fibre shows a nonlinear coefficient of $\sim$2000W$^{-1}$km$^{-1}$ and a ZDW at 1.55$\mu$m which is crucial to achieve supercontinuum generation in a scheme where the pump is at the same wavelength. (More details on supercontinuum generation can be found in Chapter 7).

The highly nonlinear coefficient that can be achieved in a $CS_2$ filled fibre can be exploited for the realisation of many devices for all-optical processing at telecom wavelengths. In order to improve the performance of many processing devices (particularly those based on four-wave mixing) a low and flat dispersion profile is required in addition to the highly nonlinear coefficient.

The work presented in [Zhang *et al.*, 2006] shows no attempt to flatten the dispersion profile of the fibre. A systematic analysis of the fibre parameters proposed by Zhang and co-workers has been carried out by Poletti and co-workers, [Poletti *et al.*, 2008]. They have found the optimum fibre parameters (d=0.9$\mu$m and $\Lambda$=1.36$\mu$m) for a $CS_2$ filled core MOF to show a highly nonlinear coefficient ($6500W^{-1}km^{-1}$) and a flat and low dispersion profile at telecom wavelengths, [Poletti *et al.*, 2008]. Figure 3.2 shows the dispersion profile that can be achieved in the fibre proposed by [Poletti *et al.*, 2008]. An extremely flat dispersion profile, with D=0$\pm$1ps/nm/km, can be achieved in the wavelength range between 1500nm and 1600nm.

Nonlinear liquid filled MOFs seem to be a still largely unexplored and attractive field and this is the reason why some time has been devoted to the investigation of the advantages that a nonlinear liquid filled fibre can present.

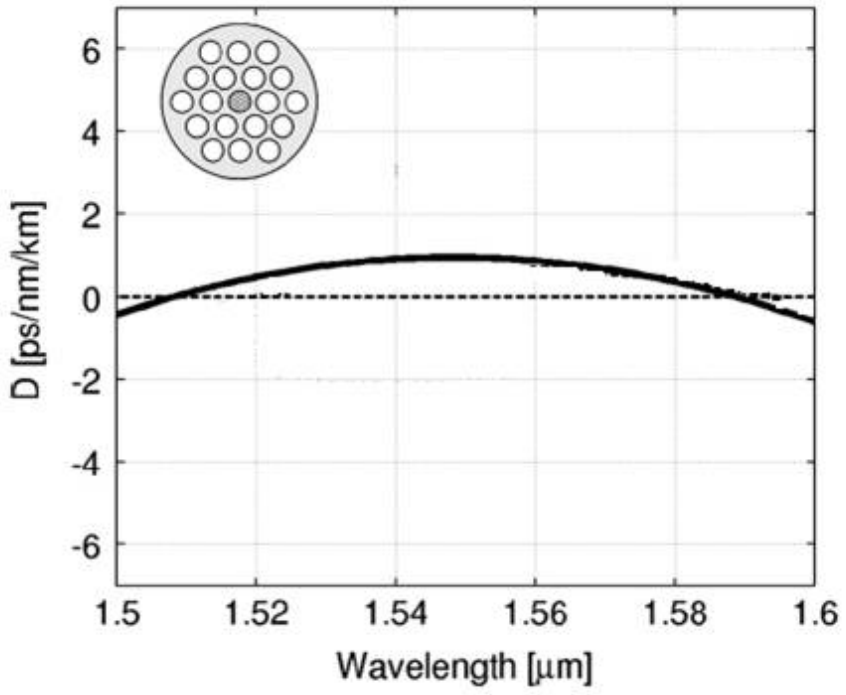


FIGURE 3.2: Dispersion profile of the $CS_2$ filled core HF proposed in [Poletti *et al.*, 2008] to achieve a flat and low dispersion profile in the wavelength range between 1500-1600nm.

In order to investigate the possibility to fill the holes of a MOF with a nonlinear liquid, suitable liquids needed to be identified. Table 3.1 lists some nonlinear liquids and shows their corresponding values of linear and nonlinear refractive indices. The values marked with a * are after [Sutherland, 1996], while those marked with a $^+$ are after [Dumais *et al.*, 2007] and those marked with a $^-$ are after [Zhang *et al.*, 2006]. The values for silica are reported for reference.

TABLE 3.1: Parameters of the most common nonlinear liquids.

| Liquid | Toluene | Carbon Disulfide | Nitrobenzene | **Silica** |
|---|---|---|---|---|
| n ($\lambda = 589nm$) | 1.496* | 1.68* | 1.551* | **1.549** |
| n ($\lambda = 1550nm$) | 1.477* | - | - | **1.444** |
| $n_2^E$ ($10^{-22}m^2/V$) | $3.97^+$ | 122 | 278 | **0.42** |
| $n_2$ ($10^{-20}m^2/W$) | 20+ | 564 | 1350 | **2.2** |
| Absorption | 0.3dB/cm @1550nm$^+$ | no absorption in visible and IR$^-$ | strong absorption if $\lambda$>1600nm$^-$ | **0.2dB/km @1550nm** |

The linear refractive index is reported at the D-line ($\lambda$=589.29nm), as this represents the standard wavelength at which the refractive index is measured and is therefore usually found in literature. Wherever available, the value of refractive index at 1550nm is also listed. When not available, the values of $n_2$ have been calculated using Eq. 3.49. Nitrobenzene looks like a very promising liquid, due to its high nonlinear refractive index value and its absorption properties, immediately followed by $CS_2$. Figure 3.3 shows the transmission curves of 1cm samples of $CS_2$ and nitrobenzene and shows clearly the advantages of $CS_2$ in terms of absorption at telecoms wavelengths [Zhang *et al.*, 2006]. Moreover, the short sample lengths used for these measurements imply that the losses of nitrobenzene will become more relevant for longer pieces of fibre. This is the reason why $CS_2$ has been considered as a more suitable liquid for nonlinear applications.

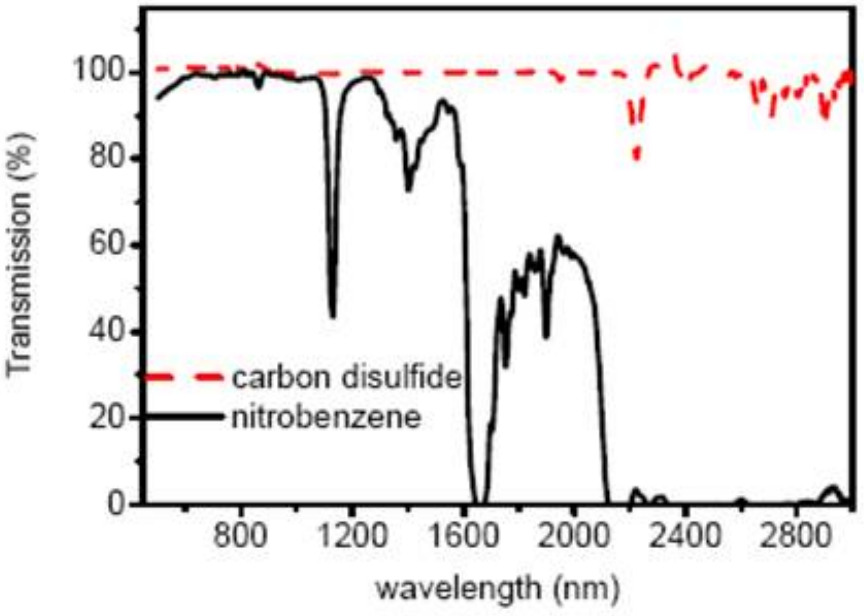


FIGURE 3.3: Transmission curve for carbon disulfide and nitrobenzene, taken from [Zhang *et al.*, 2006].

Filling a MOF represents quite a challenging task, as there are many practical issues to be taken into account. A MOF can be filled entirely or selectively, just in the core or the cladding holes, depending on the particular application it is required for. When the entire fibre needs to be filled, it is possible to simply immerse the fibre in the liquid and rely on the capillary effect. On the contrary, when selective filling is needed, then a dedicated technique needs to be applied. The next sections will illustrate the main steps taken towards the development of a filling technique.

### 3.3.1 Capillary filling

When a liquid is in contact with a capillary tube, several forces need to be taken into account in order to model the behaviour of the liquid: the capillary force, the friction force, the applied pressure and the gravity force [Nielsen *et al.*, 2005]]. The capillary force is defined as the ability of a substance to draw another substance into it. Capillary action for two different liquids is shown in Figure 3.4

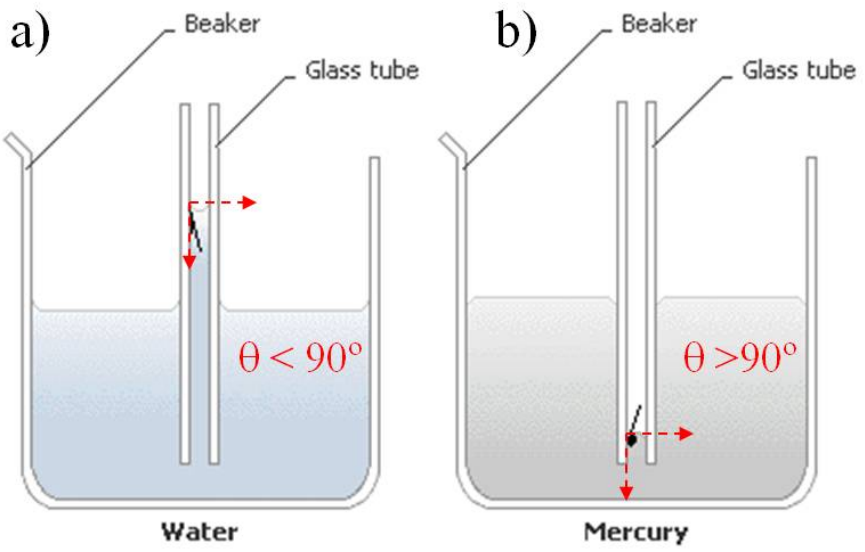


FIGURE 3.4: Schematic of capillary action for two different liquids: (a) water and (b) mercury.

When a capillary tube is immersed into a liquid, the liquid comes in contact with the inside wall of the tube, forming an angle known as the *contact angle*. The red arrows in Figure 3.4 indicate a contact angle of 90°. This represents a measure of the balance of the forces that exist in the interaction between the liquid and the surrounding solid: the cohesive and the adhesive forces.

The cohesive forces are defined as the attractive forces exerted on a liquid molecule by the neighbouring molecules, while the adhesive forces are defined as the attractive forces exerted on a liquid molecule by the molecules in the surface of the surrounding solid. The cohesive forces between liquid molecules are responsible for the phenomenon known as *surface tension*. At the surface of the liquid, the molecular cohesive forces are not balanced and therefore the surface tends to contract in order to minimize its area. The surface tension is responsible for the shape of the liquid droplets. When the adhesive

forces are stronger than the cohesive ones, the liquid is able to spread out on the solid surface. In this case the contact angle is lower than 90°and the liquid in contact with the solid wall will ascend the capillary tube as shown in Figure 3.4(a), where the capillary action for water is illustrated. On the contrary, if the cohesive forces in a liquid prevail on the adhesive ones the contact angle is greater than 90°and the liquid will avoid the contact with the capillary tube, as shown for mercury in Figure 3.4(b).

The capillary force $F_c$ for a circular tube can be expressed by:

$$F_c = 2\pi a \sigma cos\theta \tag{3.51}$$

where $a$ is the radius of the tube, $\sigma$ is the surface tension and $\theta$ the contact angle.

The friction force $F_f$ is related to the *viscosity* of the liquid, a measure of the resistance of the liquid to be deformed by external stress. The value of the viscosity, together with the dimension of the capillary tube, determines if the flow is laminar or turbulent, simply referring to the Reynolds's number:

$$Re = \frac{2\rho a U}{\mu} \tag{3.52}$$

in which $\rho$ is the density, U is the velocity of the liquid column and $\mu$ the viscosity of the liquid. If Re<2300 then the flow is *laminar*, which means that the liquid flows smoothly. On the other hand, if Re>2300, the flow is called *turbulent* which means that the liquid experiences irregular fluctuations.

The density and viscosity of the liquids used in the experiments for the present work and the dimensions of the capillary tubes always lead to a condition of laminar flow. It is therefore possible in our discussion to apply Poiseuille's law for a circular tube as follows:

$$F_f = -8\pi \mu L U \tag{3.53}$$

where L is the length of the liquid column.

In order to speed up the capillary filling process, an overhead pressure can be applied and the resulting force is expressed by:

$$F_p = \Delta P \pi a^2 \tag{3.54}$$

where ΔP is the difference between the pressure applied on the two ends of the capillary tube.

Finally the vertical column of liquid is subject to the gravitational force which can be expressed as follows:

$$F_g = -\pi \rho g a^2 L \tag{3.55}$$

where g is the gravitational constant.

The final equation that describes the filling of a circular capillary tube, and takes into account all the forces described above is known as *Navier-Stokes equation*, [Batchelor, 2000]:

$$\frac{\partial}{\partial t} = 2\pi a \sigma cos\theta + \Delta P \pi a^2 - 8\pi \mu L U - \pi \rho g a^2 L \tag{3.56}$$

Expressing the velocity U in terms of column length and time U=$\partial L/\partial t$, the equation that describes the capillary process is simplified as follows:

$$\frac{\partial^2}{\partial t^2}(L^2) + B\frac{\partial}{\partial t}L^2 + 2gL \tag{3.57}$$

where the constants A and B are respectively:

$$A = \frac{4cos\theta + 2\Delta P a}{\rho a} \qquad B = \frac{8\mu}{\rho a} \tag{3.58}$$

I have carried out experiments to verify that it is possible to accurately predict the filling time of liquid in a PBF. The fibre used for this series of experiments is presented in the images of Figure 3.5:

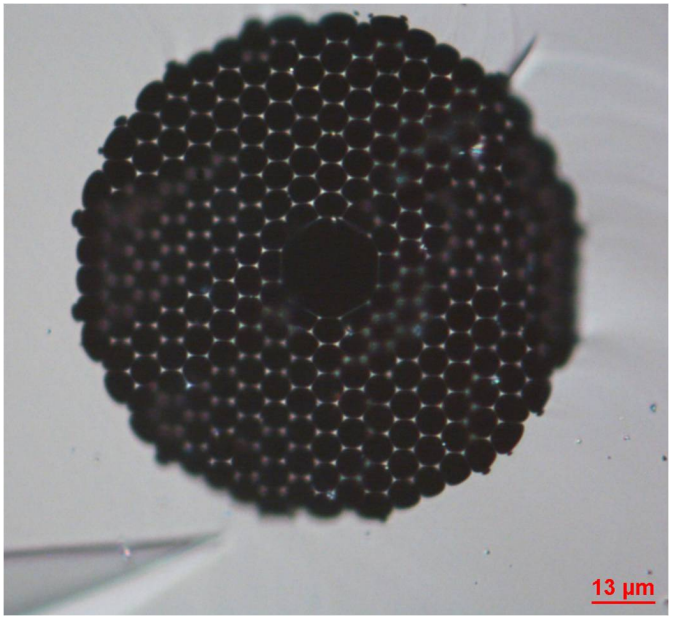


FIGURE 3.5: Microscope image of the PBF used to investigate the capillary action within this thesis.

Figure 3.5 shows a microscope image of the fibre, which was provided by Dr. Marco Petrovich. The 19-cell core fibre has a core radius of 9.15$\mu$m, while the average radius of the cladding holes is 2.40$\mu$m. Approximating the core and cladding holes to capillary tubes, it is possible to apply Eq. 3.57 to estimate the filling time of a liquid into the fibre. Water has been chosen as the liquid to test the model for various reasons: it is safe, easy to handle and it is readily available.

The parameters of water at room temperature (25°C) are reported in Table 3.2:

TABLE 3.2: Parameters of water at room temperature [Lide, 2005].

| Surface Tension [$10^{-2}$N/m] | Contact angle [deg] | Viscosity [$10^{-3}$Pa·s] | Density Kg/m$^3$ |
|---|---|---|---|
| 7.8 | ∼0 | 1 | 999 |

If the fibre is kept horizontally, it is possible to neglect the gravitational term in Eq. 3.57 and the equation can be solved analytically using the following expression:

$$L(t) = \sqrt{\frac{A}{B^2}e^{-Bt} + \frac{At}{B} - \frac{A}{B^2}} \tag{3.59}$$

where the constants A and B are the same as in Eq. 3.58.

The water infusion time has then been evaluated using the proposed mathematical model, as illustrated in Figure 3.6:

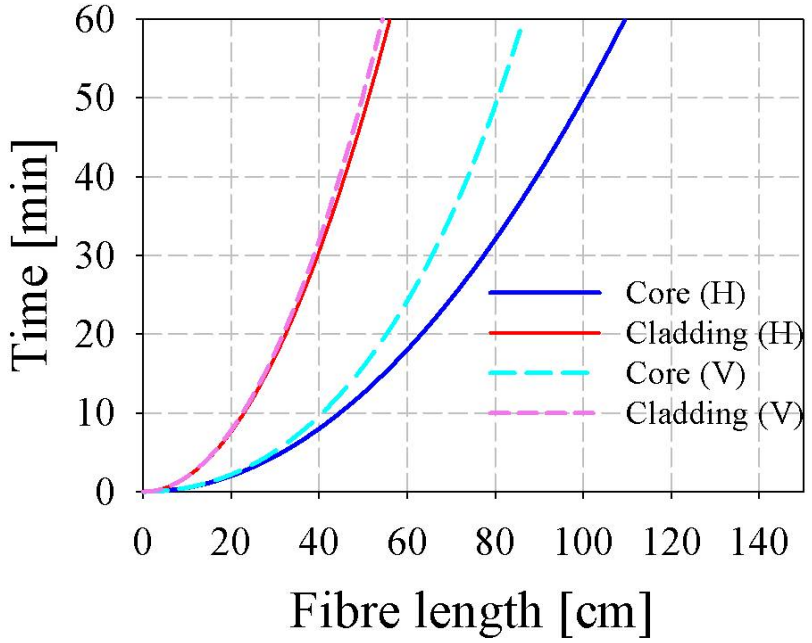


FIGURE 3.6: Simulated water filling time for the PBF core and cladding when the fibre is placed horizontally (solid lines) and vertically (dashed lines) when compared to the ground.

Figure 3.6 shows the simulated water infusion time (when no pressure is applied) when the capillary tube is placed horizontally and when it is placed vertically with respect to the ground. When no gravity is applied, that is the tube is placed horizontally, the resulting modelling time for the core hole is represented by the blue line and that for the cladding holes by the red line. As expected, the figure shows that the filling time of the core hole is significantly shorter than that of the cladding holes.

If the gravity force has also to be considered, i.e., the fibre is filled while kept in a vertical position with respect to the ground, then Eq. 3.57 must be solved numerically. The solution for the core and the cladding holes is also shown again in Figure 3.6, respectively by the light blue and the pink dashed lines. It is clear from the above figure that the gravity force has a stronger effect on the larger capillary tube, while it can be neglected for smaller capillaries. From the figure it is also possible to observe that the gravity effect is negligible with very good approximation for very short pieces of fibres ($< 15$cm).

#### 3.3.1.1 Verification of the model

In order to experimentally validate the model proposed above, it is possible to use a very simple system, consisting of a small beaker filled with the testing liquid, in this case water, and a microscope. One end of the fibre is dipped in the water, while the other end is inspected under the microscope keeping the rest of the fibre as straight as possible. The piece of fibre that is bent to be dipped into the water, as well as the one that is bent to be inspected under the microscope, is very short, <2cm, so that, according to the results shown in Figure 3.6, gravity effect does not need be taken into account. Using the microscope and pieces of fibre of various lengths it has been possible to take images such as those of Figure 3.7 that shows the filling status at various stages.

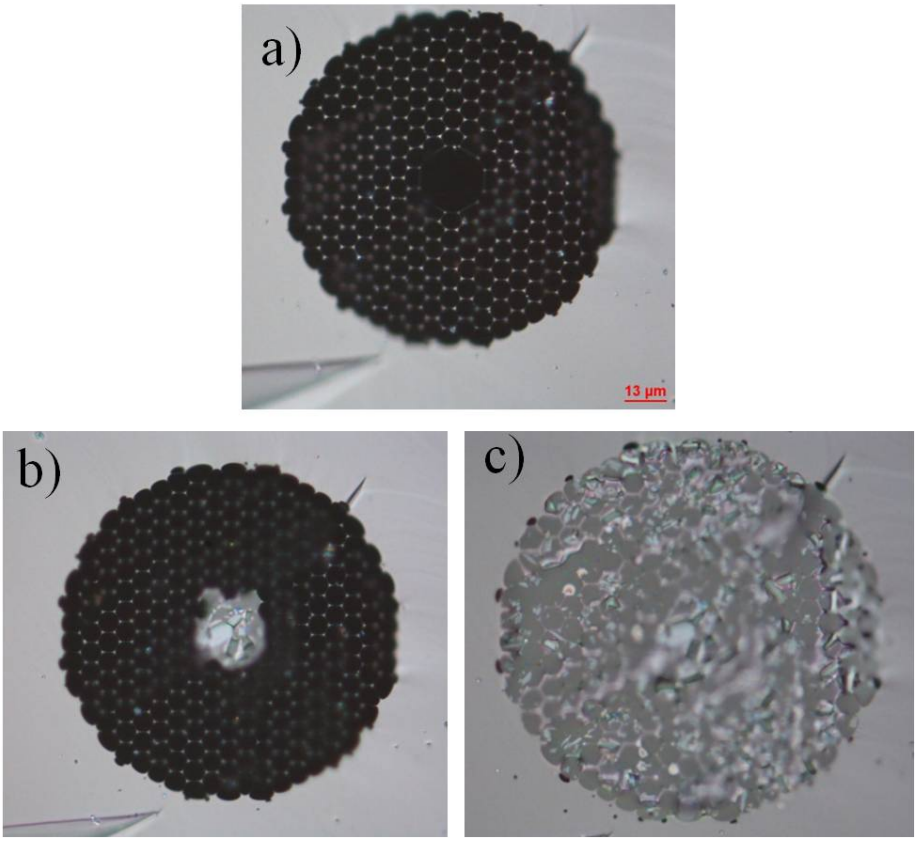


FIGURE 3.7: Microscope images of the PBF used to investigate capillary action with water at different stages: a) empty fibre; b) filled core; c) completely filled fibre.

Figure 3.7(a) shows the empty sample at the beginning of the experiment; Figure 3.7(b) shows the tip of the fibre after core only has been filled and Figure 3.7(c) shows the fibre when all the holes have been filled.

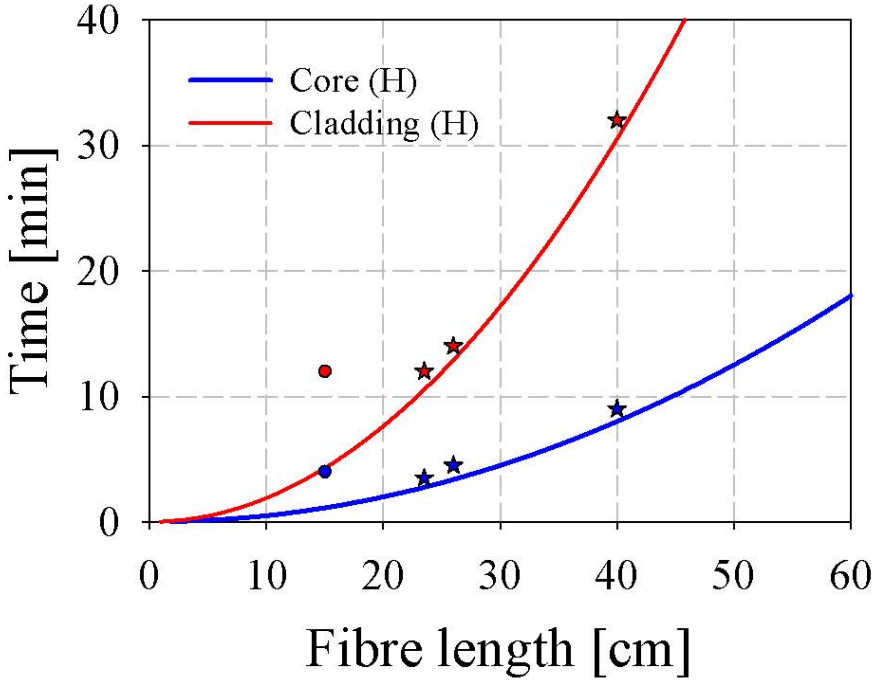


FIGURE 3.8: Measured (star points) and simulated (solid lines) infusion time of water in the PBF used within this work.

Using this simple setup, several data have been collected. Figure 3.8 shows the predicted filling time for the fibre core and cladding and the experimental data collected with the setup described above. It is possible to see that the experimental data agree with the model quite well in all the measurements but in the one which was carried out with the shortest piece of fibre (marked with a "•"). This measurement represents the very first attempt made which was carried out while keeping the light of the microscope on throughout the measurement. The heat coming from the light bulb heated the fibre up, thus resulting in the evaporation of the water and in a slower infusion process. Therefore, for the remaining experiments, the microscope lamp has been switched off and has been turned on for only ∼1 minute just before the time predicted by the model, to reduce as much as possible the influence of heat coming from the lamp on the infusion time. The remaining points on the graph have been taken following this procedure and are marked with an asterisk.

#### 3.3.1.2 Selective filling

For some applications it is important to be able to fill a microstructured fibre selectively, i.e., just its core or its cladding holes, depending on the particular application that the filled fibre is intended for. As shown in Figure 3.6 and Figure 3.7 a larger capillary tube, in this case the core of a photonic bandgap fibre will be filled in a shorter time compared to a smaller tube, the cladding holes.

It is possible to exploit this result to implement a selective filling technique [Huang *et al.*, 2004], based on the use of a UV curable liquid and on a multistep process as described in the chart of Figure 3.9.

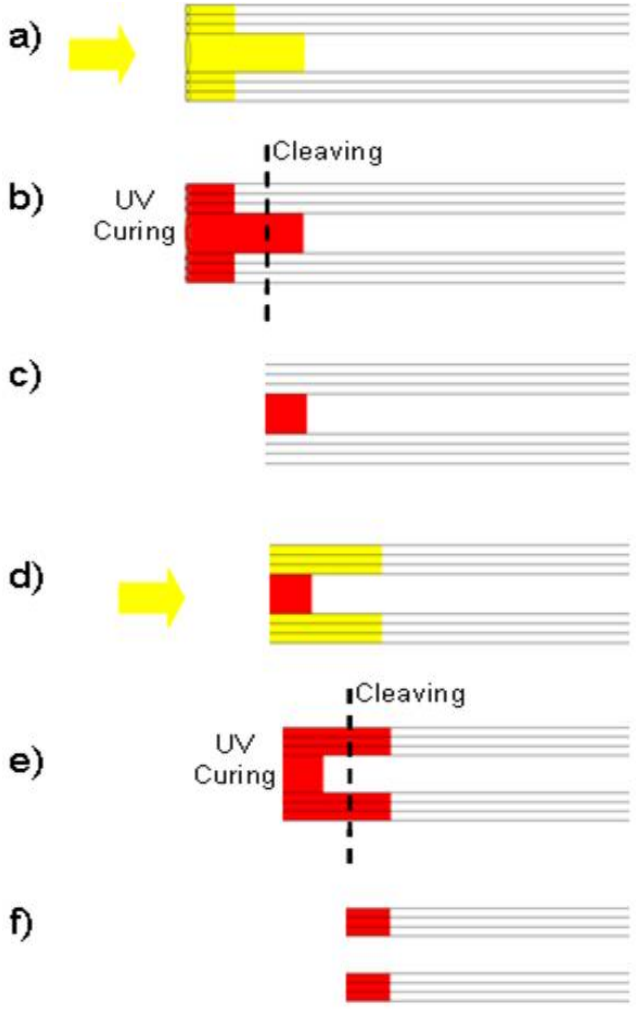


FIGURE 3.9: Schematic diagram of the selective filling technique.

The first step consists in filling the fibre with a UV curable liquid whose flow can be considered laminar, so that it is possible to apply the model studied in the previous Section. According to the numerical model, the core will be filled in a shorter time when

compared to the cladding, so that there will be a difference in the infusion length (a). The second step involves the UV curing of the liquid and the cleaving of the fibre at a convenient position (b) that leaves only the core filled (c). The cladding holes are now accessible, since the core is blocked by the UV cured liquid. If a filled cladding is needed, it is possible, at this stage, to fill the fibre with the desired liquid and, by simply cleaving the fibre after the core-filled section, a cladding-filled MOF is obtained. If, on the other hand, a selectively filled core is needed, then a few more steps are required. The fibre, having its core blocked, will be then re-dipped in the UV curable liquid (d) and another step of curing and cleaving is needed (e) to finally leave to core accessible to be filled with any liquid (f). The main advantage of this method relies on the fact that it is suitable both for only core and only cladding filling.

There are also other ways to selectively fill a fibre, such as the technique based on the use of a fusion splicer. It has been demonstrated indeed, that by setting the correct parameters of fusion current and fusion duration of the process, the outside holes of a MOF may collapse, while the central hole, the core, can remain open and ready to be filled with any liquid [Xiao *et al.*, 2005]. This method however, does not give any chance to fill just the cladding holes, unless it is used to replace the first two steps in Figure 3.9. Recently, a new technique for the selective filling of fibre holes has been presented: the fibre is covered by a UV-curable adhesive and the selected holes are sealed by a 3D UV laser writing system [Vieweg *et al.*, 2010]. The non-sealed holes are then filled by capillary action.

The first steps towards the implementation of the selective filling method described in Figure 3.9 have been made. A UV curable liquid, Efiron PC-373 from Luvantix [www.luvantix.com], which is commonly used for the purposes of fibre coating, has been chosen as the liquid to perform the experiment. Efiron PC-373 presents the following parameters, summed up in Table 3.3.

Table 3.3: Parameters of Efiron PC-373 at room temperature [Lide, 2005].

| Surface Tension [$10^{-2}$N/m] | Contact angle [deg] | Viscosity [$10^{-3}$Pa·s] | Density Kg/m$^3$ |
|---|---|---|---|
| 2.0 | ? | 5500 | 1150 |

The Reynolds's number (Eq. 3.52) for Efiron PC-373 in a micron-scale tube is below the limit of 2300, which means that the flow can be considered laminar and thus the

modelling previously reported can be applied. There is no information on the contact angle of the liquid. As shown in Figure 3.10, where various contact angles have been considered for the calculation of the infusion time of Efiron PC-373 in the core and cladding holes of the PBF of Figure 3.5, this value strongly influences the infusion time. However, from the model it is also clear that the high viscosity of the liquid makes the process really slow. After 60min, indeed, less than 1cm of fibre will be filled: under this condition, it is very difficult to apply with good accuracy the selective filling process previously described.

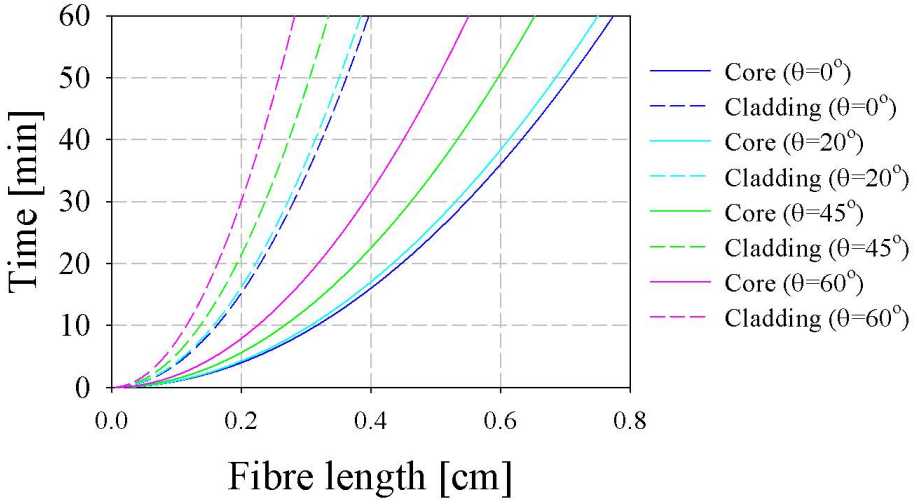


FIGURE 3.10: Dependence of the infusion time on the contact angle for Efiron PC-373.

It is necessary to speed the process up and this can be done by applying an overhead pressure to the liquid. When pressure is applied, the corresponding force is more relevant than the sole capillary force. Considering the expression of the forces due to the capillary action and the pressure applied and the value of surface tension of Efiron PC-373, it is relatively straightforward to prove numerically that the force due to the applied pressure is at least one order of magnitude higher than the one due to the capillary force.

Figure 3.11 shows that, by applying a pressure of 2 bars, the dependence of the filling time on the contact angle is strongly reduced and therefore the numerical curves for the various values of contact angles are no longer distinguishable. It is also observed that after 60 minutes a difference of nearly 4 cm in length is achieved between the liquid column in the core and the cladding holes.

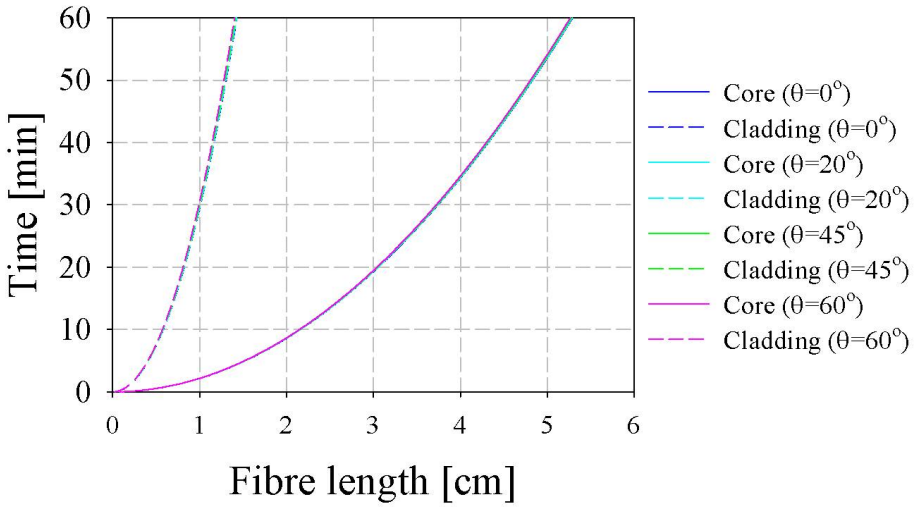


FIGURE 3.11: Dependence of the filling time of Efiron PC-373 on the contact angle when a pressure of 2 bars is applied.

A way to apply a known pressure to the liquid involves the use of a syringe pump, as shown in the set up of Figure 3.12.

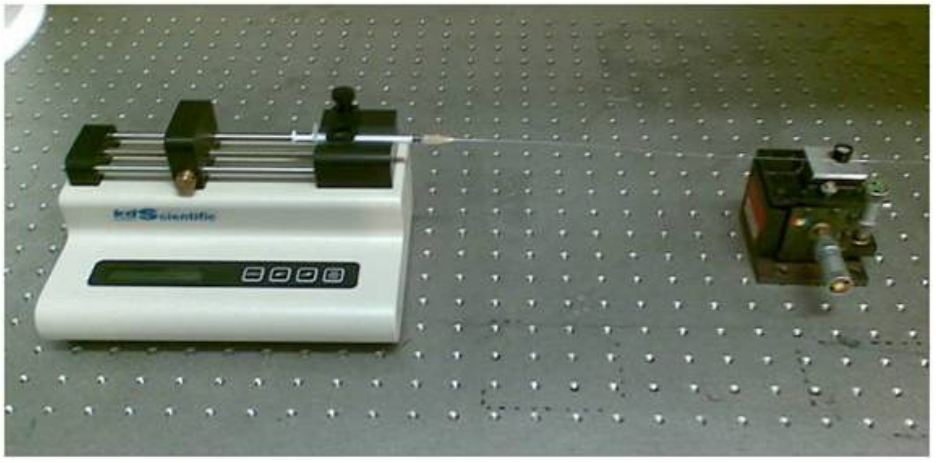

FIGURE 3.12: Setup used to fill a fibre applying a known value of pressure.

On the syringe pump used for this experiment it is possible to set the *flow rate* of the liquid passing through the orifice of a standard syringe. The flow rate is given by:

$$\Phi = AU \tag{3.60}$$

where A is the area of the section and U the velocity of the liquid column. The pressure associated to the set value of flow rate is given by *Poiseuille*'s law:

$$\Phi = \frac{\pi a^4 |\Delta P|}{8\mu L} \tag{3.61}$$

Using this formula, it is straightforward to work out the pressure that is related to a certain flow rate for a given tube with radius a and length L. Once the flow rate has been set for the aperture of the syringe that is holding the fibre, this remains constant even if the cross-section changes, that is the change in section between the diameter of the syringe and the diameter of the fibre. This is due to the property of a fluid to move in such a way that the mass is conserved. This concept is easily expressed by the continuity law:

$$A_1 U_1 = A_2 U_2 \tag{3.62}$$

where $A_1$ and $A_2$ are two different sections of a capillary tube and "$U_1$ and $U_2$ are the respective values of the speed of the liquid in the two sections.

This set up, despite its simplicity and flexibility, involves many practical problems: the choice of the syringe with the right diameter, the choice of a needle whose internal diameter is big enough to hold the fibre, or the right glue to bond together the glass of the fibre and the metal of the needle.

### 3.3.2 Toluene filled MOFs

$CS_2$ is an extremely toxic liquid [www.sciencelab.com] and therefore dedicated cells need to be used in order to avoid any contact with it. For this reason, toluene, (a less hazardous liquid) was used instead in the preliminary experiments, which were mainly intended to look at the practical problems that might arise when filling a fibre with a liquid and guiding light through it. The optical parameters for toluene are shown in Table 3.1, [Sutherland, 1996]. The infusion time model discussed in the previous Section can be easily applied to toluene. The parameters of the liquid needed for the model are shown in Table 3.4.

Toluene is a solvent and therefore is very volatile. In general, the evaporation rate of a liquid is found to be directly proportional to the diameter of the container where the

TABLE 3.4: Parameters of toluene at room temperature [Sutherland, 1996].

| Surface Tension $[10^{-2}$N/m] | Contact angle [deg] | Viscosity $[10^{-3}$Pa·s] | Density Kg/m$^3$ |
|---|---|---|---|
| 2.85 | 22.5 | 0.59 | 870 |

liquid is stored [Silberberg, 2006]. Therefore, a beaker with a small radius is needed to store the liquid for this set of experiments. The use of a small container has forced us to keep the fibre sample bent over a length of more than 15cm, when using samples of fibre longer than 30cm, and this physical arrangement has necessitated the gravity force to be taken into account when modelling the corresponding infusion time.

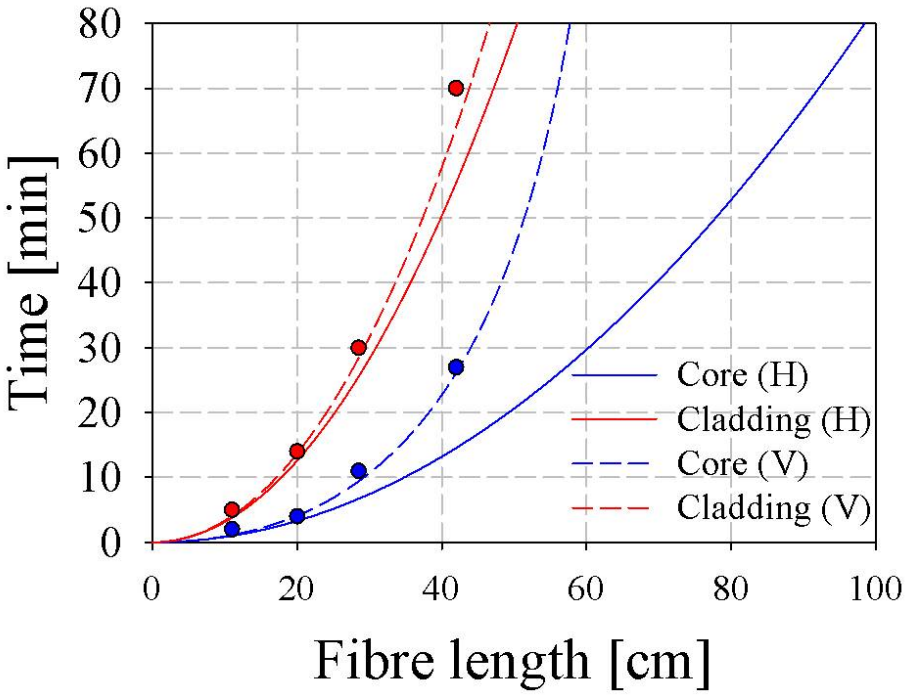


FIGURE 3.13: Measured (dots) and simulated (solid and dashed lines) infusion time of toluene in the PBF. The dashed and the solid lines represent the case in which the gravity forces is included or neglected respectively.

Figure 3.13 shows the simulated infusion time of toluene in the hollow core fibre of Figure 3.5 when the gravity effect is included and when it is not. Figure 3.13 illustrates that the experimental results are in good accordance with the model of the infusion time of toluene in a photonic bandgap fibre when the gravity effect is taken into account. The solid lines represent the case of the fibre kept horizontal with respect to the ground, while the dashed lines describe the modelled filling time for a fibre kept vertically. The figure shows that the data collected follow the model that consider the fibre placed

vertically for longer samples of fibre, while there is no difference for the shorter samples. In general, it is possible to say that the experimental results follow quite well the model, allowing the prediction of the time required to fill the fibre in the experiments with good approximation.

The MOF available for experiments, shown in Figure 3.5, is a photonic bandgap fibre that guides light at 1550nm by the photonic bandgap effect. This has been theoretically demonstrated by simulations performed by Dr. Poletti within the ORC. Figure 3.14 shows the propagation in a 1m length of the simulated structure and suggests that a single mode is supported.

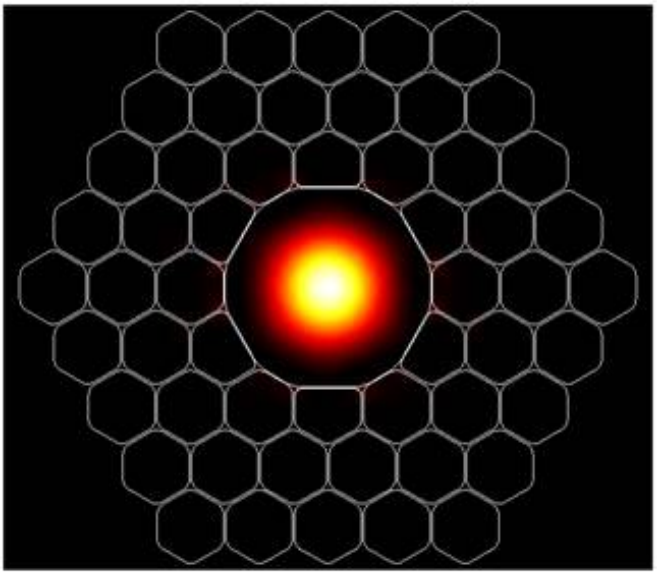

FIGURE 3.14: Simulated guidance in the hollow-core PBF by photonic bandgap effect, courtesy of Dr. Poletti.

When the fibre is completely filled with toluene, its core will present a refractive index higher than the one of the silica, while the refractive index of the cladding will be slightly lower than this value. In this case the fibre will guide light by TIR but the propagation is not single mode. Figure 3.15 shows the results of the simulation of the toluene filled sample, from which it is clear that the fibre is heavily multimoded.

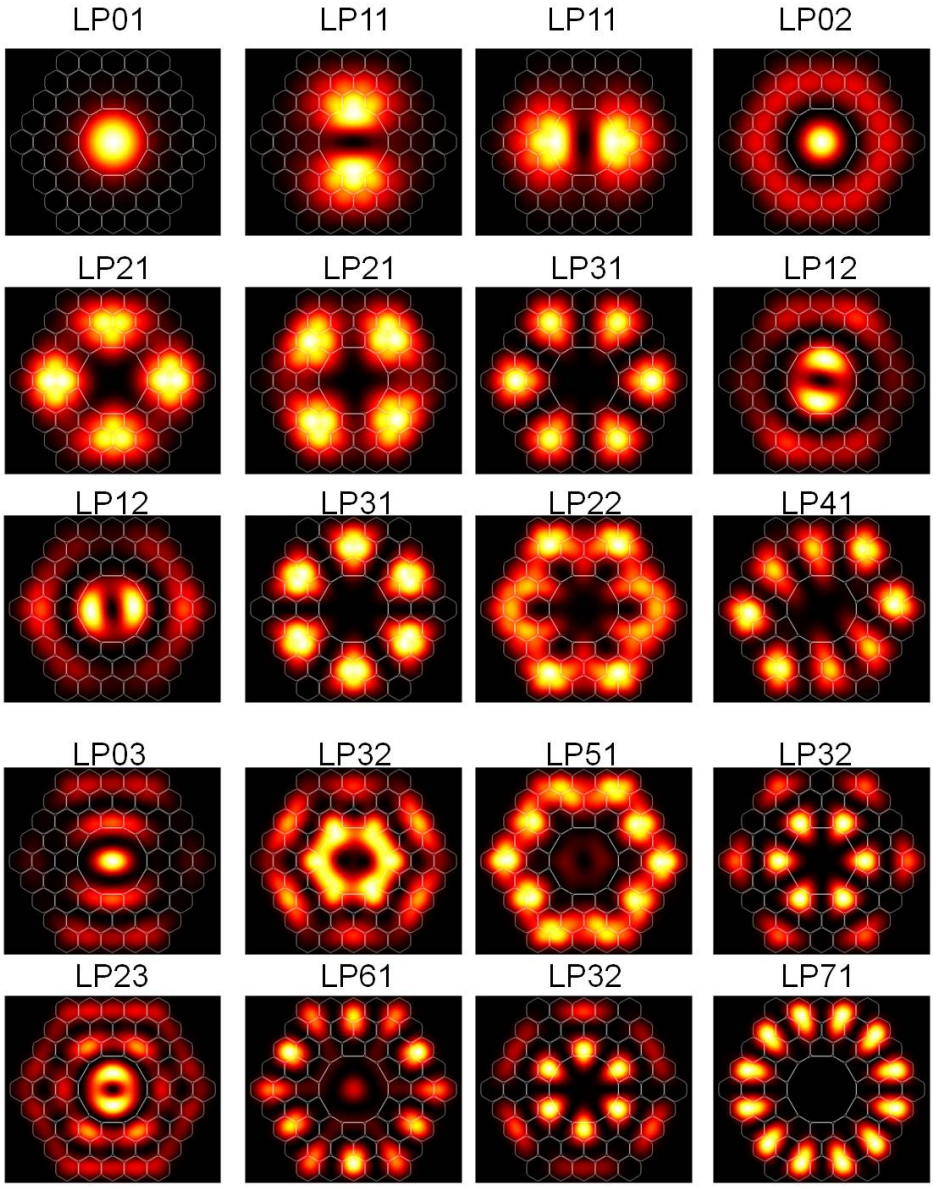


FIGURE 3.15: Simulated guidance by total internal reflection in a toluene filled sample, courtesy of Dr. Poletti.

A simple experiment, involving the use of an IR camera, has proven that the propagation in the fibre is single mode when the fibre is empty, while higher order modes are excited when the fibre is filled with toluene.

In the empty sample, indeed, Figure 3.16(a), the light is propagating by photonic bandgap effect and is well confined in the core. When the sample is filled with toluene, light is guided by TIR and more than one mode can be excited at the same time, as shown in Figure 3.16(b). Also, additional cladding modes can be clearly distinguished in the filled sample.

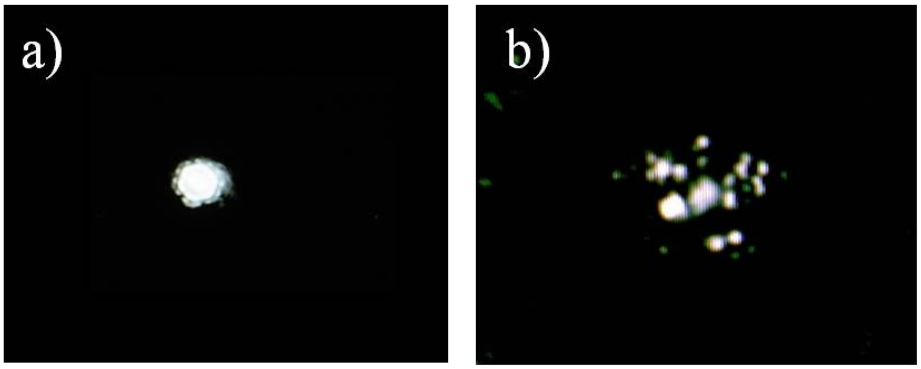


FIGURE 3.16: Propagation by (a)photonic bandgap effect in the empty sample, and(b) by TIR in the filled sample where light is guided both in the core and in the cladding.

As already mentioned before, toluene is a solvent, so it easily evaporates when in contact with air. The force exerted by surface tension and the very small size of the capillary tubes of the MOF, will prevent the toluene to evaporate from the fibre. However, it has to be taken into account that the liquid may reach high temperatures when it is heated up by the laser beam and thus evaporate, leading to a non-uniform distribution of toluene in the fibre which might affect the modal properties of the waveguide of Figure 3.16(b).

In order to understand how this could affect our measurements, the power dependence of a toluene filled short sample was investigated. A set up consisting in a CW laser, at the wavelength of 1550nm, amplified by an EDFA was used to perform this experiment. A ∼10cm long sample was then filled with toluene by capillary action: the fibre was kept horizontal and one tip was dipped into toluene. The experimentally validated capillary filling model predicts that a sample of this length would be completely filled with toluene after 5 minutes.

Figure 3.17 shows how the output power of an empty sample followed linearly the input power (red solid line). In the case of the filled sample, this linearity was kept just for low values of power. By increasing the input power, it is possible to see that the output values were not stable, but fluctuated as shown by the vertical bars, resulting in an unstable trend. The output values corresponding to the three highest input powers were recorded over a shorter period of time to prevent the evaporation of the liquid from the fibre. At the highest value of input power (10dBm), the filled fibre was illuminated for ∼5min. At the end of this period of time, the power at the output of the filled sample

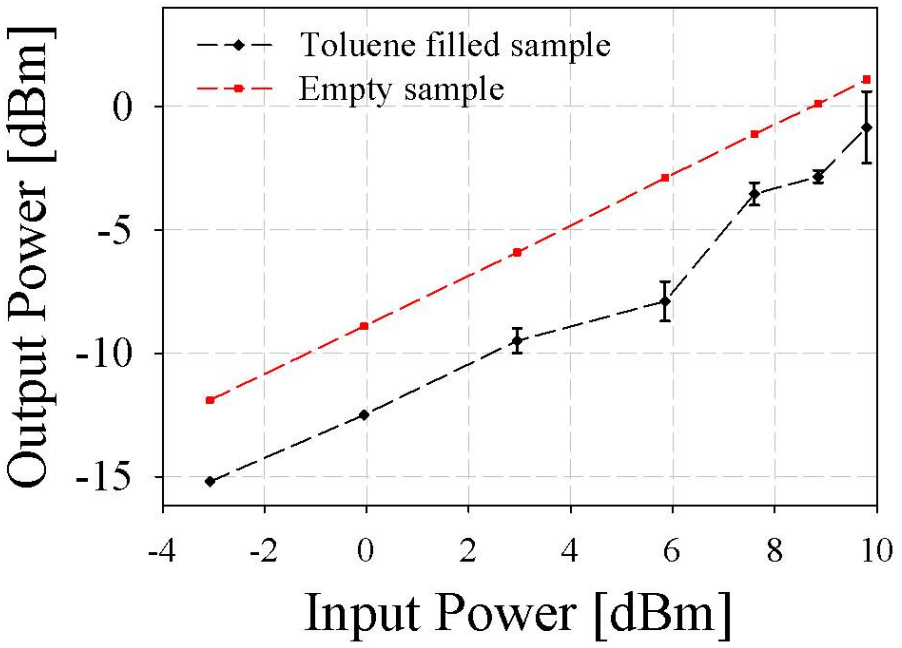


FIGURE 3.17: Comparison between the power dependence of an empty and a toluene filled sample of PBF.

increased to approximately the same output power value as that obtained in the case of the empty sample, indicating that the liquid had evaporated.

This Section has highlighted the main issues related to the development of nonlinear liquid-filled fibre techniques. The nonlinear liquid to be employed has to be chosen carefully, as most of them are highly toxic and any contact with the liquid must be avoided. Another issue that arises is represented by the filling technique. When selective filling is required, then the development of an appropriate technique is necessary. A method has been proposed and the main problems related to it have been discussed. MOFs can be also entirely filled by capillary action and a mathematical model has been reported and experimentally verified. However, once the fibre is filled with the liquid, the dependence of the liquid evaporation rate on its temperature has to be taken into account. The high temperature reached by the liquid when exposed to a light beam is responsible for unstable measurements, as experimentally verified by using a toluene filled PBF.

The difficulties encountered in developing a liquid filled fibre technology have made us move our interest towards the development of nonlinear fibres made of higher nonlinearity glasses. Some basic aspects of soft glass technology are introduced in the next Section

and the results achieved with some fibres based on this technology will be illustrated in the rest of this thesis.

## 3.4 Soft glass MOFs

For a dielectric material the linear refractive index, n, and the nonlinear refractive index, $n_2$, can attributed to the polarizability of the constituent ions [Adair *et al.*, 1989; Thomazeau *et al.*, 1985]. Therefore, glasses consisting of ions with heavy atomic weight or large ionic radii will generally exhibit high values of n and $n_2$. Figure 3.18 illustrates the relation between n and $n_2$ for various optical glasses, including fluoride glasses, silica, lead silicate glasses, tellurite glasses, other heavy metal oxide (HMO) glasses, and chalcogenide glasses.

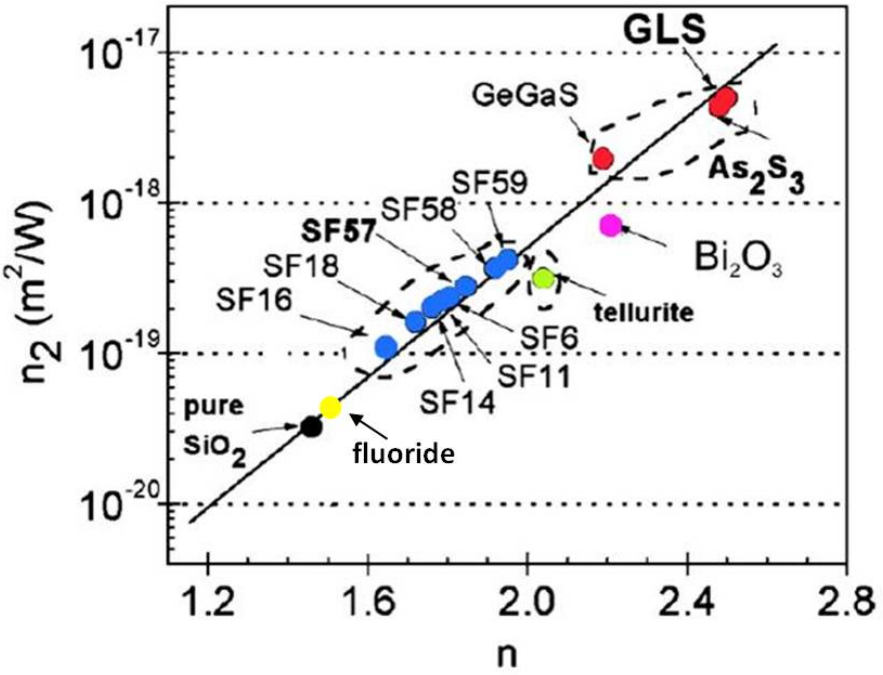


FIGURE 3.18: Comparison between the linear and the nonlinear refractive index of various available glasses, taken from [Feng *et al.*, 2005a].

It can be seen that the nonlinear refractive index $n_2$ increases with the linear refractive index n, according to the empirical Miller's rule [Miller, 1964]: the nonlinear optical response of a material is related to its linear response. In particular, high-index HMO glasses and chalcogenide glasses (based on S, and Se) exhibit a nonlinear refractive index $n_2$, which is 1-3 orders of magnitude higher than silica glass. For example, the nonlinear

coefficient $n_2$ for the lead-silicate glass SF57 is $\sim 4 \cdot 10^{-19} m^2/W$ at 1060nm [Monro and Richardson, 2003], for tellurite glass is $\sim 5.9 \cdot 10^{-19} m^2/W$ at 1550 nm [Mori *et al.*, 2004], and for bismuth-oxide glass is $\sim 3.2 \cdot 10^{-19} m^2/W$ at 1550 nm [Ebendorff-Heidepriem *et al.*, 2005]. This indicates that by choosing a high-index glass as the host material for a nonlinear fibre, the nonlinear coefficient can be enhanced by 1-3 orders of magnitude.

Chalcogenide glasses seem to be very promising as they exhibit the highest value of nonlinear coefficient amongst the other glasses. Chalcogenide fibres showing a nonlinear coefficient of $1200\text{W}^{-1}\text{km}^{-1}$ have been reported, [Ta'eed *et al.*, 2006a]. Higher values of nonlinear coefficient, up to $6800\text{W}^{-1}\text{km}^{-1}$ have been achieved in tapered chalcogenide fibres, [Mägi *et al.*, 2007] and even higher values, up to $10000\text{W}^{-1}\text{km}^{-1}$ have been reported in chalcogenide-based waveguides, [Lamont *et al.*, 2008]. Tellurite glasses show a high nonlinear refractive index, they are more stable than chalcogenide glasses [Wang *et al.*, 1994] and also show a good thermal and mechanical stability. Tellurite based fibres with a nonlinear coefficient as high as $680\text{W}^{-1}\text{km}^{-1}$ have been reported [Mori *et al.*, 2004]. Bismuth is another attractive material for the fabrication of highly nonlinear fibres. It shows a high nonlinear refractive index, and does not contain any toxic elements such as Pb, As, or Se [Sugimoto *et al.*, 1999]. Moreover, it shows good mechanical and thermal stability that facilitate the fibre fabrication. Bismuth oxide-based HFs have been fabricated showing a nonlinear coefficient $\gamma$ as high as $1100\text{W}^{-1}\text{km}^{-1}$ [Ebendorff-Heidepriem *et al.*, 2004a]. Compared to the glasses presented above, lead silicate represents an attractive family of glasses, as, in addition to the high nonlinear refractive index, they show higher thermal stability and less steep viscosity curves than other non-silica glass alternatives [Fujino *et al.*, 1998]. Lead silicate based HFs have been fabricated with a $\gamma$ up to $1860\text{W}^{-1}\text{km}^{-1}$ [Leong *et al.*, 2005b].

As illustrated in Section 2.2.5 most of these glasses exhibit a high normal material dispersion at 1550nm, which gives the main contribution to the overall dispersion of the fibre. However, for many nonlinear applications in the telecoms field, a ZDW or a low dispersion value at 1550 is highly desirable. Analogously to a silica-based MOF, the presence of micron-scale features in the cladding of a soft-glass MOF gives the possibility to engineer the dispersion profile of the final fibre.

The prospect of achieving a low and flat dispersion profile at the wavelength of interest has been investigated in many different structures made of highly nonlinear glasses.

Liao and co-workers have designed and fabricated three solid core tellurite-based HFs surrounded by six holes, with a different hole diameter in the cladding of the samples, [Liao *et al.*, 2009a]. The HFs were designed to exhibit a flat dispersion profile with two ZDWs, the first around 1$\mu$m and the second around 1.6$\mu$m. Further improvements in the structure have allowed for the fabrication of a new tellurite-based HF showing a ZDW at 1390nm [Liao *et al.*, 2009b]. Very recently, a tellurite HF with a core diameter of $\sim$2.7$\mu$m surrounded by four air holes of diameter in the range of 3 to 5$\mu$m was designed and fabricated to exhibit a ZDW at 1434nm [Qin *et al.*, 2010]. Despite the ZDW lying close to the C-band the dispersion value at 1550nm of the fibre exceeds the 200ps/nm/km.

Despite the large anomalous dispersion value at 1550nm of bismuth-oxide based glasses, as shown in Figure 2.11, acting on the cladding features of a HF has led to some interesting results. Dispersion shifted HF fibres with anomalous dispersion of 40ps/nm/km at 1550nm have been predicted in an 2.4$\mu$m air-suspended core fibre surrouded by three large holes (>5$\mu$m), [Ebendorff-Heidepriem *et al.*, 2004a]. A bismuth-oxide fibre with a low normal dispersion value of -15ps/nm/km at 1550nm has also been reported [Nagashima *et al.*, 2006].

Dispersion shifted fibres have been also fabricated using lead-silicate glasses. Fibres with ZDW in the range of 1300nm up to 1600nm have been designed and fabricated using the commercially available lead-silicate Schott SF6 glass, [Kumar *et al.*, 2002]. The relatively low dispersion value of bulk SF6 (-30ps/nm/km), [Schott, 2003], resulted in a low normal dispersion HF at 1550nm (<5ps/nm/km) for a fibre with a core diameter of 5$\mu$m. Lead-silicate based HFs with a ZDW at $\sim$1400nm and an anomalous dispersion profile at 1550nm have also been fabricated [Petropoulos *et al.*, 2003] as well as lead-silicate HFs with a ZDW in the range between 1530nm and 1600nm have also been fabricated, [Asimakis *et al.*, 2007]. These fibre structures also show a relatively low dispersion slope ($\sim$0.2ps/nm$^2$/km) resulting in low overall dispersion profile at telecoms wavelengths ($|D|$ <20ps/nm/km).

The results reported above indicate that the combination of the microstructured fibre technology with the use of highly nonlinear glasses is a promising route to the development of short length highly nonlinear fibre devices with low dispersion in the telecoms wavelength range. Conventionally, efforts in this direction have targeted the design and

fabrication of HFs. However, issues relating to the fabrication of such precisely controlled structures, as illustrated in Section 2.1 have led, in the last few years, to the development of all-solid MOFs, that combine the flexibility of a microstructured cladding with the advantages of fabricating a solid structure. By the time that work on this project had started, two different geometries had been proposed: cladding holes filled with a compatible glass or cladding structure arranged in multiple concentric layers of different glasses, and in both cases highly nonlinear fibres had been successfully drawn, [Feng *et al.*, 2003a], [Feng *et al.*, 2005c].

In this project, we have chosen lead silicate glasses as the material for the fibre fabrication and explored different designs including both holey and all-solid structures for the fabrication of a highly nonlinear fibre with low and flat dispersion at telecoms wavelengths. The results achieved within this project are reported in the following Chapters.

## 3.5 Conclusions

This Chapter illustrated the various nonlinear phenomena occurring in an optical fibre and described the main parameters of an optical fibre that contribute to enhance the nonlinear effects. It introduced the nonlinear coefficient and the fibre parameters that contribute to enhance its value. Two ways of increasing the nonlinear refractive index of an optical fibre were presented: filling a HF with a nonlinear liquid and replacing silica with a glass that shows a higher nonlinear refractive index.

Liquid filled MOFs have been used for various applications such as sensing or the realisation of tunable devices, while the field of nonlinear liquid filled HFs is still relatively unexplored. This Chapter reported the first steps taken towards the development of a fibre filling technique for nonlinear applications. Following a brief overview of the available nonlinear liquids, the challenges presented by the fibre fillings were discussed. An infusion model was described and verified using water and toluene as the test liquids and a selective filling technique was illustrated.

Replacing silica with highly nonlinear glasses and combining HF and soft glass technologies allows the development of highly nonlinear, single mode, dispersion tailored fibres. Such fibres are ideal for a number of telecom applications based on nonlinear effects,

such as wavelength conversion, pulse compression, demultiplexing and supercontinuum generation. These applications are discussed in the following Chapters.

# Chapter 4

# Characterisation of small core highly nonlinear fibres

This Chapter illustrates the results of the characterisation of highly nonlinear soft glass fibres including both holey and all-solid structure designs. Three different fibre types have been considered. A HF structure was made of commercially available Schott SF57. An all-solid multi-ring design was based on Schott SF6 (core and some cladding rings) and LLF1 (cladding rings), while a simpler W-type index profile fibre was based on SF57 (core), SF6 (first cladding) and LLF1 (second cladding). The nonlinear refractive index of the lead-silicate SF57 glass is $n_2 \sim 4 \cdot 10^{-19} m^2/W$ at 1550nm, while SF6 exhibits a $n_2 \sim 2.2 \cdot 10^{-19} m^2/W$ at 1550nm [Schott, 2003]. The three fibre designs presented here all target a high nonlinear coefficient together with a tailored dispersion profile in the C-band in order to be efficiently employed in highly nonlinear systems. The measurement techniques and the corresponding setup used to characterise the fibres are described. The experimental results for each fibre design are presented, together with the advantage of each design and its potential for the realisation of highly nonlinear systems.

## 4.1 Measurement Techniques

In order to assess the optical properties of the fibres used in the experiments presented within this thesis, suitable measurement techniques have been setup.

In all the experiments carried out in this thesis, free-space coupling was chosen for launching light into the fibre, since this provided a much better control of the launching conditions over the butt-coupling technique. Note that splicing very small core soft glass fibres is not straightforward and it was not considered during the experiments described in this thesis. The fibres were mounted over a three-axis nanopositioning stage which was driven by piezoelectric controllers with a resolution of 20nm.

The light coming from the source was coupled into the input cleaved facet of the fibre by using a combination of aspheric lenses, carefully chosen in order to maximise the coupling efficiency. The range of values for the coupling efficiency reported in this thesis is between 20% and 35%. Fragility concerns forced us to use hand cleaving with a ceramic tile in all our measurements. The quality of the cleave was assessed by inspecting the fibre with a magnifying lens, to ensure that a clean cleave was obtained. A good cleave is necessary as it minimises the scattering loss at the input surface, while a clean cleave reduces the number of undesired particles on the facet that absorbs light, leading to a reduced coupling efficiency.

The fabricated fibres were not protected by an external jacket: this means that the light launched in the input facet would be able to propagate in the core as well as in the outer glass region at the interface glass/air. In order to eliminate any portion of light propagating in the fibre cladding, a solution of a high-index graphite adhesive was applied on the surface of the fibre. This acted as a highly absorbing material and was able to remove the light propagating in the outer cladding.

This Section presents the measurement techniques I applied for the characterisation of small core compound glass fibres and the corresponding setups I used.

### 4.1.1 Single mode guidance and propagation loss

The mode profile of the fibres was investigated in order to ensure single mode guidance. A CW laser source, amplified with an EDFA, was free-space coupled in the fibres. At the output of the fibre a microscope objective was used to focus the light in an infrared (IR) camera connected to a monitor. The displayed image of the fibre was used to optimise the launching conditions and to inspect the propagation modes.

The propagation losses of the fabricated fibres were measured in the C-band by using a method known as the cutback technique. Incoherent light from an EDFA operating as an ASE source was focused into the fibre and the values of power at the output of the fibre was recorded. The fibre was then shortened by ∼30cm steps and the corresponding output power value was recorded again. If $P_1$ is the power at the output of a certain length of fibre $L_1$ and $P_2$ is the output power when the fibre length is reduced down to $L_2$, then the propagation losses of the fibre can be described by the relation [Ghatak and Thyagarajan, 1998]:

$$\alpha = \frac{10}{L} log_{10} \frac{P_1}{P_2} \qquad (dB/m) \tag{4.1}$$

where L is the difference in length between the two samples $L_1$ and $L_2$ and is measured in meters. Typical losses in the fibres that I experimented with were of the order of 1dB/m and therefore I was using samples of about 3m in length. By applying Eq. 4.1 to every pair of values, the propagation losses are expressed by the mean value and the standard deviation of the set of measurements.

During this measurement, as in every other measurement performed within this thesis, it was particularly important to ensure that the coupling efficiency was kept constant, so that the power at the input of the fibre was stable. Moreover, it was necessary to ensure that no light was propagating in the cladding by applying the graphite-based adhesive as discussed above. A non-stable coupling efficiency together with out-of-core light propagation can easily result in inaccurate measurements. The quality of the cleaves of the output end of the fibre also contributed to the accuracy of the measurement. In order to minimise the effect of the cleave on the measurement, several cleaves were applied to each cutback and only the value of power corresponding to the best cleave was considered.

### 4.1.2 Birefringence properties

The birefringence of optical fibres is usually quantified through beat length measurements. For a conventional fibre the beat length can be directly measured using helium-neon (He-Ne) lasers. When visible light is launched into the fibre at 45°relative to one of the fibre's principal axes, polarization beating takes place [Ghatak and Thyagarajan,

1998]. The polarization beating together with the Rayleigh scattering from the fibre core form alternating bright and dark regions, polarization induced fringes, at the side of the fibre. The separation distance of the dark regions provides a direct measure of the beat length.

In a MOF the Rayleigh scattered light from the core is further scattered by the cladding, making the aforementioned technique difficult to apply. An alternative indirect beat length measurement based on the fringes induced in the spectral domain has been proposed [Ortigosa-Blanch *et al.*, 2000].

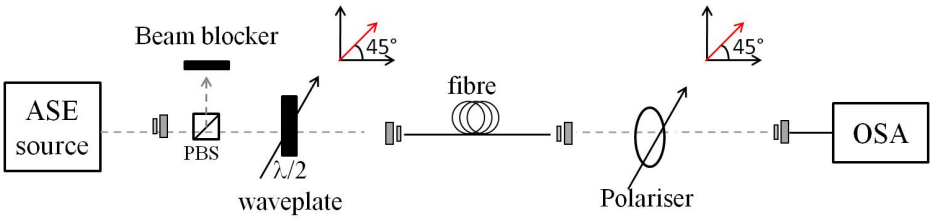


FIGURE 4.1: Experimental setup used for the measurement of the beat-length in a soft glass HFs. PBS: Polarization beam splitter.

The experimental set up implemented for the measurement of the beat length of the soft glass MOFs in the C-band is shown in Figure 4.1. The ASE light coming from an Erbium Doped Fibre Amplifier (EDFA), covering the wavelength span from 1530nm to 1570nm, was used as a broadband source. By using a polarization beam splitter and a $\lambda/2$ waveplate, the ASE light was linearly polarized at 45°relative to one of the fibre's principal polarization axes. A polarizer, acting as a polarization analyser, was placed at the output of the fibre, with its transmission axis at 45°relative to the principal polarization axis. The polarisation beating results in fringes appearing in the output spectrum. If L is the length of the fibre sample to be characterised, then the phase difference between the modes at the output of the fibre can be expressed as [Ortigosa-Blanch *et al.*, 2000]:

$$\phi(\lambda) = [\beta_x(\lambda) - \beta_y(\lambda)] = \frac{2\pi L}{L_B} \tag{4.2}$$

where $\beta_x(\lambda)$, $\beta_y(\lambda)$ are the wavelength dependent propagation constants of the two modes and $L_B$ is the beat-length. Differentiating Eq. 4.2 with respect to the wavelength leads to:

$$\frac{\Delta\phi}{\Delta\lambda} = \frac{-2\pi L}{L_B^2}\frac{dL_B}{d\lambda} \tag{4.3}$$

And therefore:

$$L_B^2 = \Delta\lambda L\left|\frac{dL_B}{d\lambda}\right| \tag{4.4}$$

The beat length can be approximated to be inversely proportional to the wavelength [Ortigosa-Blanch *et al.*, 2000]:

$$L_B \propto \lambda^{-1} \tag{4.5}$$

Using Eqs. 4.4 and 4.5, the beat length can be expressed by the relation:

$$L_B = \frac{\Delta\lambda}{\lambda}L \tag{4.6}$$

where $\lambda$ is central wavelength of the scan. Eq. 4.6 directly relates $L_B$ to the periodicity of the fringes $\Delta\lambda$ obtained in the spectral domain. The beat length is related to the birefringence by Eq. 2.8.

### 4.1.3 Nonlinear coefficient

The measurement of the nonlinear coefficient of the small core MOFs can be performed by using the SPM based technique. This technique measures the induced nonlinear phase shift of a dual frequency beat signal propagating through the fibre, where the beat signal is formed by two CW signals [Boskovic *et al.*, 1996]. The wavelength separation of the two CW signals has to be sufficiently small and the length of the fibre sufficiently short so that the effect of the dispersion can be neglected. Under these assumptions, the nonlinear phase shift of the beat signal can be expressed as [Boskovic *et al.*, 1996]:

$$\Phi_{SPM} = 2\gamma L_{eff} P \tag{4.7}$$

where $\gamma$ is the nonlinear coefficient (as defined in Eq. 3.13), $L_{eff}$ is the effective length of the fibre (as defined in Eq. 3.28), P is the average power of the beat signal. The nonlinear coefficient can be determined by measuring the SPM phase shift for different values of power in the spectral domain. The electric field that represents the beat signal is a periodic function in time and therefore it shows a discrete spectrum consisting of harmonics of the beat frequency. An example of a typical SPM spectrum is shown in Figure 4.2 where the two input CWs and the first order harmonics of the signals can be distinguished.

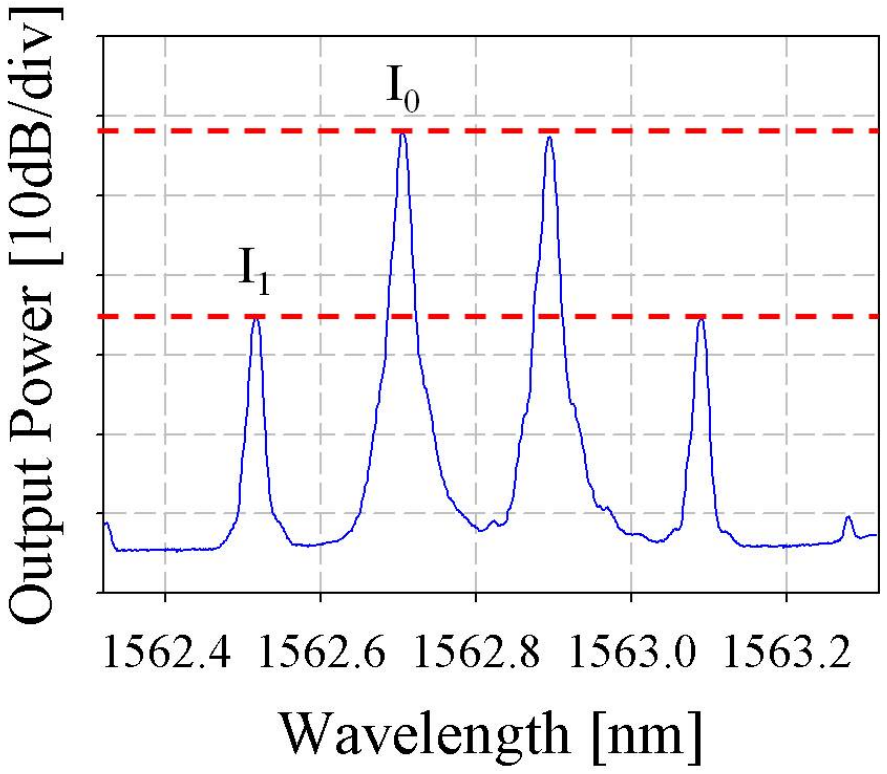


FIGURE 4.2: Typical spectrum of a beat signal that has suffered SPM, obtained from an OSA. $I_0$ and $I_1$ indicate the intensity of the zero and first order harmonics respectively.

The ratio of the peak powers has been found to be dependent only on SPM and can be expressed as follows [Boskovic *et al.*, 1996]:

$$\frac{I_0}{I_1} = \frac{J_0^2(\phi_{SPM}/2) + J_1^2(\phi_{SPM}/2)}{J_1^2(\phi_{SPM}/2) + J_2^2(\phi_{SPM}/2)} \tag{4.8}$$

where $I_0$ and $I_1$ are the intensities of the zero and first order harmonics respectively and $J_n$ indicates the Bessel function of the $n^{th}$ order [Boskovic *et al.*, 1996]. Therefore,

for a certain value of input power, the phase shift can be easily determined from a measurement of the harmonics power ratio.

As mentioned above, the SPM technique is based on the assumption that the dispersive effects in the fibre under test can be neglected. The fibre samples used in our measurements were chosen to be ∼3m in length, as for values of propagation losses of the order of a few dB/m, the maximum effective length is of the order of a few meters. Moreover, the high nonlinear coefficient of the fibres allow for a significant nonlinear phase shift even in a short length. The short fibre length, together with the choice of a small wavelength separation (0.2nm) between the two CWs, therefore ensures that the dispersive effect can be easily neglected in the nonlinear coefficient measurements.

Eq. 4.7-4.8 are valid when the signal is aligned to the principal polarisation axis of the fibre. Since all of the fibre presented in this thesis are birefringent, it was necessary to ensure that the beat signal was aligned to the primary polarisation axis in each of the measurements. In order to identify the polarisation axis of the fibre to be characterised, the setup shown in Figure 4.3 was used.

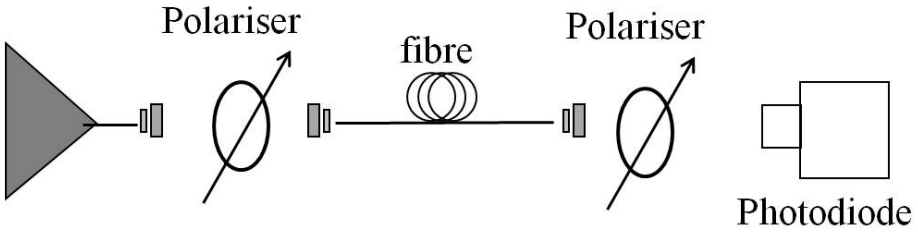


FIGURE 4.3: Experimental setup used to identify the principal polarisation axis of a fibre.

The ASE light coming from an EDFA was free-space launched into the fibre after passing through a rotating polarizer. Another polariser was placed at the output of the fibre and the output light was collected with a photodiode. The input polariser was rotated in order to find the position that allowed for the maximum extinction ratio between the maximum and minimum power values measured by the photodiode. The output polariser was rotated in order to maximise the power level measured by the photodiode. Once the polariser was aligned to one of the principal axes of the fibre, the setup shown in Figure 4.3 was slightly modified in order to measure the nonlinear coefficient of the fibres, as shown in Figure 4.4.

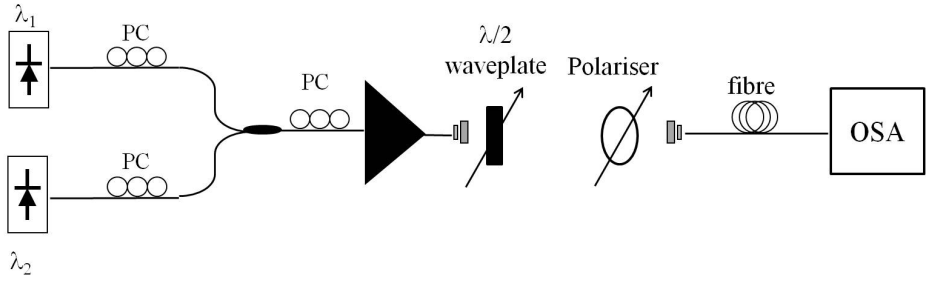


FIGURE 4.4: Experimental setup used to measure the nonlinear coefficient in a fibre.

The EDFA was replaced by a high power EDFA which was fed by two CW lasers, spaced apart by just ∼0.2nm, which acted as the beat signal. The presence of polarisation controllers (PC) ensured that the two CW signals had the same polarisation state. A $\lambda/2$ waveplate was introduced before the polariser to act as a variable attenuator: by rotating the $\lambda/2$ waveplate it was possible to control the power at the input of the fibre, without affecting its state of polarisation. The amplified signal, passing through the attenuator, was then free-space coupled into a short sample of the fibre.

The output polariser was removed and the output end of the fibre was butt-coupled to an SMF28 patch cord and connected to an OSA. By varying the input power and monitoring the output spectrum, a set of measurements of the ratio between the input signal and the first order harmonics was recorded. The nonlinear phase shift was then evaluated by using Eq. 4.8. It has to be noted that the high power EDFA was responsible for a certain nonlinear phase shift at the input of the fibre: this value was always subtracted in the measurements of the nonlinear coefficient. The evaluated nonlinear phase shift was plotted against the input power and the slope of the curve determined the nonlinear coefficient.

### 4.1.4 Dispersion

The dispersion of highly nonlinear fibres cannot be measured with conventional methods such as the pulse delay technique [Cohen and Lin, 1977] or the phase-shift method [Sugimura and Daikoku, 1979]. Both techniques, indeed, require high *dispersion x length* product and therefore long lengths of fibres need to be employed. Alternative techniques based on short fibre sample need to be investigated. The FWM-based method provides a simple technique to measure the dispersion of the fibre at one particular wavelength. This method has previously been used to measure the dispersion of various types of

fibres: silica HNLF [Hirano and Sasaki, 2009], dispersion shifted fibres [Chen, 2003] and Bi-based fibres [Hasegawa *et al.*, 2008]. The experimental setup is very similar to the one shown in Figure 4.4 and the difference consists in the wavelength separation between the two CWs. While the spacing between the two CWs was kept small in the nonlinear coefficient measurement so that the dispersion of the fibre could be neglected, in the setup for the dispersion measurement, we experiment with beams of varying wavelength spacing. When large values of spacing are set between the two CWs, the variation in the ratio between the input signals and the first order harmonics can be quantified as [Hasegawa *et al.*, 2008]:

$$R = \eta P_1 \gamma^2 P_2 \left[ \frac{1 - e^{(-\alpha L)}}{\alpha} \right]^2 \tag{4.9}$$

Where $\alpha$, $\gamma$ and L represent the loss, the nonlinear coefficient and the length of the fibre respectively, $P_1$ and $P_2$ are the values of power of the two CWs and $\eta$ is the *efficiency* of the FWM process, defined as:

$$\eta = \frac{\alpha^2}{\alpha^2 + \Delta\beta^2} \left\{ 1 + \frac{4e^{-\alpha L} sin^2(\Delta\beta L/2)}{[1 - e^{-\alpha L}]^2} \right\} \tag{4.10}$$

where $\Delta\beta$, the phase mismatch can be written as [Nikodem *et al.*, 2008]:

$$\Delta\beta = \frac{2\pi\lambda^2}{c} D \Delta f^2 \tag{4.11}$$

where D is the dispersion of the fibre at $\lambda$, the operational wavelength, and $\Delta$f is the spacing of the two CWs in the frequency domain. Eq. 4.10 shows that the efficiency and therefore the ratio R are functions that experience minima when $\Delta\beta$L/2=k$\pi$, with k being an integer. Therefore, for a fixed length of fibre L, minima can be found for the channel spacing, satisfying the relation [Nikodem *et al.*, 2008]:

$$\Delta f_k = \sqrt{\frac{kc}{\lambda^2 DL}} \tag{4.12}$$

And consequently the dispersion can be written as:

$$D = \frac{c}{\lambda^2 \Delta f^2 L} \tag{4.13}$$

where $\lambda$ is the operating wavelength.

This method has been used to characterise most of the fibres presented in this thesis. However, it suffers from some drawbacks: it allows the evaluation of the dispersion only at one particular wavelength and does not allow measuring the dispersion slope (DS) of the fibre. Numerical simulations have shown that the dispersion slope is usually less sensitive to small variations in the fibre parameters than the actual dispersion values. Therefore, we relied on the numerically predicted values for the estimation of this parameter. Moreover, the FWM-based method is not suitable to measure low dispersion values, such as D< |5|ps/nm/km in short fibre samples. For such low dispersion values, indeed, at a fixed fibre length of 2m, Eq. 4.13 dictates a separation between the two CWs >40nm which exceeds both the tunability of the laser sources and the operating bandwidth of many of the optical components available at the time of the experiments, limited only to the C-band.

When the FWM method was found to be unsuitable, an alternative method was used. A relatively simple yet accurate method to measure the dispersion in a short fibre over a wide range of wavelengths is based on the interferometric technique. The measurement of the dispersion of one of the fibres presented here has been performed using the interferometric setup implemented with the help of Mr. G. Ponzo, shown in Figure 4.5.

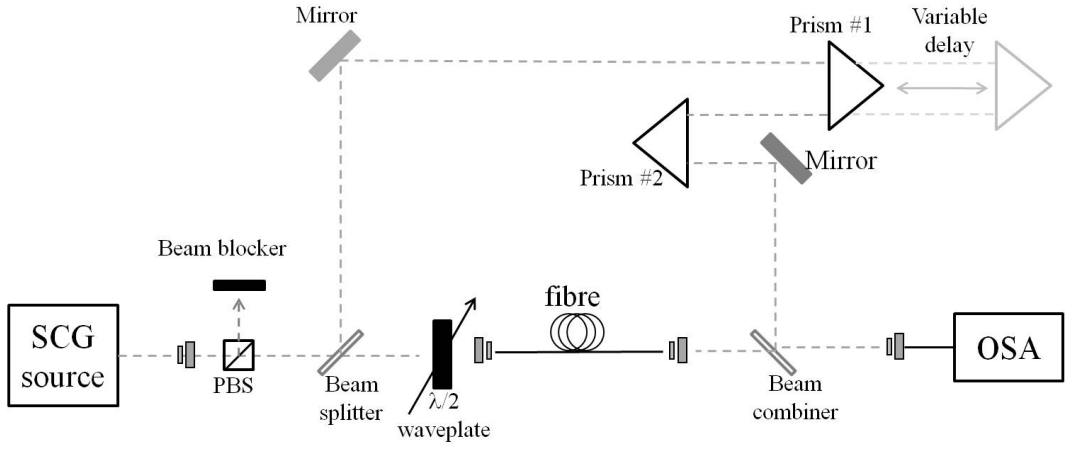


FIGURE 4.5: Experimental setup used for the measurement of the dispersion based on interferometric fringes observed in the frequency domain. PBS: Polarization beam splitter.

Light from a broadband supercontinuum source is divided in two paths by using a beamsplitter. The reference air-path has a variable length that can be adjusted by moving the prisms, which are mounted on one-dimensional platforms. Light travelling in the test path is aligned to the polarisation axis of the fibre to be characterised by means of a $\lambda/2$ waveplate. At the end of the two paths, the light is recombined through a second beamsplitter and the collected light is coupled in an OSA.

By adjusting the position of prism #1, the time delay difference between the test and the reference beam could be adjusted so that the optical path length matches for certain wavelengths. Due to the chromatic dispersion, different wavelength components of the input broadband light beam experience different group delays, $\tau_g$, as they propagate through the fibre, leading to the formation of interference fringes in the spectrum of the combined beam at the output of the system [Jasapara *et al.*, 2003]. The spectral intensity of the interference fringes followed a sinusoidal modulation, according to the following equation:

$$I(\omega) = I_{ref}(\omega) + I_{test}(\omega) + 2\sqrt{I_{ref}(\omega)I_{test}(\omega)cos(\Phi(\omega))} \tag{4.14}$$

where $\Phi(\omega)$ is the frequency-dependent phase difference between the reference and test beams, while $\mathrm{I}_{ref}(\omega)$, $\mathrm{I}_{test}(\omega)$ and $\mathrm{I}(\omega)$ are the intensity of the reference path, the test path and the intensity at the output of the system respectively. The maxima in the output spectrum correspond to those wavelengths for which the phase difference between the reference and test beams allowed constructive interference to take place. Two consecutive peaks have therefore a phase difference of $2\pi$ and the group delay can be described as a function of the frequency according to the equation:

$$\tau_g(\omega) = \frac{2\pi}{\omega_{i+1} - \omega_i} \tag{4.15}$$

where $\omega_i$ and $\omega_{i+1}$ are the wavelengths corresponding to two consecutive maxima in the output spectrum and $\omega = (\omega_i + \omega_{i+1})/2$ [Jasapara *et al.*, 2003]. The dispersion of the fibre can be obtained from Eq. 4.15 by the relation [Jasapara *et al.*, 2003]:

$$D = \frac{1}{L}\frac{\partial \tau_g}{\partial \lambda} \tag{4.16}$$

where L is the length of the fibre. Once the interferometer is balanced, the position of prism #2 is accurately adjusted so that the time delay $T_0$ induced by the reference path matches the group-delay of a wavelength falling inside the wavelength region covered by the broadband source. The formed fringes show a centre of symmetry for the wavelength at which the group delay $\tau_g$ is exactly equal to $T_0$. By changing the time delay $T_0$ for the wavelength span of the broadband source, the chromatic dispersion of the fibre could be retrieved by applying Eq. 4.16 [Shang, 1981].

## 4.2 Characterisation of the fabricated fibres

This Section illustrates the results of the characterisation of the highly nonlinear lead-silicate fibres used within this thesis. Three different fibre designs are analysed: a HF with a complex microstructured cladding, an all-solid multi-ring structure and a simpler all-solid W-type structure. For each of the fibre designs, an overview of the design and fabrication of the fibre is given before the measured properties are reported. The experimental results are supported by numerical simulations performed by Dr. Poletti, based on the SEM images of the fibres. All the fibres presented in this thesis have been fabricated by Dr. Feng.

### 4.2.1 SF57 HF

The first attempt to the design and fabrication of a dispersion-tailored highly nonlinear fibre consisted in the design of a single material HF with a solid core surrounded by rings of holes arranged in a triangular lattice. The material chosen for this fibre was Schott SF57 (n=1.80@1550nm)[Schott, 2003].

In order to identify the cladding parameters of the HF leading to the desired dispersion properties, it is useful to refer to the optical property map, shown in Figure 4.6. The optical property map visually overlaps the plot of numerically simulated optical properties such as dispersion (D), identified by the red lines, and dispersion slope (DS), identified by the blue lines, of a SF57-based HF around the cross-point of zero dispersion and zero dispersion slope at 1550nm. The numerical simulations are based on a solid core HF with 5 rings of identical holes in the cladding. Five rings of holes are required in order to keep the confinement loss to a low value (<0.1dB/m).

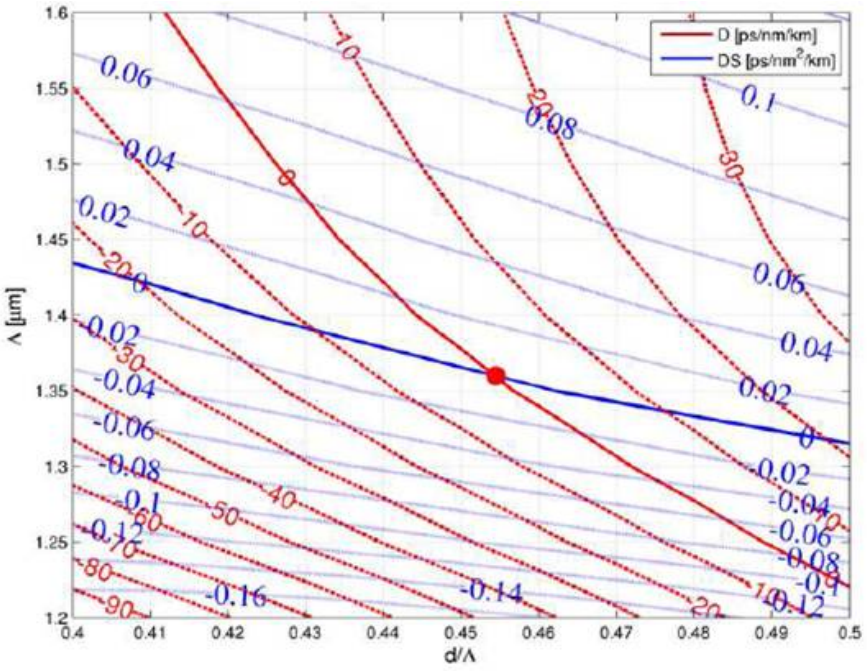


FIGURE 4.6: Optical property map (dispersion D and dispersion slope DS) of a SF57 holey fibre around the cross-point of zero dispersion and zero dispersion slope (courtesy of Dr. Poletti).

The fabrication of such a structure is not straightforward since the extrusion of a preform with 5 rings of holes is considered to be quite a challenging task, especially when the precise size and shape of the structure is crucial. However, numerical simulations have shown that the dispersion is largely determined by the structure immediately surrounding the fibre core, i.e. any features in the structure beyond the first two rings of holes have negligible influence on the waveguide dispersion. Also, a structure with slightly graded hole sizes would still provide similar dispersive characteristics to one with equally sized holes. In addition, in order to improve the confinement loss, the hole-diameter to pitch d/Λ of the holey structure outside the first 3 rings of holes should be largely increased. In the very first few attempts to fabricate this fibre, no particular attention was given to the eaxact size of the holes in the second cladding. However, the loss measurements I performed on the fibre indicated a variation in the propagation loss of the order of a few tens of dB/m even for consecutive small (shorter than 30cm) samples. By looking at the SEM images of the samples, we identified a non consistent structure throughout a short length (less than 2m) of fibre with the more significant changes occourring in the hole size of the second cladding. This problem was further investigated by Dr. Poletti, who performed numerical simulations that indicated that in order to have the confinement loss <0.1dB/m, the d/Λ ratio in the second cladding

should be greater than 0.85. Therefore the fibre design we opted for showed the structure presented in Figure 4.7. Since the dispersion of a HF is dominated by the first one and two rings of holes, the targeted HF is with the following structure parameters: (1) for the central 3-ring of holey element, the hole spacing $\Lambda$ is 1.36$\mu$m and hole diameter d is 0.62$\mu$m, i.e, d/$\Lambda$=0.454; and (2) for the 1-ring of large holes, the d/$\Lambda$ should be greater than 0.85.

The fibre was fabricated using the SEST technique (Section 2.1). A preform with three rings of holes was obtained by extrusion and is shown in the microscope image in Figure 4.7(a).

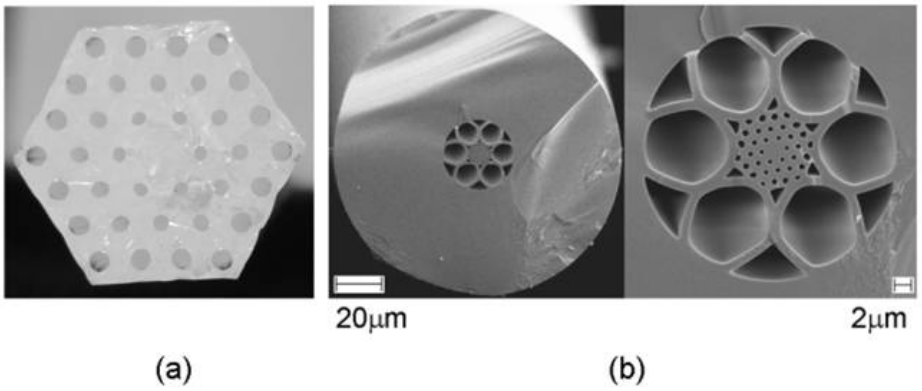


FIGURE 4.7: (a) Optical microscope image of an extruded SF57 preform with 3 rings of holes surrounding a solid core; (b) SEM images of the final double cladding HF; the central structure is surrounded by a further ring of expanded air holes (courtesy of Dr. Feng).

The extruded stacked preform was then elongated into a cane and stacked at the centre of six other thin SF57 capillaries inside an SF57 jacket tube. The assembled preform was then drawn into a fibre. Figure 4.7(b) shows SEM images of the fabricated HF, where the two different holey claddings can clearly be identified. The first cladding, immediately surrounding the core, has an average hole spacing $\Lambda$ of 1.60$\mu$m; the hole diameter $d_1$ of the first ring of holes is 0.56$\mu$m, and d/$\Lambda$ varies from 0.35 to 0.5 in the three rings composing this inner cladding. The outer cladding, consisting of six large holes, exhibits a large hole-to-spacing ratio $d_2/\Lambda_2$=0.85. According to the numerical simulations based on the structural parameters of this fibre, which do not fall in the range shown in Figure 4.6, the dispersion and dispersion slope can be anticipated to be between -10 and +20ps/nm/km and +0.04 and +0.09ps/nm$^2$/km, respectively.

It is important to highlight at this point that the hole expansion during the fibre drawing strongly depends on the fibre drawing conditions, making it difficult to obtain a consistent structure. For this reason, two fabrication attempts had been necessary in order to draw the fibre shown in Figure 4.7(b). In the first attempt the preform structure was not accurately maintained during the drawing as illustrated in Figure 4.8. It is evident that the general structure of the fibre is compromised, as confirmed by the irregularities in the outer cladding. Although not clearly visible in the SEM image, the holes in the first two rings of the inner cladding do not appear regular in size and shape, therefore affecting the optical properties of the fibre. This fibre will be denoted as SF57 HF#1, while the fibre shown in Figure 4.7 will be indicated as SF57 HF#2.

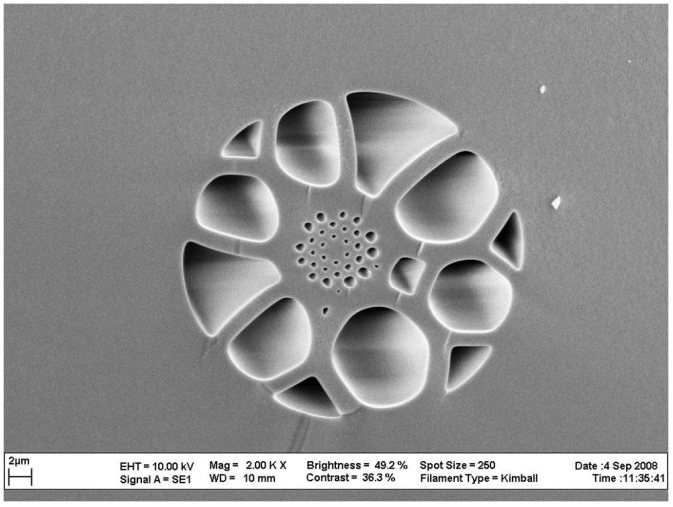


FIGURE 4.8: SEM image of the first attempt to fabricate the SF57 HF (courtesy of Dr. Feng).

The optical map of Figure 4.6 shows that the dispersive properties of the fibre depend critically on the cladding features. At a fixed value of dispersion slope, such as the DS=0ps/nm$^2$/km, a small variation in the d/$\Lambda$ from 0.45 to 0.47 results in an increase in the dispersion D from 0 to 10ps/nm/km. A precise prediction of the cladding parameters in turn relies on a highly accurate control of the drawing conditions, which is not straightforward to obtain in a holey structure as discussed in Section 2.1.

We therefore concluded that, for this HF structure, it is currently very difficult to obtain the target parameters required in order to achieve near-zero chromatic dispersion and dispersion slope at 1550nm. Moreover, the contemporary development of all-solid structures in which it was possible to accurately control the dimensions of the microstructured cladding, has made them more promising alternatives for the fabrication of fibres with

low and flat dispersion profile and therefore no further attempts to fabricate a SF57-based HF were made.

#### 4.2.1.1 Single mode guidance and propagation loss

Effectively single mode guidance has been confirmed for both fibres by using only a couple of meters long samples. Using the cutback method, the propagation losses of the fibres have been evaluated. The power at the output of the fibre after each cut is plotted against the length of the fibre, as shown in Figure 4.9.

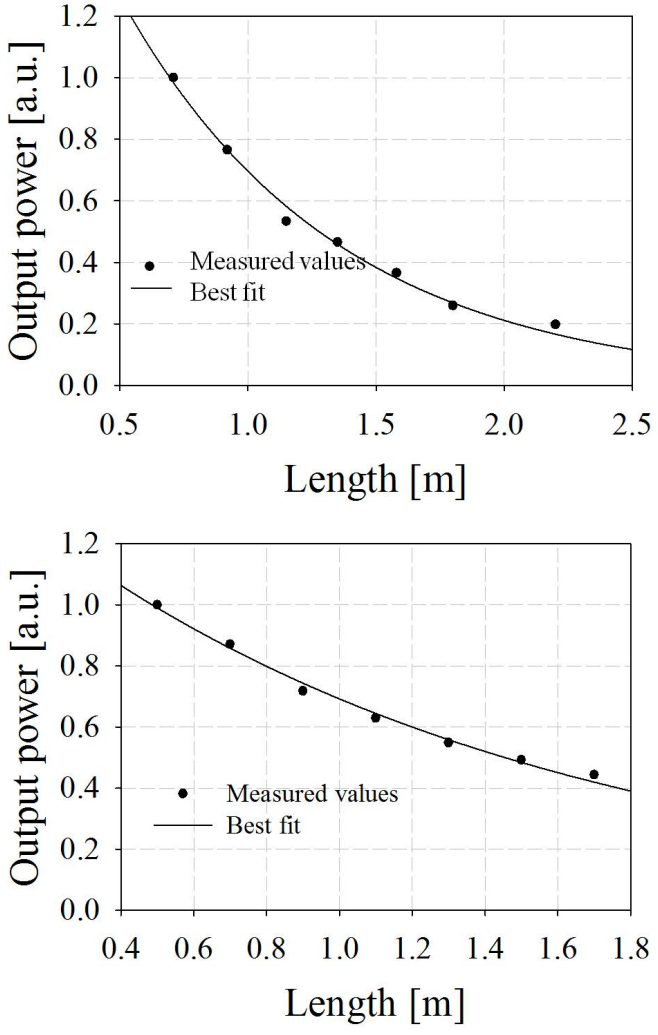


FIGURE 4.9: Diagrams of the output power against the length of sample for SF57 HF #1 (a) and SF57 HF #2 (b).

The value of propagation loss can be extracted by the slope of the fitting curves and the results from the propagation loss measurements on the two samples of SF57 HF are summarised in Table 4.1.

TABLE 4.1: Propagation losses in the SF57 HFs at 1550nm.

| Fibre | Core diameter ($\mu$m) | Propagation loss (dB/m) |
|---|---|---|
| #1 | 1.9 | 4.6±0.2 |
| #2 | 2.0 | 3.1±0.2 |

The relatively high value of propagation losses measured in the two fibres are likely to be due to the surface imperfections at the air-glass interface that are responsible for an increase in the scattering loss. In general, in a holey structure the surface roughness between air and glass can be identified as the main factor responsible for an increase in the loss value [Wen *et al.*, 2009]. However, the better control of the structure achieved in SF57 HF#2 might be the reason of the lower measured value of propagation losses, which are still at least 2dB/m higher than that of the SF57 bulk [Schott, 2003]. This is supported by numerical simulations, performed by Dr. Poletti, which have shown that the confinement loss, which depends on the outer cladding structure, in SF57 HF#1 is higher (0.1dB/m) than in SF57 HF#2 (0.002dB/m).

#### 4.2.1.2 Nonlinear coefficient

The nonlinear coefficient of the fibres was measured using the method described in 4.1.3 in samples of ∼2m in length. The nonlinear phase shift was evaluated from the ratio between the zero and first order harmonics, according to Eq. 4.8, and care was taken to ensure that the phase shift due to the EDFA was subtracted from the resulting value. The evaluated nonlinear phase shift was then plotted against the input power, i.e. the value of power launched in the two fibres. The corresponding diagrams for the SF57 HFs are shown in Figure 4.10. Note that the dynamic range of the OSA used for the measurements limited the minimum input power value for which the ratio between the zero and first order harmonics could be evaluated.

From the diagrams of Figure 4.10 it is possible to retrieve the value of the nonlinear coefficient for both fibres. The results are summarised in Table 4.2, where the value of nonlinear coefficient predicted by numerical simulations are also reported.

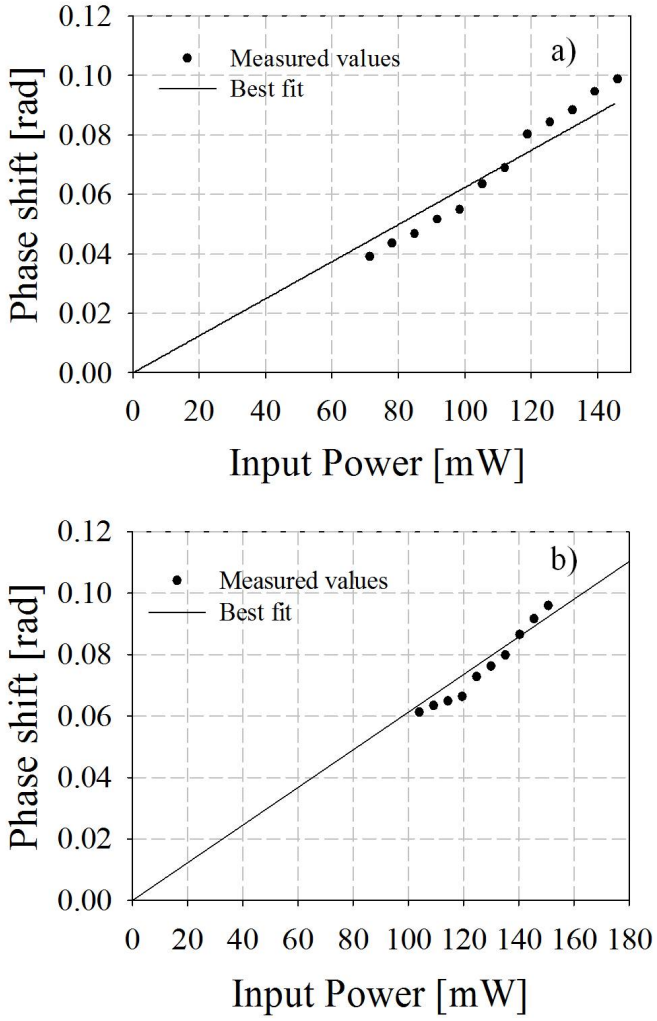


FIGURE 4.10: Diagrams of the nonlinear phase shift plotted against the input power for SF57 HF#1 (a) and SF57 HF#2 (b).

Table 4.2 shows that there is generally a good agreement between the measured values and nonlinear coefficient predicted by the simulations. The uncertainty in the measurements of $\gamma$ is affected by the uncertainty in the measured propagation loss of the fibres, which directly affected the evaluation of the launched input power and of the effective fibre length.

TABLE 4.2: Nonlinear coefficient of the SF57 HFs at 1550nm.

| Fibre | Measured $\gamma$ ($W^{-1}km^{-1}$) | Predicted $\gamma$ ($W^{-1}km^{-1}$) |
|---|---|---|
| #1 | 320±24 | 360 |
| #2 | 275±21 | 315 |

#### 4.2.1.3 Dispersion

The dispersion at 1550nm has been measured using the FWM method. One of the CW wavelengths is fixed at 1550nm, while the other is tuned within the available range. The FWM ratio is plotted against the spacing between the two CWs in Figure 4.11. I have implemented a Matlab code that evaluates the equations reported in Section 4.1.4 where the parameters are based on the experimental conditions. The resulting curves are then overlapped to the measured data and if there is good agreement between the two set of data, the dispersion value is extracted from the modeled curves. For SF57 HF#1 and SF57 HF#2, the dispersion at 1550nm can be estimated from the modeled curves to be -60ps/nm/km and -16ps/nm/km respectively.

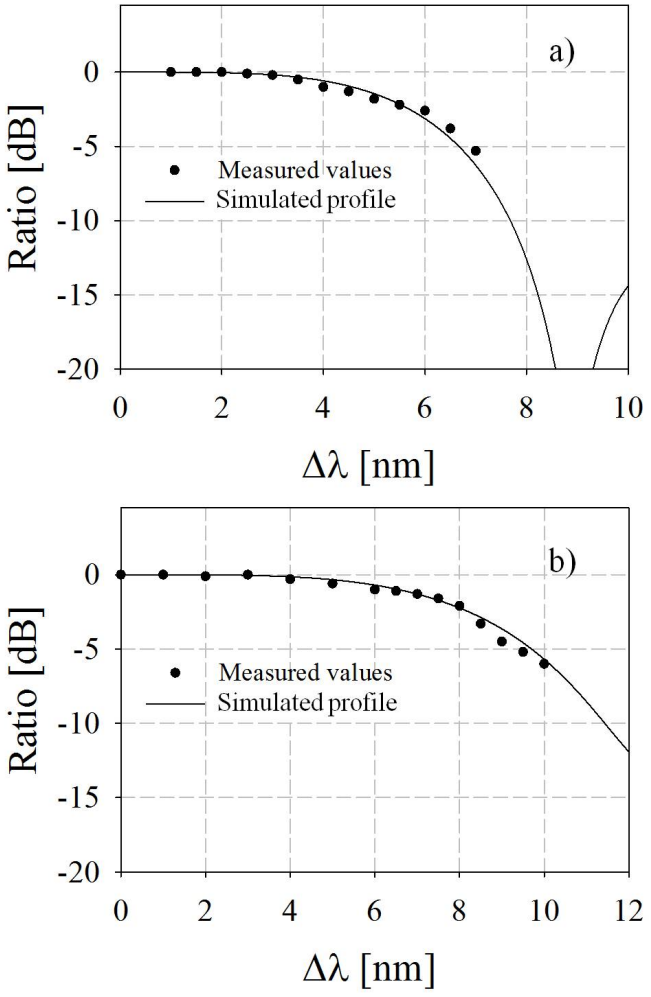


FIGURE 4.11: FWM ratio plotted against the CW spacing in the FWM-based dispersion measurement for SF57 HF#1 (a) and SF57 HF#2 (b).

The results are summarised in Table 4.3 where the dispersion values predicted by the simulations are also reported.

TABLE 4.3: Dispersion of the SF57 HFs at 1550nm.

| Fibre | Measured D (ps/nm/km) | Predicted D (ps/nm/km) | Predicted DS ($ps/nm^2/km$) |
|---|---|---|---|
| #1 | -60±5 | -63 | 0.1 |
| #2 | -16±2 | -18.3 | 0.08 |

It is clear that the micron-scale irregularities shown by the first two rings of holes of the cladding of SF57 HF#1 greatly affect the final dispersion value. This confirms that a particularly accurate control over the cladding features is necessary in order to achieve the exact dispersion characteristics specified from the design of Figure 4.6. However, the complex interactions of drawing factors such as temperature, surface tension and internal pressure are difficult to control and therefore a considerable deviation from the targeted design is very likely to occur. This, in turn, is translated in a significant deviation from the targeted optical properties of the final fibre.

### 4.2.2 All-solid multi-ring fibre

The characterisation of the two samples of the SF57-based HF has confirmed the low tolerance of the optical properties of the final fibres to any micron-scale variations in the holey structure. A possible solution to overcome this drawback is to use an all-solid fibre, rather than a HF, where holes are replaced with solid regions of a second glass. The presence of solid regions can significantly reduce the structural deformations occurring during the fibre drawing and help maintain the original relative scale factor of high/low index features of the preform during the fibre drawing [Feng *et al.*, 2003a, 2005c, 2009]. Moreover, the surface of the glass disks used to fabricate the preform can be accurately polished thus significantly reducing any loss due to scattering in the glass interface. However, the fabrication of an all-solid structure made of two or more glasses requires the glasses to be chemically and thermally compatible. Two commercial glasses were identified to meet this requirement, namely Schott SF6 (n=1.76@1550nm) and LLF1 (n=1.53@1550nm) [Schott, 2003].

The fiber design we investigated is based on a number of alternating high- and low-index coaxial rings where the layer thickness ultimately determines the optical properties of

the fiber. The structured preform was fabricated by extruding alternately stacked high- and low-index glass discs through a circular aperture (Section 2.1). By changing the drawing parameters, fibers with core diameters of 3.3$\mu$m (band#1), 3.7$\mu$m (band #2), and 4.5$\mu$m (band #3) have been fabricated from a single fibre draw over a total length of 100m.

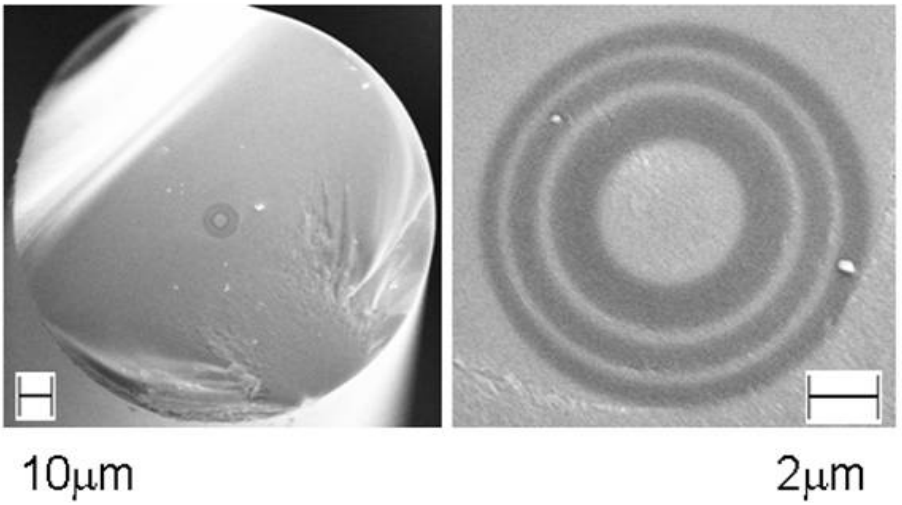


FIGURE 4.12: SEM images of the all-solid multi-ring fibre with a core diameter of 3.7$\mu$m.

Figure 4.12 shows the SEM images of the fibre, where the alternating rings are clearly visible. The fiber has an outer diameter of 150$\mu$m and a high-index SF6 core of 3.7$\mu$m in diameter (band #2). The core is surrounded by alternating LLF1 and SF6 glass rings. The three low-index rings have thicknesses of 1.1, 0.6, and 0.6$\mu$m, respectively. The two high-index rings have thicknesses of 0.4 and 0.3$\mu$m, respectively.

#### 4.2.2.1 Single mode guidance and propagation loss

A 3m sample for each band was used to investigate the guidance properties of the fibres using an IR camera. Band #3, the fibre with the biggest core diameter, was found to be dual mode, while single mode guidance was observed for band#1 and band#2. Band#3 was therefore disregarded and a full characterisation was performed for band#1 and band#2. The propagation loss was measured for band#1 and band#2 and the power-length diagrams are shown in Figure 4.13. The loss values were estimated from the fitting curves and the results are summarised in Table 4.4.

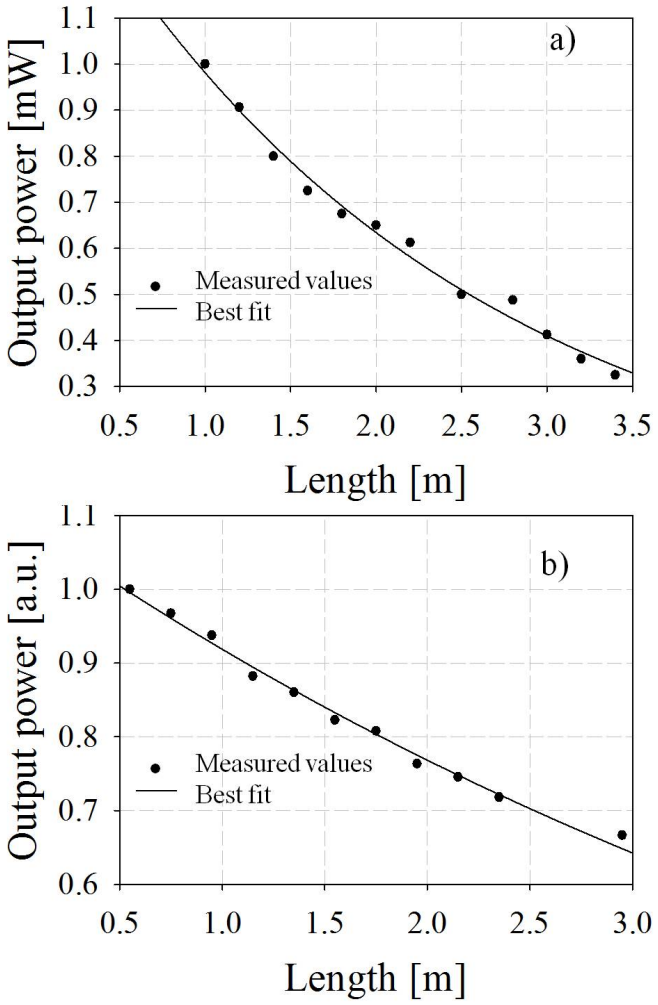


FIGURE 4.13: Diagrams of the output power against the length of sample for (a) band#1 and (b) band#2 of the all-solid multi-ring fibre.

TABLE 4.4: Propagation losses in the two bands of the all-solid multi-ring fibre at 1550nm.

| Fibre | Core diameter ($\mu$m) | Propagation loss (dB/m) |
|---|---|---|
| #1 | 3.3 | 0.9±0.2 |
| #2 | 3.7 | 0.8±0.2 |

The values of propagation loss in the two fibre bands are highly comparable. It is evident that the propagation loss for the all-solid fibre is much lower than that of the SF57 HF presented in Section 4.2.1 as an improvement of at least 2dB has been obtained. In particular, the value of propagation loss measured for band#2 is very close to the bulk attenuation value reported in the datasheet of commercial Schott SF6 glass, 0.8dB/m, [Schott, 2003]. This is a remarkable result as it represents one of the lowest ever reported values of propagation loss in a non-silica glass fibre. The low propagation loss are

attributed to the high optical quality of the polished disks used in the fabrication of the fibre preform.

#### 4.2.2.2 Nonlinear coefficient

The nonlinear coefficient was measured in a 3m long sample of band#1 and band#2. The phase shift is plotted against the input power for both fibres in Figure 4.14.

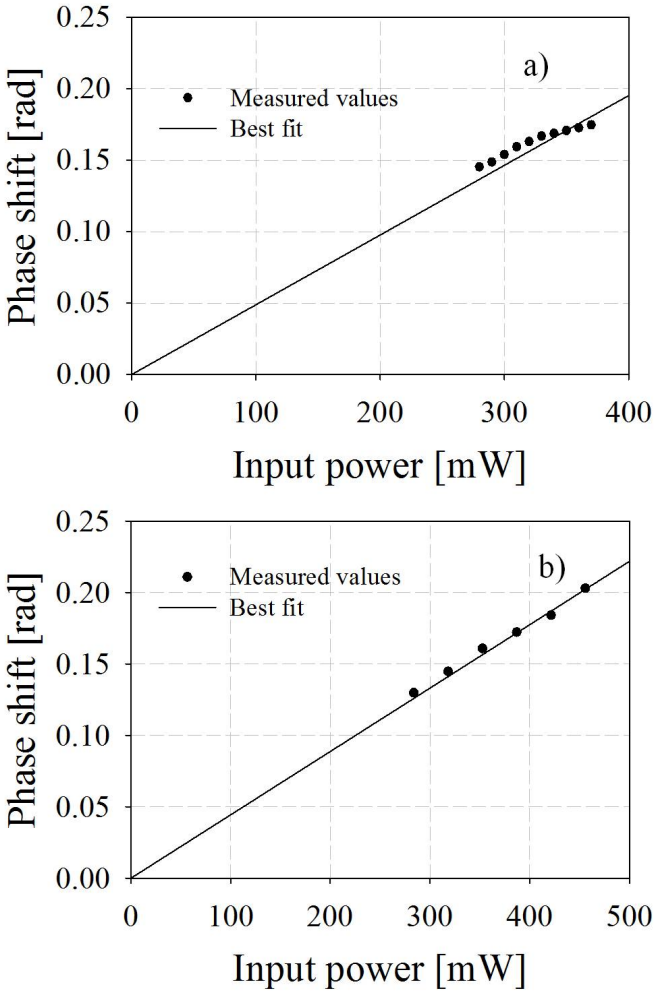


FIGURE 4.14: Diagrams of the nonlinear phase shift plotted against the input power for (a) band#1 and (b) band#2.

The results are summarised in Table 4.5, where the predicted values of nonlinear coefficient for the two fibres are also reported. Table 4.5 shows that there is a good agreement between the measured values and those predicted by the numerical simulations.

TABLE 4.5: Nonlinear coefficient of the two bands of all-solid multi-ring fibre at 1550nm.

| Fibre | Measured $\gamma$ ($W^{-1}km^{-1}$) | Predicted $\gamma$ ($W^{-1}km^{-1}$) |
|---|---|---|
| #1 | 122±22 | 150 |
| #2 | 117±24 | 130 |

#### 4.2.2.3 Dispersion

The dispersion of the two fibre bands was then measured. Both samples were 3.5m in length. As in the measurement of the SF57 HF, one of the CW wavelengths was fixed at 1550nm, while the other was tuned across the available wavelength range. Figure 4.15 shows measurements of the FWM ratio taken for the two fibres. For some values of CW spacing, the FWM component was falling below the noise level of the OSA used in the measurement setup. These values are marked with the red triangles in the two diagrams of Figure 4.15. From the modeled curves, the dispersion at 1550nm was estimated to be 25ps/nm/km for band#1 and 12.5ps/nm/km for band#2.

The results are summarised in Table 4.6 where the dispersion values predicted by the simulations are also reported.

TABLE 4.6: Dispersion of the two bands of all-solid multi-ring fibre at 1550nm.

| Fibre | Measured D (ps/nm/km) | Predicted D (ps/nm/km) | Predicted DS ($ps/nm^2/km$) |
|---|---|---|---|
| #1 | 25±5 | 21 | 0.16 |
| #2 | 12.5±1 | 15 | 0.15 |

Since both fibres showed a comparable nonlinear coefficient, band#2 was considered to be a more promising sample because of its much lower dispersion value at 1550nm. Figure 4.16 shows the simulated dispersion curve of band#2 compared against the dispersion profile of an SMF28 over a wide range of wavelengths. It is evident how the dispersion value of band#2 at 1550nm (indicated by the red cross) is very close to that of SMF28 at the same wavelength, even though the nonlinear coefficient of the all-solid multi-ring fibre is 120 times higher than that of SMF28.

A few meters of this band#2 can therefore exhibit a total nonlinearity equal to that of several hundreds of meters of SMF28 whilst exhibiting much less net dispersion. This is an important property for many nonlinear applications such as FWM as it will be described in more details in Section 5.1.

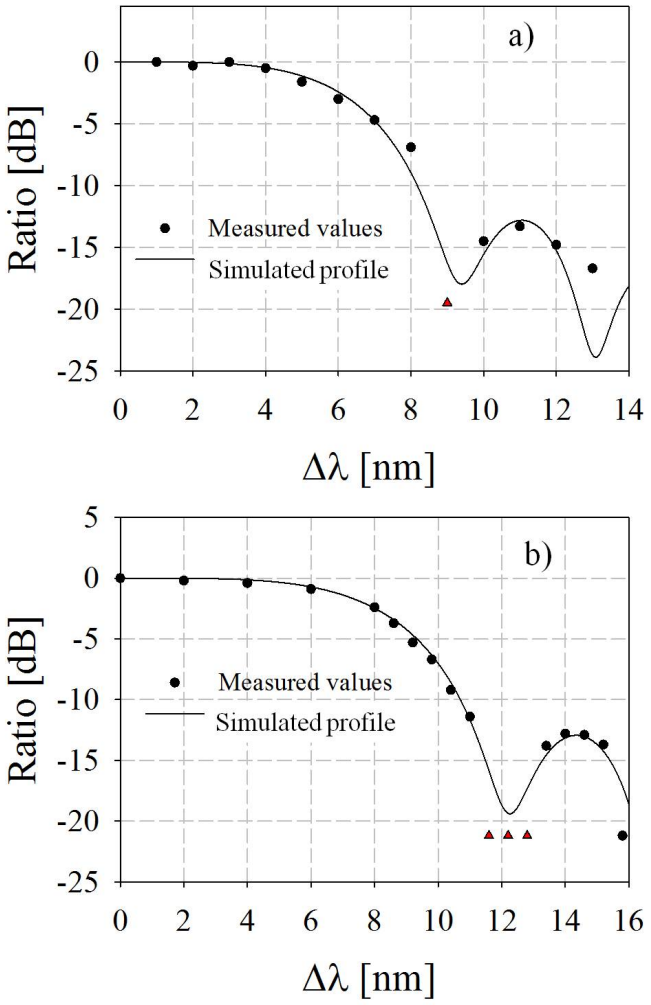


FIGURE 4.15: FWM ratio plotted against the CW spacing in the FWM-based dispersion measurement for (a) band#1 and (b) band#2 of the all-solid multi-ring fibre.

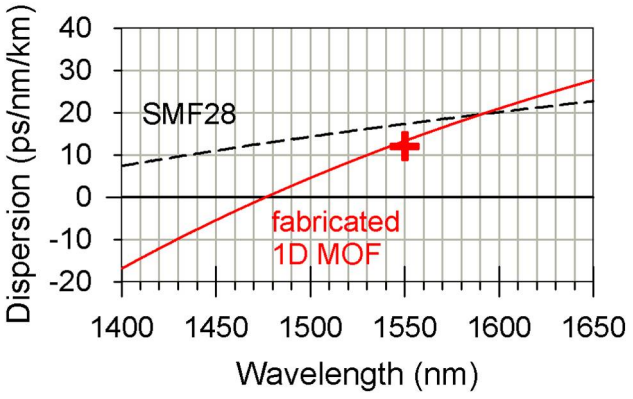


FIGURE 4.16: Simulated dispersion profile of all-solid multi-ring fibre, Band#2, (red solid line) and of an SMF28 (black dashed line). The red cross indicates the measured value at 1550nm, courtesy of Dr. Feng.

### 4.2.3 Lead silicate W-type fibre

Numerical simulations have shown that in order to control the dispersion of the all-solid multi-ring fibre, it would be necessary to obtain an accurate control of the ratio between the core size and the innermost ring. Although the all-solid fibre described in Section 4.2.2 has allowed for an excellent consistency between the structural characteristics of the preform and that of the final fibre, the independent control of multiple rings during the extrusion process has proven to be very challenging. For this reason, a much simpler design approach was considered: the W-type design.

Optical waveguide theory predicts that for any chosen core material it is always possible to engineer a step-index fiber with a core diameter $d_0$ and refractive index difference $\Delta n$, so that at a certain wavelength $\lambda_{flat}$ the waveguide dispersion exactly compensates for the material dispersion in both absolute value and slope, thus creating an overall flattened and near-zero dispersion profile around $\lambda_{flat}$. In order to fabricate such a fibre, a pair of glasses with the desired refractive indices that are also chemically and thermally compatible needs to be identified.

A systematic search was conducted within the lead silicate glasses. This family of glasses was chosen for two reasons: (1) they show a highly nonlinear refractive index and (2) they show the required compatibility as proven by the successful fabrication of the all-solid fibre presented in Section 4.2.2. Two Schott glasses were identified as suitable for the core and cladding sections: Schott SF57 in a $a_0$ $\sim$1.65$\mu$m core and Schott LLF1 in the cladding would provide exactly the right amount of waveguide dispersion for an overall flat profile at 1550nm. Figure 4.17 shows the simulated dispersion profiles for three different values of core diameter together with the dispersion profile of the bulk SF57.

The large normal dispersion value at telecom wavelengths exhibited by the bulk SF57 glass can be compensated for with the waveguide dispersion, thus resulting in a fibre with a low dispersion D ($|D|$<10ps/nm/km) across the whole wavelength range of 1450nm-1650nm when the core diameter is between 1.60$\mu$m and 1.68$\mu$m. At these wavelengths however, the optimum resultant step-index fibre would support a few guided modes. In order to ensure single mode operation, an additional outer cladding with a refractive index higher than the effective index of the high order modes in the core was added so that the propagation loss of these modes became extremely high. Another Schott

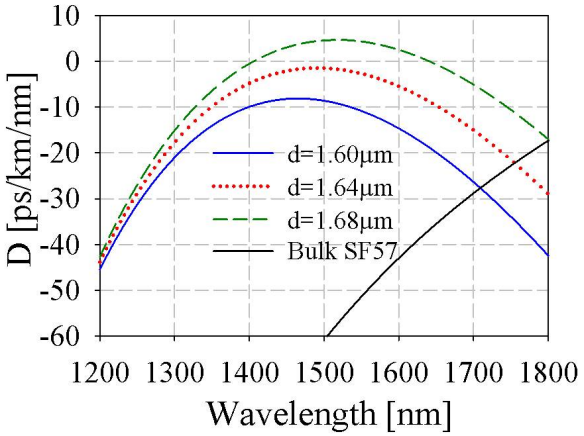


FIGURE 4.17: Simulated dispersion profile of a lead-silicate W-type fibre for various core diameters (blue solid, red dotted and green dashed lines) and dispersion of the bulk glass SF57 (black solid line).

glass, SF6, was found to be suitable for this task. Numerical simulations performed by Dr. Poletti, have shown that by carefully adjusting the inner diameter of this second cladding to $a_1 \sim 7.4\mu$m, a high differential confinement loss between the fundamental and high order modes could be imposed, thus ensuring effectively single mode operation in a meter scale length. In the first attempt to fabricate this fibre, the SF57 rod and the LLF1 and SF6 tubes were made by extrusion [Camerlingo *et al.*, 2010]. However, this process was identified to be the main cause for the high loss measured in the fibre (4.8dB/m). This fibre will be denoted as lead silicate W-type fibre (LSWF)#1.

In the attempt to reduce the propagation loss of LSWF#1 an annealing step was performed on the fibre, as it is well known that an annealing procedure on an optical fibre can reduce the propagation loss by reducing the stress between the core and the cladding that are a result of the drawing process [Anderson *et al.*, 1984]. Starting from room temperature, a sample of LSWF#1 was heated up to a temperature of 410°C at a rate of 1°C/min and kept at this temperature for five hours. The sample was then cooled down to room temperature again at a rate of 0.5°C/min. Although the annealing step confirmed a reduction in the loss of the annealed LSWF#1 sample (LSWF#1a), the resulting propagation loss (4.1dB/m) was still far from the bulk attenuation of the SF57 glass (∼1dB/m) [Schott, 2003]. A second attempt to fabricate this fibre was then made using a method based on drilling and polishing rather than extrusion. The high optical quality of the polishing steps resulted in much lower propagation losses for this sample (∼2dB/m). This fibre will be denoted as LSWF#2.

Figure 4.18 shows the SEM images of LSWF#2. The diameter of the SF57 core and the outer diameter of the LLF1 ring were measured to be 1.63$\mu$m and 7.4$\mu$m, respectively.

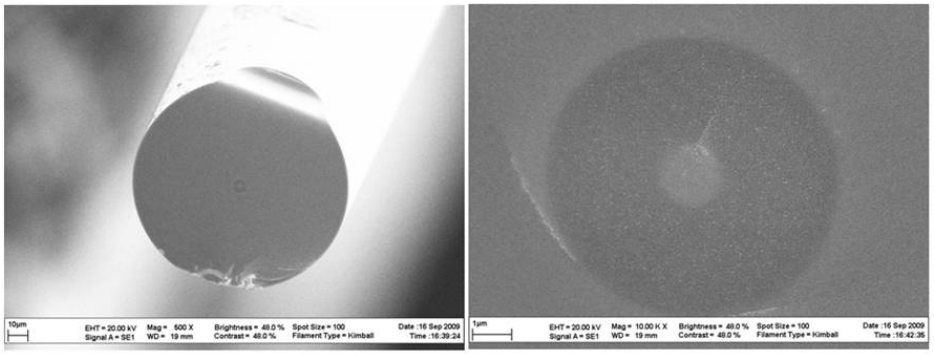


FIGURE 4.18: SEM images of a lead-silicate W-type fibre fabricated by drilling and polishing.

#### 4.2.3.1 Single mode guidance and propagation loss

Effectively single mode guidance was confirmed for both fibres by using samples of only a couple of meters in length. Using the cutback method, the propagation loss of LSWF#1, LSWF#1a and LSWF#2 were evaluated. The power measured at the output of the fibre after each cut is plotted against the length of the fibre, as shown in Figure 4.19.

The propagation loss values are summarised in Table 4.7. The propagation losses were reduced from an initial value of 4.8dB/m down to 4.1dB/m through the annealing step. The benefits of a different fabrication process based on polished rods and tubes is clearly evident in Table 4.7 where the propagation loss for LSWF#2 are reported to be 2.1dB/m.

TABLE 4.7: Propagation losses in the 3 samples of lead silicate W-type fibre at 1550nm.

| Fibre | Core diameter ($\mu$m) | Propagation loss (dB/m) |
|---|---|---|
| #1 | 1.60 | 4.8±0.2 |
| #1a | 1.60 | 4.1±0.2 |
| #2 | 1.63 | 2.1±0.2 |

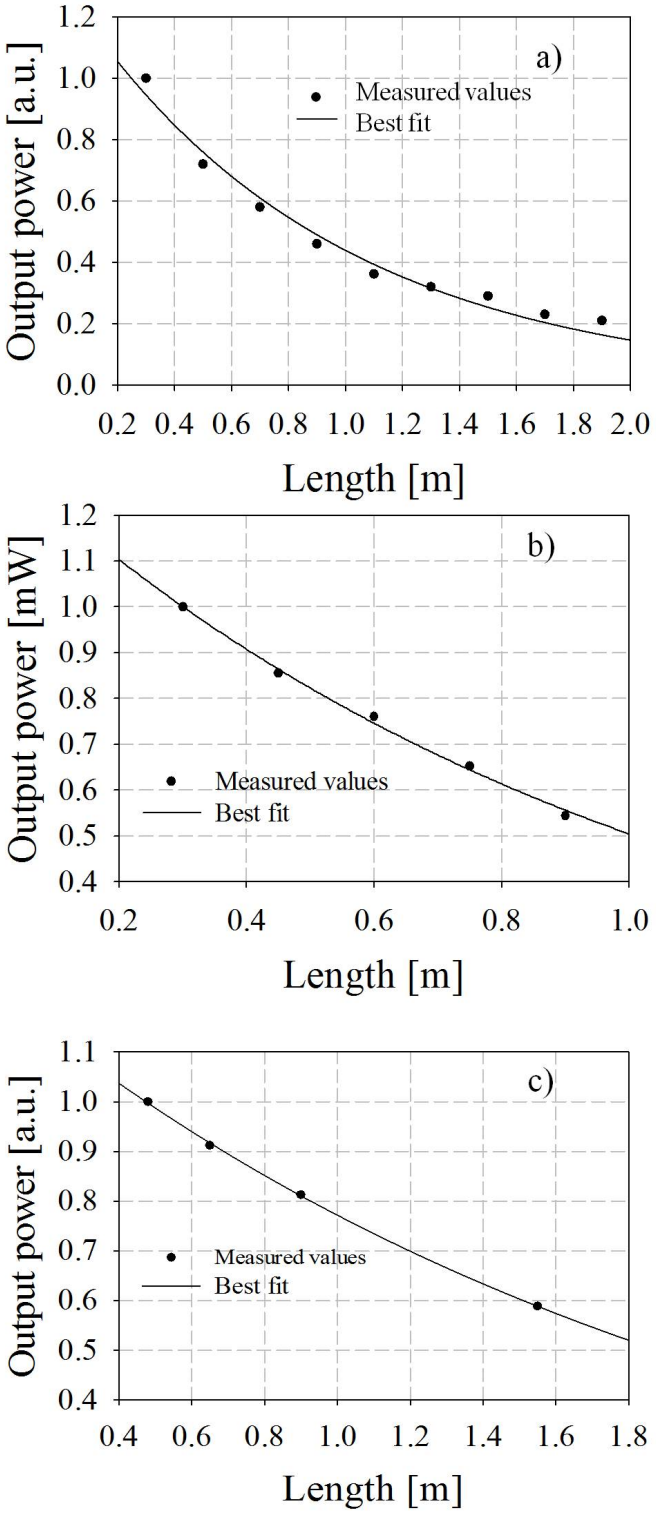


FIGURE 4.19: Diagrams of the output power against the length of sample for (a) LSWF #1, (b) LSWF #1a and (c) LSWF #2.

#### 4.2.3.2 Nonlinear coefficient

The nonlinear coefficient was measured in 2.2m long samples of LSWF#1 and LSWF#2. The phase shift is plotted against the input power for both fibres in Figure 4.20.

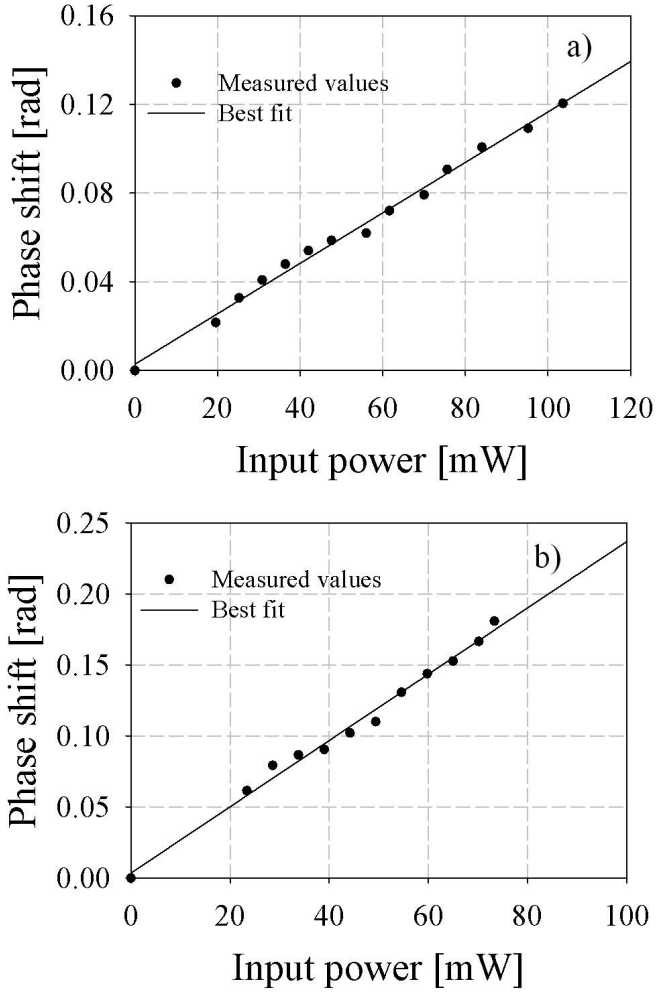


FIGURE 4.20: Diagrams of the nonlinear phase shift plotted against the input power for (a) LSWF#1, (b) LSWF#2.

The results are summarised in Table 4.8, which shows that the two fibres have very comparable nonlinear coefficient, due to the very similar core size diameter (1.60$\mu$m and 1.63$\mu$m) and that there is a good agreement between the measured values and the nonlinear coefficient values predicted by the simulations. These fibres exhibit the highest value of nonlinearity amongst the three fibre types I have experimented with for this thesis.

TABLE 4.8: Nonlinear coefficient of the lead silicate W-type fibres at 1550nm.

| Fibre | Measured $\gamma$ ($W^{-1}km^{-1}$) | Predicted $\gamma$ ($W^{-1}km^{-1}$) |
|---|---|---|
| #1 | 822±22 | 858 |
| #2 | 820±24 | 850 |

#### 4.2.3.3 Dispersion

The dispersion of a 2.2m long sample of LSWF#1 has been measured using the FWM method and the corresponding diagram is shown in Figure 4.21. Also in this case, one of the CW wavelength is fixed at 1550nm and the other is tuned within the available range of wavelengths.

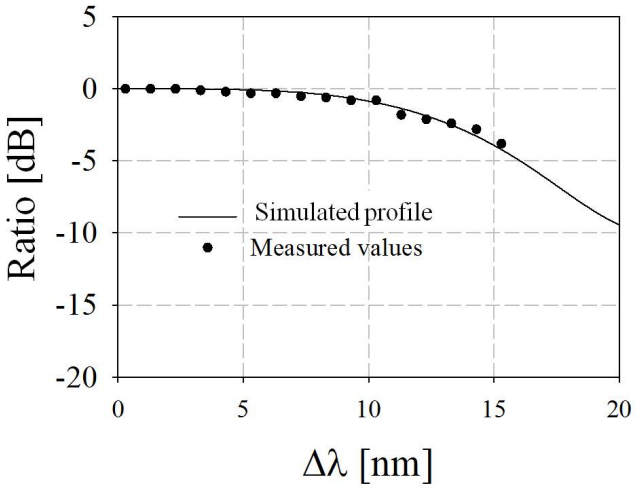


FIGURE 4.21: FWM ratio plotted against the CW spacing for the measurement of dispersion of LSWF#1.

From the fitting curve, the dispersion can be estimated to be -12ps/nm/km. This value is very close to the one predicted by the numerical simulations (-11ps/nm/km). Figure 4.21 also shows the limitation of the FWM-based technique for the measurement of dispersion. For low values of net dispersion, indeed, the FWM ratio tends to be constant within the C-band with the first minimum located in the L-band, where it cannot be recorded due to the limited tunability of the optical components.

Numerical simulations have shown that the dispersion of LSWF#2 would be very close to zero. For this reason, the FWM-based technique was considered to be inappropriate and therefore the dispersion of LSWF#2 has been measured by using the interferometric setup described in Section 4.1.4. Figure 4.22(a) shows the interferogram recorded for

one of the polarisation axes of the fibre, from which the corresponding dispersion curve has been extracted with the help of Mr G. Ponzo. Figure 4.22(b) shows the measured dispersion profile (black solid line) and the predicted dispersion profile (red dashed line), highlighting a good agreement between the two curves over a wide range of wavelengths.

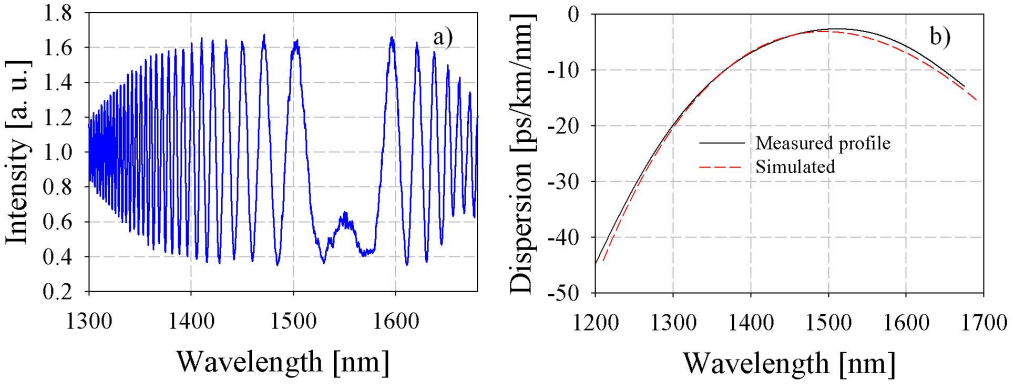


FIGURE 4.22: (a): Interference fringes obtained for the measurement of the dispersion of LSWF#2; (b): Predicted (red dashed line) and measured (black solid line) dispersion profile of LSWF#2.

The results for both fibres are summarised in Table 4.9.

TABLE 4.9: Dispersion of the lead silicate W-type fibre at 1550nm.

| Fibre | Measured D (ps/nm/km) | Predicted D (ps/nm/km) | Predicted DS ($ps/nm^2/km$) |
|---|---|---|---|
| #1 | -12±1 | -11 | 0.1 |
| #2 | -3.2±1 | -4 | 0.05 |

#### 4.2.3.4 Birefringence

The annealing procedure has previously shown not only to reduce the propagation loss of the fibre but also to reduce its birefringence as well [Stone, 1988; Tang *et al.*, 1991]. The effect of the annealing on the beat length has therefore been investigated for LSWF#1. The beat length of a sample of this fibre has been measured by launching ASE light at 45°with respect to the polarisation axis of the fibre. The same sample has then been annealed, following the procedure described in Section 4.2.3, and any changes in the beat length of this sample (LSWF#1a) have been investigated. The spectra at the output of the two samples are shown in Figure 4.23.

The effect of the annealing on the fringes is clearly visible and confirmed by the summary of the results presented in Table 4.10.

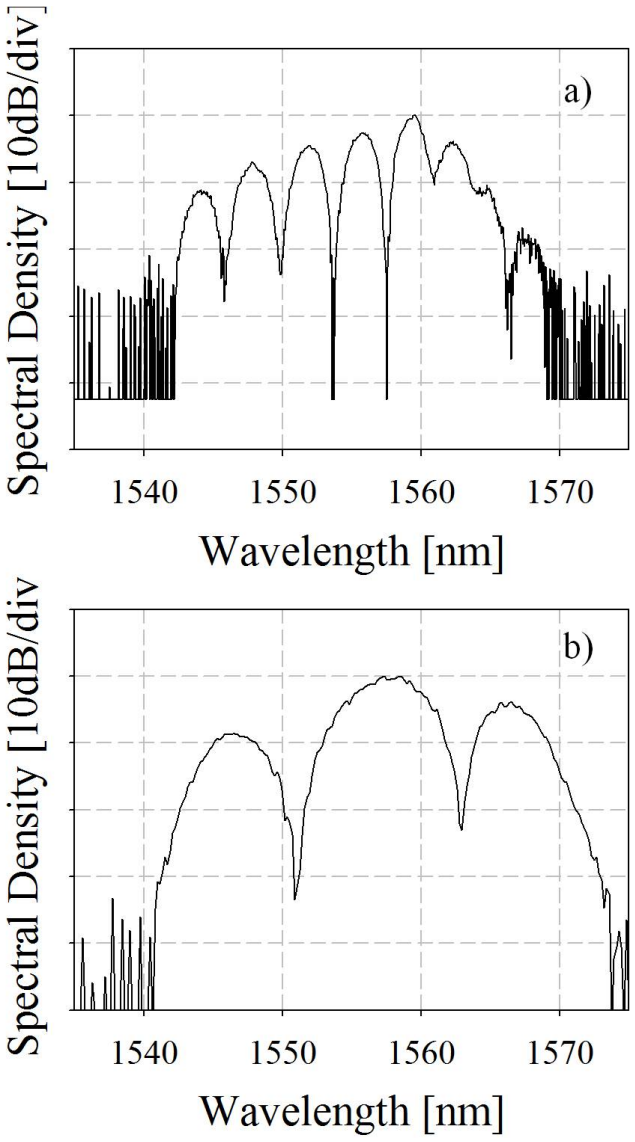


FIGURE 4.23: Spectra at the output of (a) LSWF#1 and (b) LSWF#1a when ASE light is launched at 45°relative to a principal birefringence axis.

TABLE 4.10: Birefringence in LSWF#1 and LSWF#1a

| Fibre | Length of sample (m) | Periodicity of fringes (nm) | Beat length (mm) | Birefringence $B_m$ |
|---|---|---|---|---|
| #1 | 0.96 | 4.2 | 2.6 | $5.9{\cdot}10^{-4}$ |
| #1a | 0.90 | 11 | 5.8 | $2.6{\cdot}10^{-4}$ |

The periodicity of the fringes is increased from 4.2nm in LSWF#1 up to 11nm for LSWF#1a, resulting in a beat length for the two samples of 2.6mm and 5.8mm respectively. Note that the annealed sample is slightly shorter than the original sample. This is simply because the annealed sample needed to be cleaved again after having been removed from the measurement setup to ensure the light was efficiently coupled in the sample. The increase in beat length for the annealed sample results in a reduction of birefringence parameter from $5.9{\cdot}10^{-4}$ to $2.6{\cdot}10^{-4}$.

Using the same setup, the beat length of LSWF#2 has also been measured in a 2m long sample. The spectra at the output of the sample is shown in Figure 4.24 and the results are summarised in Table 4.11.

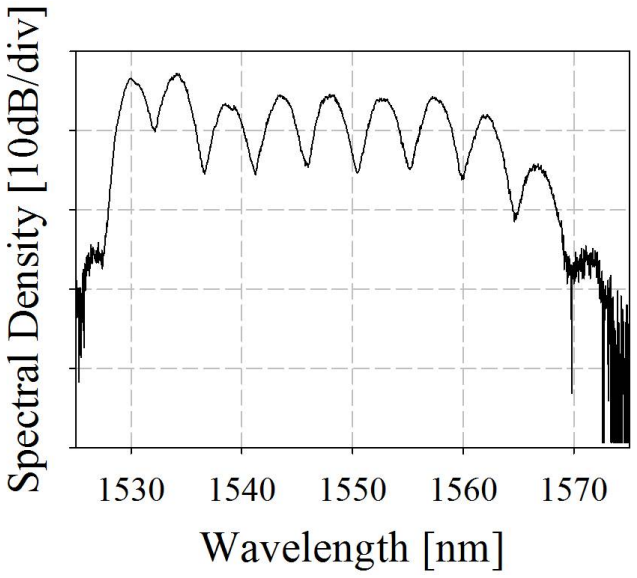


FIGURE 4.24: Spectra at the output of the LSWF#2 when ASE light is launched at 45°relative to a principal birefringence axis.

TABLE 4.11: Birefringence in the polished W-type fibre sample.

| Fibre | Length of sample (m) | Periodicity of fringes (nm) | Beat length (mm) | Birefringence $B_m$ |
|---|---|---|---|---|
| #2 | 2 | 4.75 | 6.12 | $2.5{\cdot}10^{-4}$ |

The beat length and the birefringence values of LSWF#2 are highly comparable to those achieved in LSWF#1a. This confirms the high quality of the polishing step introduced during the fabrication of the fibre aiming at reducing the stress in the fibre.

## 4.3 Conclusions

The aim of this Chapter was to characterise non-silica fibres in order to identify the best samples to employ in nonlinear signal processing systems.

Small-core HFs and all-solid fibres made of lead-silicate glasses were characterised in terms of loss, nonlinear coefficient, dispersion and birefringence. The measurement techniques and the corresponding setup used were described.

An SF57 HF showing a double cladding made of two different structures was characterised. The best attempt to the fabrication of such a structure resulted in a fibre with a core diameter of 2.0$\mu$m exhibiting a highly nonlinear coefficient of 275W$^{-1}$km$^{-1}$ and a relatively low dispersion at 1550nm (-16ps/nm/km). The surface roughness of the holey structure resulted in propagation losses of 3.1dB/m. However, the fibre properties were proven to be strongly dependent on any microscale variation that might occur during the fibre drawing.

In order to overcome this problem, an all-solid structure was investigated. The all-solid multi-ring fibre proved that the preform structure can be accurately preserved during the fabrication step and that the optical properties are less sensitive to any variations that might occur. Amongst the drawn fibres, one sample was disregarded as the bigger core diameter (4.5$\mu$m) made the fibre dual mode. The other two samples showed a highly nonlinear coefficient ($\sim$120W$^{-1}$km$^{-1}$) but the fibre with a slightly bigger core (3.3$\mu$m) resulted in a dispersion value at 1550nm of 12ps/nm/km, while the smaller fibre (core diameter 3.1$\mu$m) exhibited a dispersion value of 25ps/nm/km. Moreover the high optical quality of the glass disks used for the fibre preform resulted in a sample showing one of the lowest value of propagation losses reported so far in a non-silica fibre (0.8dB/m).

Despite the interesting properties of the all-solid multi-ring fibre, more impressive results were obtained in the lead silicate W-type fibre. A first fabrication attempt, where the three tubes were made by extrusion, resulted in a fibre with a core diameter of 1.60$\mu$m exhibiting propagation loss of 4.8dB/m, a nonlinear coefficient of 822W$^{-1}$km$^{-1}$ and a dispersion of -12ps/km/nm at 1550nm. By optimising the fabrication process based on polished rods and tubes, a sample of 1.63$\mu$m core diameter showed relatively

low propagation loss of 2.1B/m, a high nonlinear coefficient of $820W^{-1}km^{-1}$ and low dispersion (-3ps/nm/km) at 1550nm with a low dispersion profile in the C-band.

The high nonlinear coefficient and the low dispersion profile of the all-solid multi-ring fibre and the lead silicate W-type fibres make these fibres good candidates for the realisation of FWM-based devices. The performance of both fibres in a wavelength conversion setup have been analysed and will be discussed in detail in Chapter 5.

# Chapter 5

# Four wave mixing-based wavelength conversion in small core all-solid fibres

All-optical wavelength conversion plays a central role in ultra-high speed optical networks since it can be used to avoid wavelength blocking and give flexibility in the network design [Danielsen *et al.*, 1998]. Efficient wavelength conversion of On-Off-Keyed (OOK) signals can be realised in fibres by exploiting nonlinear processes, such as XPM in a nonlinear optical loop mirror [Blow *et al.*, 1990], XPM or SPM followed by a filter [Parmigiani *et al.*, 2008], [Kylemark *et al.*, 2006]. In addition to these, FWM is regarded as one of the most promising mechanisms for wavelength conversion, due to its transparency in terms of bit rate and modulation format. Efficient FWM generally requires a fibre with a high effective nonlinear coefficient, a low dispersion with a flat dispersion profile and a short length [Hansryd *et al.*, 2002]. The recently developed capability to accurately tailor the dispersion of both silica and soft-glass fibres has enabled all of the aforementioned features to be achieved in such fibres [Asimakis *et al.*, 2007; Camerlingo *et al.*, 2009; Chaudhari *et al.*, 2009; Chow *et al.*, 2005, 2007; Ebendorff-Heidepriem *et al.*, 2004a; Feng *et al.*, 2005b; Hansen *et al.*, 2003; Hirano *et al.*, 2010; Mori *et al.*, 2004; Reeves *et al.*, 2002; Takahashi *et al.*, 2010].

Wavelength conversion of 10 Gb/s nonreturn-to-zero (NRZ) pulses was demonstrated in the C-band with a *conversion efficiency*, defined as the ratio of the idler power to the

corresponding input signal power, of -16 dB over a ∼10nm bandwidth in a silica HF for a pump power of 21.4dBm [Lee *et al.*, 2003]. The polarisation maintaining HF was 15m long and showed a nonlinear coefficient $\gamma$=70W$^{-1}$km$^{-1}$, dispersion and dispersion slope of -30ps/nm/km and -0.6ps/nm$^2$/km respectively at 1550nm. Wavelength conversion of 10Gbit/s pulses over a -3dB bandwidth of ∼100nm and with a conversion efficiency of -16dB was reported in only 20m of a silica HF for an input power of 21.5dBm. The fibre exhibited a nonlinear coefficient $\gamma$=30W$^{-1}$km$^{-1}$, a ZDW at 1550nm and a low dispersion slope of 0.004ps/nm$^2$/km [Zhang and Demokan, 2005]. An even broader 3dB conversion bandwidth of 150nm was achieved in [Andersen *et al.*, 2005] at the higher bit rate to 40Gbit/s. By using 50m of silica HF with a nonlinear coefficient of $\gamma$=11W$^{-1}$km$^{-1}$ and a dispersion variation smaller than 1.5ps/nm/km in the range 1500-1650nm, Andersen and co-workers achieved a -3dB bandwidth of 150nm and a conversion efficiency of -19dB.

Replacing silica with highly nonlinear materials, fibres with 2-3 orders of magnitude higher nonlinearity than standard single-mode fibres are feasible. This has allowed for a further reduction in the fibre length down to just a few meters. Wavelength conversion based on FWM has also been reported in soft glass fibres. Wavelength conversion of 10Gbit/s signals in a 1m long bismuth-based HF has been demonstrated over a -3dB bandwidth of 35nm [Chow *et al.*, 2007]. Using a 2.2m of a lead-silicate HF, a -3dB bandwidth of 30nm with a conversion efficiency of -6dB has also been achieved [Asimakis *et al.*, 2007].

This Chapter presents the experiments on FWM-based wavelength conversion carried out with some of the fibres presented in Chapter 4. First, an analysis of the origin of FWM is presented, together with a simplified model of FWM in the CW regime. The advantages of soft-glass MOF technology in FWM-based wavelength conversion are then demonstrated. By using 1.5m of all-solid lead-silicate multi-ring fibre and 1.1m of lead-silicate W-type fibre Wavelength conversion over a -3dB bandwidth of 17nm and 20nm is demonstrated. In both experiments, the quality of the conversion process is evaluated through an analysis of both eye diagrams and BER measurements.

The role of fibre loss and the dispersion profile towards a broadband and efficient FWM-based wavelength conversion process has been investigated with numerical simulations and the conclusions have been experimentally verified. By using a 2.2m sample of the lead silicate W-type fibre showing reduced propagation loss and lower dispersion profile

than the previous sample, a flat conversion efficiency of 0db is demonstrated across the whole C-band.

## 5.1 Origin of Four Wave Mixing

FWM occurs when two photons from one or more waves are annihilated, creating new photons at different frequencies, so that the energy and the momentum are conserved in the process. This Section will focus on the degenerate case in which a single strong pump at a frequency $\omega_p$ is launched together with a weak signal at a frequency $\omega_s$ in a nonlinear medium. In this case, the signal will be amplified and a new wave at a frequency $\omega_i$ will be generated. The frequency condition expressed by Eq. 3.42 can be rewritten as:

$$2\omega_p = \omega_s + \omega_i \tag{5.1}$$

The idler frequency is therefore related to the frequency of the pump and that of the signal. In order to study the evolution of the pump, signal and idler, it is possible to derive three coupled equations from the basic propagation equations in a dispersive fibre. The resulting NLSEs are complex and therefore a numerical approach is necessary in order to obtain an exact solution. A considerable simplification of the NLSEs can be obtained if the pump wave is assumed to be much more intense than the signal wave, so that no pump depletion needs to be taken into account. Another simplification assumes the input waves to be CW and that all the overlap integrals are the same, which is a valid assumption in single mode fibres [Agrawal, 2006]. The resulting NLSEs, can be written in terms of power and phase in the following form [Inoue and Mukai, 2001]:

$$\frac{dP_p}{dz} = -\alpha P_p - 4\gamma (P_p^2 P_s P_i)^{1/2} sin\theta \tag{5.2}$$

$$\frac{dP_s}{dz} = -\alpha P_s + 2\gamma (P_p^2 P_s P_i)^{1/2} sin\theta \tag{5.3}$$

$$\frac{dP_i}{dz} = -\alpha P_i + 2\gamma (P_p^2 P_s P_i)^{1/2} sin\theta \tag{5.4}$$

$$\frac{d\theta}{dz} = \Delta\beta + \gamma(2P_p - P_s - P_i) \approx \Delta\beta + 2\gamma P_p \tag{5.5}$$

where $P_s$, $P_i$, $P_p$ are the power levels of the signal, idler and pump respectively, $\alpha$ and $\gamma$ are the loss and the nonlinear coefficient parameter respectively and $\Delta\beta$ is the phase mismatch, as defined in Eq. 3.43. The parameter $\theta$ represents the phase difference between the interacting waves. $\Delta\beta$ is indicated as the *linear phase mismatch*, while the product $2\gamma P_p$ as the *nonlinear phase mismatch*. If the propagation constant $\beta(\omega)$ is expanded in Taylor series up to the third order around the ZDW, $\Delta\beta$ can be approximated as [Inoue, 1992]:

$$\Delta\beta = -\frac{2\pi c}{\lambda^2}\frac{dD}{d\lambda}(\lambda_p - \lambda_0)(\lambda_p - \lambda_s)^2 \tag{5.6}$$

where D is the dispersion of the fibre, $\lambda_0$ its ZDW and $\lambda_p$, $\lambda_s$ the pump and signal wavelength respectively. Another assumption needed to reach an analytical solution of Eq. 5.2 - 5.5 is that the propagation loss of the signal (and idler) wave through the fibre is negligible compared to its FWM-induced gain and that the pump is not depleted during the propagation in the fibre. Incorporating the effect of the pump loss by substituting the length of the fibre with its effective length, Eq. 3.28 and setting $dP_p/dz=0$ in Eq. 5.2 the following equations for the signal and idler gain can be obtained [Hansryd *et al.*, 2002; Stolen and Bjorkholm, 1982]:

$$G_s = \frac{P_s(L)}{P_s(0)} = \left[1 + (\gamma P_p L_{eff})^2 \left(\frac{sinh(gL_{eff})}{gL_{eff}}\right)\right] \tag{5.7}$$

$$G_i = \frac{P_i(L)}{P_s(0)} = (\gamma P_p L_{eff})^2 \left(\frac{sinh(gL_{eff})}{gL_{eff}}\right) \tag{5.8}$$

where the parameter $g$, usually referred to as the *parametric gain*, is defined as:

$$g = \sqrt{\gamma^2 P_p^2 - \left(\frac{1}{2}\frac{d\theta}{dz}\right)^2} \tag{5.9}$$

When the signal and the pump are placed very close, $\Delta\beta$, and consequently $g$, can be approximated to zero. Since

$$lim_{x->0}\left[\frac{sinh(x)}{x}\right] = 1 \tag{5.10}$$

Then Eq. 5.8 can be approximated as:

$$G_i = (\gamma P_p L_{eff})^2 \tag{5.11}$$

In the region of the ZDW, the conversion efficiency is maximised when the fibre length is chosen so that [Kikuchi and Lorattanasane, 1994]:

$$L_{opt} = \frac{ln(3)}{\alpha} \tag{5.12}$$

The optimum fibre length depends therefore only on the fibre loss and is of the order of a meter for a value of propagation loss in the range of a few dB/m. The fibre length represents a trade off between the maximum achievable gain and bandwidth. This can be easily understood by looking at Eq. 5.6, 5.8 and 5.9. For a fixed $\gamma$PL product, the gain will decrease more quickly when the signal is detuned from the pump in a longer fibre length [Hansryd *et al.*, 2002]. On the other hand, the maximum gain achievable is directly proportional to the length of the fibre.

Based on the equations illustrated so far, it is possible to analyse the evolution of the signal and idler gain according to the dispersion regime that the pump wavelength is placed in. If the pump is in the anomalous regime, then from Eq. 5.6, it is clear that by detuning the pump wavelength from the signal, $\Delta\beta$ increases in magnitude and compensates for the value of nonlinear phase mismatch, resulting in a reduction of the overall phase mismatch shown in Eq. 5.5. A reduction of the phase mismatch results in an increase of $g$ and consequently an increase in the signal and idler gain. The maximum gain is reached when the pump and signals are placed so that $\Delta\beta$=-2$\gamma$P$_p$ and therefore the phase mismatch is zero. When the signal and the pump are detuned further away from this point, the magnitude of the phase mismatch increases and consequently the signal and idler gain decreases.

From Eq. 5.5 and 5.6 it is easy to see that the gain also depends on the pump power. As the pump power increases, the position of the signal for which the phase mismatch is zero moves away from the pump. This has an effect on the gain bandwidth, defined as the wavelength range between the two gain peaks.

This situation is illustrated by the numerical simulations I have performed which are illustrated in Figure 5.1 for a typical germanosilicate HNLF with a nonlinear coefficient of 10.5 $W^{-1}km^{-1}$, propagation loss of 0.78dB/km, dispersion and dispersion slope of -0.3ps/nm/km and 0.018ps/$nm^2$/km at 1550nm and ZDW at 1567.2nm, where the pump is placed 2nm away from the ZDW. Figure 5.1(a) clearly shows how the idler gain bandwidth increases by increasing the pump power. However, the gain bandwidth also depends on the relative position of the pump and the ZDW. At a fixed value of pump power ($P_{pump}$=200mW), as the pump is detuned from the ZDW, the gain peaks are achieved for signals placed closer to the pump wavelength, as illustrated in Figure 5.1(b).

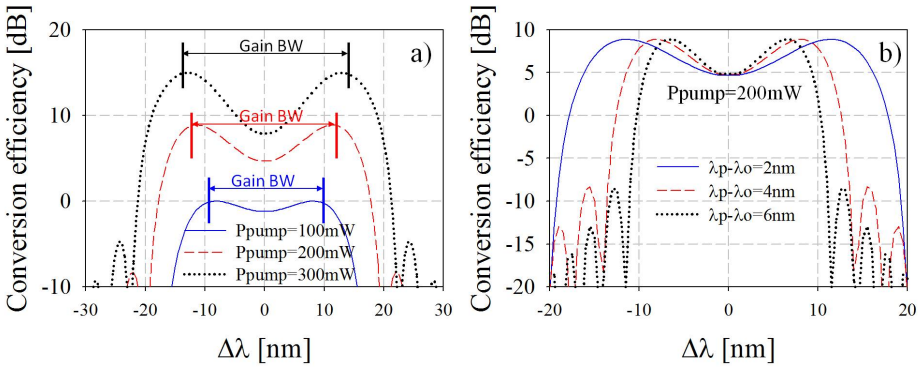


FIGURE 5.1: Simulated idler gain profile when the pump is placed in the anomalous regime for (a) various values of pump power and (b) various pump wavelengths relative to the ZDW. Fibre parameters: nonlinear coefficient= 10.5$W^{-1}km^{-1}$, dispersion=-0.3ps/nm/km, loss=0.78dB/km, dispersion slope=0.018ps/$nm^2$/km, length=1km.

g The gain evolves in a different way when the pump is placed in the normal dispersion regime. In this case, both the linear and nonlinear phase match contributions show the same sign and therefore the phase mismatching increases as the signal is detuned from the pump wavelength. The numerical simulations for the same HNLF when the pump wavelength is placed in the normal regime are shown in Figure 5.2(a). If the gain bandwidth is defined as the 3dB bandwidth of the gain profile, then it is clear that the 3dB bandwidth decreases by increasing the power, although the maximum achievable gain increases. The maximum gain bandwidth also depends on the detuning between the pump wavelength and the ZDW, as it occurs for the anomalous regime. This is illustrated in Figure 5.2(b).

The analysis reported so far can be used to obtain useful indications on how to improve the FWM-based wavelength conversion process in fibres which is the subject of this Chapter. Amongst the fibres described in Chapter 4, the all-solid multi-ring and the

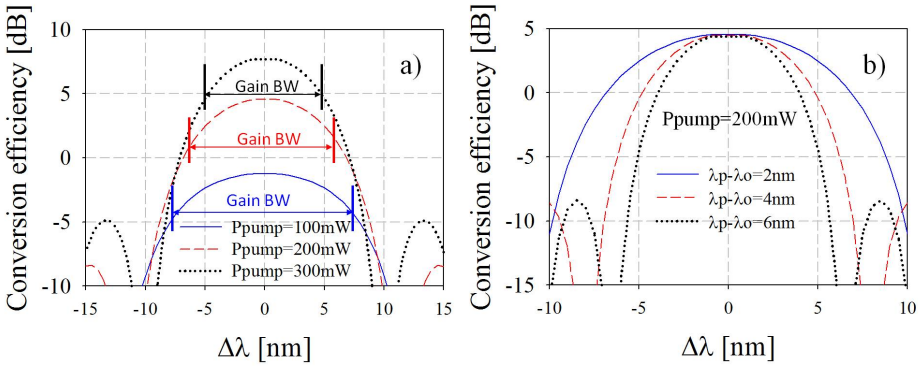


FIGURE 5.2: Simulated idler gain profile when the pump is placed in the normal regime for (a) various values of pump power and (b) various pump wavelengths relative to the ZDW. Fibre parameters: same as in Figure 5.1

lead-silicate W-type fibres have been selected as the nonlinear media for the realisation of FWM-based wavelength conversion devices. The SF57-based HF has not been employed in such systems as at the time of the experiments the more promising multi-ring fibre became available and was therefore selected in place of the HF.

## 5.2 FWM-based wavelength conversion in all-solid multi-ring fibres

The first highly nonlinear fibre considered in a FWM-based wavelength conversion system is the all-solid multi-ring fibre, band#2. The characterisation of the fibre was reported in Chapter 4 and its properties are summarised in Table 5.1 below.

TABLE 5.1: Main properties of the all-solid multi-ring fibre, band#2, at 1550nm.

| Nonlinear Coefficient ($W^{-1}km^{-1}$) | Propagation loss (dB/m) | Dispersion (ps/nm/km) | Dispersion Slope ($ps/nm^2/km$) |
|---|---|---|---|
| 117 | 0.8 | 12.5 | 0.15 |

### 5.2.1 Experimental setup

The experimental setup for the FWM-based wavelength converter is shown in Figure 5.3. The pump signal was generated by a 10GHz mode locked laser, which produced ∼7ps full-width-half-maximum (FWHM) pulses at 1545nm. The pulses were amplitude modulated by a $2^{31}$-1 pseudorandom bit sequence (PRBS) using a lithium-niobate Mach-Zehnder

modulator (MOD) and amplified using a high power erbium-doped fibre amplifier (HP-EDFA). A band pass filter (BPF) was used to reject any undesired amplified spontaneous emission (ASE) noise arising from the HP-EDFA. The probe signal was generated by a CW tunable laser, amplified and filtered to reject any out-of-band ASE noise. In order to independently control the power of the pump and signal, two different amplifiers were used.

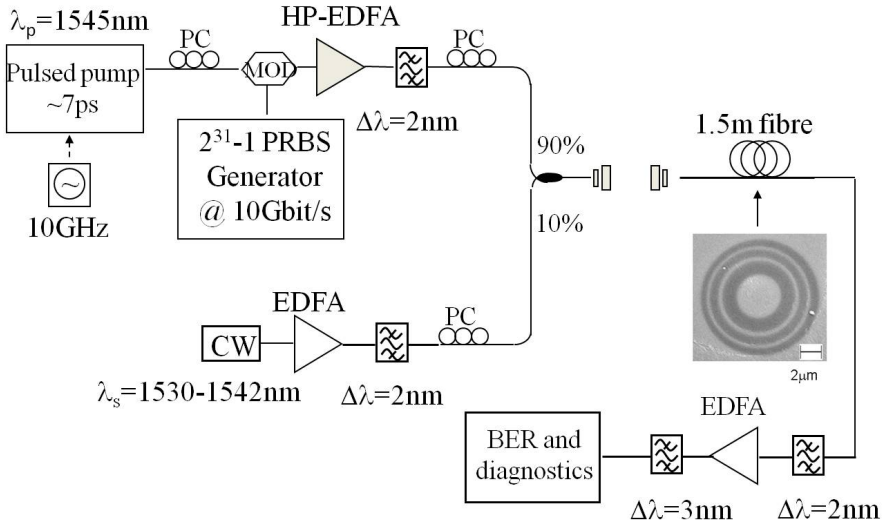


FIGURE 5.3: Experimental setup for the demonstration of FWM-based wavelength conversion in a 1.5m sample of all-solid multi-ring fibre.

Polarization controllers were used to align the state of polarization of the two beams to the polarization axis of the all-solid multi-ring fibre. The pump pulses and the CW signal were then combined in a 90/10 coupler and free-space launched into 1.5m of fibre with a coupling efficiency of ∼35%. This relatively short fibre length was chosen in order to achieve a broad wavelength conversion bandwidth. More details will be given at the end of this Section. The average powers of the signal and the pump at the very input of the fibre were 3dBm and 24.5dBm respectively, which corresponded to a peak power of 2.6W.

### 5.2.2 Experimental results

Owing to the low loss, low dispersion and the high nonlinearity per unit length of the MOF, it was possible to observe wavelength conversion of pulses over a range of wavelengths that cover the upper part of the C-band in the experiments, even if the pump wavelength was sitting far away from the ZDW (1475nm). This is illustrated in

Figure 5.4, which shows the spectral traces at the output of the system when the CW wavelength was tuned from 1542nm to 1530nm.

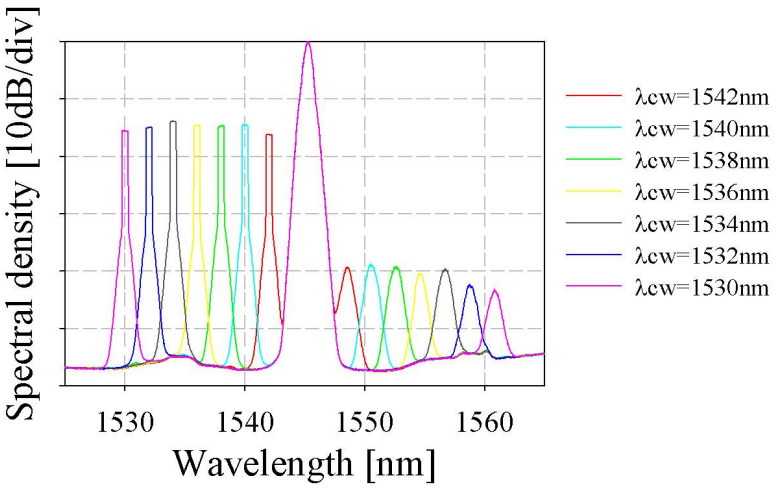


FIGURE 5.4: Spectral traces taken at the output of the 1.5m sample of the all-solid multi-ring fibre when the CW signal was tuned from 1542nm to 1530nm. Resolution=0.5nm.

Figure 5.4 shows that an optical signal to noise ratio (OSNR) of $\sim$ 12-18dB was achieved at the output of the system. It is worth noting however, that this is mainly limited by the dynamic range of the spectrum analyser, and in reality the OSNR was much higher than this (the BER measurements presented below are in support of this argument). The *conversion efficiency*, here defined as ratio of the power of the generated idler to the pump power at the input of the fibre, varies by $\sim$4.5 dB across the 12nm tuning range. Figure 5.4 also shows newly generated frequency components around the CW wavelengths, which are due to the combined effects of cross-phase modulation and parametric amplification. I have performed numerical simulations of the NLSE based on the Split-Step-Fourier method [Agrawal, 2006], and for one particular wavelength ($\lambda_{idler}$=1552 nm) a comparison of the result of the modelling and the measured trace is shown in Figure 5.5. Note that the resolution chosen for the simulations is responsible for the not perfect agreement between the simulated and the measured trace around the CW signal.

In order to assess the quality of the conversion process, the generated pulses were filtered and further characterised at the selected wavelength ($\lambda_{idler}$=1552 nm) in terms of their noise properties and pulse width. The filtered idler is shown in Figure 5.6 (blue solid line), together with the signal recorded at the output of the fibre (red dashed line).

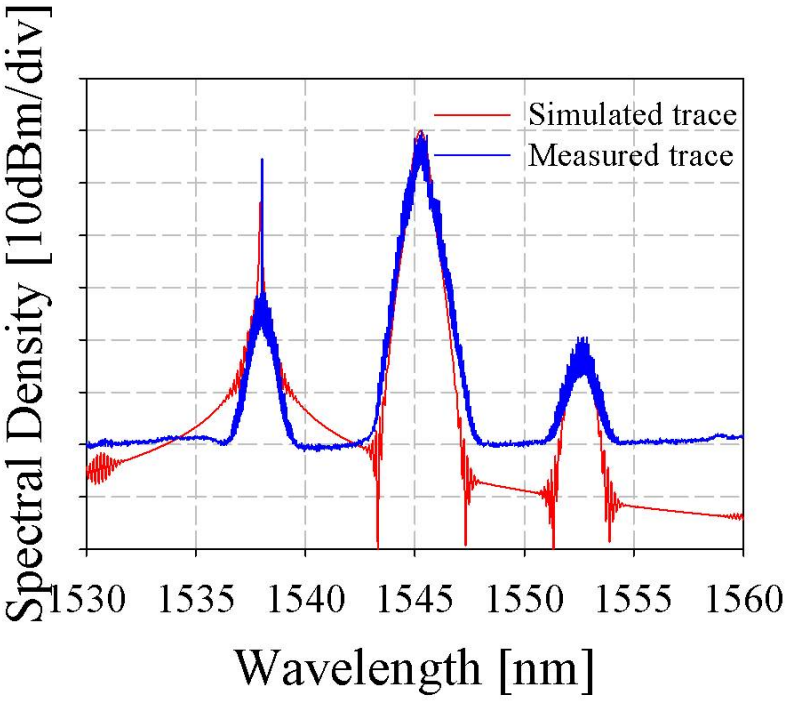


FIGURE 5.5: Simulated FWM trace (red line) and measured trace (blue line) in a 1.5m sample of the all-solid multi-ring fibre when $\lambda_{CW}$=1538nm.

Figure 5.6 shows that a small component of the pump is still visible in the filtered spectrum. However, the magnitude of the pump is so small that its effect can be ignored.

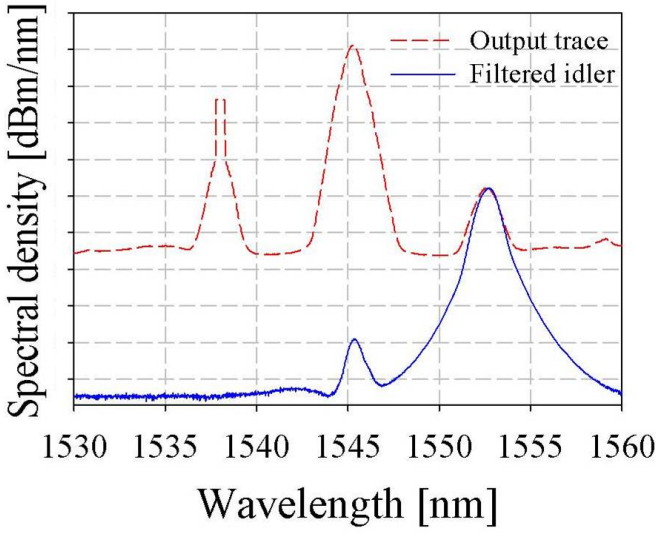


FIGURE 5.6: Filtered idler used for the characterisation of the generated pulses in a 1.5m sample of all-solid multi-ring fibre-based wavelength converter.

The eye diagram of the filtered idler was then recorded. Figure 5.7(a) shows the eye diagram of the input signal ($\lambda_{CW}$=1538nm), while Figure 5.7(b) shows the eye diagram

of the filtered idler ($\lambda_{CW}$=1552nm), which appears to be clean and open with low intensity noise.

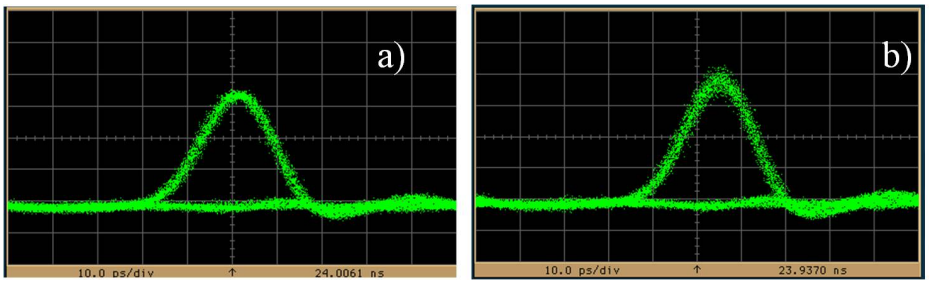


FIGURE 5.7: Eye diagrams of (a) the input signal and (b) filtered idler at $\lambda_{idler}$ = 1552nm in a 1.5m sample of all-solid multi-ring fibre-based wavelength converter.

The filtered idler was connected to an electrically amplified receiver and then to a BER tester. The high quality of the eye diagram is reflected in the corresponding BER measurement shown in Figure 5.8. The wavelength converted signal shows a power penalty of only ~0.5 dB as compared to the input signal at BER=$10^{-9}$ (error-free operation), confirming the good quality of the conversion process.

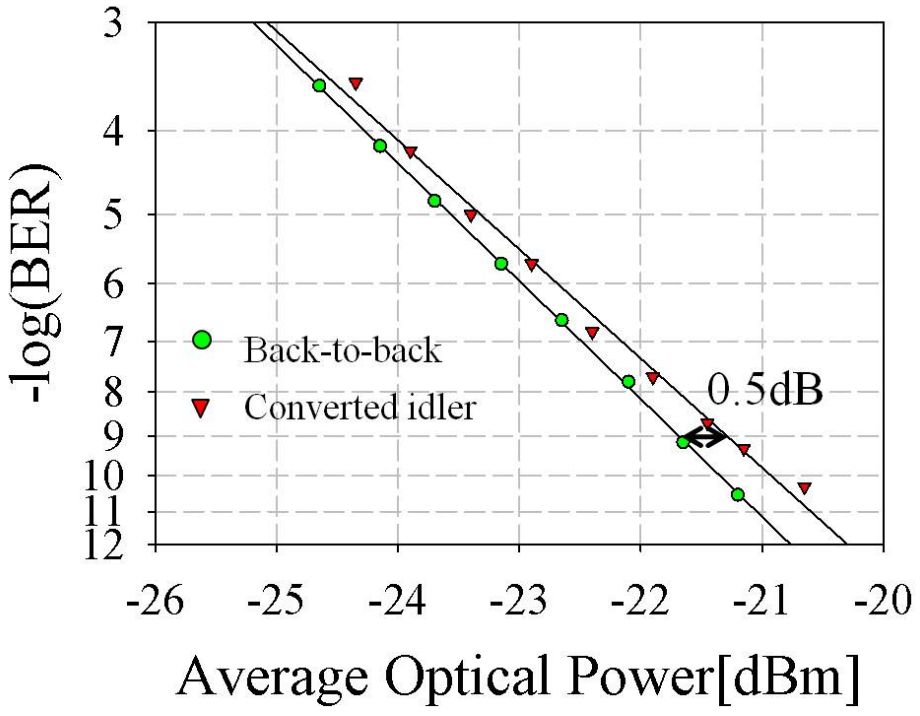


FIGURE 5.8: BER measurement of the converted idler (red triangles) and of the input signal (green dots) in a 1.5m sample of all-solid multi-ring fibre-based wavelength converter.

Finally, the autocorrelation traces of the input and output signals have been measured. The input pulse was measured to be 7ps, while the converted pulse duration was measured to be 4.8ps, as shown in Figure 5.9. The measured value of the output pulse duration was predicted by numerical simulations performed on our wavelength conversion system.

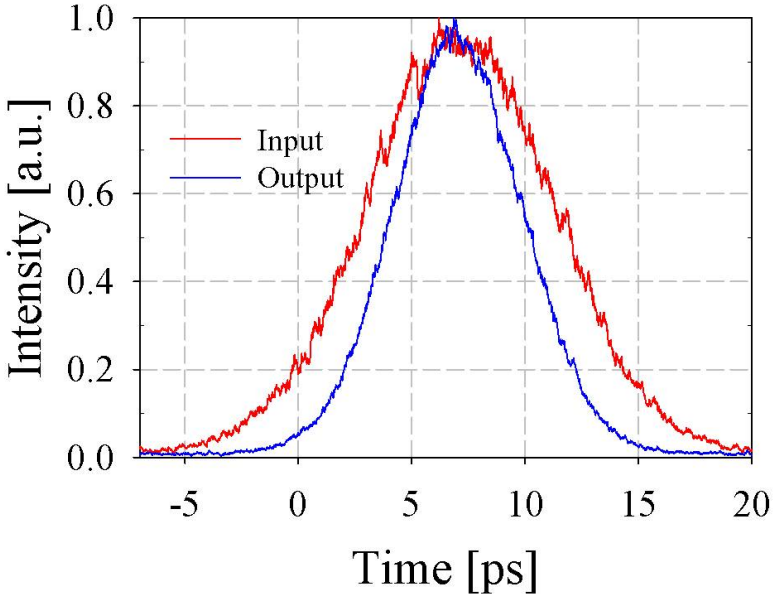


FIGURE 5.9: Autocorrelation traces at the input (red trace) and output (blue trace) of in a 1.5m sample of all-solid multi-ring fibre-based wavelength converter.

Eq. 5.8 and 5.9, although derived for a CW regime, can be also applied to pulsed signals, assuming that the broadening of the pump spectrum due to SPM can be neglected, and have been successfully used to predict optical pulse compression by FWM in optical fibres [Yamamoto and Nakazawa, 1997]. I have performed numerical simulations on a 1.5m long sample of the all-solid multi-ring fibre under the above presented experimental conditions. Figure 5.10(a) shows the input waveform of the pump at 1545nm, where the full width at half maximum (FWHM) of the signal is 7.0ps. According to the work of Yamamoto and Nakazawa, the time dependence of the pump power is translated in a time dependence of the parametric gain $g$, which shows a pulsewidth of 4.8ps, as illustrated in Figure 5.10(b). Therefore,according to Eq. 5.8, the output waveform shows the same FWHM of 4.8ps.

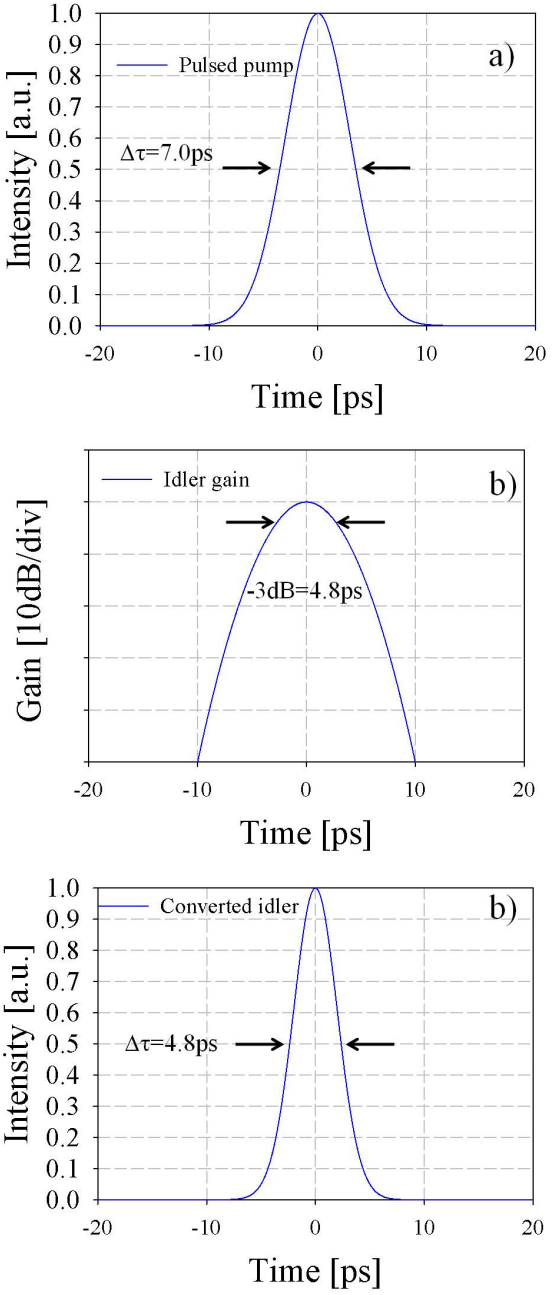


FIGURE 5.10: FWM-based pulse compression: (a) Waveform of the input pump at 1545nm; (b) Time dependent gain profile for the idler gain; (c) Waveform of the converted idler at 1552nm. The simulations are based on the experimental conditions reported in Section 5.2.1

A good agreement can be seen between the predicted and the recorded traces, as shown in Figure 5.11.

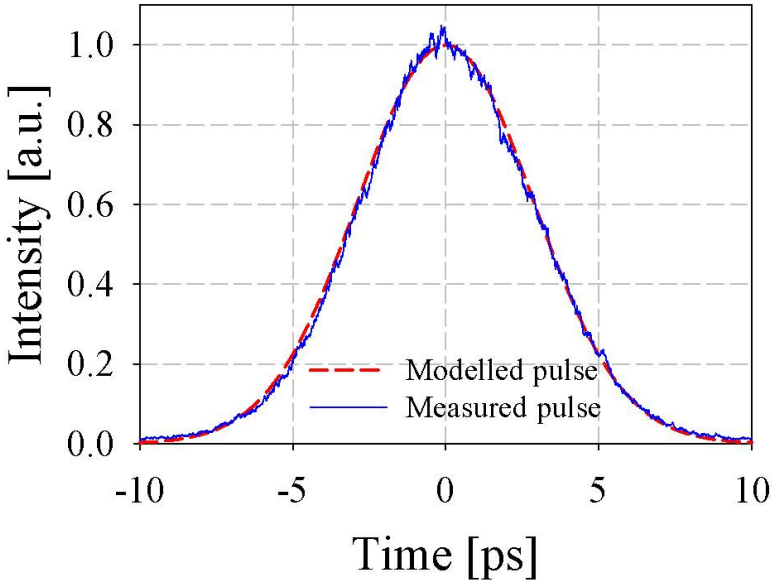


FIGURE 5.11: Comparison between the simulated pulse (red line) and the measured pulse (blue line) at the output of the all-solid multi-ring fibre-based wavelength converter system.

Further numerical simulations were performed in order to study the trade off that exists between highest conversion efficiency and maximum bandwidth. Figure 5.12 shows the calculated conversion efficiency for various fibre lengths ranging from 1.5m to 6.0m. The power levels and the pump and signal wavelengths were chosen to be the same as in the experimental setup reported in Section 5.2.1. The -3dB gain bandwidth improves from 11nm to 12nm as the fibre length varies from 6 to 1.5m. On the other hand, the conversion efficiency is higher for the longer fibre lenggth, decreasing from -33dB to -40dB for this length range. Figure 5.12 also shows that the simulation results for the 1.5m long fibre are in good agreement with my experiments. Note that the trend shown by the curves in Figure 5.12 is in agreement with what discussed in Section 4.1.4. According to Eq. 4.13, for a fixed value of dispersion D, and increasing lengths of fibre samples, the first minimum in the conversion efficiency is found at decreasing values of wavelength separation between the two pumps.

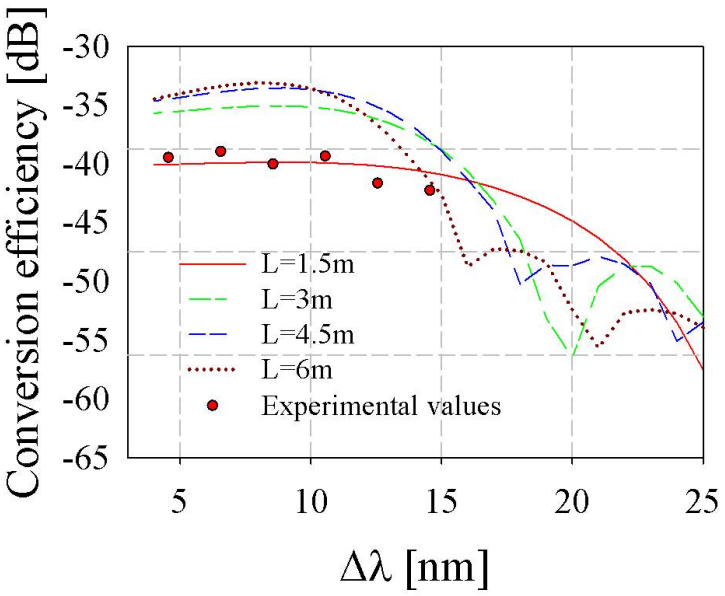


FIGURE 5.12: Calculated curves of the FWM conversion efficiency using different fibre length under the experimental conditions of Section 5.2.1 and measured conversion efficiency (red dots) in a 1.5m all-solid multi-ring fibre-based wavelength converter.

### 5.2.3 Conclusions

Using just a 1.5m long sample of all-solid multi-ring fibre, FWM-based wavelength conversion of a pulsed signal over 17nm was demonstrated. Although the pump signal sits at wavelengths relatively far from the fibre ZDW, efficient wavelength conversion could be achieved accompanied by compression of the converted pulses. The quality of the wavelength conversion process has been assessed for one particular wavelength in terms of eye diagram and BER measurements. The trade off between maximum conversion efficiency and -3dB bandwidth has also been investigated through numerical simulations.

## 5.3 FWM-based wavelength conversion in a W-type fibre

The fabrication of lead-silicate W-type fibres has allowed a significant improvement in both the nonlinear coefficient and the dispersion profile when compared to the all-solid multi-ring fibre. This was reflected in FWM experiments performed even with the rather lossy, first generation fibres (LSWF#1), see Section 4.2.3. The main properties of this fibre are summarised in Table 5.2. Despite the high value of propagation losses

of the fibre, the possibility to use this sample as the nonlinear medium in a FWM-based wavelength conversion system seemed to be promising and has therefore been investigated.

TABLE 5.2: Main properties of the high loss lead-silicate W-type fibre, LSWF#1, at 1550nm.

| Nonlinear Coefficient ($W^{-1}km^{-1}$) | Propagation loss (dB/m) | Dispersion (ps/nm/km) | Dispersion Slope ($ps/nm^2/km$) |
|---|---|---|---|
| 822 | 4.8 | -12 | -0.1 |

The results presented in this Section (as well as in Section 5.4) showed significant potential and prompted the initiation of efforts for an improvement in the fabrication process, which in turn led to the improved, next generation of the W-type fibre and the experimental investigations which will be presented in Chapter 6.

### 5.3.1 Experimental setup

The setup used for this experiment is shown in Figure 5.13. The setup is very similar to the one presented in Figure 5.3.

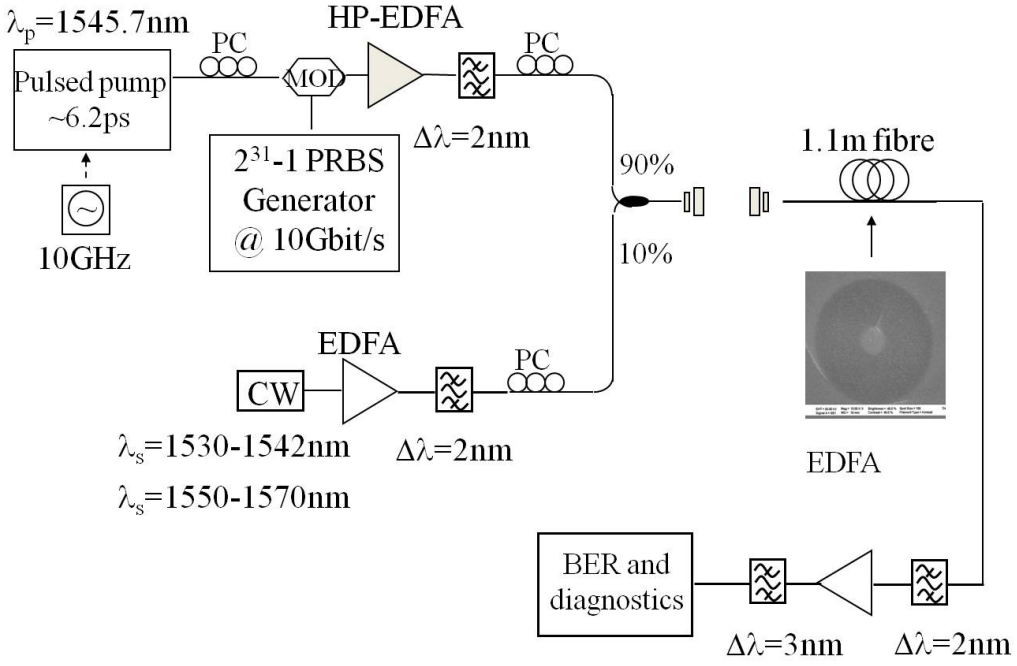


FIGURE 5.13: Experimental setup for the demonstration of FWM-based wavelength conversion in a 1.1m sample of high loss lead-silicate W-type fibre.

The all-solid multi-ring fibre was replaced with a 1.1m long sample of the lead-silicate W-type fibre and the pump wavelength was placed at 1545.7 and had a pulse duration of

6.2ps. The CW signal was tuned from 1530 to 1542nm and from 1550 to 1570nm. The coupling efficiency in this case was estimated to be ∼25% and the average powers of the pulsed pump and the CW signal at the very input of the fibre were 23dBm and 2.1dBm respectively. The peak power of the pump wave in the fibre was of 1.9W. The fibre length was chosen in order to achieve a broadband wavelength conversion bandwidth.

### 5.3.2 Experimental results

The spectra taken at the output of the wavelength converter are shown in Figure 5.14.

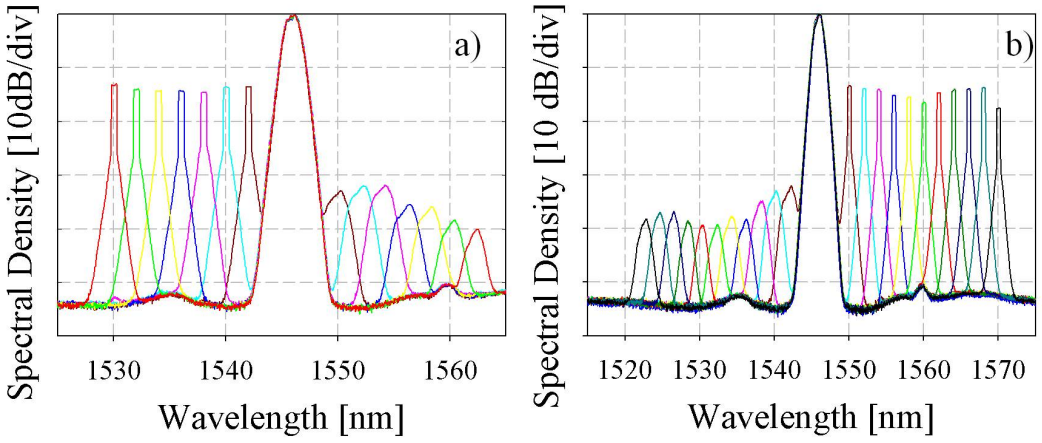


FIGURE 5.14: Spectra taken at the output of a 1.1m sample of high loss lead-silicate W-type fibre-based wavelength converter when the CW wavelength is tuned (a) from 1530nm to 1542nm and (b) from 1550nm to 1570nm.

The higher nonlinear coefficient of this fibre and the lower dispersion when compared to the all-solid multi-ring fibre, allowed for wavelength conversion over the whole C-band. Numerical simulations were performed to support the experimental results. Figure 5.15 shows the comparison between the simulated and measured spectra at the output of the wavelength converter for two particular signal wavelengths: (a) $\lambda_{CW}$=1540nm and (b) $\lambda_{CW}$=1552nm. It can be seen that the simulated and measured traces are in good agreement, although any additional FWM components, which were well below 50dB from the pump, could not be observed due to the limited dynamic range of the OSA used for the experiment.

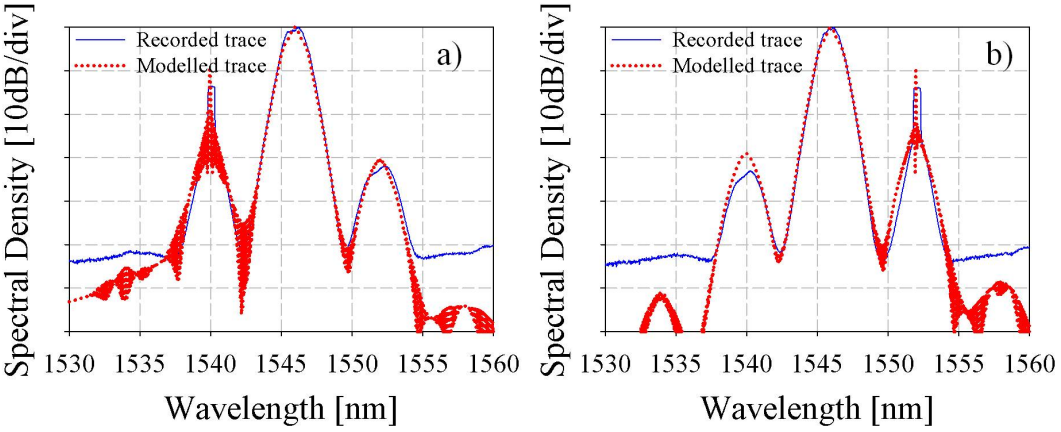


FIGURE 5.15: Comparison between the simulated spectra (red dotted line) and measured spectra (blue solid line) at the output of a 1.1m sample of high loss lead-silicate W-type fibre-based wavelength converter when (a) $\lambda_{CW}$ = 1540nm and (b) $\lambda_{CW}$ = 1552nm.

The conversion efficiency is summarised in Figure 5.16, where it is clear that the conversion process spans across the whole 30nm C-band range, with a 3dB bandwidth of 20nm. The dependence of the FWM gain on the dispersion for this fibre will be further investigated in Section 5.4.

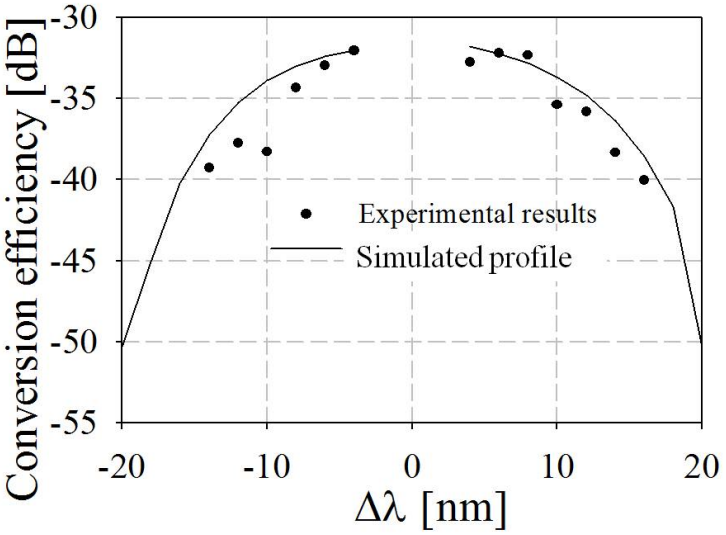


FIGURE 5.16: Calculated curve of the conversion efficiency and measured values (black dots) at the output of a 1.1m sample of high loss lead-silicate W-type fibre.

The converted signals were then filtered and characterised in terms of noise properties and pulse width. Due to the limited filters available at the time of the experiment, only the converted signals at the following wavelengths were analysed: $\lambda_{idler}$ = 1540nm, $\lambda_{idler}$ = 1552nm, $\lambda_{idler}$ = 1554nm, $\lambda_{idler}$ = 1556nm, and $\lambda_{idler}$ = 1558nm. The eye diagrams

of the input signal and filtered idlers are shown in Figure 5.17. Clean and open eye diagrams were recorded for all the filtered idlers.

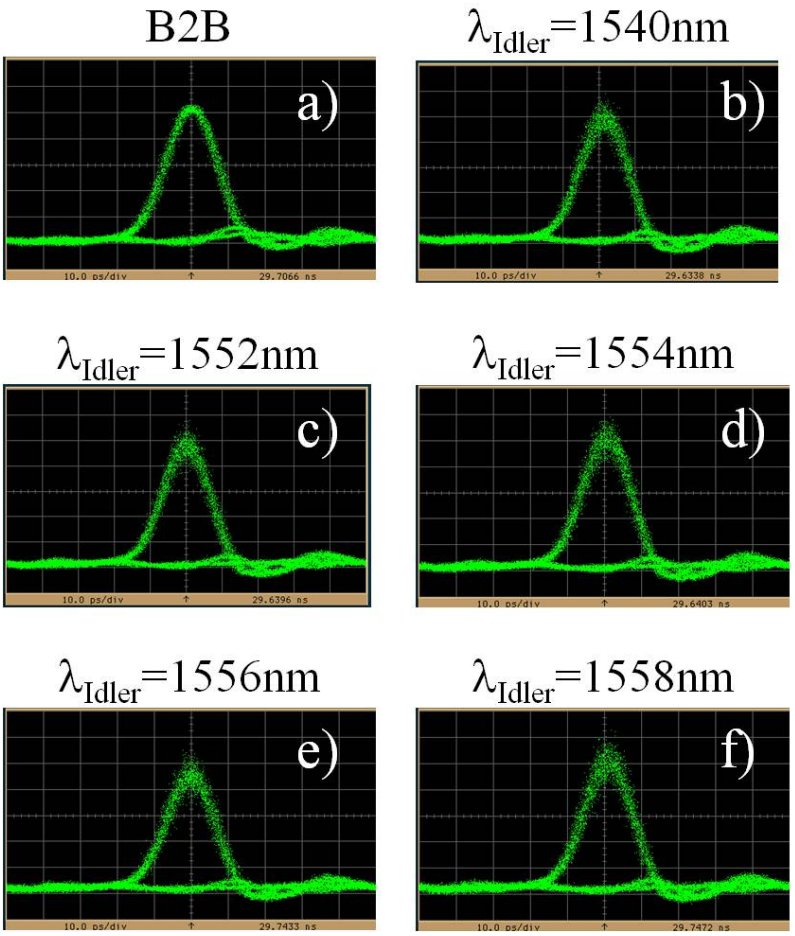


FIGURE 5.17: Eye diagrams at the output of a 1.1m sample of high loss lead-silicate W-type fibre-based wavelentgth converter of (a) the input signal (B2B), (b) $\lambda_{idler}$ = 1540nm, (c) $\lambda_{idler}$ = 1552nm, (d) $\lambda_{idler}$ = 1554nm, (e) $\lambda_{idler}$ = 1556nm, (f) $\lambda_{idler}$ = 1558nm.

The back-to-back (B2B) power at which error free operation could be achieved was measured to be -19.5dBm. For every idler, the power penalty at error free operation, when compared to the B2B value, was measured and the results are summarised in Figure 5.18.

Figure 5.18 shows that error free operation was obtained for all of the filtered idlers, with the lowest values of power penalty corresponding to the two idlers wavelengths showing the cleanest eye diagrams: $\lambda_{idler}$ = 1540nm, $\lambda_{idler}$ = 1552nm. For reference, the full BER curves for these two particular cases are shown in Figure 5.19.

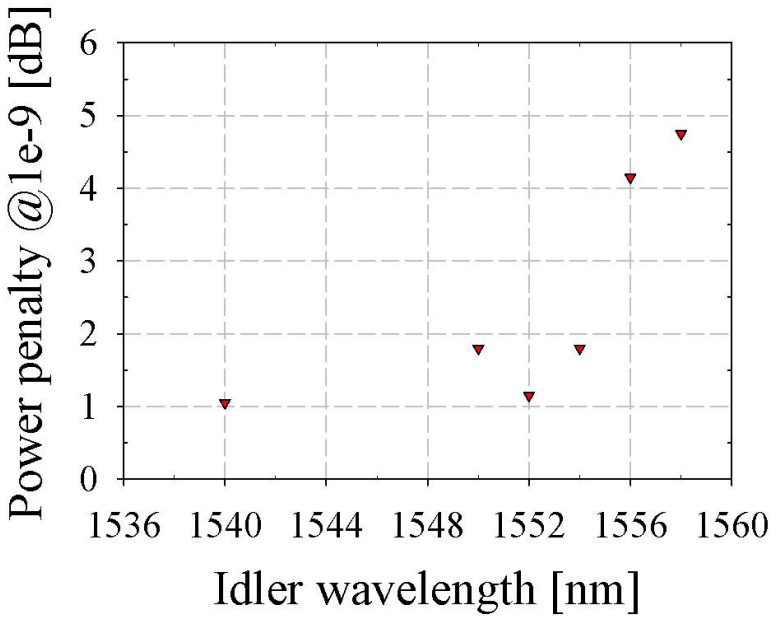


FIGURE 5.18: Measurements of the power penalties of the filtered idlers as a function of the idler wavelength at the output of a 1.1m sample of high loss lead-silicate W-type fibre-based wavelength converter.

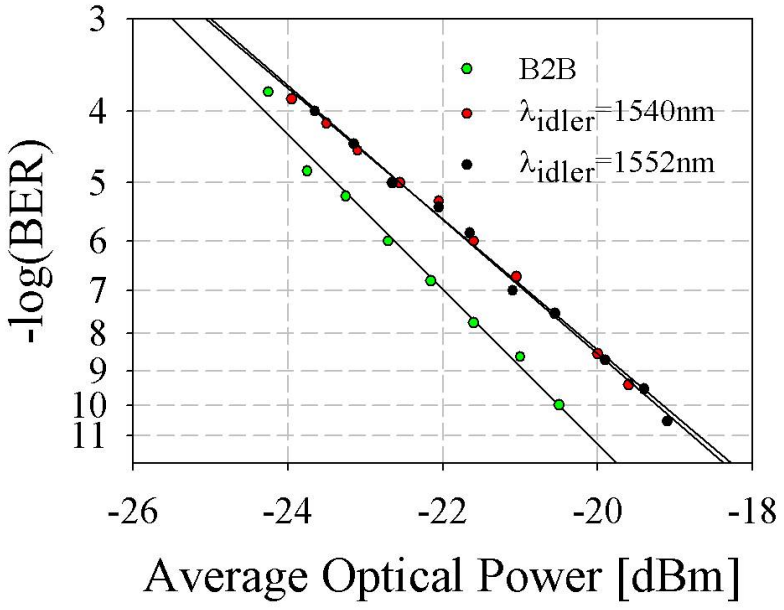


FIGURE 5.19: BER measurement of the input signal (green dots), and of the converted idler at $\lambda_{idler}$ = 1540nm (red dots), $\lambda_{idler}$ = 1552nm (black dots) in a 1.1m sample of high loss lead-silicate W-type fibre-based wavelength converter.

In order to complete the characterisation of the filtered idlers, the autocorrelation traces of the pulses were recorded. The traces for all the filtered idlers are shown in Figure 5.20. The FWHM of the input pulse was measured to be 6.2ps, while the output pulses show a FWHM in the range of 3.9ps to 4.4ps, where the lowest values have been measured for $\lambda_{idler}$=1540nm, $\lambda_{idler}$=1552nm. As discussed for the all-solid multi-ring fibre, in the pulsed pump regime, the FWM-based wavelength conversion process results in compression of the output pulses when compared to the input pulses. Numerical simulations supporting the experimental results confirm the value of the measured pulse duration, as shown in Figure 5.21.

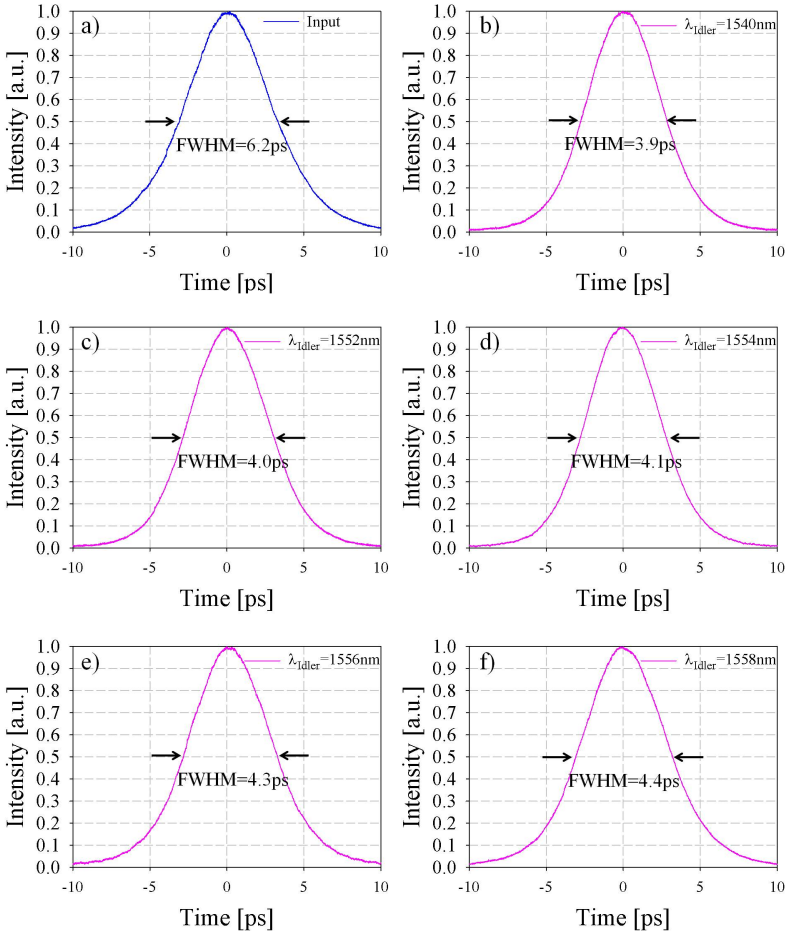


FIGURE 5.20: Autocorrelation traces of (a) the input signal and the converted idler at (b) $\lambda_{idler}$ = 1540nm, (c) $\lambda_{idler}$ = 1552nm, (d) $\lambda_{idler}$ = 1554nm, (e) $\lambda_{idler}$ = 1556nm, (f) $\lambda_{idler}$ = 1558nm in a 1.1m sample of high loss lead-silicate W-type fibre-based wavelength converter.

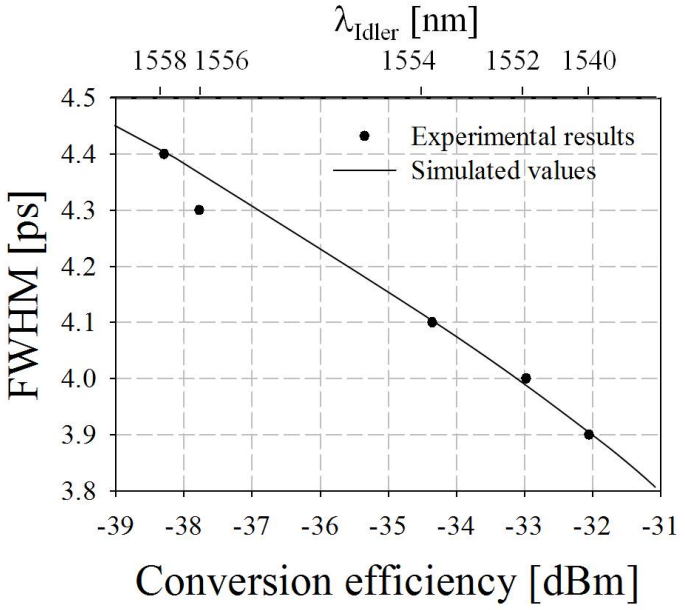


FIGURE 5.21: Simulated and measured pulse width FWHM for various values of conversion efficiency in a 1.1m sample of high loss lead-silicate W-type fibre-based wavelength converter.

In particular, a comparison between the simulated and measured autocorrelation traces for $\lambda_{idler}$=1552nm is shown in Figure 5.22.

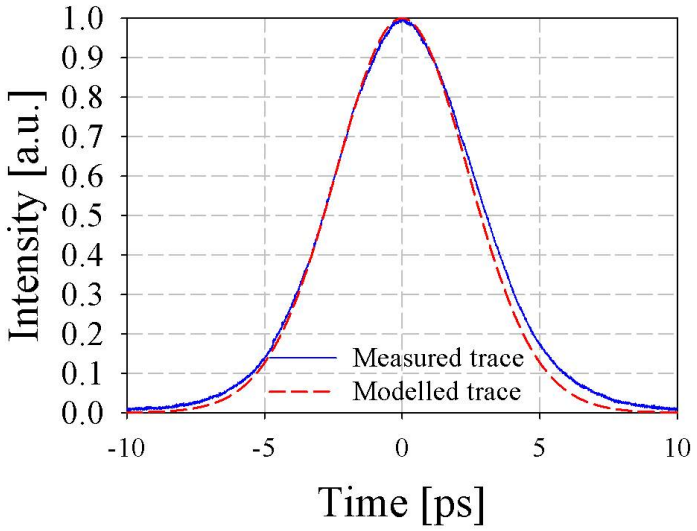


FIGURE 5.22: Simulated autocorrelation trace (red dashed line) and measured autocorrelation trace (blue solid line) for $\lambda_{idler}$ = 1552nm in a 1.1m sample of high loss lead-silicate W-type fibre-based wavelength converter.

### 5.3.3 Conclusions

Tunable and broadband wavelength conversion has been achieved in only 1.1m of the lead-silicate W-type fibre. Despite the high loss of the particular fibre used in this experiment, the high nonlinear coefficient and the tailored dispersion profile allow for a successful FWM-based wavelength conversion over a range of 30nm, with a -3dB bandwidth of 20nm. The quality of the conversion process has been assessed through eye diagrams and BER curves. The pulse duration of the converted idlers has also been measured and the pulse compression due to FWM has been confirmed both experimentaly and by numerical simulations.

## 5.4 Towards flat FWM gain profile in a lead-silicate W-type fibre

For a fixed $\gamma$P product in a fibre, the maximum conversion efficiency is strictly related to the fibre loss while the gain bandwidth is dependent on the fibre dispersion profile. The maximum conversion efficiency for the lead-silicate W-type fibre reported in Section 5.3 is therefore limited by the high propagation loss of the sample. In Section 4.2.3 an annealing step on the fibre has shown to reduce the propagation loss from 4.8dB/m to 4.1dB/m. The annealing step is therefore expected to have an effect also on the maximum conversion efficiency that can be obtained in the fibre. I compared the FWM performance achieved in a 1.1m long sample of high loss fibre used in the previous Section to that of the same sample after the annealing step was performed.

The setup used for this experiment is shown in Figure 5.23. A CW laser was used as a pump while a second tunable CW laser was used as the signal. The pump was modulated using a $LiNbO_3$ Mach Zehnder modulator driven with 100ps rectangular pulses with a duty cycle of 1:64. The modulated pump was amplified and filtered in order to remove the undesired ASE noise and then combined with the signal in a 90/10 coupler. The signal was also amplified and filtered before being coupled to the pump. The signal was then free-space launched into the two fibre samples. The coupling efficiency in both cases was $\sim$20%. The average pump and signal power at the input of the fibres was 17.7dBm and 9dBm respectively. The corresponding peak power for the pump wave in both cases was 3.7W.

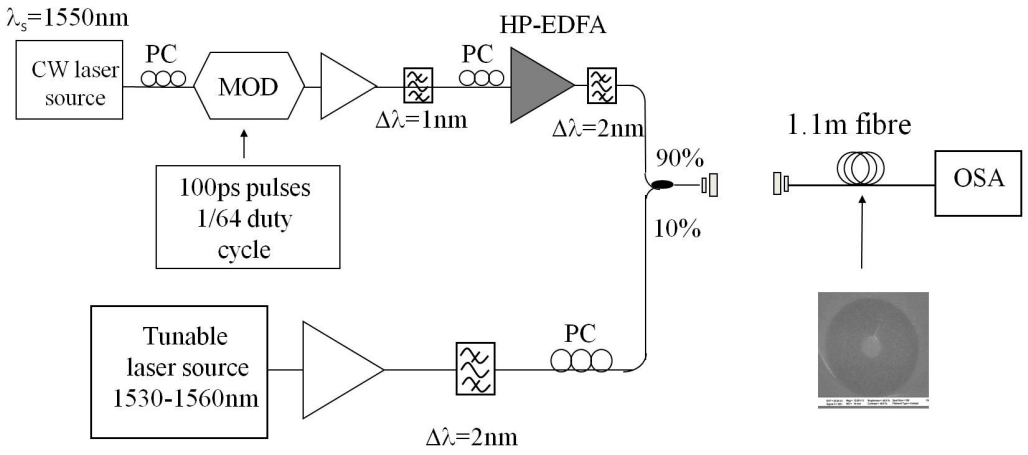


FIGURE 5.23: Experimental setup for the demonstration of FWM-based wavelength conversion in a lead-silicate W-type fibre.

The spectral traces at the output of the fibre before annealing are shown in Figure 5.24. Figure 5.24(a) shows the spectral traces recorded when the signal was tuned from 1532nm to 1546nm, while Figure 5.24(b) shows the traces recorded when the signal was tuned from 1554nm to 1570nm.

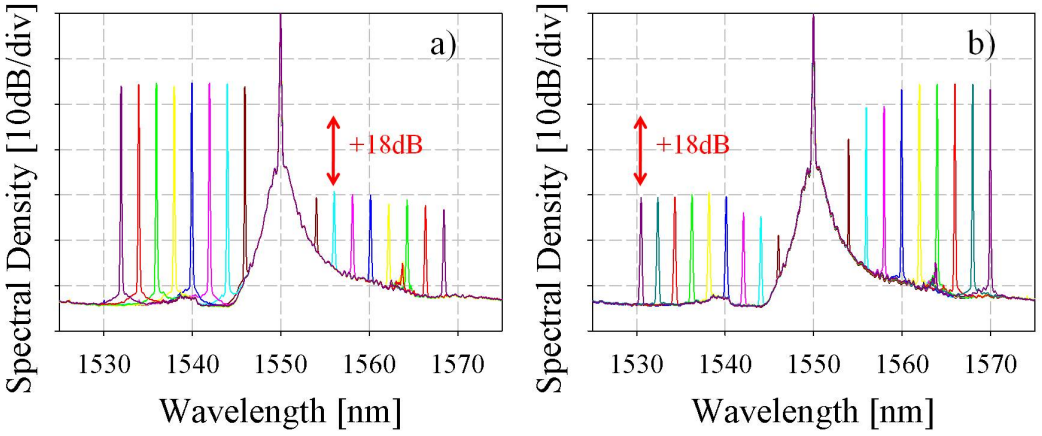


FIGURE 5.24: Spectral traces at the output of the high loss W-type fibre before annealing when the CW signal is tuned (a) from 1532nm to 1546nm and (b) from 1552nm to 1570nm.

Since the pump, and therefore the converted idlers as well, was modulated with a duty cycle of 1:64, the peak power of the idler was 18dBm higher than the value recorded on the OSA. The conversion efficiency, here defined as the ratio between the converted idler and the input signal, is shown in Figure 5.25, where a maximum conversion efficiency of -6dB can be appreciated. Figure 5.25 also shows the simulated conversion efficiency

based on the set of equations developed in Section 5.1. The asymmetry in the conversion efficiency reflects the asymmetry in the dispersion profile of the fibre around the operational wavelength of 1550nm as shown in Figure 4.17

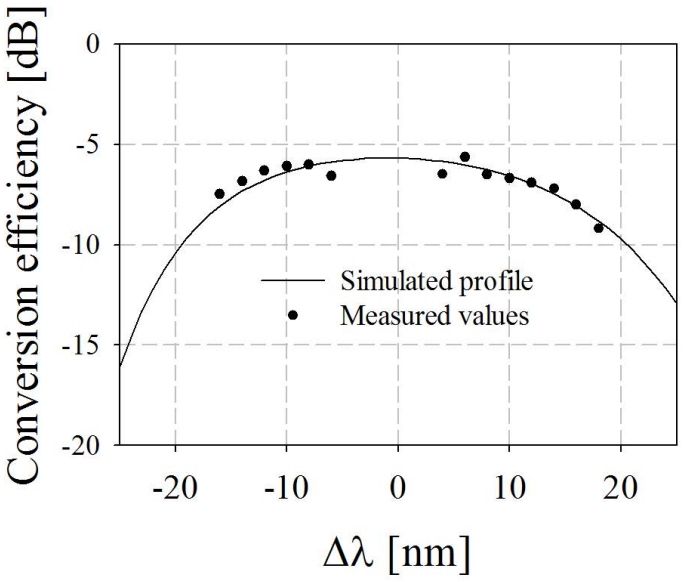


FIGURE 5.25: Simulated curve for the FWM conversion efficiency in a 1.1m of high loss lead-silicate W-type fibre before the annealing and experimental results (black dots).

After the annealing step, which was carried out under the conditions discussed in Section 4.2.3, the measurement was repeated using the same setup as shown in Figure 5.23, taking care to reach the same value of power in the fibre. The output traces are shown in Figure 5.26, where the CW signal was set at the same wavelengths as in the previous case, before the annealing step.

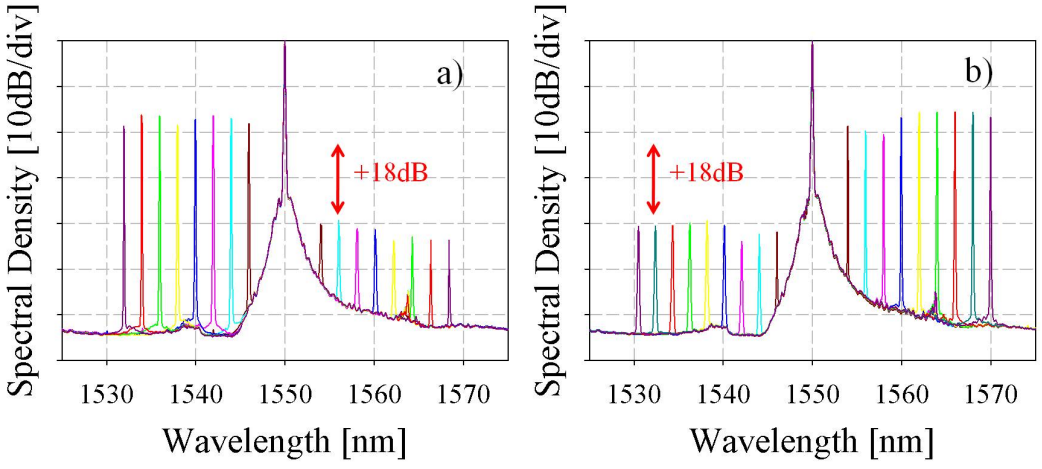


FIGURE 5.26: Spectral traces at the output of the high loss W-type fibre after annealing when the CW signal is tuned (a) from 1532nm to 1546nm and (b) from 1552nm to 1570nm.

Adding 18dBm at the idler output power, the FWM gain is plotted in Figure 5.27. The maximum conversion efficiency in this case was -4dBm, which is 2dB higher than that achieved in the same sample before annealing. The increase in the conversion efficiency comes at the cost of a reduction, although small, of the -3dB bandwidth which is reduced from 36nm to 35nm. The reduction in bandwidth is expected, as the pump wavelength is placed in the normal dispersion regime, as explained in Section 5.1. In order to increase the bandwidth of the FWM-based wavelength conversion process it is necessary to act on the fibre dispersion properties.

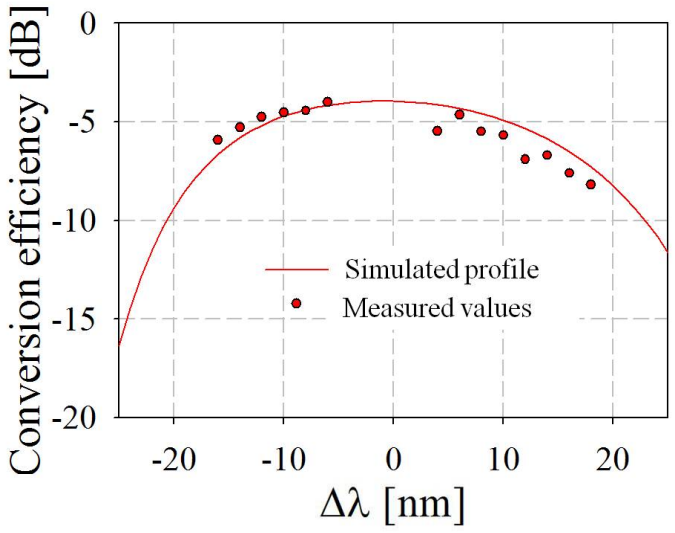


FIGURE 5.27: Simulated curve for the FWM conversion efficiency in a 1.1m of high loss W-type fibre after the annealing and experimental results (red dots).

For the lead-silicate W-type fibre reported in Section 4.2.3, the fibre core diameter influences the fibre dispersion profile and therefore the FWM gain profile. By carefully controlling the core diameter, a flat and close to zero dispersion profile is achieved in the wavelength range between 1500nm and 1600nm. This is illustrated in Figure 5.28(a), where the simulated dispersion profile is shown for three values of core diameter, 1.60$\mu$m, 1.64$\mu$m, 1.68$\mu$m. Under the same experimental conditions used for the investigation of FWM-based wavelength conversion in the high loss W-type fibre, the FWM gain profile corresponding to the three selected values of core diameters have been simulated. The resulting modeled gain profiles are shown in Figure 5.28(b).

It is evident how the -3dB bandwidth increases from 24nm up to 40nm by increasing the core size from 1.60$\mu$m to just 1.64$\mu$m. When the fibre core is 1.68$\mu$m, the dispersion of the considered range of wavelengths changes sign. The gain profile shows therefore the

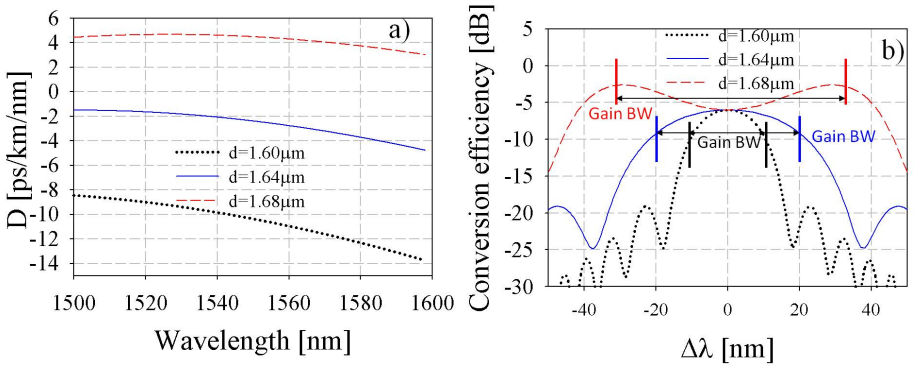


FIGURE 5.28: (a): Simulated dispersion profile of a lead-silicate W-type fibre for three values of core diameter: 1.60$\mu$m (dashed line), 1.64$\mu$m (solid line) and 1.68$\mu$m (dashed line); (b): corresponding simulated FWM conversion efficiency profiles.

typical profile of the case when the pump wavelength is placed in the anomalous regime and the FWM bandwidth extends even further than in the previous cases (50nm).

The third sample of lead-silicate W-type fibre reported in Section 4.2.3 shows much lower propagation loss than the previous sample due to the improved fabrication process and a much lower dispersion profile due to the bigger core. The main properties of the fibre sample are summarised in Table 5.3 below.

TABLE 5.3: Main properties of the low loss lead-silicate W-type fibre, LSWF#2, at 1550nm.

| Nonlinear Coefficient ($W^{-1}km^{-1}$) | Propagation loss (dB/m) | Dispersion (ps/nm/km) | Dispersion Slope ($ps/nm^2/km$) |
|---|---|---|---|
| 820 | 2.1 | -3.2 | 0.05 |

The FWM-based wavelength conversion process is been investigated also in 2.2m of this fibre, using again the same setup as in Figure 5.23. The fibre length has been chosen to be as close as possible to the value of optimum length defined by Eq. 5.12. The coupling efficiency was measured to be 22% and the average power for the pump and the signal were 18.2dBm and 9.5dBm respectively. The spectral traces at the output of the fibre are shown in Figure 5.29. It is evident that the lower loss and the lower dispersion profile of the fibre result in a much more efficient FWM gain when compared to the previous fibres.

As previously, due to the fact that the pump is modulated, the idler peak was 18dBm higher than the value recorded by the OSA. The results are summarised in Figure 5.30, where it is possible to see that a conversion efficiency of ~0dBm has been achieved across the whole C-band.

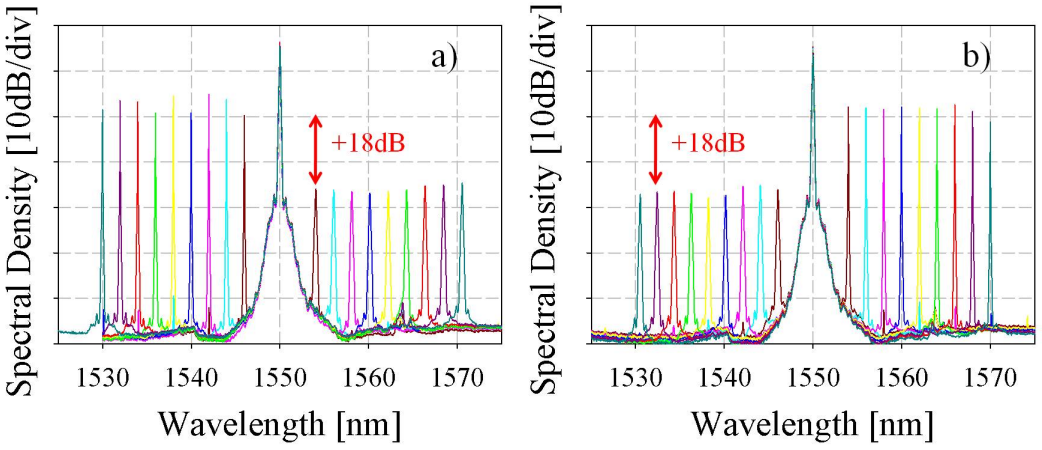


FIGURE 5.29: Spectral traces at the output of the low loss lead-silicate W-type fibre when the CW signal is tuned (a) from 1532nm to 1546nm and (b) from 1552nm to 1570nm.

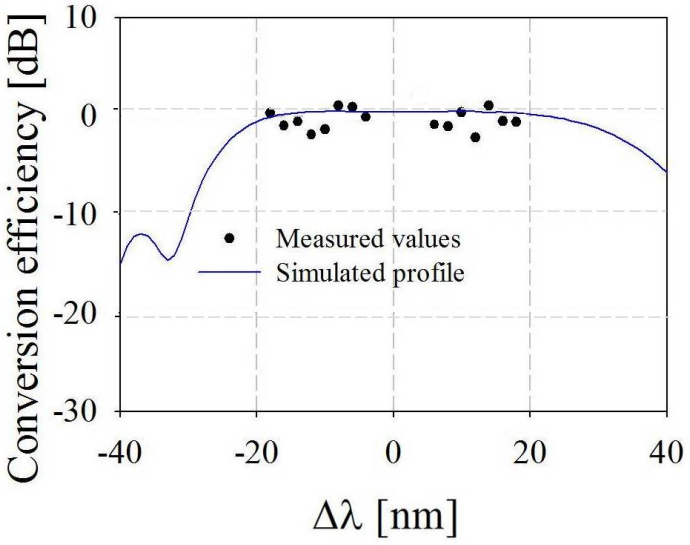


FIGURE 5.30: Simulated curve and experimental results for FWM efficiency in a 2.2m sample of the low loss lead-silicate W-type fibre.

## 5.5 Conclusions

This Chapter investigated FWM-based wavelength conversion in lead-silicate fibres. The first Section was dedicated to the derivation of a simplified set of equations to describe the FWM-based parametric processes in the CW or quasi-CW regime. In order to identify the main fibre parameters that contribute to an efficient FWM process in a fibre and to describe the difference between the normal and anomalous operation regime, a study on a commercially available HNLF was initially numerically carried out. A summary of

the results achieved in the fibres used to investigate the wavelength conversion process together with the main properties of the fibres is reported in Table 5.4.

FWM-based wavelength conversion of pulsed signals was demonstrated in a 1.5m of all-solid multi-ring fibre. A maximum conversion efficiency of -40dB and a -3dB bandwidth of 17nm was experimentally achieved. These results were improved using a sample of lead-silicate W-type fibre, exhibiting propagation losses of 4.8dB/m. Despite the high propagation loss of this sample, a maximum conversion efficiency of -33dB and a -3dB bandwidth of 20nm could be achieved in only 1.1m of this fibre. In both cases the quality of the conversion process was assessed in terms of eye diagrams and BER measurements.

The effect of propagation loss and dispersion of the lead-silicate W-type fibre on the FWM gain was experimentally explored. In particular the effect of annealing the high loss sample of lead-silicate W-type fibre on the conversion efficiency has been demonstrated. Before annealing, a maximum conversion efficiency of CW signals of -6dB over a -3dB bandwidth of 36nm was experimentally achieved in a 1.1m long sample. After annealing a maximum conversion efficiency of -4dB over a -3dB bandwidth of 35nm was achieved in the same sample.

The influence of the fibre dispersion on the FWM bandwidth was investigated with numerical simulations. The effect of both lower dispersion and a lower propagation loss was evidenced in FWM-based wavelength conversion in a sample of the second fabrication attempt of the lead-silicate W-type fibre. Flat conversion efficiency of 0dB across the whole C-band was achieved in only 2.2m of the fibre. This confirms the potential of this lead-silicate fibre for FWM-based applications, and this potential will be explored further in Chapter 6.

TABLE 5.4: Main properties of the fibres selected for wavelength conversion and results achieved.

| Fibre | Length (m) | Loss (dB/m) | Nonlinear coefficient (W-1km-1) | Dispersion (ps/nm/km) | Dispersion slope (ps/nm2/km) | Pumping Scheme | Pump Peak Power (W) | -3dB Bandwidth (nm) | Gain (dB) |
|---|---|---|---|---|---|---|---|---|---|
| All solid fibre | 1.5 | 0.8 | 117 | 12.5 | 0.15 | Pulsed (7ps) | 2.6 | 12 | -40 |
| High loss W-type | 1.1 | 4.8 | 820 | -12 | 0.1 | Pulsed (6.2ps) | 1.9 | 20 | -32 |
| High loss W-type | 1.1 | 4.8 | 822 | -12.5 | 0.1 | CW (Modulated) | 3.7 | 36 | -6 |
| High loss W-type (annealed) | 1.1 | 4.7 | 822 | -12.5 | 0.1 | CW (Modulated) | 3.7 | 35 | -4 |
| Low loss W-type | 2.2 | 2.1 | 820 | -3 | 0.05 | CW (Modulated) | 4 | >40 | 0 |

# Chapter 6

# FWM-based applications based on a W-type lead-silicate fibre

This chapter investigates the potential of the low loss dispersion tailored highly nonlinear lead-silicate W-type fibre introduced in Section 4.2.3 for the realisation of compact (meter-long) FWM-based highly nonlinear devices. The main properties of the fibre used in the experiments presented in this Chapter are summarised in Table 6.1.

TABLE 6.1: Main properties of the low loss lead-silicate W-type fibre at 1550nm.

| Nonlinear Coefficient ($W^{-1}km^{-1}$) | Propagation loss (dB/m) | Dispersion (ps/nm/km) | Dispersion Slope ($ps/nm^2/km$) |
|---|---|---|---|
| 820 | 2.1 | -3.2 | -0.05 |

When evaluating the properties of a highly nonlinear fibre, it is often useful to also investigate its Brillouin gain characteristics. This is particularly important for applications that require a strong CW pump such as some of the experiments described in this Chapter. The maximum value of the CW pump power that can be launched in a fibre without giving rise to Brillouin scattering is limited by the SBS threshold, as expressed by Eq. 3.44. The Brillouin shift in SF57 was previously measured to be 7.65GHz and a SBS threshold of 30dBm can be estimated according to Eq. 3.44 for a true CW signal in a 3m long sample, [Poletti *et al.*, 2007]. In order to investigate the Brillouin properties of LSWF#2 a true CW signal (with narrow linewidth) was launched in a 3m long sample and the light reflected back from it was collected and analysed. It was found that no stimulated backscattered signal could be detected at the expected wavelength for

values of power as high as 29dBm in the fibre (the maximum possible launch power in the experiments). Figure 6.1 shows the input signal (red dotted line) together with the signals reflected back from the fibre (solid lines) for values of input power into the fibre ranging from 20dBm to 29dBm. The blue dashed reference line indicates the wavelength at which the Brillouin reflected signal was expected.

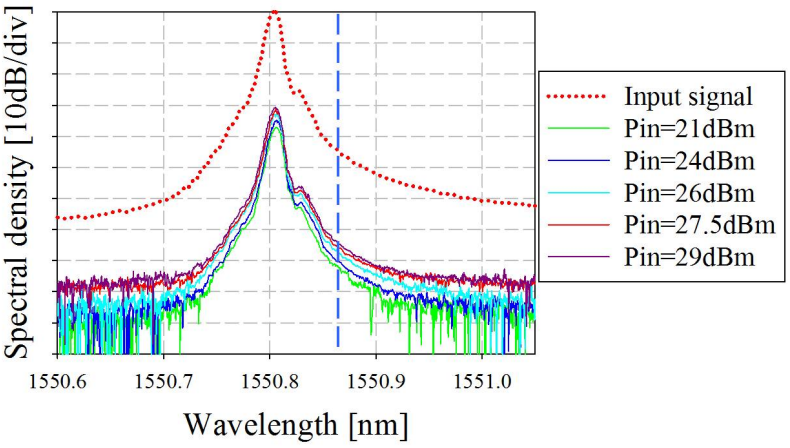


FIGURE 6.1: Spectra of the input (red dotted line) and the output (solid lines) signals reflected back from the LSWF#2 fibre for power levels ranging from 20 to 29dBm into the fibre. The vertical dashed line indicates where the SBS shift is expected. The input signal has been scaled up for visual purposes.

The low and flat dispersion of the fibre in the C-band, together with its high nonlinear coefficient, makes it a good candidate for FWM-based applications based on CW signals. Moreover, the high SBS threshold allows for the use of true CW signals with relatively high power without the need of an additional SBS suppression scheme. In order to illustrate the potential of this fibre, the performance of the fibre for three different applications is investigated.

Section 6.1 presents a wavelength conversion scheme based on 2.2m of this fibre where three 40Gbit/s Non-Return-to-Zero (NRZ) Differential Phase Shift Keying (DPSK) data signals are simultaneously converted to different wavelengths. Section 6.2 illustrates the potential of lead silicate W-type fibre for the generation of high repetition rate pulses. The generation of pulse trains at 160GHz and 200GHz through FWM temporal compression of a dual frequency beat signal is experimentally demonstrated, and the perspective of employing this fibre for the generation of pulses in the THz regime is also investigated. Finally, in Section 6.3 the fibre is successfully employed in an all-optical 160-to-40GHz demultiplexing scheme for On-Off-Keyed (OOK) signals.

## 6.1 Multiwavelength conversion of 40Gbit/s DPSK signals

An attractive feature of FWM-based wavelength conversion techniques is the potential to allow simultaneous conversion of several input channels, thereby decreasing the number of wavelength converters in an optical system, thus reducing the total number of components in the network [Inoue and Toba, 1992]. So far, multi-wavelength conversion of OOK signals based on FWM has been reported in highly nonlinear silica fibres [Watanabe *et al.*, 1998], in semiconductor optical amplifiers (SOAs) [Gosset and Duan, 2002] and periodically poled lithium niobate (PPLN) devices [Yamakazi *et al.*, 2008]. However, in a multichannel conversion scheme of OOK signals, the power of each channel needs to be carefully controlled in order to avoid undesired nonlinear effects such as inter-channel crosstalk. In a FWM-based wavelength conversion scheme of OOK signals, inter-channel crosstalk is due to the data-pattern-dependent pump depletion, [Xu *et al.*, 2004] and can severely degrade the quality of the wavelength conversion process. Therefore, the use of a data format that does not suffer from this issue represents an advantage for the implementation of a multi-wavelength conversion scheme.

Recently, DPSK signals have been widely adopted in high-speed transmission, exploiting the advantages of phase-encoded formats over OOK in terms of optical signal to noise ratio (OSNR), resilience to the various transmission impairments, as well as for their potential for the implementation of high spectral efficiency data encoding [Linke and Gnauck, 1988; Zhu *et al.*, 2004]. Furthermore, especially in the context of FWM-based multi-channel wavelength conversion, in modulation formats like non-return-to-zero (NRZ) DPSK the optical power remains constant over most of the time, thus ensuring that the signals do not suffer from pump-depletion-induced data patterning when relatively high powers are involved (as it happens for OOK signals) [Devgan *et al.*, 2006]. Multi-wavelength conversion of 10Gbit/s DPSK signals has been demonstrated in HNLFs [Devgan *et al.*, 2006] as well as in SOAs [Lacey *et al.*, 1997; Politi *et al.*, 2006] and PPLN devices [Jansen *et al.*, 2006].

In this Section the simultaneous conversion of three 40 Gbit/s NRZ DPSK signals in a 2.2m sample of the W-type lead-silicate fibre (LSWF #2) is presented. A uniform conversion efficiency of -12dB is achieved and error-free performance is confirmed for the three signals with a power penalty lower than 2dB.

### 6.1.1 Experimental setup

The experimental setup for the demonstration of the FWM-based wavelength converter of the three 40Gbit/s NRZ DPSK signals is shown in Figure 6.2.

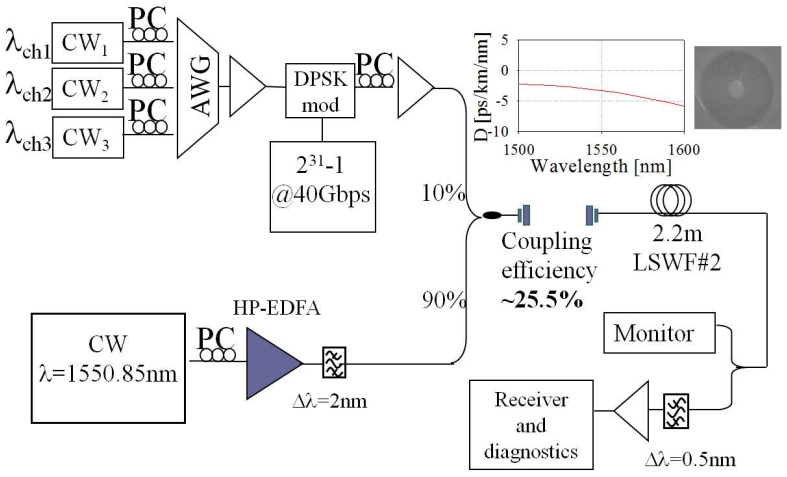


FIGURE 6.2: Experimental setup for the demonstration of multi-wavelength conversion in a 2.2m sample of LSWF #2. Insets: fibre SEM image and dispersion profile of the W-type fibre.

Three consecutive CW lasers on a 100GHz frequency grid, $\lambda_{Ch1}$ = 1556.86nm, $\lambda_{Ch2}$ = 1558.58nm, and $\lambda_{Ch3}$ = 1560.20nm, were multiplexed together using an arrayed waveguide grating (AWG) and modulated with a $2^{31}$-1 pseudorandom bit sequence (PRBS) at 40Gbit/s. The CW pump signal ($\lambda_p$=1550.85nm) was amplified using a high power erbium-doped fibre amplifier (HP-EDFA), followed by a band-pass filter to reject any undesired out-of-band amplified spontaneous emission noise. The three data channels were amplified separately from the pump using a second EDFA. This allowed independent control of the relative power levels of the pump and the signals, while at the same time any undesired nonlinear interaction in the EDFA itself was avoided. The states of polarization of the various beams were controlled by in-line polarization controllers (PCs) in order to maximize the FWM components in the fibre. The CW pump and the data channels were then combined in a 90/10 coupler and free-space launched into the fibre. The coupling efficiency was estimated to be 25.5% and the average powers of the CW pump and the three DPSK signals at the input of the fibre were 23dBm and 8.7dBm, respectively. Despite the relatively high power launched into the fibre, no SBS suppression scheme was employed, due to the high SBS threshold exhibited by the W-type lead silicate fibre. SBS suppression is normally an important issue in CW-pumped parametric processes in fibres [Lacey *et al.*, 1997], and therefore, the absence of

an SBS suppression scheme represents an important advantage of the system reported here. Moreover, it is worth noting that no synchronisation amongst the various channels was required, as a CW pump was used.

### 6.1.2 Experimental results

Figure 6.3 shows the measured optical spectra before (red dotted line) and after the lead silicate W-type fibre (blue solid line), where the signals and the corresponding newly generated idlers can be observed.

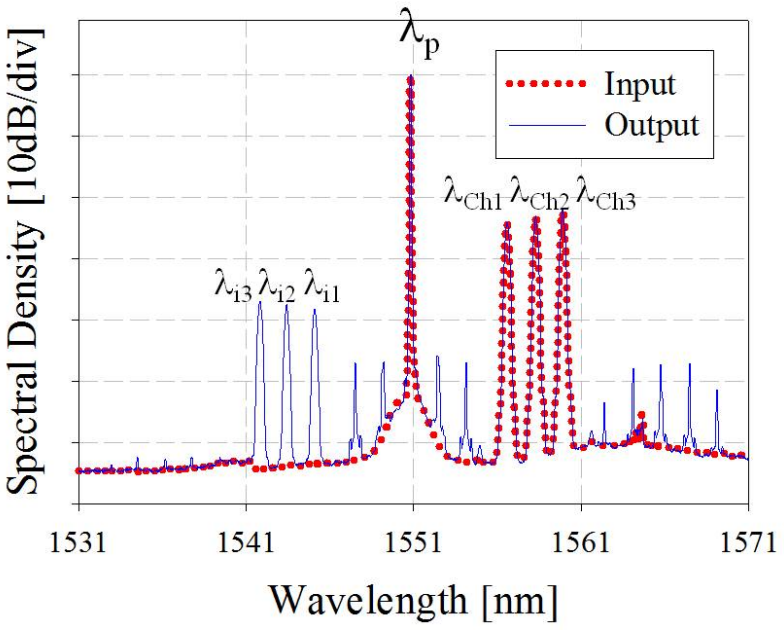


FIGURE 6.3: Spectrum at the input (dotted line) and output (solid line) of the multi-wavelength converter scheme based on a 2.2m sample of LSWF #2.

The output spectrum in Figure 6.3 also highlights the generation of some undesired low-power frequency components, which are FWM products between pairs of the WDM channels and the pump, as well as each WDM channel and the pump, which are located at longer wavelengths. However, these components were clearly at different wavelengths as compared to the WDM channels or their desired idlers, and did not affect the performance of the system, as discussed in more detail below. The filtered idlers are shown in Figure 6.4. The idlers exhibit an OSNR greater than 25dB and a uniform conversion efficiency of -12dB.

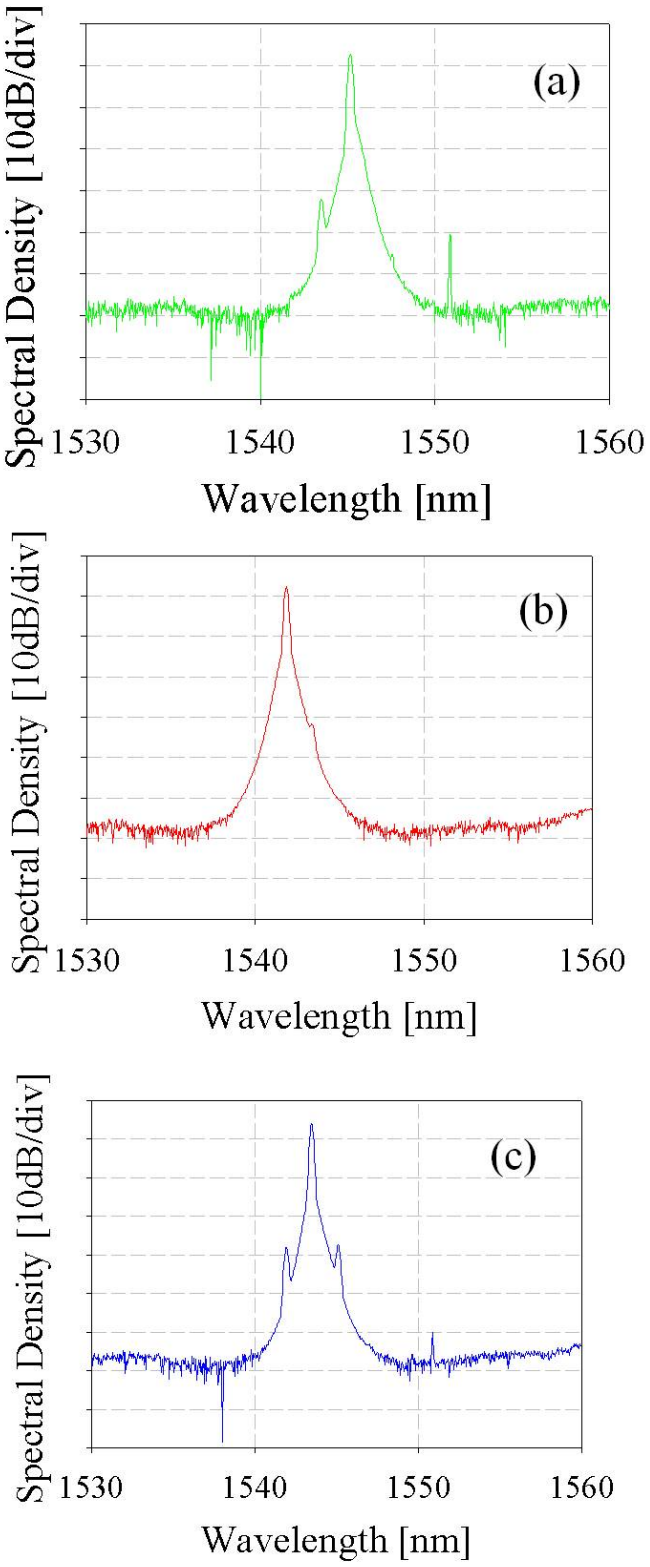


FIGURE 6.4: Spectra of the filtered idlers at the output of the multi-wavelength conversion scheme based in a 2.2m sample of LSWF #2: (a) Idler1; (b) Idler 2; (c) Idler 3.

In order to assess the presence of possible crosstalk between the various channels, we compared the eye diagrams of each of the filtered idlers to those of the input channels, (see left column of Figure 6.5) for two cases: (a) multi-wavelength operation (i.e. when all the channels were on simultaneously - see middle column in Figure 6.5) and (b) single wavelength operation (i.e. when only one channel was on - see right column in Figure 6.5).

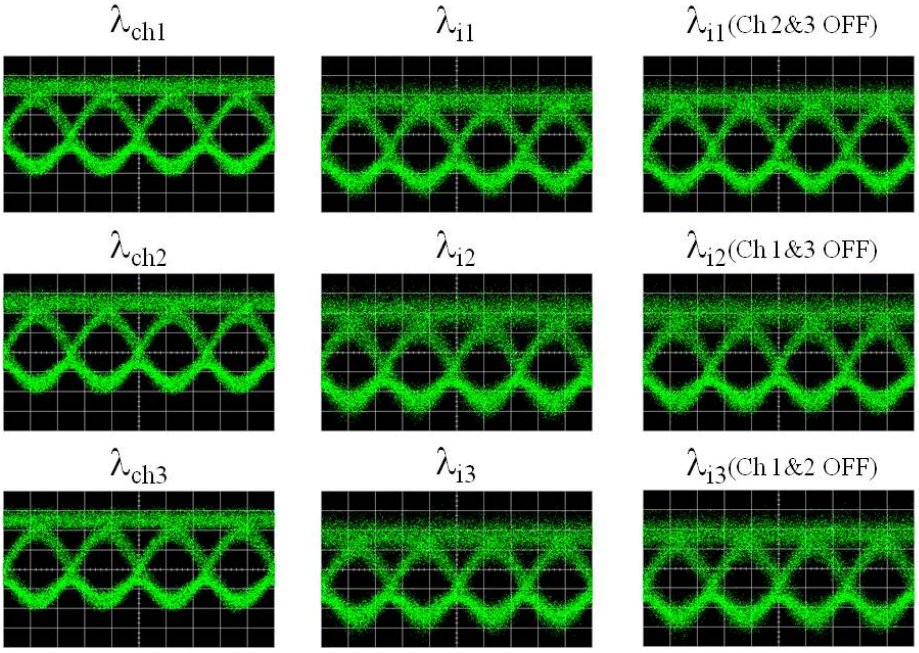


FIGURE 6.5: Eye diagrams of the various channels at the input (first column) and corresponding idlers at the output of the wavelength converter based on a 2.2m sample of LSWF #2 in multi- (second column) and single-wavelength operation (third column).

It is apparent that the eye diagrams are clean and open in both cases, suggesting that the quality of each filtered idler is good and most importantly not affected by the presence of the other signals. The good quality of the converted signals was reflected in the bit-error ratio (BER) measurements presented below.

Figure 6.6 compares the BER curves of the input channels (back-to-back) to those of the filtered idlers for both single and multi-channel operation. Figure 6.6(a) shows the curves for Channel 1 while Figure 6.6(b) and Figure 6.6(c) for Channel 2 and 3 respectively. In all cases we measured a power penalty at error free operation ($10^{-9}$) ranging between 0.5dB and 2dB for the three converted channels as compared to the back-to-back and a low penalty (in the range of 0.2-0.8dB) between the single- and multi-channel operation

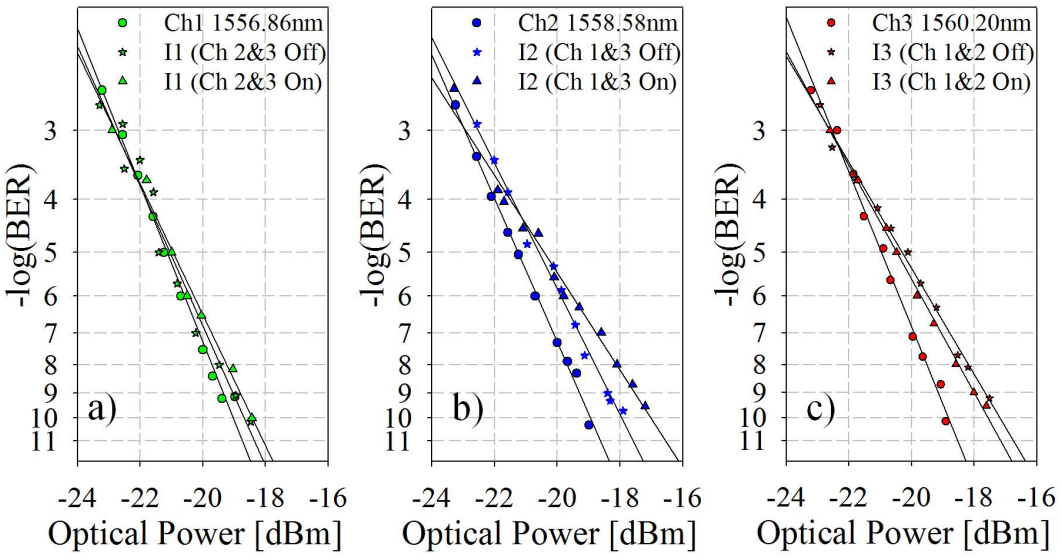


FIGURE 6.6: BER of the input channels and of the filtered idlers of the multi-wavelength converter scheme based on a 2.2m sample of LSWF #2 when all the channels are simultaneously on and off: (a) curves for Channel 1, (b), curves for Channel 2 and (c) curves for Channel 3.

cases. The slight power penalty variation between the various channels is attributed to small differences in the filtering and amplification gain at the idler wavelengths.

Since independent transmitters were not available for the three data signals to allow us to perform measurements using decorrelated PRBS for each WDM signal, the inter-channel crosstalk in the fibre was further analysed through additional spectral measurements. Figure 6.7 shows the output spectra taken when one channel out of the three was switched off: Ch.1 is switched off in Figure 6.7(a), Ch.2 in Figure 6.7(b) and Ch.3 in Figure 6.7(c). In none of the three cases could new frequency components be observed at the missing signal/idler wavelength at least down to the -25dB level, which represents the OSNR of the converted signals.

The scenario when one out of the three signals was not modulated (one CW signal and two DPSK signals) was also investigated. In every case, the power of each signal was carefully controlled so that the overall input power of the system would be kept constant. Examples of the measured traces for this case are shown in Figure 6.8. In none of the analysed cases any spectral distortion of the converted idlers was apparent, implying that they did not suffer from any inter-channel cross-talk, down to the -25dB level, the OSNR of the converted signals.

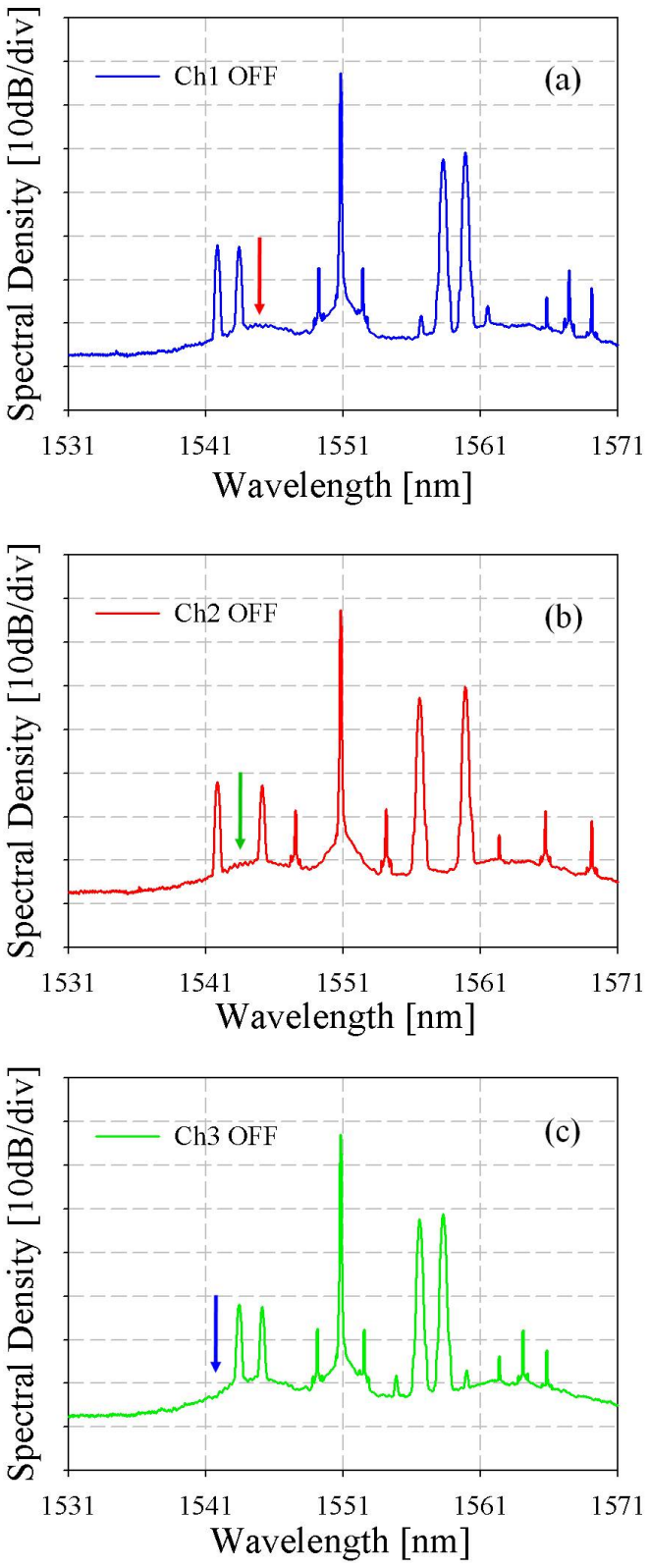


FIGURE 6.7: Spectra taken at the output of the multi-wavelength converter based on a 2.2m sample of LSWF #2 when only 2 of the 3 channels were on: (a) Ch.1 is off; (b) Ch.2 is off; (c) Ch.3 is off.

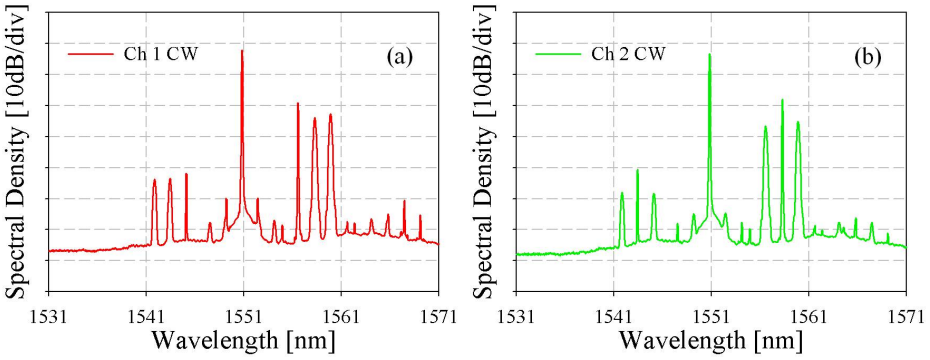


FIGURE 6.8: Spectra taken at the output of the multi-wavelength converter based on a 2.2m sample of LSWF #2 when 1 of the 3 DPSK signals is replaced by a CW signal: (a) Ch.1 is CW; (b) Ch.2 is CW.

### 6.1.3 Conclusions

A multi-wavelength converter of 40 Gbit/s NRZ DPSK signals based on a 2.2m-long W-type lead silicate fibre was experimentally demonstrated. Thanks to the high nonlinearity and low dispersion of the fibre, a CW pump was used, avoiding any synchronisation between the WDM signals and the pump, while thanks to the high SBS threshold of the fibre, no additional SBS suppression schemes was applied to the CW pump. The converted idlers were analysed in the case of single and multi-channel operation. Error-free operation with a power penalty below 2dB was achieved when all three signals were on and negligible power penalty was observed when compared to the case of single channel conversion. Additional spectral measurements have shown negligible inter-channel crosstalk in the multi-channel wavelength conversion scheme.

## 6.2 High repetition rate pulse generation

The development of ultrashort pulse generators that allow for ultra high repetition rates is of great interest in the context of a growing demand of high capacity transmission systems [Pitois *et al.*, 2002]. Moreover, the generation of high repetition rate, high quality optical pulse trains finds several applications in other area of the technology such as optical switching [Yamamoto *et al.*, 1998], metrology [Bogoni *et al.*, 2004b] and optical clock generation [Meloni *et al.*, 2005].

Generation of high repetition rate pulses based on harmonically mode-locked lasers systems has been proposed and experimentally demonstrated [Gee *et al.*, 2005; Nakazawa *et al.*, 1994]. However, this approach suffers from a limited frequency tunability and frequency stability of the mode-locked laser, which requires the introduction of a control system. Moreover, the current bandwidth of optoelectronic devices allows for the generation of pulses with repetition rate not higher than 50GHz and with a temporal width of a few picoseconds [Fatome *et al.*, 2010].

Recently, another approach has been proposed for the generation of high repetition rate pulses. The harmonics at the output of a comb generator at low repetition rate (∼1GHz) are selectively optically filtered using a narrow bandwidth Fabry-Perot cavity, thus increasing the repetition rate of the final pulses [Diddams *et al.*, 2009]. The drawbacks of this technique consist in the fine control of the high finesse Fabry-Perot cavity that is needed, as well as the corresponding high losses usually associated with the scheme.

An optical pulse train can also be generated through compression of a beat signal in optical fibres. The initially sinusoidal signal can be obtained from the beating of two continuous wave (CW) lasers with a frequency separation corresponding to the desired repetition rate. Pulse compression based on the formation of solitons has been demonstrated [Igarashi *et al.*, 2005; Mamyshev *et al.*, 1991; Ozeki *et al.*, 2005]. Solitons are optical pulses that can propagate in an optical fibre with a constant shape i.e., without any temporal broadening caused by dispersion. Their manifestation requires a balance between dispersive and nonlinear effects which can only occur under conditions of anomalous dispersion. Various fibres have been employed for the realisation of the soliton-based compression stage, such as dispersion-decreasing fibres [D'Errico *et al.*, 2003], step-like [Chernikov *et al.*, 1994b] and comb-like dispersion profiled fibres [Chernikov *et al.*, 1994a], made of one or more pairs of standard SMFs and HNLFs so that the final dispersion of the compression system has a step-like or comb-like profile over its hole length. However, the use of such fibres for the compression stage requires careful control on the fibre dispersion along the propagation length, leading to complicated fibre systems.

A valid alternative to the soliton-based pulse compression stage is the approach based on FWM temporal compression of the beat signal in an optical fibre. The generation of high repetition rate pulses through FWM-based nonlinear temporal compression of a dual-frequency beat signal in a highly nonlinear fibre followed by a linear dispersive

medium has proven to deliver high quality (sub-) picosecond signals [Inoue *et al.*, 2007; Pitois *et al.*, 2002].

Usually, independent CW sources are used [Inoue *et al.*, 2007] leading to significant timing jitter on the pulses, which can represent a significant issue for many applications. In [Parmigiani *et al.*, 2010] this issue was addressed by phase-locking the two CWs via stable injection-locking of two semiconductor lasers to an optical comb, thus simultaneously performing narrow-bandwidth filtering and amplification. In that case the two phase-locked lasers were then combined together into a 2m-long highly nonlinear bismuth oxide fibre (Bi-NLF), which shows a high nonlinear coefficient, but also a high dispersion and dispersion slope in the C-band, which is not particularly desirable for a FWM-based application.

In this Section the generation of high repetition rate (160GHz and 200GHz) pulses through stable injection-locking of two semiconductor lasers in a 3m-long sample of LSWF #2 is experimentally demonstrated. A set of simulations has been implemented in order to confirm the results achieved. Also, the role of the tailored dispersion profile for the generation of ultra-short high repetition rate pulses in the THz regime is investigated.

### 6.2.1 Experimental setup

The experimental setup is shown in Figure 6.9. A CW laser was fed into a 10GHz spaced optical frequency comb generator (OFCG), that produces pulses with a timing jitter below 10fs [Parmigiani *et al.*, 2010]. The output of the comb was demultiplexed using a 100GHz array waveguide grating (AWG) and then coupled into two semiconductor lasers to injection-lock them and ensure that their outputs were synchronised in phase relative to each other. The frequency spacing between the two lasers could be controlled (in 10GHz steps) by changing their operational temperature. This allowed direct control of the repetition rate of the generated pulse stream. The combined phase-locked lasers were then amplified and free-space launched into a 3m sample of the W-type fibre with a coupling efficiency of 25%. The output end of the fibre was then connected to a few tens of meters of standard single mode fibre (SMF) to temporally compress the pulses. The actual length of SMF-28 depends on the frequency separation that was chosen.

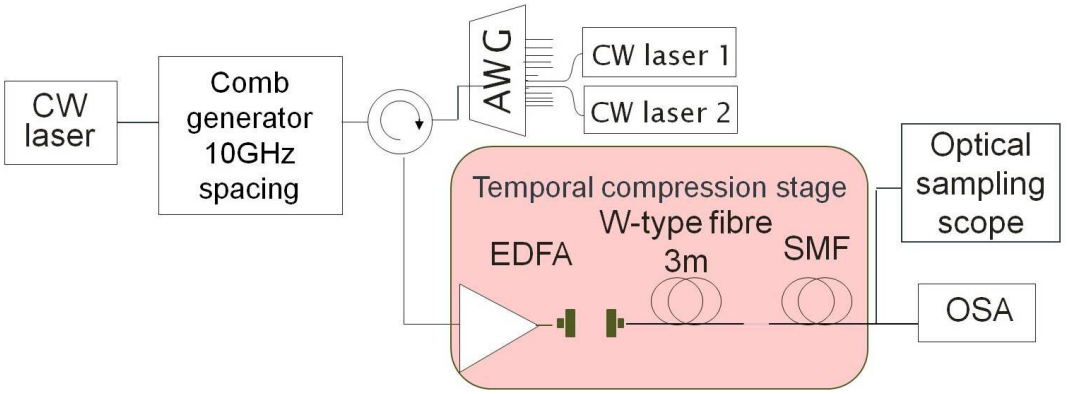


FIGURE 6.9: Experimental setup for the generation of high repetition rate pulses in a 3m sample of LSWF #2.

For this experiment, two values of repetition rates (160GHz and 200GHz) and three values of input power were considered. The highest value of power launched into the fibre (160mW) was limited by the relatively low free space coupling efficiency. The experimental results are supported by numerical simulations of the FWM process based on an approximation of the Split-Step Fourier method [Agrawal, 2006]. The simulations were based on the experimental conditions and the fibre properties. The approximated method did not take into account higher order dispersion and can therefore give more reliable results when considering only the first order idler.

### 6.2.2 Experimental results at 160GHz

Figure 6.10 shows the spectra recorded at the output of the fibre when the frequency between the two injection-locked lasers was 160GHz for various values of input power: 80mW (a), 125mW (b) and 160mW(c). The red traces represent the recorded traces at the output of the fibre, while the blue traces represent the results of my simulations. Also in this case, the resolution of the simulations is not accurate enough to reproduce correctly the CW signals. However, the aim of the simulations was to mainly check the agreement between the predicted and measured power levels of the generated components. Note that the measured spectral traces show some of the residual 10GHz comb lines that are due to reflections from the facet of the slave lasers. However, these components were suppressed down to -40dB level. Together with the two input CW lasers it is possible to distinguish the additional spectral components generated by FWM. The strength of the generated idlers increased as expected with the input power.

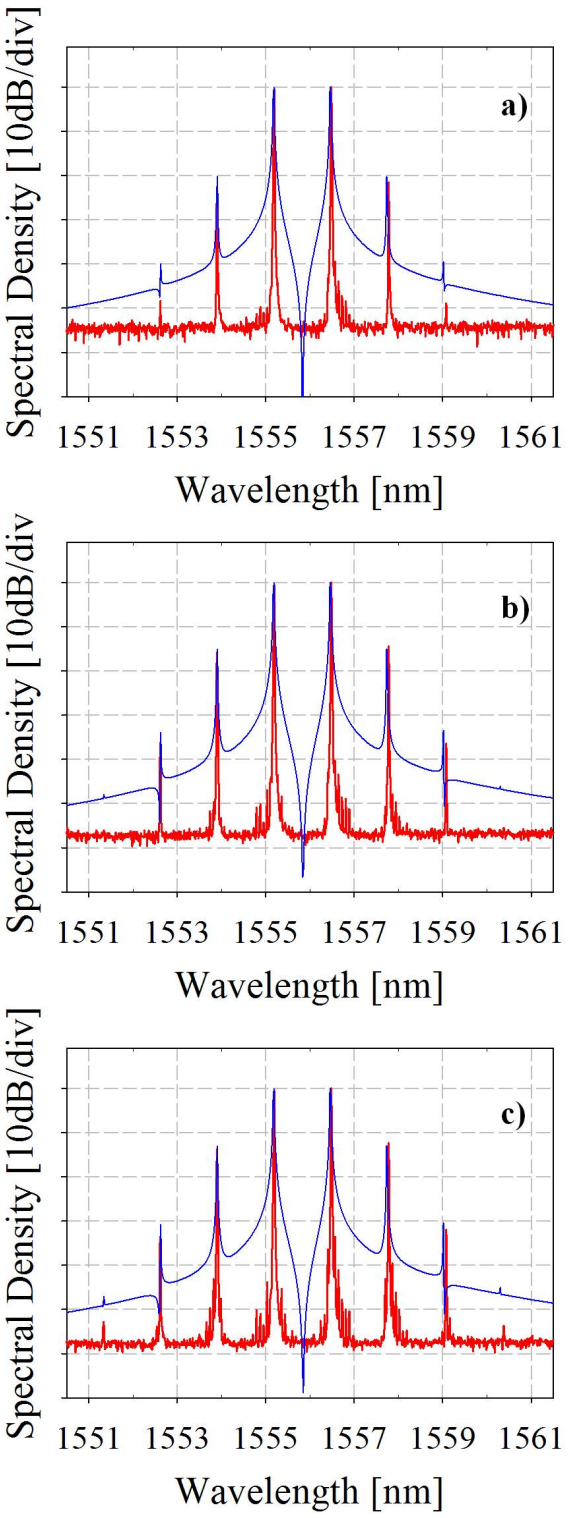


FIGURE 6.10: Spectra at the output pulse compression scheme based on a 3m sample of LSWF #2, when the input power was 80mW (a), 125mW(b) and 160mW(c) for a frequency separation of 160GHz.

The temporal waveforms were measured using an optical sampling oscilloscope (OSO) that was electrically triggered by the OFCG. The initially sinusoidal wave shows a full-width-at-half-maximum (FWHM) corresponding to the half of the beat signal period: 3.1ps for a repetition rate of 160GHz as shown in Figure 6.11.

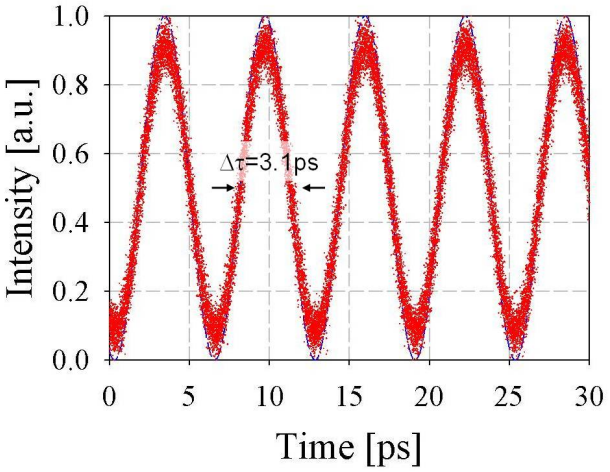


FIGURE 6.11: Temporal waveform of the input signal to the pulse compression scheme for a repetition rate of 160GHz.

The pulses at the output of the W-type fibre are shown in the first column of Figure 6.12 for the three values of input power that were considered. They present negligible temporal broadening as compared to the initial pulses, due to the very low dispersion of the fibre and the short length of sample that was employed in the setup. After 46m of SMF-28, the pulses were compressed down to 2.8ps (Pin=80mW), 2.3ps (Pin=125mW) and 2.0ps (Pin=160mW) as shown in the second column of Figure 6.12 corresponding to a compression factor of 1.1, 1.4 and 1.6 respectively. For the lowest value of input power considered during the experiment, it is possible to see that the pulses are slightly noisy: this is due to the limited dynamic range of the OSO. For the highest value of input power, corresponding to the maximum value of compression ratio, the timing jitter was measured on the OSO to be ∼150fs. This value is very close to the specification value of the measuring instrument and therefore it is possible to conclude that the generated pulses exhibited a timing jitter that was lower than the measured value.

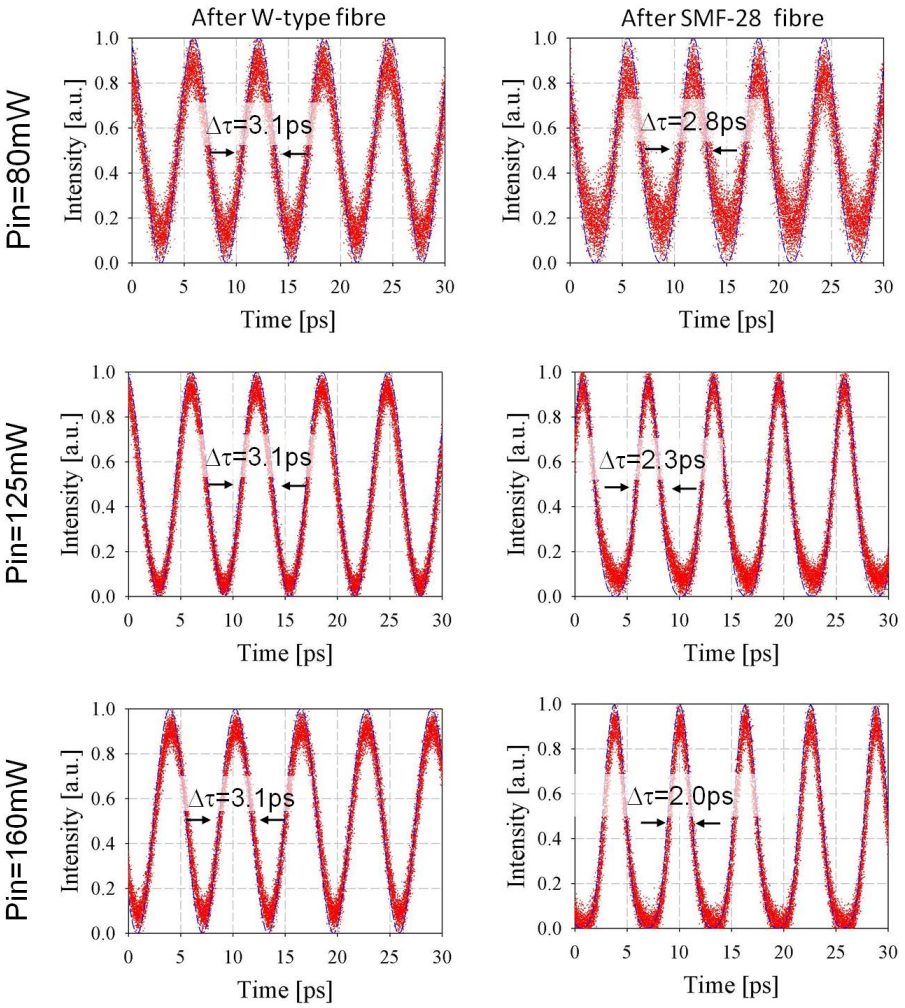


FIGURE 6.12: Temporal traces taken at the output of the pulse compression scheme based on a 3m sample of LSWF #2 (first column) and after 46m of SMF-28 fibre (second column) for the three values of input power and a repetition rate of 160GHz.

The time-bandwidth product of the pulses was then evaluated. The output spectra can be fitted to a Gaussian shape, as shown in Figure 6.13 for the three values of input power considered in the experiment. The estimated -3dB bandwidth in the three cases is 0.16THz, 0.2THz and 0.23THz respectively. These yield a time-bandwidth product for all the three cases of ∼0.46, value that is very close to the maximum time-bandwidth product for a Gaussian pulse (0.44).

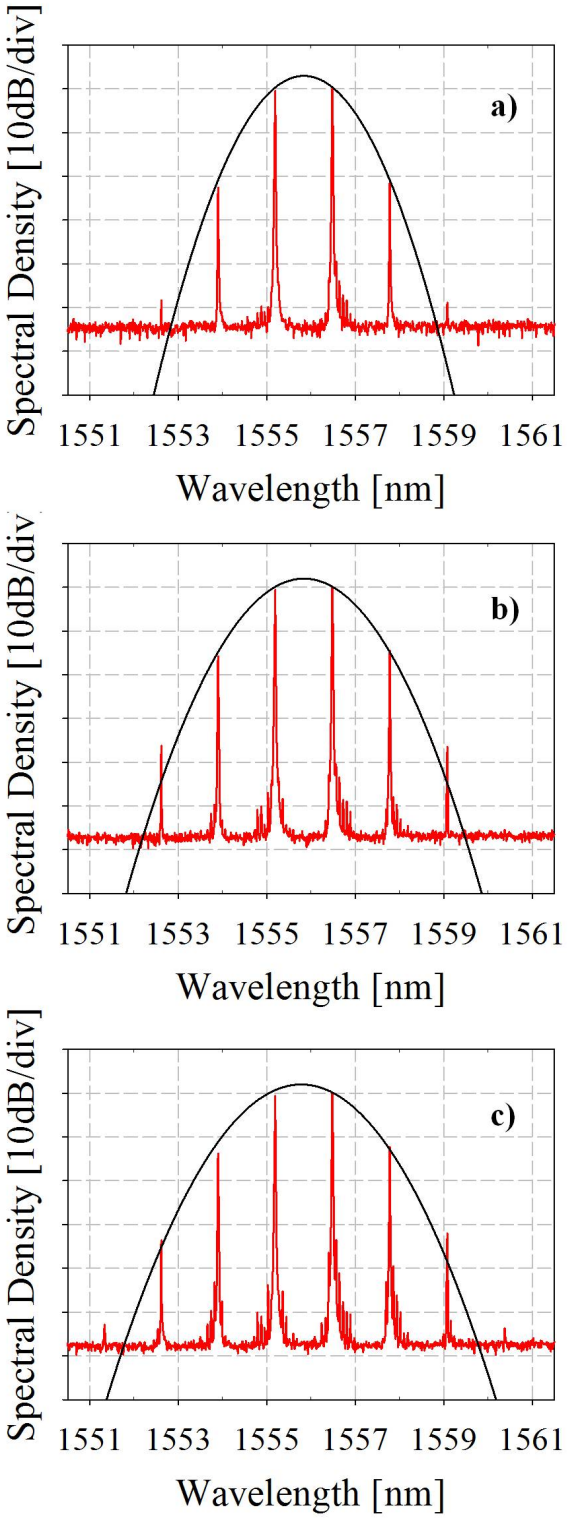


FIGURE 6.13: Spectra at the output of the pulse compression scheme based on a 3m sample of LSWF #2 when the input power was 80mW (a), 125mW(b) and 160mW(c) for a frequency separation of 160GHz (red lines) and corresponding Gaussian fit (black lines).

### 6.2.3 Experimental results at 200GHz

A very similar discussion applies to the case when the frequency separation of the two CWs was set at 200GHz. Figure 6.14 shows the spectra taken at the output of the fibre when the input power levels were 80mW (a), 125mW (b) and 160mW (c). Also in this case, there is good agreement between the measured and simulated traces.

The sinusoidal wave shows a full-width-at-half-maximum (FWHM) corresponding to a half of the signal period: 2.5ps for a repetition rate of 200GHz as shown in Figure 6.15.

The pulses at the output of the W-type fibre are shown in the first column of Figure 6.16 for the three values of input power that have been considered. Despite the broader bandwidth and similarly to the case presented in the previous Section, there is negligible temporal broadening of the generated pulses as compared to the initial pulses. After 30m of SMF-28 the pulses were compressed down to 2.2ps (Pin=80mW), 1.9ps (Pin=125mW) and 1.5ps (Pin=160mW) as shown in the second column of Figure 6.16, corresponding to a compression factor of 1.1, 1.4 and 1.7 respectively. Analogously to the case of a frequency separation of 160GHz, the signal to noise ratio is compromised for the case of the lowest value of input power. For the highest value of input power the timing jitter has been measured to be again $\sim$150fs and the same consideration as the previous Section applies.

In the case of highest compression factor, corresponding to the highest value of input power, the time-bandwidth product of the pulses has been evaluated. The output spectrum fitted with a Gaussian shape is shown in Figure 6.17. The estimated -3dB bandwidth is 0.3THz that leads to a time-bandwidth product of 0.46 for a pulse duration of 1.5ps. As in the previous Section, the time-bandwidth product of the pulses was then evaluated. The output spectra can be fitted to a Gaussian shape, as shown in Figure 6.17 for the three values of input power considered in the experiment. The estimated -3dB bandwidth in the three cases is 0.21THz, 0.24THz and 0.31THz respectively. As in the previous case, these values result in time-bandwidth product of 0.46 for all the three cases.

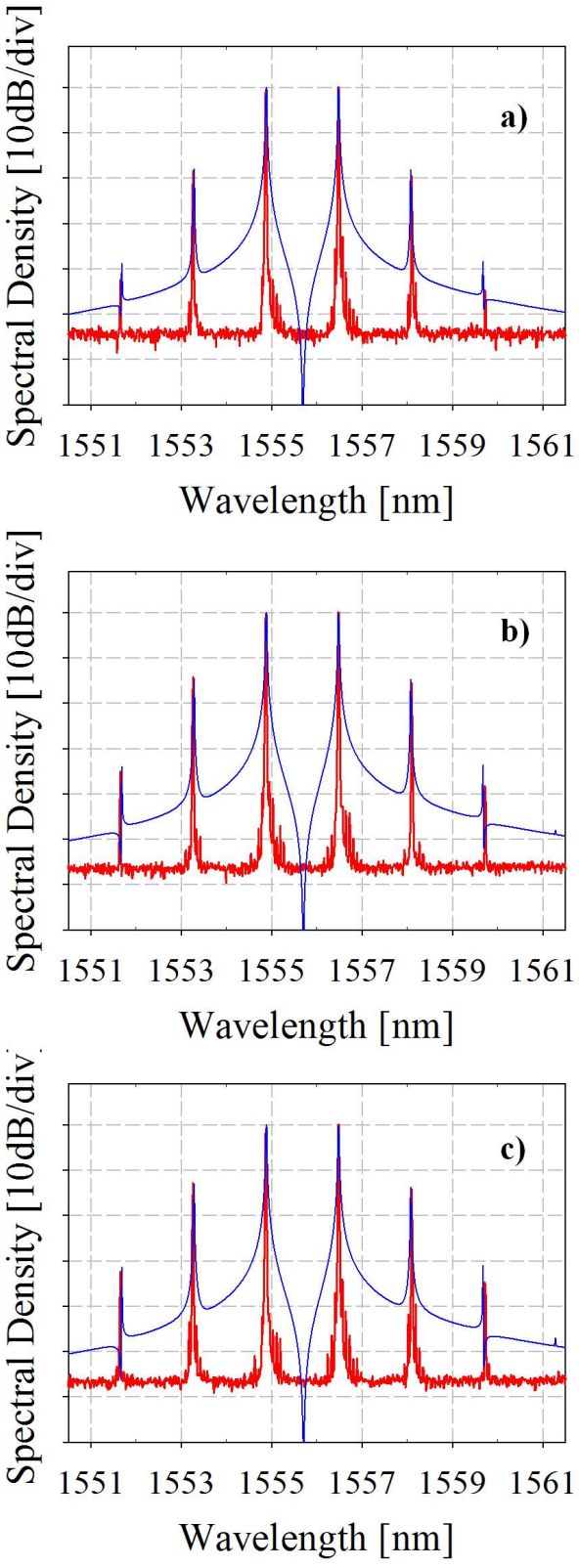


FIGURE 6.14: Spectra at the output of the pulse compression scheme based on a 3m sample of LSWF #2 taken when the input power was (a) 80mW, (b) 125mW and (c) 160mW for a frequency separation of 200GHz.

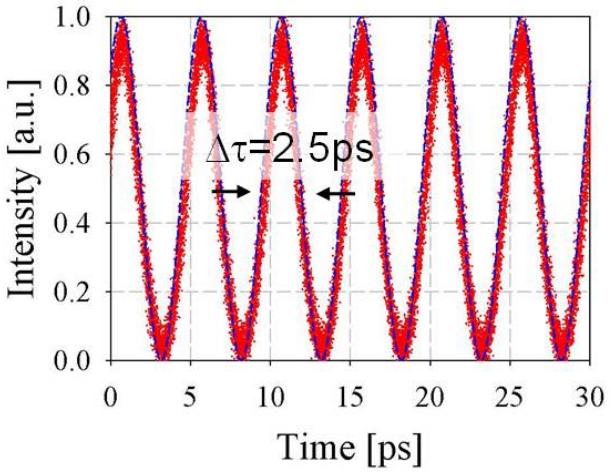


FIGURE 6.15: Temporal waveform of the input signal to the pulse compression scheme for a repetition rate of 200GHz.

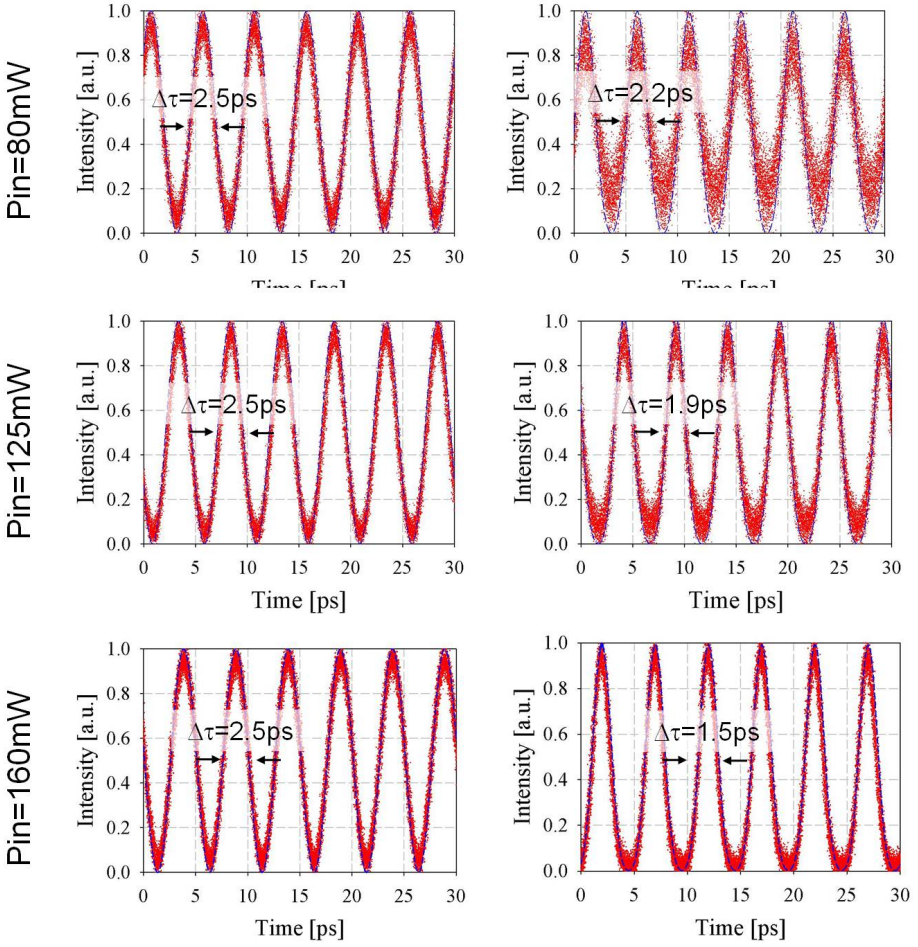


FIGURE 6.16: Temporal traces taken at the output of the pulse compression scheme based on a 3m sample of LSWF #2 (first column) and after 30m of SMF-28 fibre (second column) for the three values of input power and a repetition rate of 200GHz.

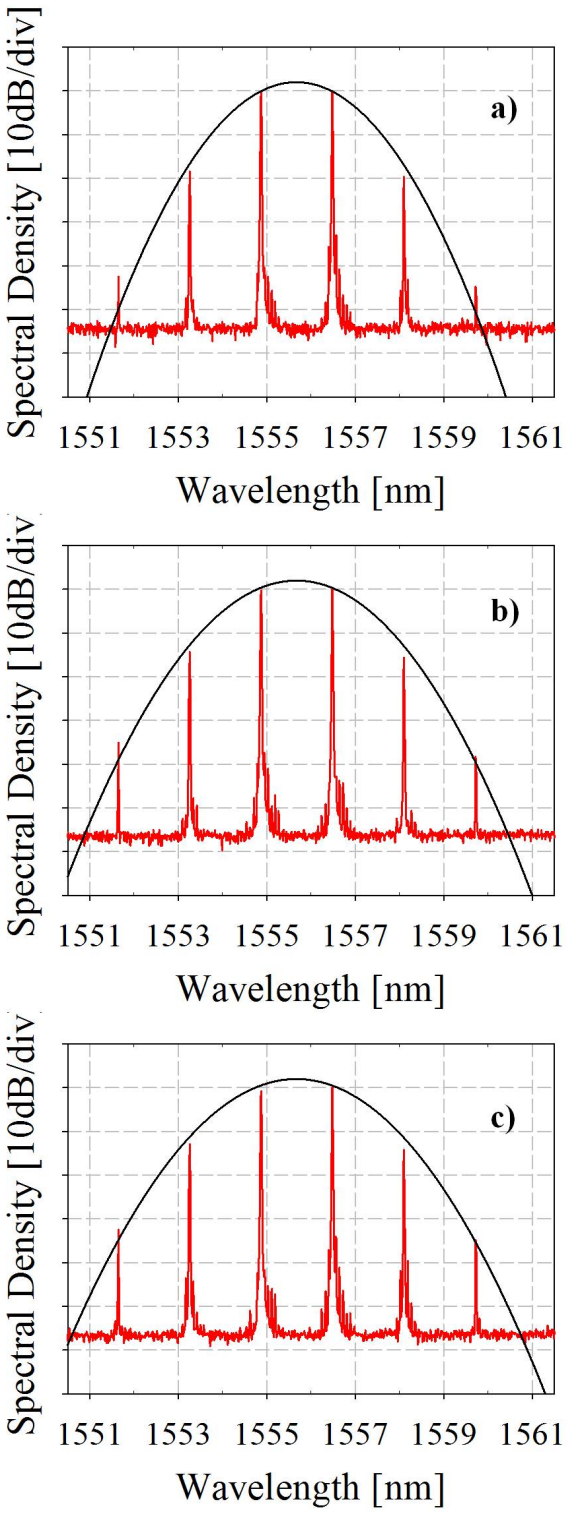


FIGURE 6.17: Spectra at the output of the pulse compression scheme based on a 3m sample of LSWF #2 taken when the input power was 80mW (a), 125mW(b) and 160mW(c) for a frequency separation of 200GHz (red lines) and corresponding Gaussian fit (black lines).

### 6.2.4 Comparison with a Bi-oxide based fibre

Generation of high repetition rate pulses based on dual frequency beating was previously demonstrated in a germanium-doped HNLF [Inoue *et al.*, 2007]. However, the relatively low nonlinear coefficient of the silica HNLF forces the use of long lengths of fibre, of the order of hundreds of meters. This represents a two-fold disadvantage: for a long length of fibre it is generally necessary to introduce a SBS suppression scheme, therefore making the system overall more complex. Moreover, in a long length of fibre sample, maintaining the polarisation of the two synchronised CWs is a nontrivial task.

In the context of the generation of high repetition rate pulses in short lengths of soft glass-fibres, it is possible to compare the performance of the W-type fibre with that of a Bi-NLF. Such an experiment has also been carried out in our lab using the same setup as that described in Section 6.2.1 [Parmigiani *et al.*, 2010]. The main properties of the Bi-oxide fibre used for the experiment are reported in Table 6.2, along with the corresponding properties of the W-type lead silicate fibre for a more immediate comparison. In the two experiments the product $\gamma \mathrm{PL}_{eff}$, where $\gamma$ is the nonlinear coefficient, P is the input power and $\mathrm{L}_{eff}$ is the effective length of the fibres was highly comparable and therefore the compression factors achieved in the fibres are very similar.

TABLE 6.2: Main properties of the Bi-oxide fibre used in [Parmigiani *et al.*, 2010] and the lead silicate W-type fibre.

| Fibre | Bi-oxide | Lead silicate |
|---|---|---|
| Nonlinear Coefficient ($\mathrm{W^{-1}km^{-1}}$) | 1100 | 820 |
| Propagation loss (dB/m) | 0.8 | 2.1 |
| Dispersion @1550nm (ps/nm/km) | -260 | -3 |
| Length of sample (m) | 2 | 3 |
| Input Power (mW) | 140 | 160 |
| SBS Threshold (mW) | 300 | >730 |
| $\gamma \mathrm{PL}_{eff}$ | 0.2 | 0.2 |

Although the Bi-NLF shows a higher nonlinear coefficient and lower propagation losses, the dispersion of the fibre is much larger than that exhibited in the W-type lead-silicate fibre. Moreover, the Bi-NLF shows a higher dispersion slope when compared to the W-type lead-silicate fibre, as reported in Figure 6.18(a) where the simulated dispersion profiles for both the Bi-oxide and the W-type lead silicate fibre are illustrated.

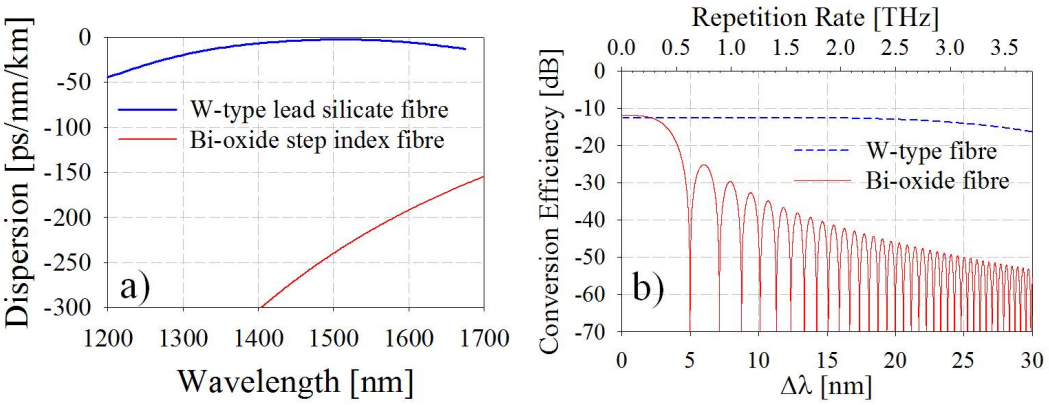


FIGURE 6.18: (a) Dispersion profile of the W-type lead silicate fibre (blue line) and Bi-oxide fibre (red line); (b): Conversion efficiency versus spacing of the CWs input lasers for the W-type fibre (blue dashed line) and Bi-oxide fibre (red solid line).

Even though a direct comparison between the two experiments does not reveal any major differences, the benefits of using a low-dispersion fibre, such as the lead-silicate W-type fibre, can be appreciated in Figure 6.18(b) where the FWM conversion efficiency is plotted versus the CW spacing for the two different fibre types. The conversion efficiency is fairly constant for the W-type lead-silicate fibre (blue dotted line) for a CW spacing up to at least 20nm, corresponding to a repetition rate of ∼2.5THz. On the contrary, the large value of dispersion of the Bi-NLF has a drastic effect on the conversion efficiency (red solid line in Figure 6.18(b)) which decreases by at least 10dB from the original value for values of repetition rate greater than 500GHz. A way to increase the conversion efficiency in the two fibres is to increase the input power in the fibres. Also in this case, the dispersion has an effect on the maximum achievable conversion efficiency, as shown in Figure 6.19.

Figure 6.19(a) shows the simulated conversion efficiency versus the input power for several values of CW spacing (100GHz, 300GHz, 500GHz, 800GHz, 1THz, 2THz and 3 THz). It is possible to see how the maximum achievable conversion efficiency decreases for higher values of repetition rates. As the two CWs are spaced further apart, the increased net phase mismatch is translated in a reduced conversion efficiency, as discussed

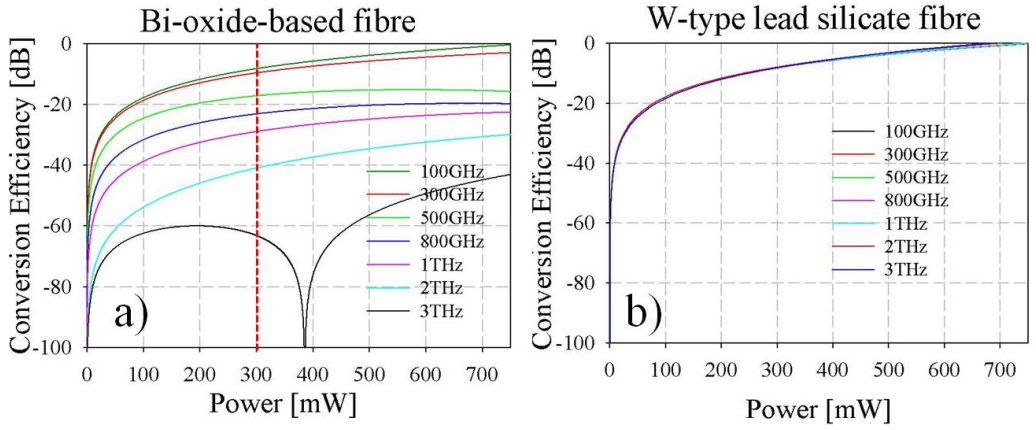


FIGURE 6.19: (a): Conversion efficiency versus input power for various values of line spacing for the BI-NLF fibre. The vertical red line indicates the SBS threshold in the fibre; (b) Conversion efficiency versus input power for various values of line spacing for the lead silicate W-type fibre.

in Section 5.1. Moreover, as discussed in this Section, a reduced value of conversion efficiency results in longer output pulses and therefore limited values of compression factors. The flat dispersion profile of the W-type fibre solves this problem. Figure 6.19(b) shows indeed how the maximum achievable conversion efficiency is fairly constant for any of the considered values of line spacing. When increasing the input power, it is necessary to ensure that operation remains below the SBS threshold in order to avoid the inclusion of a SBS suppression scheme in the experimental setup. The W-type lead-silicate fibre shows a much higher SBS threshold compared to that of the Bi-NLF fibre, as reported in Table 6.2. The input power launched in the Bi-NLF in the experiment reported in [Parmigiani *et al.*, 2010] was very close to the SBS threshold of the fibre, meaning that a significant improvement in compression factor could not be achieved unless an SBS suppression scheme was introduced. On the contrary, the value of power used in the W-type fibre is far from the SBS threshold, meaning that much higher values of compression factors can be envisaged without the need of introducing an SBS suppression scheme. However, in my experiments the performance limitation was introduced by the free space coupling which limited the maximum input power that could effectively be coupled into the fibre.

### 6.2.5 Conclusions

The generation of short high quality, ultra high repetition rate pulses (beyond 160GHz) formed by two phase locked CW lasers and nonlinearly compressed in a 3m-long highly

nonlinear, dispersion tailored W-type lead-silicate fibre was demonstrated. The pulse characteristics have been evaluated for various power levels and two repetition rates: 160GHz and 200GHz. The results achieved in the W-type lead silicate fibre have been compared to those achieved in a Bi-oxide fibre. The role of the dispersion and dispersion slope of the W-type fibre has been investigated for the generation of short pulses when much higher repetition rates (up to 3THz) and higher values of input powers are considered.

## 6.3 FWM based 160-to-40Gbit/s demultiplexing

All-optical time-domain demultiplexing is likely to be a key technology in future high speed all-optical communication network systems over 100Gbit/s. SOAs have been successfully employed in the demonstration of all-optical demultiplexing signals. Demultiplexing of 640Gbit/s signals to 40Gbit/s or 160Gbit/s to 10Gbit/s in SOAs based on XPM and FWM respectively has been demonstrated [Tangdiongga *et al.*, 2007],[Jansen *et al.*, 2002]. A FWM-based demultiplexing scheme from 640Gbit/s down to 10Gbit/s was demonstrated in a 5cm chalcogenide glass waveguide chip with a nonlinear coefficient $\gamma$ of 4100W$^{-1}$km$^{-1}$ [Galili *et al.*, 2009]. A 6mm long integrated organic-silicon-on-insulator compound waveguide with a $\gamma$ of 104000W$^{-1}$km$^{-1}$ was employed to demultiplex a signal from 130Gbit/s to 10Gbit/s in [Koos *et al.*, 2009]. Although the above mentioned technologies offer significant advantages in terms of compactness, the control of waveguide dispersion is not straightforward.

Highly nonlinear silica-based optical fibres, on the other hand, represent a more technologically mature alternative, and are usually preferred for their superior control over the dispersion characteristics, high compatibility with fibre systems and low splicing losses (typically 0.1dB/splice). Fibre-based all-optical demultiplexing systems have been demonstrated in highly nonlinear fibres by XPM [Li *et al.*, 2008] or FWM [Hu *et al.*, 2009]. However, the relatively low nonlinear coefficients (of $\sim$20W$^{-1}$km$^{-1}$) require the use of fibre lengths of the order of a few hundreds of meters. Long fibre samples are not ideal, not only because they result in the realisation of relatively bulky devices, but also because maintaining the polarization of the interacting signals in a long fibre length is not a trivial task.

Attractive solutions are represented by soft-glass fibres that exhibit a high nonlinear coefficient and allow for the realisation of ultrafast optical devices in metre-long samples. On the other hand, soft glasses exhibit high losses (in comparison to silica) and a high material dispersion at telecommunication wavelengths. Despite the high fibre dispersion, FWM-based demultiplexing of a 160Gbit/s signal down to 10Gbit/s was demonstrated in a 1m long sample of Bi-NLF [Scaffardi *et al.*, 2006], confirming the potential of non-silica fibres for these kind of applications. However, the large dispersion of the Bi-NLF limited the wavelength range in which efficient FWM could be observed. In order to propose a solution to this issue, we have employed the lead-silicate W-type fibre in an attempt to compensate for the material dispersion with a controllable degree of waveguide dispersion. This Section illustrates the results of the demultiplexing of 160Gbit/s to 40Gbit/s signals in a 2.2m sample of LSWF #2.

### 6.3.1 Experimental setup

The experimental setup used for the implementation of the FWM-based demultiplexer is shown in Figure 6.20. The pump and the signal were synchronised by using the same RF clock at 20GHz which was splitted and then appropriately scaled down to 10GHz and up to 40GHz, before the multiplexing stage by using an RF frequency divider and doubler respectively. A 10GHz mode-locked laser (ERGO, $\lambda_p$=1550nm) was optically multiplexed to generate 40GHz pulses which were used as the pump signal. The pump signal was launched into a 3dB coupler. A second mode locked laser (EFRL, $\lambda_s$=1560nm) operating at 40GHz was modulated by a $2^{31}$-1 pseudorandom bit sequence (PRBS) and then multiplexed to 160Gbit/s. Note that the EFRL, the modulator and the multiplexer are polarisation maintaining (PM) components. At the time of the experiment a PM EDFA was not available in the lab and therefore the power was amplified only at the output of the multiplexer. This has an effect on the quality of multiplexed signal and therefore the converted idler as well, as it will be explained in Section 6.3.2. An optical delay line was used to temporally align the pump pulse with the desired channel of 160Gbit/s signal to be demultiplexed. The signal and the pump were amplified using two independent EDFA, then combined in a 3dB coupler and free space launched in 2.2m of W-type lead silicate fibre. The states of polarisation of both the pump and the signal were aligned to the polarisation axis of the fibre through polarisation controllers. The coupling efficiency was 25% and the pump and signal power levels at the input of

the fibre were 21.1dBm and 14.5dBm respectively. The output of the fibre was filtered and then characterised in terms of eye diagrams and BER measurements.

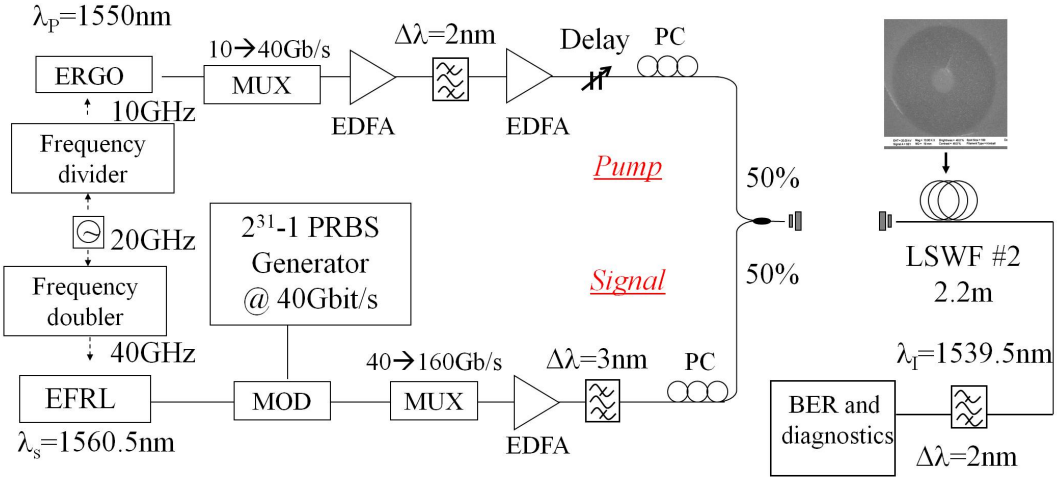


FIGURE 6.20: Experimental setup for the demonstration of demultiplexing of 160-to-40Gbit/s pulses in a 2.2m sample of LSWF #2.

### 6.3.2 Experimental results

The optical spectra at the input and output of the fibre are shown in Figure 6.21(a) and (b) respectively. The 40Gbit/s idler generated by FWM was maximised by optimising both the relative delay between the two signals and their polarisation states. Although the wavelength span is restricted to 40nm in the figures, the presence of higher order FWM components can still be appreciated.

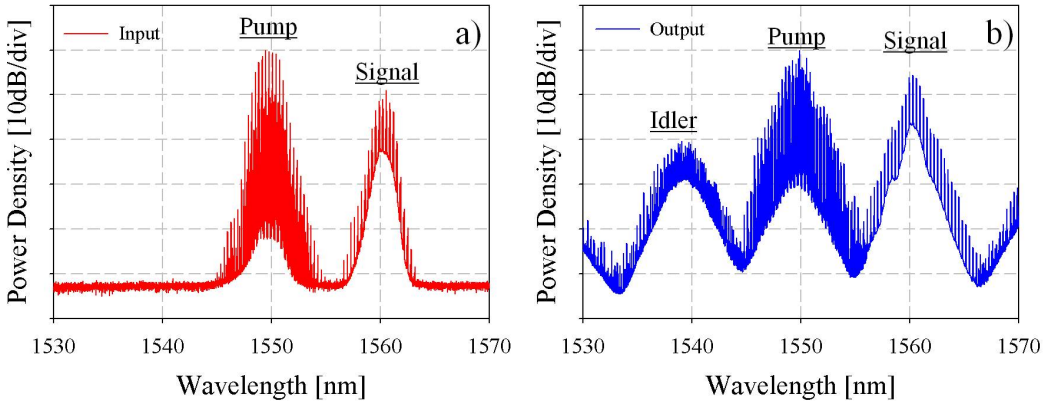


FIGURE 6.21: Optical spectra at the input (a) and output (b) of the demultiplexing scheme based on a 2.2m sample of LSWF #2.

The tailored dispersion profile together with the high nonlinear coefficient and the short length of sample of the fibre used in the experiment, contribute towards the generation of efficient FWM components. In particular, the 40Gbit/s idler component was about -15dB lower with respect to the 160Gbit/s input signal. Considering the difference in the repetition rate between the data signal and the idler a conversion efficiency of more than 10% for a pump power of just 21dBm was achieved. In order to assess the quality of the demultiplexing process, the 40Gbit/s idler was accurately filtered and characterised in terms of eye diagrams. The filtered idler is shown in Figure 6.22.

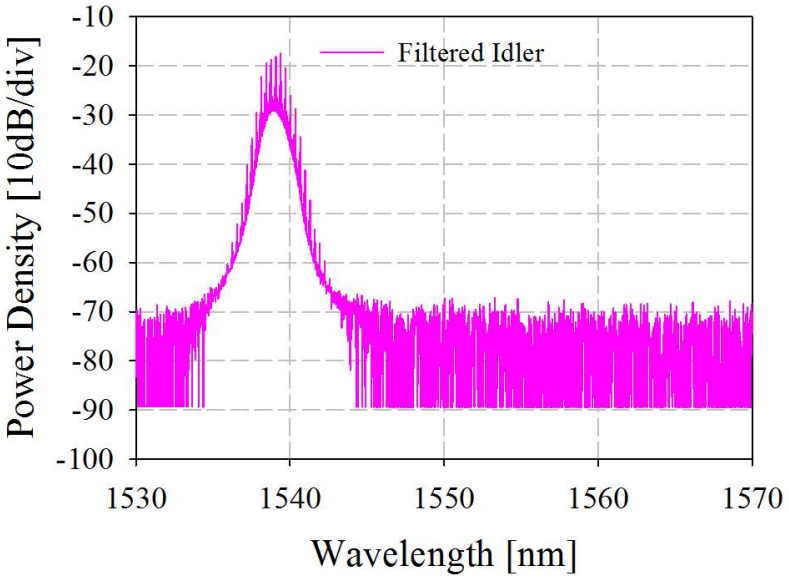


FIGURE 6.22: Spectrum of the filtered idler at the output of the demultiplexing scheme based on a 2.2m sample of LSWF #2.

All the eye diagrams have been measured by an OSO. The eye diagrams of the signal at 40Gbit/s are clean and open as shown in Figure 6.23(a). The quality of the eye diagrams slightly degrades when the 40Gbit/s signal is multiplexed at 160Gbit/s as shown in Figure 6.23(b). This degradation in the signal performance is attributed mainly to the limited in-band OSNR of the original signal after the multiplexer. Indeed all signals show an out-of-band OSNR better that 30dB, as shown in Figure 6.21(b). However, the quality of the data signal is somewhat compromised after multiplexing, as can be appreciated from a comparison with the eye diagrams shown in Figure 6.23. Despite this, the eye diagrams of the multiplexed signals are still quite open and clear.

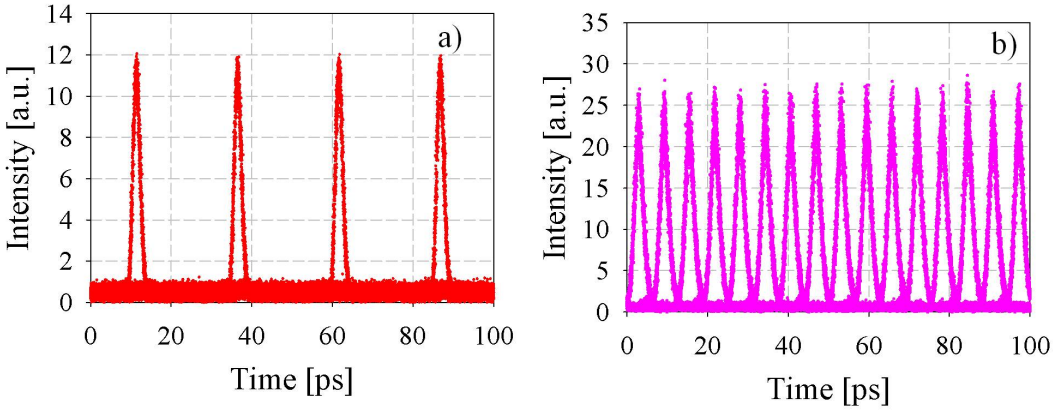


FIGURE 6.23: Eye diagram of the 40Gbit/s signal in the demultiplexing scheme before (a) and after (b) being multiplexed at 160Gbit/s.

The eye diagrams of the 4 demultiplexed channels are shown in Figure 6.24. The 4 channels have been named Ch. 1 (a), Ch. 2 (b), Ch. 3 (c) and Ch. 4 (d). The nomenclature and the colour coding are kept the same throughout this discussion.

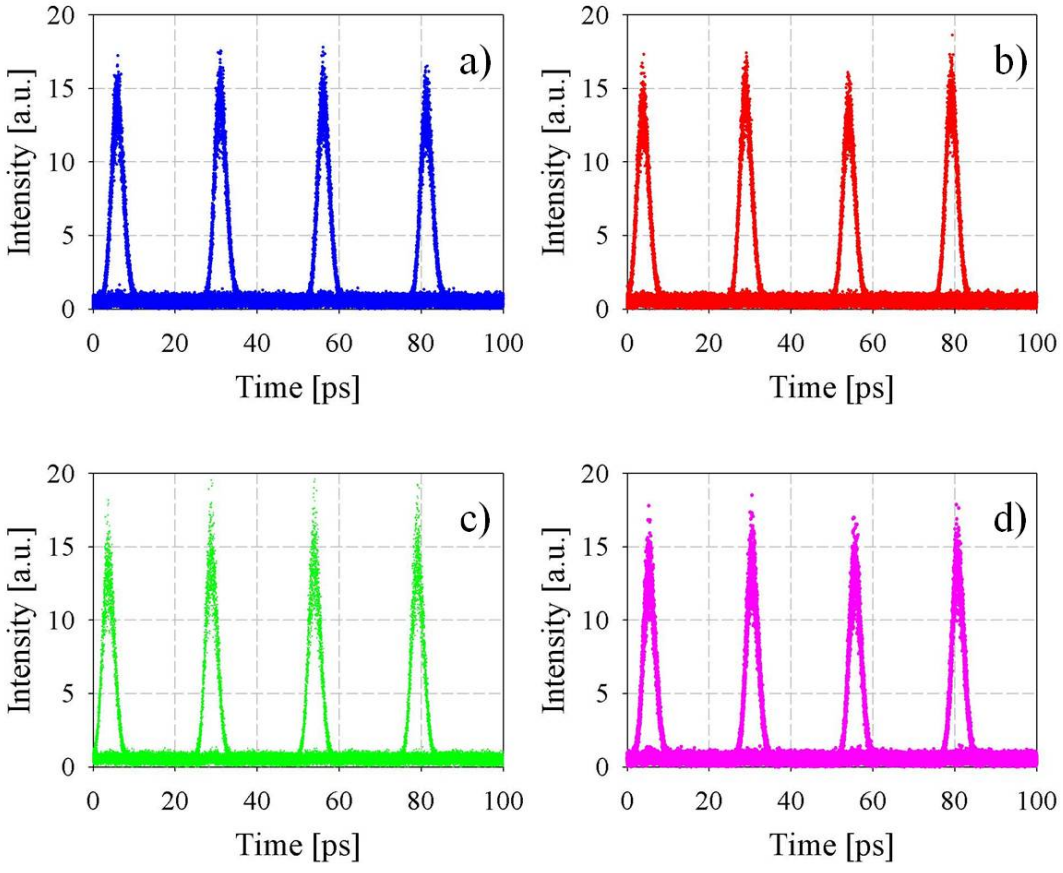


FIGURE 6.24: Eye diagrams of the demultiplexed idlers at 40Gbit/s at the output of a 2.2m sample of LSWF #2.

Figure 6.24 shows clean and open eye diagrams in all of the four cases, which are slightly noisier than that of the 40Gbit/s signal shown in Figure 6.23(a), but highly comparable to that of the 160Gbit/s signal shown in Figure 6.23(b). The corresponding pulsewidth was measured to be ∼3ps resulting in a time-bandwidth product of 0.44. This quality of the eye diagrams is reflected in the BER measurements, shown in Figure 6.25. The power penalty at error free operation is very similar between the four demultiplexed channels, showing a variation smaller than 0.3dB, while the maximum power penalty between the B2B signal and the 4 demultiplexed channel is <4dB.

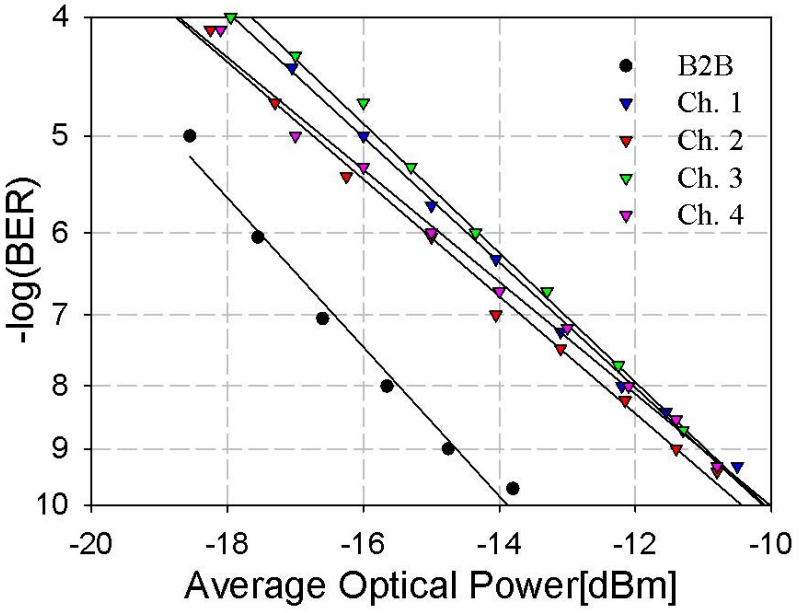


FIGURE 6.25: BER measurement of the 40Gbit/s (B2B) and of the 4 demultiplexed idlers at the output of a 2.2m sample of LSWF #2.

### 6.3.3 Conclusions

The use of a 2.2m sample of lead-silicate W-type fibre in a FWM-based demultiplexing scheme of a 160Gbit/s signal down to 40Gbit/s was demonstrated. The converted idler was filtered and characterised in terms of eye diagrams and BER measurements. The good quality of the demultiplexing process was confirmed by clean and open eye diagrams and BER measurements with a power penalty lower than 4dB. This value could be further improved by optimising the 160Gbit/s system to decrease undesired ASE noise coming from the EDFAs.

## 6.4 Conclusions on the applications of the lead-silicate W-type fibre

This chapter has illustrated the possibility of realising all-optical highly nonlinear devices based on short samples of dispersion tailored highly nonlinear lead silicate W-type fibre. A multi-wavelength conversion scheme with negligible interchannel crosstalk and low BER power penalty has been demonstrated. The generation of high repetition rate (>160GHz) pulses has been achieved in such a fibre and its potentials for the generation of pulses in the THz regime has been numerically investigated. Finally a 160Gbit/s to 40Gbit/s demultiplexing scheme has been proposed and experimentally demonstrated.

The experiments reported in this Chapter were based on very short fibre lengths, thus demonstrating the advantages of soft-glass technology for the realisation of compact devices. Moreover, the combination of a highly nonlinear coefficient and a dispersion-tailored profile confirmed the potential of lead-silicate W-type fibres for the realisation of ultra-fast and stable all-optical signal processing systems.

Although the design of the all-solid lead-silicate W-type fibre was found to be suitable for targeting a highly nonlinear, dispersion tailored fibre, there are a few issues that could be addressed in order to improve the performance of the systems based on this fibre.

First of all, the propagation loss value could be further reduced. Although a reasonably low value of propagation loss (2.1dB/m) has been achieved, further improvements in the fabrication process and drawing conditions seem to be a promising route to reduce the overall losses of the fibre. It is expected that improvements in the fabrication process will lead to a reduction in the fibre losses down to the bulk values, below 1 dB/m.

Moreover, improving the coupling efficiency also represents a critical issue. In the experiments presented in this project, free-space coupling was applied, resulting in reduced coupling efficiency values due to the issues related to coupling light into a small fibre core. A way to overcome this problem could be represented by the possibility to splice the fibre with a standard SMF. Work in this direction in currently undergoing within the ORC.

# Chapter 7

# Soft glass MOFs for supercontinuum generation in the Mid IR

Supercontinuum generation (SCG) is the formation of a broad and continuous spectrum by propagation of high power pulses through a nonlinear medium. SCG was first observed in bulk glass in 1970 [Alfano and Shapiro, 1970], while the first demonstration in a conventional silica-based optical fibers was reported in 1976 [Lin and Stolen, 1976].

The generation of a broad spectrum is not the result of a single nonlinear effect, but it is rather the result of the interaction of several of the nonlinear effects presented in Chapter 3. The determining factors for generation of a SC spectrum are the dispersion of the fiber relative to the pumping wavelength, the pulse width and the peak power. In particular, the sign of the dispersion determines the type of nonlinear effects involved in the formation of the continuum spectrum and its spectral shape. In terms of pulse duration, SCG can be investigated by using nanosecond, picosecond and femtosecond pulsed sources. When pumping with femtosecond pulses in the normal dispersion regime, the effects of SPM result in a spectrum broadened symmetrically around the pump wavelength of the input pulses. Also, the effect of SRS has to be taken into account, since it is responsible for a spectrum extending towards longer wavelengths [Birks *et al.*, 2000; Hansen and Kristiansen].

In the anomalous dispersion regime, SCG is dominated by the generation of soliton effects. The formation of solitons in the anomalous regime gives the main contribution to the generation of the output spectrum which results to be broader than in the case of normal regime but not smooth [Ortigosa-Blanch *et al.*, 2002]. When the pump wavelength is close to the ZDW of the fibre, then all the nonlinear processes mentioned above take place. However, in this case, FWM becomes the process that gives the main contribution, as the phase-matching conditions are usually satisfied when pumping near the ZDW [Husakou and Herrmann, 2002].

The generation of a broad spectrum finds applications in several fields such as metrology [Cundoff *et al.*, 2001], optical coherence tomography (OCT) [Hartl *et al.*, 2001] or IR spectroscopy [Kano and Hamaguchi, 2003]. Most of the aforementioned demonstrations have been carried out in the near-IR regime, where mature source and fibre technologies are available. However, moving into the mid-IR regime, applications for wavelengths beyond 2$\mu$m include light-imaging detection and ranging (LIDAR) in the range from 2 to 12$\mu$m. Beyond a wavelength of 2$\mu$m, because of the limited transparency of silica, it is necessary to consider alternative glasses for generation of broadband radiation. The fundamental material properties of non-silica soft glasses, such as the higher nonlinear coefficient and a ZDW at longer wavelengths when compared to silica, can enhance SCG across the mid-IR.

Recently, MOFs have attracted significant attention for the generation of SC, due to the great flexibility they offer in terms of tailoring the dispersion profile and several silica-based MOFs have been successfully employed for the demonstration of SCG [Dudley *et al.*, 2006; Husakou and Herrmann, 2001, 2002; Ortigosa-Blanch *et al.*, 2002; Ranka *et al.*, 2000].

The development of non-silica MOFs offers advantages over silica MOFs in the mid-IR region, as non-silica glasses show a larger transmission window than silica. SCG in the Mid-IR has been successfully demonstrated in bismuth based fibres as well as tellurite fibres [Brambilla *et al.*, 2005], [Delmonte *et al.*, 2006], [Domachuk *et al.*, 2008]. The fibres used in the applications mentioned above show a core diameter in the range of 1 to 10$\mu$m. However, in order to scale up the output power levels, a fibre with a larger mode area rather than small core fibres seem to be a more practical choice, as the damage power thresholds of the former class of fibres would be considerably higher.

This chapter discusses the possibility to combine MOFs technology with the use soft glasses for efficient supercontinuum generation in the MID IR regime based on LMA fibres. First, an overview of the main glasses that are suitable for this application is given. Then, the fibres that have been designed and fabricated within the ORC to be employed in SCG experiments at $\sim 2\mu$m are presented. After the description of the setup used to measure the SCG and the issues related to it, the results obtained with two of these fibres are presented.

## 7.1 Supercontinuum generation in mid IR

SCG at mid IR wavelengths requires not only the use of a highly nonlinear optical medium but also high mid IR transparency. In order to extend the current MOF technology developed at visible and near-IR wavelengths (0.4-1.7$\mu$m) up to the mid-IR region ($>2\mu$m) it is necessary to consider the characteristics of the available glasses also in terms of mid-IR transparency. When looking at possible alternatives to silica for the fabrication of a suitable fibre for SCG applications, some of the HMO glasses presented in Figure 3.18 have been considered. Figure 7.1 shows the transmission spectra of some bulk glasses: a 4mm thick sample of silica is compared with a 3mm thick ZBLAN (zirconium, barium, lanthanum, aluminium, sodium)-fluoride bulk glass, a 3mm thick tellurite and a 2mm thick chalcogenide (selenide) glass.

Chalcogenide glasses show the largest transmission window, extending up to 11$\mu$m, together the highest nonlinear refractive index (three orders of magnitude higher than silica). However, this class of glasses are highly toxic and quite unstable, making the drawing of a fibre a very difficult task. ZBLAN, one of the available fluoride glasses, could be considered as a potential candidate as it also shows a broader transmission window than that of tellurite or silica, extending from 0.2 to 8$\mu$m. However the value of the nonlinear refractive index of fluoride glasses is comparable to that of silica and therefore it does not represent the ideal choice. Tellurite glasses show good transparency for applications in the range from 1 to 3$\mu$m, while silica shows high transparency from 0.2 to 2.5$\mu$m. When compared to the other alternatives, tellurite glasses are more stable, both chemically and thermally, and less toxic than ZBLAN and chalcogenide glasses. Moreover, tellurite also shows a high nonlinear refractive index which is two orders of magnitude higher than that of silica. Consequently, tellurite can be considered

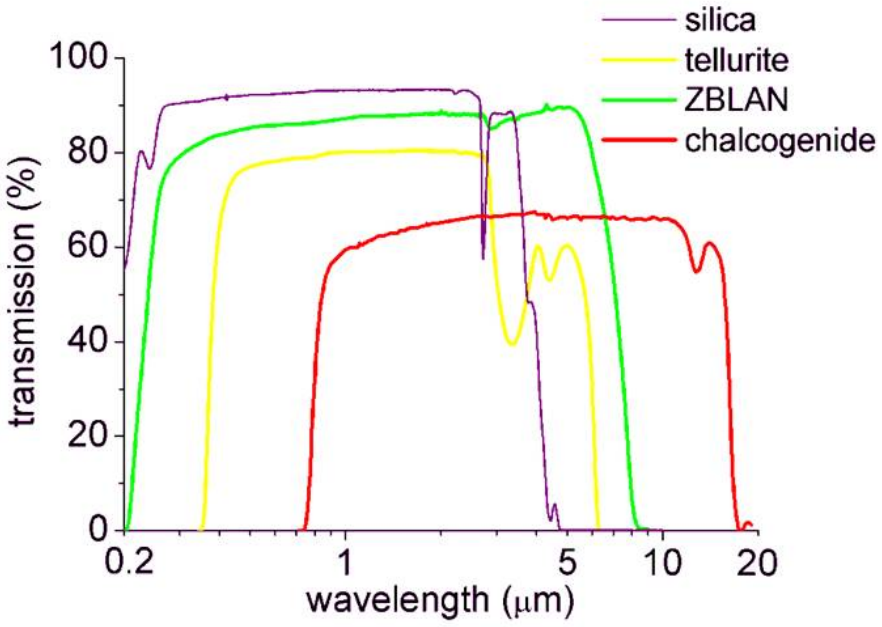


FIGURE 7.1: Comparison of the mid-IR transmission spectra of some non-silica glasses, courtesy of Dr. Feng.

as a highly suitable material for the fabrication of soft glass fibres for supercontinuum generation in the mid-IR. Note that lead silicate glasses are not shown in Figure 7.1 as they show a transmission window narrower than that of silica and this makes them not particularly attractive for SCG in the mid-IR [Feng *et al.*, 2005a].

Once the suitable glass is identified, some considerations on the fibre design are needed. In order to increase the output power of the SCG radiation to several tens of mW or higher, it is necessary to use fibres with large-mode area (LMA) rather than small core fibres. The use of an LMA fibre then enables to limit the risk of damaging the facet of the fibre when light intensities of the order of a few watts are launched in the fibre. This requirement becomes even more critical for a fibre made of non-silica glasses as they typically show intensity damage thresholds much lower than that of silica. HMO glasses usually show higher value of propagation losses when compared to silica and therefore the length of the sample has to be chosen carefully. Although SCG is achieved in moderately short fibre lengths ranging from a few centimetres up to a few meters, SCG has also been demonstrated in sub-cm fibre lengths [Omenetto *et al.*, 2006]. Therefore, choosing a short fibre sample can mitigate the high propagation losses exhibited by the fibre. Finally, the dispersion profile of the fibre has to be carefully designed so to achieve a ZDW in the wavelength region of interest.

Two LMA fibres made of tellurite glass that satisfy the criteria discussed above have been designed within the ORC and drawn by Dr. Feng. Both fibres have been employed in an experimental setup to measure SCG and the results are presented in the following Section.

## 7.2 Supercontinuum generation in tellurite fibres

### 7.2.1 Characteristics of the tellurite fibres

The fibres employed in SCG experiments are two HFs made of tellurite. Table 7.1 shows a comparison between silica and tellurite in terms of their linear and nonlinear refractive index.

TABLE 7.1: Comparison between linear and nonlinear refractive index of silica and tellurite at 1550nm.

| Material | Refractive index (n) | Nonlinear refractive index ($n_2$) [$10^{-19}m^2/W$] |
|---|---|---|
| Silica | 1.444 | 0.22 |
| tellurite | 2.030 | 1.7 |

The two fibres were drawn from the same preform: a LMA fibre and a smaller core fibre. The details on the fabrication and characterisation of the two fibres can be found in [Feng *et al.*, 2008b,c]. An SEM image of the LMA tellurite fibre, which will be denoted as Fibre #1, is reported in Figure 7.2.

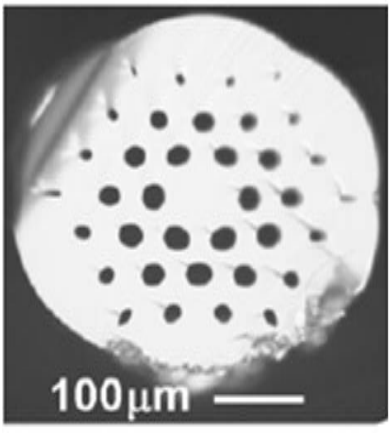


FIGURE 7.2: SEM image of the tellurite LMA HF used for the supercontinuum generation experiment.

The core diameter $a$ of the fibre was 80$\mu$m and the value of d/$\Lambda$ was decreasing from 0.53 for the inner holes to 0.44 for the second ring of holes, down to 0.26 for the outer ring, for values of $d$ of 28.1$\mu$m, 23.3$\mu$m and 13.8$\mu$m respectively. This structure was designed to exhibit very high losses for higher order modes, while maintaining negligible losses for the fundamental mode and therefore allowing single mode propagation in the fibre. Single mode guidance at 1.55$\mu$m was observed in a 1.5m sample of the fibre, as shown in Figure 7.3(a), in good agreement with the simulated field profile, shown in Figure 7.3(b).

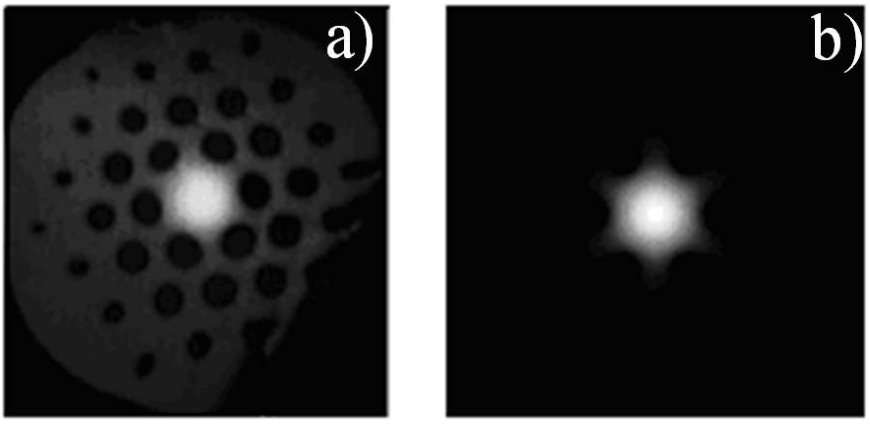


FIGURE 7.3: Observed (a) and simulated (b) mode field profile of the tellurite LMA HF at 1550nm. Note that the images are not in the same scale.

The fibre exhibited a mode area of 3000$\pm$200$\mu$m$^2$ for the fundamental mode at 1.5$\mu$m and represents one of the largest single mode fibres obtained in a non-silica glass so far. The nonlinear coefficient of the fibre at 1550nm was estimated to be $\gamma$=0.23W$^{-1}$km$^{-1}$ from Eq. 3.13. The attenuation of this fibre was measured using the cutback method and a value of 2.9dB/m at 1.55$\mu$m was obtained.

In order to place this value in context, an unclad-unstructured fibre was also drawn from an extruded glass rod with the same composition as that used to draw the tellurite fibre. The spectrum of the fibre attenuation in the wavelength range of 0.6 to 2.4$\mu$m was recorded. A more detailed analysis can be found in [Feng *et al.*, 2008a]. From the measured spectrum, it can be seen that across the whole range from 1 to 2.4$\mu$m the unclad fibre shows no more than 3dB/m attenuation. The maximum value of attenuation was found in the wavelength range between 1.7 and 2$\mu$m, while the minimum value (0.8B/m) was found in the region between 1.1-1.3$\mu$m and 2.0-2.3$\mu$m. The presence of the absorption peak in the wavelength range between 1.7 and 2$\mu$m is due to the

fundamental vibration, in the same range of wavelengths, of the hydroxyl groups (OH) existing in the tellurite glass matrix. When comparing the attenuation of the unclad fibre with that of the LMA HF at 1.55$\mu$m, a ~1.5dB/m loss increase can be observed for the LMA HF. Since the LMA HF and the unclad fiber had very similar thermal history and fabrication process, from glass melting, extrusion, to fibre drawing, the enhanced attenuation of the LMA HF at 1.55$\mu$m over the unclad fiber could be attributed to the surface roughness inside the holes of the HF, and some additional impurities involved into the preform during extrusion. Although the propagation loss of the LMA HF was measured only at 1.55$\mu$m, the study of the attenuation across the range 0.6 to 2.4$\mu$m gives an indication of the trend expected in tellurite fibres drawn with the considered composition in terms of propagation loss.

A smaller core fibre was also drawn from the same preform used for the LMA HF. More details on the fabrication of the fibre can be found in [Feng *et al.*, 2008c]. This fibre, denoted as Fibre #2, showed a core diameter of 14$\mu$m and still presented a large effective mode area of ~80$\mu$m$^2$ for the fundamental mode at 1.5$\mu$m. An SEM image of the fibre is shown in Figure 7.4(a). Numerical simulations have shown that for this fibre the confinement losses for the first two modes in this fibre are ~$10^{-4}$ dB/m, while higher order modes show confinement losses of the order of a few dB/m. This explains why the guidance of two modes was observed in this second fibre, as shown in Figure 7.4(b). (Note that the images in Figure 7.4 are not in the same scale.) Using Eq. 3.13, the nonlinear coefficient of Fibre #2 at 1550nm has been estimated to be $\gamma$=8.6W$^{-1}$km$^{-1}$. The main parameters of the two fibres are summarised in Table 7.2.

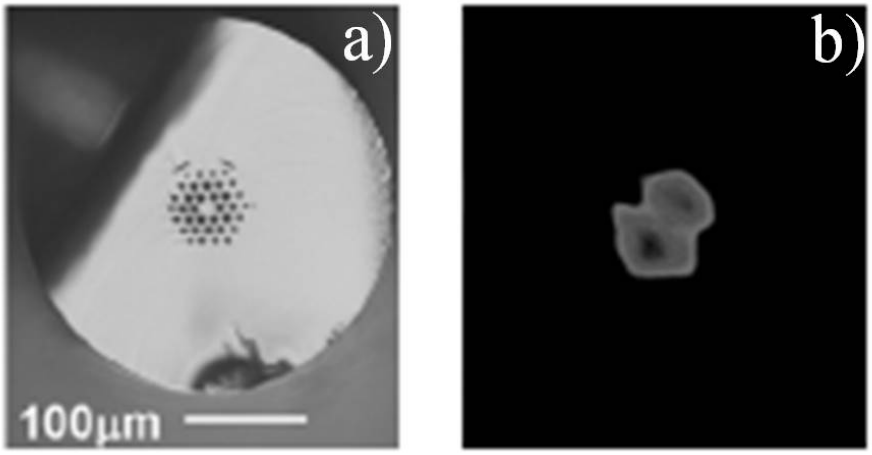


FIGURE 7.4: (a) SEM image of the small core Te-fibre; (b): Observed near field mode profile in the fibre.

TABLE 7.2: Parameters of the two fibres used in the experiments

| Fibre | Core diameter ($\mu$m) | $A_{eff}$ ($\mu m^2$) | Nonlinear Coefficient ($W^{-1}km^{-1}$) |
|---|---|---|---|
| #1 | 80 | 3000 | 0.22 |
| #2 | 14 | 80 | 8.6 |

The dispersion profile of the two fibres has not been measured, but numerical simulations on the SEM images of the two fibres have been performed by Dr. Baggett. The results of the simulations are shown in Figure 7.5. The estimated ZDW for Fibre #1 and Fibre #2 are 2.150$\mu$m and 2.085$\mu$m respectively.

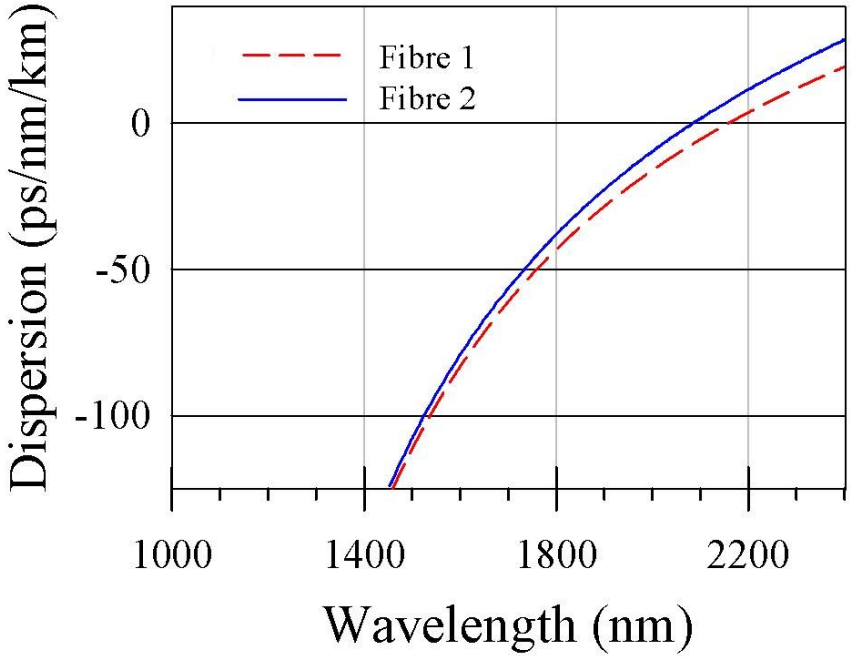


FIGURE 7.5: Simulated dispersion profiles for the Fibre#1 (red line) and Fibre#2 (blue line).

### 7.2.2 Experimental setup

In order to investigate the generation of supercontinuum in the two tellurite fibres, the experimental setup shown in Figure 7.6 was used. A tunable optical parametric oscillator (OPO) pumped by a Coherent Mira femtosecond laser ($\lambda_{pump}$=800nm) was used as the source. The pulse duration obtained ($\sim$120fs) was monitored throughout the experiment using a frequency-resolved optical gating set-up.

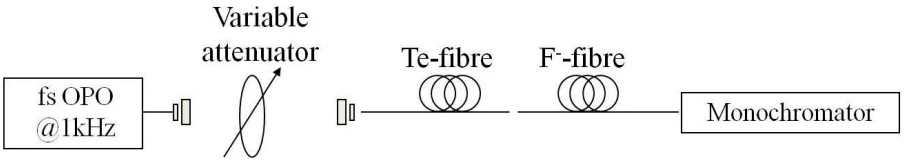


FIGURE 7.6: Experimental setup used to measure SCG.

In an OPO the pump, the signal and the idler are related as follows [Baumgartner and Byer, 1979]:

$$\frac{1}{\lambda_{pump}} = \frac{1}{\lambda_{signal}} + \frac{1}{\lambda_{idler}} \tag{7.1}$$

Eq. 7.1 shows that the idler wavelength is dictated by that of the pump and that of the OPO signal. By tuning the signal in the 1.3$\mu$m range, idlers at wavelengths beyond 2$\mu$m can be obtained, when the OPO pump is set at 800nm. The optical spectrum at the output of the OPO was recorded before the launch into the fibre and is illustrated in Figure 7.7. While the strong idler at 2.05$\mu$m can easily be appreciated, the presence of the weak signal at 1.312$\mu$m could not be easily observed by looking at the spectrum.

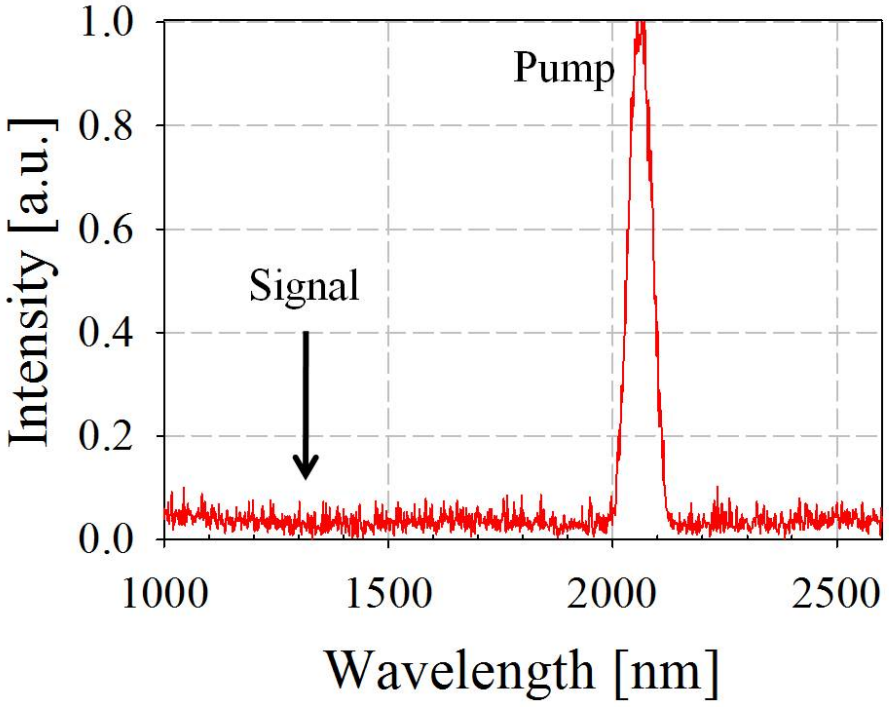


FIGURE 7.7: Spectrum recorded at the input of the fibre. While the strong idler at 2050nm is clearly visible, the weak signal at 1312nm could not obviously observed.

The idler beam, which will be indicated as the SCG pump in our experiments, was then focused into the tellurite HFs, using a microscope objective with NA of 0.1, with a coupling efficiency of ∼25%.

The tellurite fibre under test was then butt-coupled into a multimode fluoride glass fiber with 160$\mu$m core diameter and NA of 0.28 (GFF-160/200-230, Fiberlabs, Japan). The collecting fibre was chosen to be a fluoride fibre as it shows a transmission spectrum wide enough to match the range covered by the monochromator. The output was finally recorded by a DM501 monochromator (DONGWOO OPTRON) with a cooled extended InGaAs photodiode (J23TE3-66C-R02M-2.4) covering the range 500nm to 2600nm.

### 7.2.3 Experimental results

Ideally, the pump wavelength should be chosen as close as possible to the ZDW of the two fibres. However, some technical issues with the laser at the time of the first experiment limited the longest wavelength achievable with the system to be set at 2.050$\mu$m. Also, it has to be noted that no filter was used before the fibre and therefore the OPO signal was coupled into the fibre together with the 800nm pump. The input power was set at the maximum value achievable by the system in this instance, 1.4mW. This power could be controlled through a variable attenuator to values down to 0.1mW. The launched pump power values used in our experiments of 0.1-1.4mW corresponded to peak pulse power values of 800kW-12MW, with a pulse energy of 0.1-1.4$\mu$J.

Figure 7.8 shows the observed SCG in 70cm of Fibre#1, for various input powers. A bandwidth of ∼500nm was achieved for the highest input power of 1.4mW. The output can be considered symmetric with good approximation, indicating that SPM was the dominant nonlinear effect in the broadening process. The ZDW of this fibre indeed, is slightly higher than the pump wavelength and the pump is therefore in the normal regime. The SCG power from the output end of Fibre#1 was measured to be 0.40±0.05mW, for the maximum input power of 1.4mW.

A 63cm long sample of Fibre#2 was then investigated using the same setup. For this sample, the generated supercontinuum from 1.0 to 2.4$\mu$m was much broader and flatter, as shown in Figure 7.9. As the pump pulses in this case are very close to the ZDW of Fibre#2, a significant contribution of FWM towards the shorter wavelengths and of

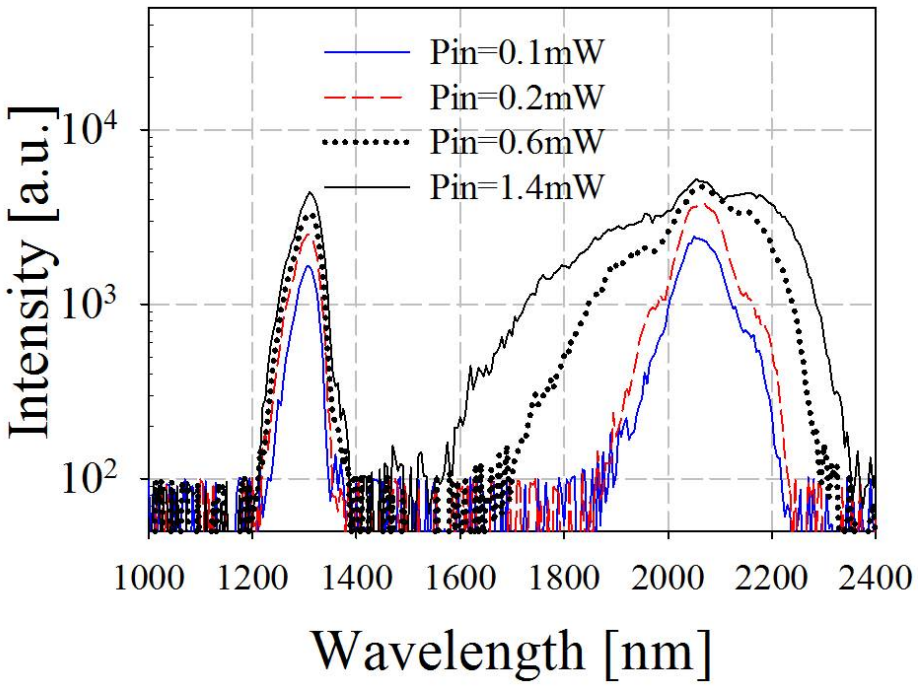


FIGURE 7.8: Observed SCG in a 70cm long sample of Fibre#1 for various input powers.

self-frequency shifted solitons extending towards the longer wavelengths help broadening the spectrum. The SCG power from Fibre#2 was measured to be 0.45±0.05mW, for an average input power of 1.4mW.

Both Figure 7.8 and Figure 7.9 show that the very weak signal at 1.312$\mu$m which is residual from the OPO gives a significant contribution to the output spectra. This indicates that the pump at 2.05$\mu$m, which reduced to be now comparable in strength with the signal, was quite effectively converted into a broad spectrum. During the experiments, the measured tellurite HFs showed no facet damage. The launched pump power values used in our experiments of 0.1mW-1.4mW corresponded to peak pulse power values of 800kW-12MW, with a pulse energy of 0.1-1.4$\mu$J.

The results shown above can be further optimised by scaling the input power in the fibre, and consequently the output power, and optimising the fibre length. However, scaling the power to higher levels is more practical in the larger mode area fibre as the damage power threshold would be considerably higher than in a smaller core one. For this reason, and because of the limited time available to use the femtosecond laser

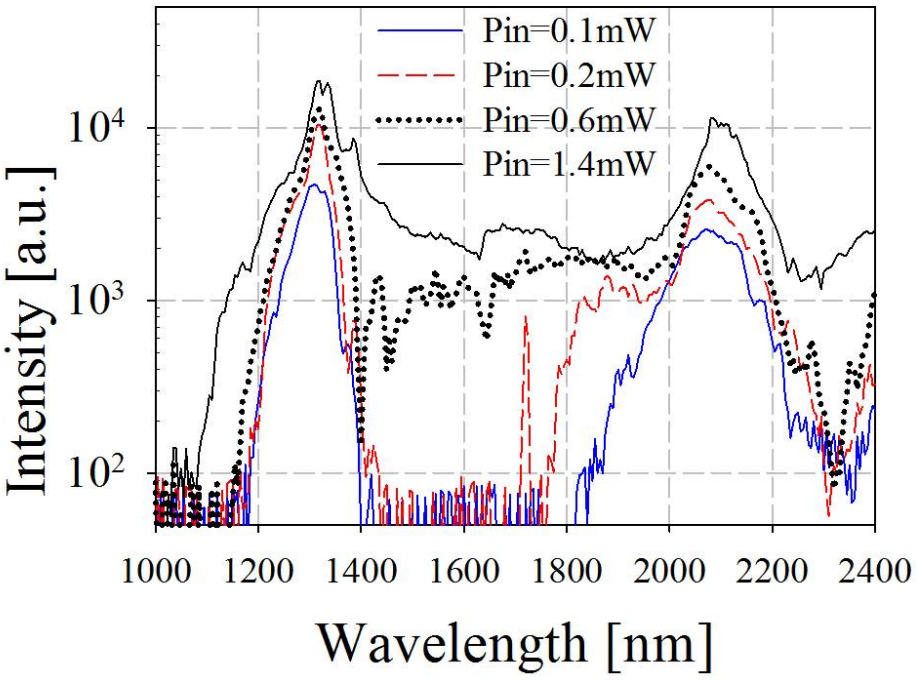


FIGURE 7.9: Observed SCG in a 63cm long sample of Fibre#2 for various input powers.

system, the SCG experiments were further investigated only in a sample of the LMA Te-fibre (Fibre #1).

During the second set of experiments, a long-wavelength pass filter (Thorlabs FEL1500) was placed before the microscope objective in front of the fibre in order to filter out the residual signal from the OPO for wavelengths shorter than 1.5$\mu$m. At the time of this experiment, the femtosecond laser was more stable and it was possible to achieve higher values of power when compared to the first experiment. Analogously to the previous measurement, the average input power in the fibre was set to the maximum value and then scaled down through an attenuator and the output spectra were recorded for three different values of fibre length. Figure 7.10 shows the recorded spectra at the output of the fibre for various power levels and fibre lengths: in Figure 7.10(a) the fibre was 90cm in length, in Figure 7.10(b) the sample was reduced to 50cm, in Figure 7.10(c) to 18.5cm. The measurements of Figure 7.10 show that a higher input power corresponds to a larger spectral broadening and also that the spectral broadening is highly comparable in the three samples for the maximum input power. These results indicate that a broad spectrum can be obtained in a short sample of fibre and that the propagation loss in a

longer sample is responsible for a reduced output power and does not contribute to the achievement of a broader spectrum.

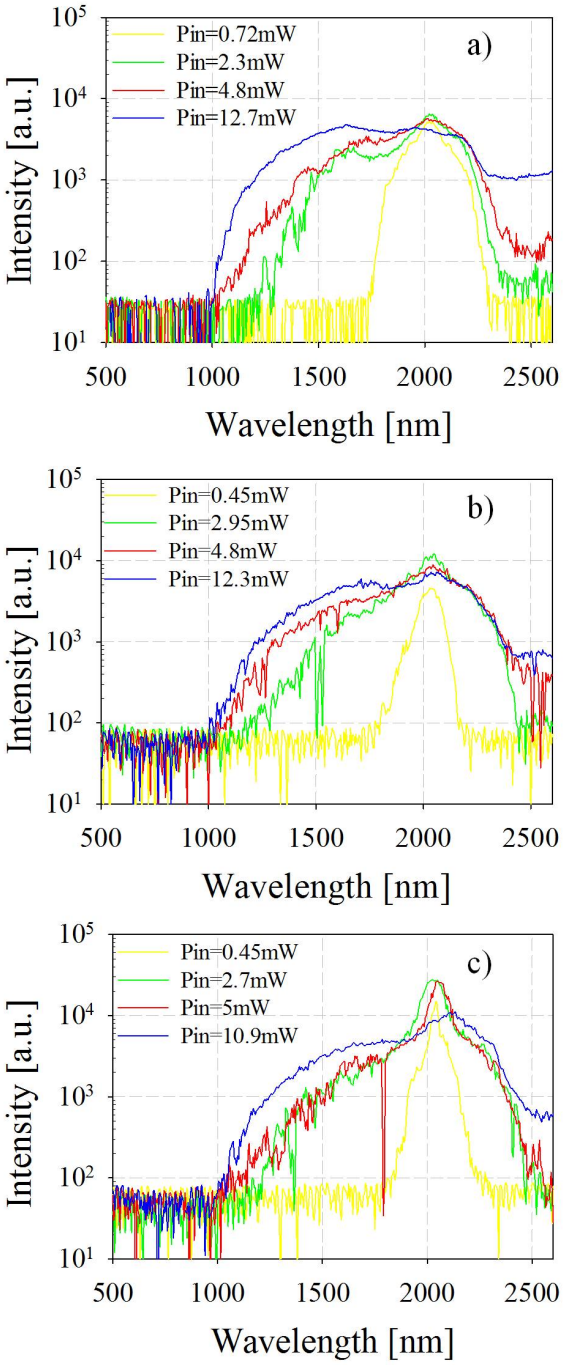


FIGURE 7.10: Recorded spectra at the output of the Te-LMA when the fibre length was (a) 90cm, (b) 50cm, and (c) 18.5cm.

For these reasons, the sample of tellurite LMA HF was reduced in length even further down to a value of 9cm. During this measurement, it was possible to set the pump wavelength at 2.15$\mu$m, which corresponds to the ZDW of the fibre and even achieve slightly higher values of input power, as the issue with the laser stability was resolved. The output spectra recorded for various values of power in the 9cm length sample are illustrated in Figure 7.11.

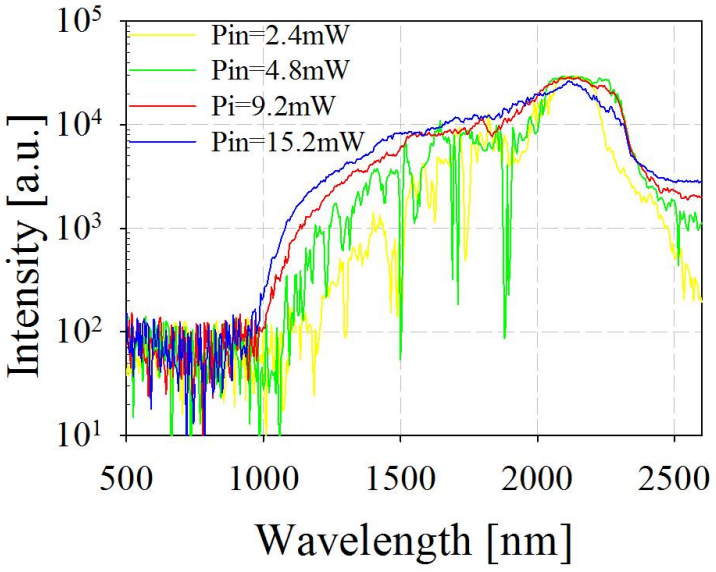


FIGURE 7.11: Recorded spectra at the output of the Te-LMA when the fibre length was 9cm.

Analogously to the previously analysed cases, the SC spectrum spans from 0.9$\mu$m to at least 2.5$\mu$m at the maximum input power of 15.2mW, which corresponds to energy values of 15.2$\mu$J per pulse. Beyond 2.6$\mu$m, the spectrum could not be measured due to the long-wavelength limit of the detector. The power at the output of the 9cm sample was measured to be 6.0mW, corresponding to an energy value of 6$\mu$J per pulse.

At the maximum input power (15mW), the spectrum at the output of the 9cm long sample was also recorded when the pump wavelength was set at 2.05$\mu$m and compared to that achieved when the pump wavelength was tuned to 2.15$\mu$m. The results are shown in Figure 7.12, where no substantial difference in the spectra can be appreciated. This might be due to the ZDW of Fibre#1 being in reality very close to the value estimated by the numerical simulations. Note that the deep at around 1500nm is an artifact of the measurement.

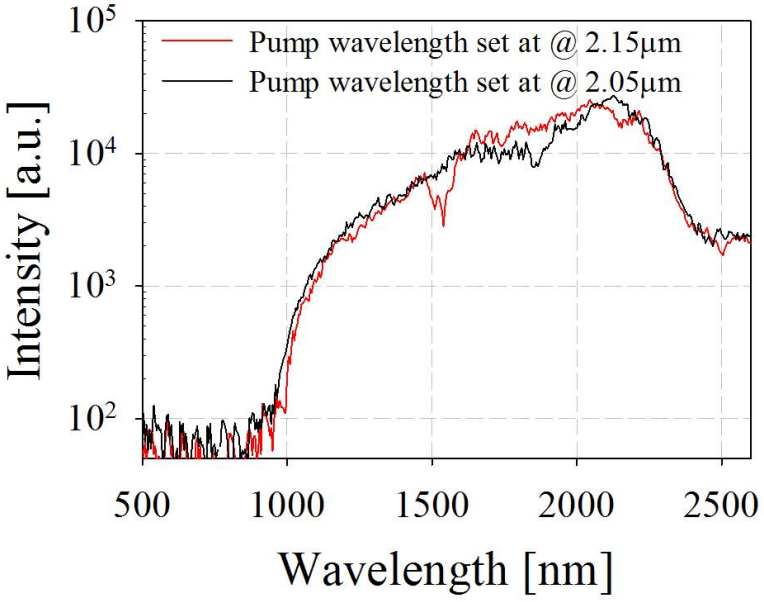


FIGURE 7.12: Comparison of the output spectra in a 9cm length of Te-LMA fibre when the pump wavelength is set at 2.05$\mu$m and 2.15$\mu$m.

The benefits of using a short sample can be better appreciated in Figure 7.13, where the spectra at the output of each of the fibre samples considered above at the corresponding maximum input power are compared when the pump wavelength is 2.05$\mu$m.

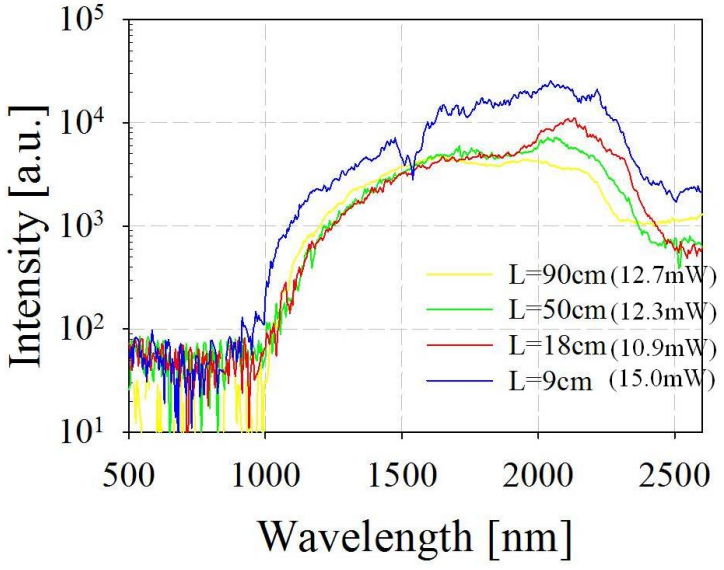


FIGURE 7.13: Recorded spectra at the output of the tellurite LMA HF at the maximum input power for several fibre lengths.

Note that the pump power is slightly higher in the 9cm long sample. It is possible to see that with good approximation the same spectral broadening can be obtained in all of the

samples at the maximum pump power, while the output power is clearly increasing when the samples are shortened, confirming the role of the propagation loss of the samples.

## 7.3 Conclusions

This chapter has investigated the possibility of generating a SC spectrum in the mid IR using non-silica fibres. First of all, a brief overview of the interaction between the main phenomena involved in the generation of a SC spectrum has been given. An analysis of the available HMO glasses in terms of nonlinear refractive index and transparency in the mid-IR has helped to identify a suitable glass for the fabrication of a fibre to employ in the SCG experiments. Two tellurite-based HFs have been investigated.

For relatively high values of pulse energies (1.4$\mu$J), a broad spectrum has been obtained for both fibres when pumping close to the ZDW, in the normal dispersion regime. In order to obtain higher values of power at the output of the fibre, further experiments have been performed only in the LMA HF. The small core fibre has not been considered as it shows a lower damage threshold when compared to the LMA HF.

The results obtained with the LMA HF confirm the importance of the fibre length on the quality of the SCG process. Using only 9cm of the LMA HF indeed, a spectrum ranging from 0.9$\mu$m up to 2.5$\mu$m has been obtained with a pulse energy of 6$\mu$J.

The fact that during the experiments the fibre did not suffer any damage on the input facet suggests that the values of input power can be scaled up to even higher values, leading to the generation of even broader spectra. The experiments illustrated here confirm the potential of the tellurite HF for the generation of efficient SC spectra.

# Chapter 8

# Conclusions and future directions

The objective of this thesis was to investigate the possibility to use highly nonlinear, dispersion tailored fibres for applications at telecoms wavelengths. In order to achieve a fibre with a high nonlinear coefficient and a tailored dispersion profile, two fibre-based technologies were considered: nonlinear liquid filled fibres and soft glass fibres. With regards to the nonlinear liquid filled fibre technology, the first steps taken towards the development of a suitable technique for filling a HF entirely or selectively, were described. A numerical model for the infusion process was described and then verified using water and toluene as test liquids. The experiments confirmed that the infusion time in a holey structure can be predicted by the numerical model with good accuracy. However, the issues presented by the development of the nonlinear liquid filled fibre technology at the time of the experiments moved the attention of my research towards the development of soft glass fibres, at the time a more mature technology.

With respect to soft glass fibres for telecoms applications, a lead silicate holey structure as well as two all solid fibres have been considered. The choice of lead silicate glasses was dictated by their high thermal and chemical stability which offer great advantages in terms of fibre fabrication over other glasses. The optical properties of the fibres have been investigated by applying suitable measurement techniques. Moreover, the results of the characterisation of the fibres have been of particular importance as a feedback to the fabrication group, since the values confirmed the dependence of optical parameters such as dispersion and dispersion slope on the fibre structure and ultimately on the fabrication conditions.

The first structure investigated was a small core holey fibre made of the commercially available lead silicate Schott SF57. The 2.0$\mu$m core fibre was single mode at 1550nm and exhibited a nonlinear coefficient $\gamma$ of 275W$^{-1}$km$^{-1}$ and a dispersion and dispersion slope of -16ps/nm/km and 0.08ps/nm$^2$/km respectively at 1550nm. Despite the high nonlinear coefficient and the relatively low dispersion and dispersion slope, the fibre was not considered to be very promising as its properties were proven to be strongly dependent on any microscale variation that might occur during the fibre drawing. A solution to this problem was identified in the use of all-solid structures as they have proven that the preform structure can be preserved during the fibre drawing with great accuracy.

One of the two all-solid fibre designs investigated within this thesis showed a solid core surrounded by a number of alternating high and low-index coaxial rings with different layer thicknesses which determined the optical properties of the fibre. A 3.3$\mu$m core diameter fibre was effectively single mode at 1550nm and exhibited a nonlinear coefficient of 120W$^{-1}$km$^{-1}$ and a dispersion value of 12ps/nm/km at 1550nm. The high optical quality of the glass disks used for the fibre preform resulted in a sample showing one of the lowest value of propagation losses reported so far in a non-silica fibre (0.8dB/m). The potential of this fibre for the realisation of FWM-based application was then investigated. Using a sample of only 1.5m in length a FWM-based wavelength conversion scheme of pulsed signals was implemented. A -3dB bandwidth of 17nm was achieved with a conversion efficiency of -40dB and the wavelength conversion was accompanied by compression of the converted pulses.

The second all-solid design investigated within this thesis was a fibre with a W-type refractive index profile based on three commercially available lead-silicate glasses. Two different fabrication approaches were used to fabricate the two samples investigated in this thesis. Based on the extrusion technique, a fibre with high nonlinear coefficient of 822W$^{-1}$km$^{-1}$ and low dispersion of -12ps/nm/km at 1550nm was achieved. Despite the high propagation losses exhibited by the sample (4.8dB/m), the high nonlinear coefficient and the relatively low dispersion profile of the fibre, contributed to the realisation of a broadband wavelength conversion scheme in a sample of only 1.1m in length. FWM-based wavelength conversion with a -3dB bandwidth of 20nm with a conversion efficiency of -33dB was achieved and the experimental values have been supported by numerical simulations of the FWM process. Additional numerical simulations have been

performed in order to investigate the role of the fibre loss and dispersion for an efficient FWM conversion efficiency. The numerical simulations suggested that the W-type fibre design, with the appropriate structure parameters, could potentially lead to a flat FWM conversion efficiency within the whole C-band and therefore represent a promising structure for FWM-based applications. For these reasons, a second attempt to fabricate a W-type fibre was performed.

The improvement in the fabrication process of the W-type fibre, obtained by replacing the extrusion steps with a process based on drilling and polishing of the tubes, has led to the fabrication of a fibre with a 1.63$\mu$m core diameter exhibiting propagation losses of 2.1dB/m, a high nonlinear coefficient of 820W$^{-1}$km$^{-1}$ and low dispersion of -3ps/nm/km at 1550nm and a low overall dispersion profile. The investigation of FWM-based wavelength conversion in this fibre has confirmed the predicted fibre performance and a flat FWM conversion efficiency in the whole C-band was achieved in only a 2.2m long sample of the fibre.

The optical properties of this fibre made it an ideal candidate for FWM-based applications and therefore the feasibility of the realisation of FWM-based highly nonlinear devices in short samples of the lead silicate W-type fibre was investigated. The W-type fibre was employed for the realisation of a multi-wavelength conversion scheme, where the simultaneous conversion of three DPSK signals at 40Gbit/s was demonstrated with negligible interchannel crosstalk. The fibre was also employed to demonstrate the generation of high repetition rate (>160GHz) and high quality pulses and the fibre suitability for the THz regime was investigated. Finally, the fibre was successfully used in a 160-to-40Gbit/s demultiplexing scheme.

The experiments presented in this thesis prove the suitability of the lead silicate W-type fibre design for highly nonlinear applications. In particular, the combination of the W-type design with the use of highly nonlinear glasses such as lead silicate, can offer a high nonlinear coefficient and a low and flat dispersion profile at the wavelengths of interest at the same time. Moreover, the experiments presented within this thesis were all based on short fibre samples and therefore revealed the potential of all solid soft glass fibre designs for the realisation of compact highly nonlinear devices with low power requirement at telecoms wavelengths.

In order to reduce the power requirement of the devices even further, an increase in the nonlinear coefficient of the fibres could be envisaged. The lead silicate glasses used for the fabrication of the fibres presented within this thesis show a nonlinear refractive index at least two orders of magnitude higher than silica and therefore fibres with a nonlinear coefficient as high as $820\text{W}^{-1}\text{km}^{-1}$ could be fabricated. However, other soft glasses exist that show a higher nonlinear refractive index than lead silicate glasses, such as chalcogenide glasses. At present, these glasses present some issues in terms of chemical stability and this makes the fibre fabrication quite challenging. However, some remarkable results have been achieved so far in this direction, making the fabrication of fibres made of chalcogenide glasses a feasible route [Mägi *et al.*, 2007; Ta'eed *et al.*, 2006b].

This thesis also focused on the applications of soft glass fibres for the generation of a broad supercontinuum spectrum in the mid-IR. Tellurite glasses show a high thermal and chemical stability, similarly to lead silicate glasses, but a better transparency in the mid-IR region. For this reason, tellurite glasses represented the glasses of choice for this applications and in particular two tellurite based HFs were identified as suitable structures for the investigation of supercontinuum generation in the mid-IR regime.

A 9cm long sample of a tellurite HF showing one of the largest values of mode area reported so far, $3000\pm200\mu\text{m}^2$ at 1550nm, was employed to achieve a broad spectrum ranging from $0.9\mu$m up to $2.5\mu$m with a pulse energy of $6\mu$J. The extremely short sample used in the experiment clearly revealed the potential of tellurite HFs for supercontinuum generation in the Mid-IR.

One way to improve the spectral broadening at the output of the fibre, is to act on the dispersion profile of the fibre. The fibres presented here exhibited a ZDW very close to the available pump wavelength and this had a positive effect on the enhancement of the output spectrum. However, fibres that exhibit 2 ZDWs close to the pump wavelength are considered to be very promising for the realisation of a broad spectrum [Dudley *et al.*, 2006]. Moreover, the fact that the fibres did not suffer any damage during the experiments, indicates that higher power levels can be obtained at the output of the fibres. Therefore, improving the tellurite fibre design and increasing the input power seem to be a promising route for the realisation of ultra bright broadband sources.

# References


R. Adair, L.L. Chase, and S. A. Payne. Nonlinear refractive index of optical crystals. *Phys. Rev. B, Condens. Matter*, 39(5):3337–3350, 1989.

G. P. Agrawal. *Nonlinear fiber optics, fourth edition.* Academic Press, 2006.

R. R. Alfano and S. L. Shapiro. Observation of self-phase modulation and small scale filaments in crystals and glasses. *Physical Review Letters*, 24(11):592–594, 1970.

P. A. Andersen, T. Tokle, Y. Geng, C. Peucheret, and P. Jeppensen. Wavelength conversion of a 40-Gb/s RZ DPSK signal using four wave mixing in a dispersion flattened highly nonlinear photonic crystal fibre. *IEEE Photonics Technology Letters*, 17(9):1908–1910, 2005.

W. T. Anderson, P. F. Glodis, D. L. Philen, A. A. Schenk, and C. L. Bice. Thermally induced refractive-index changes in a singlemode optical-fiber preform. In *Technical Digest Optical Fiber Communication Conference (OFC)*, pages 78–79, New Orleans, LA, 1984. paper TuN10.

S. Asimakis, P. Petropoulos, F. Poletti, J. Y. Y. Leong, R. C. Moore, K. E. Frampton, X. Feng, W. H. Loh, and D. J. Richardson. Towards efficient and broadband four-wave mixing using short-length dispersion tailored lead silicate holey fibers. *Optics Express*, 15(2):596–601, 2007.

J. C. Baggett. Microstructured optical fibres. $1^{st}$ Year post-graduate student lecture notes, 2006.

G. K. Batchelor. *An Introduction to Fluid Dynamics.* Cambridge University Press, 2000.

R. A. Baumgartner and R. K. Byer. Optical parametric amplification. *IEEE J. Quantum. Electron*, 15:432–444, 1979.

W. Belardi, J. H. Lee, K. Fusakawa, Z. Yusoff, and P. Petropoulos. A 10 Gbit/s tuneable wavelength converter based on four-wave mixing in highly nonlinear holey fibre. In *The European Conference on Optical Communication (ECOC), Copenhagen, Denmark*, 2002.

T. A. Birks, P. J. Roberts, P. S. J. Russell, D. M. Atkin, and T. J. Shepherd. Full 2-D photonic bandgap in silica air structures. *Electronics Letters*, 31(22):1941–1943, 1995.

T. A. Birks, J. C. Knight, and P. S. J. Russell. Endlessly single-mode photonic crystal fiber. *Optics Letters*, 22:961–963, 1997.

T. A. Birks, W. J. Wadsworth, and P. St. J. Russell. Supercontinuum generation in tapered fibers. *Optics Letters*, 25(19):1415–1417, 2000.

K. J. Blow, N. J. Doran, B. K. Nayar, and B. P. Nelson. Two-wavelength operation of the nonlinear fibre loop mirror. *Optics Letters*, 15(4):248–250, 1990.

A. Bogoni, P. Ghelfi, M. Scaffardi, and L. Poti'. All-optical regeneration and demultiplexing for 160-Gb/s transmission systems using a NOLM-based three-stage scheme. *IEEE Journal of Selected Topics in Quantum Electronics*, 10(1):192–196, 2004.

A. Bogoni, M. Scaffardi, P. Ghelfi, and L. Poti. Nonlinear optical loop mirrors: investigation solution and experimental validation for undesirable counterpropagating effects in all-optical signal processing. *IEEE Journal of Quantum Electronics*, 10(5):1115–1123, 2004.

A. Boskovic, S. V. Chernikov, J. R. Taylor, I. Gruner-Nielsen, and O. A. Levring. Direct continuous-wave measurement of n(2) in various types of telecommunication fiber at 1.55$\mu$m. *Optics Letters*, 21(24):1966–1968, 1996.

R. W. Boyd. *Nonlinear Optics 2nd Edition.* Academic Press, San Diego, 2003.

G. Brambilla, F. Koizumi, V. Finazzi, and D. J. Richardson. Supercontinuum generation in tapered bismuth silicate fibres. *Electronics Letters*, 41(14):795Ű797, 2005.

L. Brilland, F. Smektala, G. Renversez, T. Chartier, J. Troles, T. Nam Nguyen, N. Traynor, and A. Monteville. Fabrication of complex structures of holey fibers in chalcogenide glass. *Optics Express*, 14(3):1280–1285, 2006.

J. Broeng, S. E. Barkou, A. Bjarklev, J. C. Knight, T. A. Birks, and P. S. J. Russell. Highly increased photonic band gaps in silica/air structures. *Optics Communications*, 156(4-6):240–244, 1998.

J. Broeng, T. Sondergaard, S. E. Barkou, P. M. Barbeito, and A. Bjarklev. Waveguide by the photonic bandgap effect in optical fibres. *Journal of Optics A: Pure and Applied Optics*, 1:477–482, 1999.

J. Broeng, S. E. Barkou, T. Sondergaard, and A. Bjarklev. Analysis of air-guiding photonic bandgap fibres. *Optics Letters*, 25(2):96–98, 2000.

A. Camerlingo, F. Parmigiani, X. Feng, F. Poletti, P. Horak, W. H. Loh, D. J. Richardson, and P. Petropoulos. Four wave mixing based wavelength conversion in a short length of a solid 1D microstructured fibre. In *Proc. European Conference on Optical Communications (ECOC), Vienna, Austria*, Vienna, 2009.

A. Camerlingo, F. Parmigiani, X. Feng, F. Poletti, P. Horak, W. H. Loh, D. J. Richardson, and P. Petropoulos. Wavelength conversion in a short length of a solid lead-silicate fibre. *IEEE Photonics Technology Letters*, 22(9):628–630, 2010.

S. Chandrasekhar. *Liquid Crystals*. Cambridge University Press, 1977.

C. Chaudhari, T. Suzuki, and Y. Ohishi. Chalcogenide core photonic crystal fibers for zero chromatic dispersion in the C-band. In *Technical Digest Optical Fiber Communication Conference (OFC), OTuC4*, 2009.

H. Chen. Simultaneous measurements of non-linear coefficient, zero-dispersion wavelength and chromatic dispersion in dispersion-shifted fibers by four-wave mixing. *Optics Communications*, 220(4-6):331–335, 2003.

S. V. Chernikov, J. R. Taylor, and R. Kashyap. Comblike dispersion-profiled fiber for soliton pulse train generation. *Optics Letters*, 19(8):539–541, 1994.

S. V. Chernikov, J. R. Taylor, and R. Kashyap. Experimental demonstration of steplike dispersion profiling in optical fibre for soliton pulse generation and compression. *Electronics Letters*, 30(5):433–435, 1994.

K. K. Chow, C. Shu, C. Lin, and A. Bjarklev. Polarization insensitive widely tunable wavelength converter based on four wave mixing in a dispersion flattened nonlinear photonic crystal fibre. *IEEE Photonics Technology Letters*, 17(3):624–626, 2005.

K. K. Chow, K. Kikuchi, T. Nagashima, T. Hasegawa, S. Ohara, and N. Sugimoto. Four-wave mixing based widely tunable wavelength conversion using 1-m dispersion shifted bismuth-oxide photonic crystal fiber. *Optics Express*, 15(23):15418–15423, 2007.

L. G. Cohen and C. Lin. Pulse delay measurements in the zero material dispersion wavelength region for optical fibers. *Applied Optics*, 16(12):3136–3139, 1977.

R. F. Cregan, B. J. Mangan, J. C. Knight, T. A. Birks, P. S. J. Russell, P. J. Roberts, and D. C. Allan. Single mode photonic bandgap guidance of light in air. *Science*, 285:1537–1539, 1999.

S. T. Cundoff, J. Ye, and J. L. Hall. Optical frequency synthesis based on mode-locked laser. *Review of Scientific Instruments*, 72(10):3749–3771, 2001.

S. L. Danielsen, P. B. Hansen, and K. E. Stubkjaer. Wavelength conversion in optical packet switching. *Journal of Lightwave Technology*, 16(12):2095–2108, 1998.

T. Delmonte, M. A. Watson, E. J. O Driscoll, T. M. Monro, V. Finazzi, P. Petropoulos, J. H. V. Price, W. Loh, X. Feng, J. C. Baggett, D. J. Richardson, and D. P. Hand. Generation of mid-IR continuum using tellurite microstructured fiber. In *Conference on Lasers and Electro-Optics/Quantum electronics and Laser Science (CLEO/QELS), Long Beach, CA, USA, Paper CTuA4.*, 2006.

A. D'Errico, C. Loiacono, M. Presi, G. Contestabile, and E. Ciaramella. Widely tunable 40GHz pulse source for 160Gbit/s OTDM by simultaneous soliton generation and compression. In *Proc. European Conference on Optical Communications (ECOC), Rimini, Italy*, page We 2.6.5, Rimini, 2003.

P. Devgan, R. Tang, V. S. Grigoryan, and P. Kumar. Highly efficient multichannel wavelength conversion of DPSK signals. *Journal of Lightwave Technology*, 24(10):3677–3682, 2006.

S. A. Diddams, M. Kirchner, T. Fortier, D. Braje, A. M.Weiner, and L. Hollberg. Improved signal-to-noise ratio of 10 GHz microwave signals generated with a mode-filtered femtosecond laser frequency comb. *Optics Express*, 17(5):3331–3340, 2009.

P. Domachuk, N. A. Wolchover, M. Cronin-Golomb, A. Wang, A. K. George, N. A. Cordeiro, J. C. Knight, and F. G. Omenetto. Over 4000 nm bandwidth of mid-IR

supercontinuum generation in sub-centimeter segments of highly nonlinear tellurite PCFs. *Optics Express*, 16(10):7161–7168, 2008.

J. M. Dudley, G. Genty, and S. Coen. Supercontinuum generation in photonic crystal fiber. *Rev. Mod. Phys.*, 78:1135– 1184, 2006.

P. Dumais, C. Callender, J. Noad, and C. Ledderhof. Integrated liquid core waveguide for nonlinear optics. *Applied Physics Letters*, 90(10):101101–3, 2007.

H. Ebendorff-Heidepriem, P. Petropoulos, S. Asimakis, V. Finazzi, R. C. Moore, K. Frampton, F. Koizumi, D. J. Richardson, and T. M. Monro. Bismuth glass holey fibers with high nonlinearity. *Optics Express*, 12(21):5082–5087, 2004.

H. Ebendorff-Heidepriem, P. Petropoulos, R. C. Moore, K. Frampton, D. J. Richardson, and T. M. Monro. Fabrication and optical properties of lead silicate glass holey fibers. *J. Non-Crystalline Solids*, 345:293–296, 2004.

H. Ebendorff-Heidepriem, P. Petropoulos, V. Finazzi, S. Asimakis, J. Y. Y. Leong, F. Koizumi, K. Frampton, R. C. Moore, D. J. Richardson, and T. M. Monro. Heavy metal oxide glass holey fibers with high nonlinearity. In *Technical Digest Optical Fibre Communication Conference (OFC), Anaheim, CA, USA*, Anaheim (USA), 2005.

J. Fatome, S. Pitois, C. Fortier, B. Kibler, C. Finot, G. Millot, C. Curder, M. Lintz, and E. Samain. Real time monitoring of an all-fibered 20 GHz optical pulse source and generation of high quality 1.5-2THz femtosecond pulse sources based on multiple four wave mixing approach. *Optics Communications*, 283(11):2425–2429, 2010.

X. Feng, T. M. Monro, P. Petropoulos, V. Finazzi, and D. Hewak. Solid microstructured optical fiber. *Optics Express*, 11(18):2225–2230, 2003.

X. Feng, T. M. Monro, P. Petropoulos, V. Finazzi, and D. W. Hewak. SoHo (solid holey) fiber. In *Proc. European Conference on Optical Communications (ECOC), Rimini, Italy*, Rimini, 2003.

X. Feng, A. K. Mairaj, D. W. Hewak, and T. M. Monro. Non-silica glasses for holey fibres. *Journal of Lightwave Technology*, 23(6):2046–2054, 2005.

X. Feng, T. M. Monro, V. Finazzi, R. C. Moore, K. Frampton, P. Petropoulos, and D. J. Richardson. Extruded single-mode high-nonlinearity tellurite glass holey fibre. *Electronics Letters*, 41(15):835–837, 2005.

X. Feng, T. M. Monro, P. Petropoulos, V. Finazzi, and D. J. Richardson. Extruded single-mode high-index-core one-dimensional microstructured optical fiber with high index-contrast for highly nonlinear optical devices. *Applied Physics Letters*, 87:81110–81125, 2005.

X. Feng, J. C. Flanagan, K. Frampton, P. Petropoulos, N. M. white, J. H. V. Price, W. H. Loh, H. N. Rutt, and D. J. Richardson. Developing single-mode tellurite glass holey fiber for infrared nonlinear applications. *Advances in Science and Technology*, 55:108–117, 2008.

X. Feng, J. C. Flanagan, K. E. Frempton, P. Petropoulos, N. W. White, W. H. Loh, H. N. Rutt, and D. J. Richardson. Single mode tellurite glass holey fibre with extremely large mode area for infrared applications. In *Technical Digest Optical Fiber Communication Conference (OFC)*, San Diego, USA, 2008.

X. Feng, W. H. Loh, A. Camerlingo, S. Dasgupta, J. C. Flanagan, P. Petropoulos, K. E. Frampton, N. M. White, H. N. Rutt, and D. J. Richardson. Broadband supercontinuum using single-mode/dual-mode tellurite glass holey fibers with large mode area. In *Conference on Lasers and Electro-Optics/Quantum Electronics and Laser Science (CLEO/QELS), San Jose, CA, USA*, San Jose, 2008.

X. Feng, F. Poletti, A. Camerlingo, F. Parmigiani, P. Horak, P. Petropoulos, W. H. Loh, and D. J. Richardson. Dispersion-shifted all-solid high index-contrast microstructured optical fiber for nonlinear applications at 1.55$\mu$m. *Optics Express*, 17(22):20249–20255, 2009.

A. Ferrando, E. Silvestre, J. J. Miret, and P. Andres. Nearly zero ultraflattened dispersion in photonic crystal fibers. *Optics Letters*, 25(11):790–792, 2000.

A. Ferrando, E. Silvestre, P. Andres, J. J. Miret, and M. V. Andres. Designing the properties of dispersion-flattened photonic crystal fibers. *Optics Express*, 9(13):687–697, 2001.

V. Finazzi, T. M. Monro, and D. J. Richardson. Small core silica holey fibres: nonlinearity and confinement trade-offs. *Journal of the Optical Society of America B*, 20(7):1427–1436, 2003.

J. M. Fini. Microstructured fibers for optical sensing in gases and liquids. *Measurement Science and Technology*, 15(6):1120–1128, 2004.

S. Fujino, H. Ijiri, F. Shimizu, and K. Morinaga. Measurement of viscosity of multi-component glasses in the wide range for fibre drawing. *J. Jpn. Instrum.Met.*, 62(1):106–110, 1998.

K. Furusawa, T. M. Monro, P. Petropoulos, and D. J. Richardson. Modelocked laser based on ytterbium doped holey fibre. *Electronics Letters*, 37(9):560–561, 2001.

M. Galili, H. C. H. Xu, J. Mulvad, L. K. Oxenl∅we, A. T. Clausen, P. Jeppesen, B. Luther-Davies, S. Madden, A. Rode, D. Choi, M. Pelusi, F. Luan, and B. J. Eggleton. Breakthrough switching speed with an all-optical chalcogenide glass chip: 640 Gbit/s demultiplexing. *Optics Express*, 17(4):2182–2187, 2009.

W. A. Gambling and D. Payne. Gigahertz bandwidhts in multimode, liquid core optical fibre waveguide. *Optics Communications*, 6(4):317–322, 1972.

S. Gee, F. Quinlan, S. Ozharar, and P.J. Delfyett. Simultaneous optical comb frequency stabilization and super-mode noise suppression of harmonically mode-locked semiconductor ring laser using an intracavity etalon. *IEEE Photonics Technology Letters*, 17(1):199–201, 2005.

A. Ghatak and K. Thyagarajan. *Introduction to fibre optics.* Cambridge University Press, 1998.

J. T. Gopinath, H. M. Shen, H. Sotobayashi, E. P. Ippen, T. Hasegawa, and T. Nagashima. Highly nonlinear bismuth-oxide fibre for supercontinuum generation and femtosecond pulse compression. *Journal of Lightwave Technology*, 23(11):3591–3596, 2005.

C. Gosset and G. H. Duan. Multi-wavelength conversion and resynchronization of wavelength division multiplexed signals by use of four-wave-mixing in a semiconductor optical amplifier. In *Technical Digest Optical Fiber Communication Conference (OFC), Anaheim, CA, USA*, Anaheim, CA, 2002.

K. P. Hansen and R. E. Kristiansen. Supercontinuum generation in photonic crystal fibers. http://www.thorlabs.com/Thorcat/10700/10736-A02.pdf.

T. P. Hansen, J. Broeng, E. B. Libori, E. Knudsen, A. Bjarklev, J. R. Jensen, and H. Simonsen. Highly birefringent index guiding photonics crystal fibres. *IEEE Photonics Technology Letters*, 13(6):588–590, 2001.

K. P. Hansen, J. R. Folkenberg, C. Peucheret, and A. Bjarklev. Fully dispersion controlled triangular core nonlinear photonic crystal fiber. In *Technical Digest Optical Fiber Communication Conference (OFC), (Postdeadline), Atlanta, GA, USA, paper PD2.1*, volume 3, pages 1–3, 2003.

J. Hansryd, P. A. Andrekson, M. Westlund, J. Li, and P. Hedekvist. Fiber-based optical parametric amplifiers and their applications. *IEEE Journal of Selected Topics in Quantum Electronics*, 8(3):506–521, 2002.

I. Hartl, X. D. Li, C. Chudoba, R. K. Ghanta, T. H. Ko, J. G. Fujimoto, J. K. Ranka, and R. S. Windeler. Ultrahigh-resolution optical coherence tomography using continuum generation in an air-silica microstructure optical fiber,. *Optics Letters*, 9:608–610, 2001.

T. Hasegawa, T. Nagashima, and N. Sugimoto. Determination of nonlinear coefficient and group-velocity-dispersion of bismuth-based high nonlinear optical fiber by four-wave-mixing. *Optics Communications*, 281(4):782–787, 2008.

E. Hecht. *Optics $4^{th}$ Edition*. Cambridge University Press, 1998.

M. Hirano and T. Sasaki. Straightforward chromatic dispersion measurement based on phase mismatching FWM. In *Proc. European Conference on Optical Communications (ECOC), Vienna, Austria, paper 4.1.6*, 2009.

M. Hirano, T. Nakanishi, T. Okuno, and M. Onishi. Broadband wavelength conversion over 193-nm by HNL-DSF improving higher-order dispersion performance. In *European Conference in Optical Communication (ECOC), Glasgow, United Kingdom, paper Th4.4.4.*, 2005.

M. Hirano, T. Nakanishi, and T. Sasaki. FWM-based flexible wavelength conversion in whole C-band using realistic HNLF having dispersion slope. In *Technical Digest Optical Fiber Communication Conference (OFC), San Diego, CA, USA*, 2010.

Y. L. Hoo, H. L. Ho, and D. N. Wang. Evanescent-wave gas sensing using microstructured fibres. *Optical Engineering*, 41(1):8–9, 2001.

H. Hu, H. C. H. Mulvad, M. Galili, E. Palushani, A. T. Clausen, L. K. Oxenlwe, and P. Jeppesen. Polarization-insensitive 640 Gbit/s demultiplexing using a polarization

maintaining highly non-linear fibre. In *Photonics in Switching, Pisa, Italy, paper Fr I1-2*, 2009.

Y. Huang, Y. Xu, and A. Yariv. Fabrication of functional microstructured optical fibres through a selective filling technique. *Applied Physics Letters*, 85(22):5182–5184, 2004.

A.V. Husakou and J. Herrmann. Supercontinuum generation of higher order solitons by fission in photonic crystal fibers. *Phys Rev. Lett.*, 87(9):203901–1–203901–4, 2001.

A. V. Husakou and J. Herrmann. Supercontinuum generation, four-wave mixing, and fission of higher-order solitons in photonic-crystal fibres. *Journal of Optical Society of America B*, 19(9):2171–2182, 2002.

K. Igarashi, J. Hiroishi, T. Yagi, and S. Namiki. Comb-like profiled fibre for efficient generation of high quality 160 GHz sub-picosecond soliton train. *Electronics Letters*, 41(12):688–690, 2005.

K. Inoue and T. Mukai. Signal wavelength dependence of gain saturation in a fiber optical parametric amplifier. *Optics Letters*, 26(1):10–12, 2001.

K. Inoue and H. Toba. Wavelength conversion experiment using fibre four-wave-mixing. *IEEE Photonics Technology Letters*, 4(1):69–72, 1992.

T. Inoue, J. Hiroishi, T. Yagi, and Y. Mimura. Generation of in-phase pulse train from optical beat signal. *Optics Letters*, 32(11):1596–1598, 2007.

K. Inoue. Four-wave mixing in an optical fiber in the zero-dispersion wavelength region. *Journal of Lightwave Technology*, 10(11):1553–1561, 1992.

A. A. Ishaaya, C. J. Hensley, B. Shim, S. Schrauth, K. W. Koch, and A. L. Gaeta. Highly-efficient coupling of linearly- and radially-polarized femtosecond pulses in hollowcore photonic band-gap fibers. *Optics Express*, 17(21):18630–18637, 2009.

J. Jackle and K. Kawasaki. Intrinsic roughness of glass surfaces. *Journal of Physics: Condensed Matter*, 7(5):4351–4358, 1995.

S. L. Jansen, M. Heid, S. Spalter, E. Meissner, C. J. Weiske, A. Schopflin, D. Khoe, and H. de Waardt. Demultiplexing 160 Gbit/s OTDM signal to 40Gbit/s by FWM in SOA. *Electronics Letters*, 38(17):978–980, 2002.

S. L. Jansen, D. van den Borne, B. Spinnler, S. Calabro, H. Suche, P. M. Krummrich, W. Sohler, G. D. Khoe, and H. de Waardt. Optical phase conjugation for ultra long-haul phase-shift-keyed transmission. *Journal of Lightwave Technology*, 24(1):54–64, 2006.

J. Jasapara, R. Bise, T. Her, and J. Nicholson. Effect of mode cut-off on dispersion in photonic bandgap fibers. In *Technical Digest Optical Fiber Communication Conference (OFC), Atlanta, GA, USA*, pages 492–493, Atlanta U.S.A., 2003.

J. B. Jensen, L. H. Pedersen, P. E. Hoiby, and L. B. Nielsen. Photonic crystal fiber based evanescent-wave sensor for detection of biomolecules in aqueous solutions. *Optics Letters*, 29:1974–1976, 2004.

P. Kaiser, E. A. J. Mercantili, and S. E. Miller. A new optical fibre. *Bell. Syst. Tech. J.*, 52(2):265–269, 1973.

I. Kaminow. Polarization in optical fibers. *IEEE Journal of Quantum Electronics*, 17(1):15–22, 1981.

H. Kano and H. Hamaguchi. Characterization of a supercontinuum generated from a photonic crystal fiber and its application to coherent Raman spectroscopy. *Optics Letters*, 28(23):2360–2362, 2003.

K. C. Kao and G. A. Hocham. Dielectric fibre surface waveguides for optical frequencies. *IEE Proceedings J. Optoelectronics*, 113(3):1151–1158, 1966.

F. P. Kapron, D. B. Keck, and R. D. Maurer. Radiation losses in glass optical waveguides. *Applied Physics Letters*, 17(10):423–425, 1970.

K. M. Kiang, K. Frampton, T. M. Monro, R. Moore, J. Tucknott, D. W. Hewak, D. J. Richardson, and H. N. Rutt. Extruded single mode nonsilica glass holey optical fibre. *Electronics Letters*, 38(12):546–547, 2002.

K. Kikuchi and C. Lorattanasane. Design of highly efficient four-wave mixing devices using optical fibers. *IEEE Photonics Technology Letters*, 6(8):992–994, 1994.

K. Kikuchi, K. Taira, and N. Sugimoto. Highly-nonlinear bismuth oxide-based glass fibers for all-optical signal processing. In *Technical Digest Optical Fiber Communication Conference (OFC), Anaheim, CA, USA, paper ThY6.*, 2002.

J. C. Knight, T. A. Birks, P. S. J. Russell, and D. M. Atkin. All-silica single mode optical fiber with photonic crystal cladding. *Optics Letters*, 21(19):1547– 1549, 1996.

J. C. Knight, J. Broeng, T. A. Birks, and P. S. J. Russell. Photonics band gap guidance in optical fibres. *Science*, 282(5393):1476–1478, 1998.

C. Koos, P. Vorreau, T. Vallaitis, P. Dumon, W. Bogaerts, R. Baets, B. Esembeson, I. Biaggio, T. Michinobu, F. Diederich, W. Freude, and J. Leuthold. All-optical high-speed signal processing with silicon-organic hybrid slot waveguides. *Nature Photonics*, 3:216–219, 2009.

V. Kumar, A. K. George, W. H. Reeves, J. C. Knight, P. S. J. Russell, F. G. Omenetto, and A. J. Taylor. Extruded soft glass photonic crystal fiber for ultrabroad supercontinuum generation. *Optics Express*, 10(25):1520–1525, 2002.

V. Kumar, A. K. George, J. C. Knight, and P. St. Russell. Tellurite photonic crystal fiber. *Optics Express*, 11(20):2641–2645, 2003.

P. Kylemark, M. Karlsson, and P. Andrekson. Impact of phase modulation and filter characteristics on dual-pumped fiber-optical parametric amplification. *IEEE Photonics Technology Letters*, 18(2):439–441, 2006.

J. P. R. Lacey, S. J. Madden, and M. A. Summerfield. Four-channel polarization-insensitive optically transparent wavelength converter. *IEEE Photonics Technology Letters*, 9(10):1355–1357, 1997.

M. R. E. Lamont, B. Luther-Davies, D. Choi, S. Madden, X. Gai, and B. J. Eggleton. Net-gain from a parametric amplifier on a chalcogenide optical chip. *Optics Express*, 16(25):20374–20381, 2008.

T. T. Larsen and A. Bjarklev. Optical devices based on liquid crystal photonic bandgap fibres. *Optics Express*, 11(20):2589–2596, 2003.

T. T. Larsen and A. Bjarklev. Distributed optical fibre devices based on liquid crystal infiltrated photonic crystal fibres. In *Technical Digest Optical Fiber Communication Conference (OFC), Los Angeles, CA, USA*, 2004.

S. Lebrun, P. Delaye, R. Frey, and G. Roosen. High efficiency single mode Raman generation in a liquid filled photonic bandgap fibre. *Optics Letters*, 32(4):337–339, 2007.

J. H. Lee, W. Belardi, K. Furusawa, P. Petropoulos, Z. Yusoff, T. M. Monro, and D. J. Richardson. Four-wave mixing based 10Gbit/s tuneable wavelength conversion using a holey fiber with a high SBS threshold. *IEEE Photonics Technology Letters*, 15(3):440–442, 2003.

J. Y. Y. Leong, S. Asimakis, F. Poletti, P. Petropoulos, X. Feng, R. Moore, K. Frampton, T. M. Monro, H. Ebendorff-Heidepriem, W. Loh, and D. J. Richardson. Towards zero dispersion highly nonlinear lead silicate glass holey fibres at 1550nm by structured-element-stacking. In *European Conference in Optical Communication (ECOC), Post-deadline, Glasgow, United Kingdom*, Glasgow, 2005.

J. Y. Y. Leong, P. Petropoulos, S. Asimakis, H. Ebendorff-Heidepriem, R. C. Moore, K. Frampton, V. Finazzi, X. Feng, J. H. V. Price, T. M. Monro, and D. J. Richardson. A lead silicate holey fibre with $\gamma$=1860 $W^{-1}km^{-1}$ at 1550 nm. In *Technical Digest Optical Fiber Communication Conference (OFC), Anaheim, CA, USA*, Anaheim, 2005.

J. Y. Y. Leong, P. Petropoulos, J. H. V.Price, H.Ebendorff-Heidepriem, S. Asimakis, R. Moore, K. Frampton, V. Finazzi, X. Feng, T. M. Monro, and D. J. Richardson. High-nonlinearity dispersion-shifted lead-silicate holey fibres for efficient 1$\mu$m pumped supercontinuum generation. *Journal of Lightwave Technology*, 24(1):183–190, 2006.

J. Li, A. Berntson, and G. Jacobsen. Polarization-independent optical demultiplexing using XPM-induced wavelength shifting in highly nonlinear fiber. *IEEE Photonics Technology Letters*, 20(9):691–693, 2008.

M. S. Liao, C. Chaudhari, G. S. Qin, X. Yan, T. Suzuki, and Y. Ohishi. Tellurite microstructure fibers with small hexagonal core for supercontinuum generation. *Optics Express*, 17(14):12174–12182, 2009.

M. S. Liao, X. Yan, G. S. Qin, C. Chaudhari, T. Suzuki, and Y. Ohishi. A highly nonlinear tellurite microstructure fiber with multi-ring holes for supercontinuum generation. *Optics Express*, 17(18):15481–15490, 2009.

D. R. Lide. *Handbook of Chemistry and Physics, 85$^{th}$ edition.* CRC Press. CRC Press, 2005.

J. Limpert, O. Schmidt, J. Rothhardt, F. Röser, T. Schreiber, and A. Tünnermann. Extended single-mode photonic crystal fiber lasers. *Optics Express*, 14(7):2715–2720, 2006.

C. Lin and R. H. Stolen. New nanosecond continuum for excited state spectrocopy. *Applied Physics Letters*, 28:216–218, 1976.

R. A. Linke and A. H. Gnauck. High capacity coherent lightwave systems. *Journal of Lightwave Technology*, 6(11):1750–1769, 1988.

E. C. Mägi, L. B. Fu, H. C. Nguyen, M. R. E. Lamont, D. I. Yeom, and B. J. Eggleton. Enhanced Kerr nonlinearity in sub-wavelength diameter $As_2Se_3$ chalcogenide fiber tapers. *Optics Express*, 15(16):10324–10329, 2007.

P. V. Mamyshev, S. V. Chernikov, and E. M. Dianov. Generation of fundamental soliton trains for high-bit-rate optical fiber communication lines. *IEEE Journal of Quantum Electronics*, 27(10):2347–2355, 1991.

D. Marcuse. Field deformation and loss caused by curvature of optical fibers. *Journal of Optical Society of America A*, 66(4):311–320, 1976.

D. Marcuse. Loss analysis of single-mode fiber splice. *Bell Syst. Tech. J.*, 56(5):703, 1977.

C. Martelli, J. Canning, K. Lyytikainen, and N. Groothoff. Water-core Fresnel fiber. *Optics Express*, 13(10):3890–3895, 2005.

G. Meloni, G. Berrettin, M. Scaffardi, A. Bogoni, L. Poti, and M. Guglielmucci. 250-times repetition frequency multiplication for 2.5 Thz clock signal generation. *Electronics Letters*, 41(23):1294–1295, 2005.

R. C. Miller. Optical second harmonic generation in piezoelectric crystals. *Applied Physics Letters*, 5(1):17–19, 1964.

T. Miya, Y. Terunuma, T. Hosaka, and T. Miyashita. Ultimate low-loss single mode fibre at 1.55$\mu$m. *Electronics Letters*, 15(4):106–108, 1979.

T. M. Monro and D. J. Richardson. Holey optical fibres: fundamentals properties and device applications. *Comptes Rendus Physique*, 4(1):175–186, 2003.

T. M. Monro, D.J. Richardson, and P.J Bennett. Developing holey fibres for evanescent filed devices. *Electronics Letters*, 35:1188–1189, 1999.

T. M. Monro, Y. D. West, D. W. Hewak, N. G. R. Brodcrick, and D. J. Richardson. Chalcogenide holey fibres. *Electronics Letters*, 36(24):1998–2000, 2000.

T. M. Monro, K. M. Kiang, J. H. Lee, K. Frampton, Z. Yusoff, R. Moore, J. Tucknott, D. W. Hewak, H. N. Rutt, and D. J. Richardson. High nonlinearity extruded single-mode holey optical fibres. In *Technical Digest Optical Fiber Communication Conference (OFC), (Postdeadline), Anaheim, CA, USA, paper FA1-1*, Washington, USA, 2002.

A. Mori, K. Kobayashi, M. Yamada, T. Kanamori, K. Oikawa, Y. Nishida, and Y. Ohishi. Low noise broadband tellurite-based $er^{3+}$-doped fibre amplifiers. *Electronics Letters*, 34(9):887–888, 1998.

A. Mori, K. Shikano, W. Enbutsu, K. Oikawa, K. Naganuma, M. Kato, and S. Aozasa. 1.5$\mu$m band zero dispersion shifted tellurite photonic crystal fibre with a nonlinear coefficient of 675 $W^{-1}$ $km^{-1}$. In *Proc. European Conference on Optical Communication (ECOC), Stockholm, Sweden, paper Th3.3.6.*, Sweden, 2004.

N. A. Mortensen, J. R. Folkenberg, M. D. Nielsen, and K. P. Hansen. Modal cutoff and the V parameter in photonic crystal fibres. *Optics Letters*, 28(20):1879–1881, 2003.

N. A. Mortensen, M. D. Nielsen, J. R. Folkenberg, A. Petersson, and H. R. Simonsen. Improved large mode-area endlessly single-mode photonic crystal fibres. *Optics Letters*, 28(6):393–395, 2003.

N. A. Mortensen. Effective area of photonic crystal fibres. *Optics Express*, 10(7):341–348, 2002.

K. Mukasa, M. N. Petrovich, F. Poletti, A. Webb, J. Hayes, A. van Brakel, R. A. Correa, L. Provost, J. Sahu, P. Petropoulos, and D. J. Richardson. Novel fabrication method of highly nonlinear silica holey fibres. In *Conference on Lasers and Electro-Optics/Quantum electronics and Laser Science (CLEO/QELS), Long Beach, CA, USA, paper CMC5*, 2006.

T. Nagashima, T. Hasegawa, S. Ohara, and N. Sugimoto. Dispersion shifted $Bi_2O_3$-based photonic crystal fiber. In *Proc. European Conference on Optical Communications (ECOC), Cannes, France, paper We1.3.2*, 2006.

M. Nakazawa, E. Yoshida, and Y. Kimura. Ultrastable harmonically and regeneratively modelocked polarisation-maintaining erbium fibre ring laser. *Electronics Letters*, 30(19):1603–1605, 1994.

K. Nielsen, D. Noordegraaf, T. Sorensen, A. Bjarklev, and T. P. Hansen. Selective filling of photonic crystal fibres. *Journal of Optics A: Pure and Applied Optics*, 7(8):L13–L20, 2005.

M. P. Nikodem, W. Zurawski, and K. Abramski. Four-wave-mixing in non-zero-dispersion shifted fibres. In *International Conference on Transparent Optical Networks (ICTON), Athens, Greece, pp. 342.245*, 2008.

M. Ohashi, K. Shiraki, and K. Tajima. Optical loss property of silica-based single-mode fibers. *Journal of Lightwave Technology*, 10(5):539–543, 1992.

Y. Ohishi, S. Sakaguchi, and S. Takahashi. Transmission loss characteristics of fluoride glass single-mode fibre. *Electronics Letters*, 22(20):1034–1035, 1986.

T. Okuno, M. Onishi, T. Kashiwada, S. Ishikawa, and M. Nashimura. Silica-based functional fibres with enhanced nonlinearity and their applications. *IEEE Journal of Quantum Electronics*, 5(5):1385–1391, 1999.

F. G. Omenetto, N. A. Wolchover, M. R. Wehner, M. Ross, A. Efimov, A. J. Taylor, V. V. R. K. Kumar, A. K. George, J. C. Knight, N. Y. Joly, and P. St. J. Russell. Spectrally smooth supercontinuum from 350 nm to 3$\mu$m in sub-centimeter lengths of soft-glass photonic crystal fibers. *Optics Express*, 14(11):4928–4934, 2006.

A. Ortigosa-Blanch, J. C. Knight, W. J. Wadsworth, J. Arriaga, B. J. Mangan, T. A. Birks, and P. S. J. Russell. Highly birefringent photonic crystal fibres. *Optics Letters*, 25(18):1325–1327, 2000.

A. Ortigosa-Blanch, J. C. Knight, and P. St. J. Russell. Pulse breaking and supercontinuum generation with 200-fs pump pulses in photonic crystal fibers. *Journal of Optical Society of America B*, 19(11):2567–2572, 2002.

Y. Ozeki, S. Takasaka, J. Hiroishi, R. Sugizaki, T. Yagi, M. Sakano, and S. Namiki. Generation of 1 THz repetition rate, 97 fs optical pulse train based on comb-like profiled fibre. *Electronics Letters*, 41(19):1048–1050, 2005.

F. Parmigiani, M. Ibsen, T. T. Ng, L. Provost, P. Petropoulos, and D. J. Richardson. An efficient wavelength converter exploiting a grating-based saw-tooth pulse shaper. *IEEE Photonics Technology Letters*, 20(17):1461–1463, 2008.

F. Parmigiani, R. Slavik, R. Phelan, P. Petropoulos, J. O. Gorman, and D. J. Richardson. Generation of compressed optical pulses beyond 160GHz based on two injection-locked CW lasers. In *Conference on Lasers and Electro-Optics/Quantum electronics and Laser Science (CLEO/QELS), San Jose, CA, USA, paper CTuA3*, 2010.

P. Petropoulos, H. Ebendorff Heidepriem, V. Finazzi, R.C. Moore, K. Frampton, D.J. Richardson, and T.M. Monro. Highly nonlinear and anomalously dispersive lead silicate glass holey fibers. *Optics Express*, 11(26):3568–3573, 2003.

M. N. Petrovich, F. Poletti, A. Van Brakel, and D. J. Richardson. Robustly single mode hollow core photonic bandgap fiber. *Optics Express*, 16(6):4337–4346, 2008.

S. Pitois, J. Fatome, and G. Millot. Generation of a 160GHz transform-limited pedestal-free pulse train through multi-wave mixing compression of a dual frequency beat signal. *Optics Letters*, 27(19):1729–1731, 2002.

F. Poletti, K. Furusawa, Z. Yusoff, N. G. R. Broderick, and D. J. Richardson. Nonlinear tapered holey fibers with high SBS threshold and controlled dispersion. *Journal of Optical Society of America B*, 24(9):2185–2194, 2007.

F. Poletti, A. Camerlingo, P. Petropoulos, and D. J. Richardson. Dispersion management in highly nonlinear carbon disulfide filled holey fibres. In *IEEE/LEOS Winter Topicals, Sorrento, Italy, pp. 154 - 155*, Sorrento, 2008.

C. Politi, D. Klonidis, and M. J. O'Mahony. Waveband converters based on four-wave mixing in SOAs. *Journal of Lightwave Technology*, 24(3):1203 – 1217, 2006.

G. Qin, X. Yan, C. Kito, M. Liao, T. Suzuki, A. Mori, and Y. Ohishi. Highly nonlinear tellurite microstructure fibers for broadband wavelength conversion and flattened supercontinuum generation. *Journal of Applied Physics*, 107:0431081–0431081, 2010.

J. K. Ranka, R. S. Windeler, and A. J. Stentz. Visible continuum generation in air-silica microstructure optical fibers with anomalous dispersion at 800 nm. *Optics Letters*, 25(1):25–27, 2000.

W. Reeves, J. Knight, P. Russell, and P. Roberts. Demonstration of ultraflattened dispersion in photonic crystal fibers. *Optics Express*, 10(14):609–613, 2002.

J. Riishede, S.E. Barkou Libori, A. Bjarklev, J. Broeng, and E. Knudsen. Photonic crystal fibres and effective index approaches. In *Proc. European Conference on Optical Communications (ECOC), Amsterdam, The Netherlands, pp. 522 - 523*, 2001.

P. J. Roberts, F. Couny, H. Sabert, B. J. Mangan, T. A. Birks, J. C. Knight, and P. S. J. Russell. Loss in solid-core photonic crystal fibers due to interface roughness scattering. *Optics Express*, 13(20):7779–7793, 2005.

P.J. Russell. Photonic crystal fibers. *Science*, 299(5605):358–362, 2003.

K. Saitoh and M. Koshiba. Leakage loss and group velocity dispersion in air core photonic bandgap fibres. *Optics Express*, 11(23):3100–3109, 2003.

K. Saitoh and M. Koshiba. Highly nonlinear dispersion-flattened photonic crystal fibers for supercontinuum generation in a telecommunication window. *Optics Express*, 12(10):2027–2032, 2004.

K. Saitoh and M. Koshiba. Numerical modeling of photonic crystal fibers. *Journal of Lightwave Technology*, 23(11):3580–3590, 2005.

A Sano, H. Masuda, T. Kobayashi, M. Fujiwara, K. Horikoshi, E. Yoshida, Y. Miyamoto, M. Matsui, M. Mizoguchi, H. Yamazaki, Y. Sakamaki, and H. Ishii. 69.1Tb/s (432 x 171Gb/s) C and Extended L band transmission over 240 km using PDM 16 QAM modulation and digital coherent detection. In *Technical Digest Optical Fiber Communication Conference (OFC), (Postdeadline), Los Angeles, CA, USA, paper PDPB7.*, 2010.

M. Scaffardi, F. Fresia, G. Meloni, A. Bogoni, L. Poti', N. Calabretta, and M. Guglielmucci. Ultra-fast 160:10 Gbit/s time demultiplexing by four wave mixing in 1 m-long $Bi_2O_3$-based fiber. *Optics Communications*, 268(1):38–41, 2006.

Glass Catalogue Schott, 2003.

H. T. Shang. Chromatic dispersion measurement by white-light interferometry on metre-length single-mode optical fibres. *Electronics Letters*, 17(17):603–605, 1981.

J. Shephard, J. Jones, D. Hand, G. Bouwmans, J. Knight, P. S. J. Russell, and B. Mangan. High energy nanosecond laser pulses delivers single-mode through hollow-core pbg fibres. *Optics Express*, 12(4):717–723, 2004.

R. Shuker and R. W. Gammon. Raman-scattering selection-rule breaking and the density of states in amorphous materials. *Physical Review Letters*, 25(4):222–225, 1970.

M. A. Silberberg. *Chemistry ($4^{th}$ edition).* New York: McGraw-Hill, 2006.

C. M. Smith, N. Venkataraman, M. T. Gallagher, D. Muller, J. A. West, N. F. Borrelli, D. C. Allan, and K. W. Koch. Low-loss hollow-core silica/air photonic bandgap fiber. *Nature*, 424(6949):657–659, 2003.

M. J. Steel, T. P. White, C. M. de Sterke, R. C. McPhedran, and L. C. Botten. Symmetry and degeneracy in microstrucutred optical fibres. *Optics Letters*, 26(8):488–490, 2001.

R. H. Stolen and J. E. Bjorkholm. Parametric amplification and frequency conversion in optical fibers. *IEEE Journal of Quantum Electronics*, 18(7):1062–1072, 1982.

J . Stone. Stress-optic effects, birefringence. and reduction of birefringence by annealing in fiber fabry-perot interferometers. *Journal of Lightwave Technology*, 6:1245–1248, 1988.

N. Sugimoto, H. Kanbara, S. Fiujiwara, K. Tanaka, Y. Shimizugawa, and K. Hirao. Third-order optical nonlinearities and their ultrafast response in $Bi_2O_3$-$Bi_2O_3$-$BiO_2$ glasses. *Journal of Optical Society of America B*, 16:1904–1908, 1999.

N. Sugimoto, T. Nagashima, T Hasegawa, S. Ohara, K. Taira, and K. Kikuchi. Bismuth-based optical fiber with nonlinear coefficient of 1360 $W^{-1}km^{-1}$. In *Technical Digest Optical Fiber Communication Conference (OFC), (Postdeadline), Los Angeles, California, USA, paper PDP26*, 2004.

A. Sugimura and K. Daikoku. Wavelength dispersion of optical fibers directly measured by difference method in the 0.8-1.6$\mu$m range. *Rev. Sci. Instrum*, 50(3):343–346, 1979.

R. L. Sutherland. *Handbook of nonlinear optics.* Marcel Dekker Inc., 1996.

V.G. Ta'eed, L. Fu, M. Pelusi, M. Rochette, I. C. M. Littler, D. J. Moss, and B. J. Eggleton. Error free wavelength conversion in $As_2Se_3$ singlemode chalcogenide fiber. *Optics Express*, 14(22):10371–10376, 2006.

V.G. Ta'eed, L. Fu, M. Pelusi, M. Rochette, I. C. M. Littler, D. J. Moss, and B. J. Eggleton. Error free wavelength conversion in $As_2Se_3$ singlemode chalcogenide fiber. In *Australian Conference on Optical Fibre Technology/Australian Optical Society, Melbourne, Australia, pp. 133-135*, 2006.

K. Tajima, J. Zhou, K. Kurokawa, and K. Nakajima. Low water peak photonic crystal fibers. In *Proc. European Conference on Optical Communications (ECOC), Rimini, Italy, pp. 42-43*, Rimini, 2003.

M. Takahashi, S. Takasaka, R. Sugizaki, and T. Yagi. Arbitrary wavelength conversion in entire CL-band based on pump wavelength tunable FWM in a HNLF. In *Technical Digest Optical Fiber Communication Conference (OFC), Los Angeles, CA, USA*, San Diego, CA, 2010.

T. Tanemura, C. S. Goh, K. Kikuchi, and S. Y. Set. Highly efficient arbitrary wavelength conversion within entire C-band based on nondegenerate fiber four-wave mixing. *IEEE Photonics Technology Letters*, 16(2):551–553, 2004.

D. Tang, A. H. Rose, G. W. Day, and S. M. Etzel. Annealing of linear birefringence in single-mode fiber coils: application to optical fiber current sensors. *Journal of Lightwave Technology*, 9(8):1031–1037, 1991.

E. Tangdiongga, Y. Liu, H. de Waardt, G. D. Khoe, A. M. J. Koonen, H. J. S. Dorren, X. Shu, and I. Bennion. All-optical demultiplexing of 640 to 40 Gbits/s using filtered chirp of a semiconductor optical amplifier. *Optics Letters*, 37(7):835–837, 2007.

I. Thomazeau, J. Etchepare, G. Grillon, and A. Migus. Electronic nonlinear optical susceptibilities of silicate glasses. *Optics Letters*, 10(5):223–225., 1985.

J. Troles, F. Smektala, L. Brillant, P. Houizot, F. Desevedavy, G. Boudebs, T. Chartier, and N. Traynor. Preparation of chalcogenide step-index and micro-structured fiber for telecommunication. In *International Conference on Transparent Optical Networks (ICTON), Nottingham, United Kingdom, pp. 112-115*, 2006.

R. S. Tucker, K. Hinton, and G. Raskutti. Energy consumption limits in high speed optical and electronic signal processing. *Electronics Letters*, 43(17):906–908, 2007.

M. Vieweg, T. Gissibl, and H. Giessen. Selectively filled photonic crystal fibers. In *Nonlinear Photonics, Karlsruhe, Germany, paper CThB2*, Karlsruhe, Germany, 2010. NThA2.

S.J. Wang, E. M. Vogel, and E. Snitzer. Tellurite glass: a new candidate for fibre devices. *Opt. Mat.*, 3:187–203, 1994.

S. Watanabe, S. Takeda, and T. Chikama. Interband wavelength conversion of 320Gb/s (32x10 Gb/s) WDM signals using a polarisation insensitive fibre four-wave-mixer. In *Proc. European Conference on Optical Communications (ECOC), Madrid, Spain*, Madrid, 1998.

S. A. V. Wen, Q. Zhang, H. Ebendorff-Heidepriem, and T. M. Monro. Small core optical waveguides are more nonlinear than expected: experimental confirmation. *Optics Letters*, 34(22):3577–3579, 2009.

T. P. White, R. C. McPhedran, C. M. de Sterke, L. C. Botten, and M. J. Steel. Confinement losses in microstructured optical fibers. *Optics Letters*, 26(21):1660–1662, 2001.

T. L. Wu and C. H. Chao. A novel ultraflattened dispersion photonic crystal fiber. *IEEE Photonics Technology Letters*, 17(1):67–69, 2005.

www.luvantix.com.

www.nktphotonics.com.

www.sciencelab.com.

L. Xiao, W. Jin, M. S. Demokan, H. L. Ho, Y. L. Hoo, and C. Zhao. Fabrication of selective injection microstructured optical fibers with a conventional fusion splicer. *Optics Express*, 13(22):9014–9022, 2005.

C Xu, X Liu, and X Wei. Differential phase-shift keying for high spectral efficiency optical transmissions. *IEEE Journal of Sel*, 10(2):281–293, 2004.

E. Yablonovitch. Inhibited spontaneous emission in solid state physics and electronics. *Physical Review Letters*, 58(20):2059–2062, 1987.

E. Yamakazi, A. Takada, J. Yamawaku, T. Morioka, O. Tadanaga, and M. Asobe. Widely tunable multichannel wavelength conversion using multiple wavelength quasi-phase-matched $LiNbO_3$ waveguides. *Electronics Letters*, 40(8):492–494, 2008.

T. Yamamoto and M. Nakazawa. Active optical pulse compression with a gain of 29.0 dB by using Four Wave Mixing in an optical fibre. *IEEE Photonics Technology Letters*, 9(12):1595–1597, 1997.

T. Yamamoto, E. Yoshida, and M. Nakazawa. Ultrafast nonlinear optical loop mirror for demultiplexing 640 Gbit/s TDM signals. *Electronics Letters*, 34(10):1013–1014, 1998.

S. Yiou, P. Delaye, A. Rouvie, J. Chinaud, R. Frey, and G. Roosen. Stimulated Raman scattering in an ethanol core microstructured optical fibre. *Optics Express*, 13(12):4786–4791, 2005.

S. J. B. Yoo. Wavelength conversion technologies for WDM network applications. *Journal of Lightwave Technology*, 14(6):955–966, 1996.

J. Yu, P. Jeppensen, and S. N. Knudsen. 80Gbit/s pulsewidth-maintained wavelength conversion based on HNL DSF-NOLM including transmission over 80km of conventional SMF. *Electronics Letters*, 37(9):577–579, 2001.

A. Zhang and M. S. Demokan. Broadband wavelength converter based on four-wave mixing in a highly nonlinear photonic crystal fiber. *Optics Letters*, 30(18):2375–2377, 2005.

R. Zhang, J. Teipel, and H. Giessen. Theoretical design of a liquid core photonic crystal fiber for supercontinuum generation. *Optics Express*, 14(15):6800–6812, 2006.

J. Zhou, K. Tajima, K. Nakajima, K. Kurokawa, C. Fukai, T. Matsui, and I. Sankawa. Progress on low loss photonic crystal fibers. *Optical Fibre Technology*, 11(2):101–110, 2005.

B. Zhu, L. E. Nelson, S. Stulz, A. H. Gnauck, C. Doerr, J. Leuthold, L. Gruner-Nielsen, M. O. Pedersen, J.Kim, and J. R. L. Lingle. High spectral density long-haul 40Gb/s transmission using CSRZ-DPSK format. *Journal of Lightwave Technology*, 22(1):208–214, 2004.

# List of Publications

Listed below are the publications arising from the work in this thesis.

**A. Camerlingo**, F. Parmigiani, X. Feng, F. Poletti, W. H. Loh, D. J. Richardson, P. Petropoulos. 160-to-40Gibt/s Time Demultiplexing in a low dispersion lead-silicate W-Index profile fiber, Technical Digest Optical Fiber Communication Conference (OFC), Los Angeles, CA, USA (accepted).

D. J. Richardson, X. Feng, F. Poletti, S. Dasgupta, **A. Camerlingo**, F. Parmigiani, P. Petropoulos, W. H. Loh, S. Herstrom, L. Gruner-Nielsen, Recent advances in highly nonlinear fibres, *Proc. European Conference on Optical Communications (ECOC)*, Turin 19-23 Sep 2010 (Invited).

**A. Camerlingo**, F. Parmigiani, X. Feng, F. Poletti, P. Horak, W. H. Loh, D. J. Richardson, P. Petropoulos. Multichannel wavelength conversion of 40-Gb/s nonreturn-to-zero DPSK signals in a lead-silicate fiber, *IEEE Photonics Technology Letters*, Vol.22(15) pp.1153-1155, 2010.

F. Poletti, X. Feng, **A. Camerlingo**, P. Petropoulos, W. H. Loh, D. J. Richardson. Recent advances in highly non-linear microstructured optical fibers for telecoms applications. *Workshop on Specialty Optical Fibers and their Applications*, Oaxaca Mexico, 13-15 Oct 2010 (Invited).

X. Feng, G. M. Ponzo, F. Poletti, **A. Camerlingo**, F. Parmigiani, M. N. Petrovich, P. Petropoulos, N. M. White, W. H. Loh, D. J. Richardson. A single-mode, high index-contrast, lead silicate glass fibre with high nonlinearity, broadband near-zero dispersion at telecommunication wavelengths. *Proc. European Conference on Optical Communications (ECOC)* 2010 Turin 19-23 Sep 2010.

X. Feng, F. Poletti, **A. Camerlingo**, F. Parmigiani, P. Petropoulos, P. Horak, G. M. Ponzo, M. Petrovich, W. H. Loh, D. J. Richardson, Dispersion controlled highly nonlinear fibers for all optical processing at telecoms wavelengths, *Optical Fiber Technology* 2010, (Submitted),(Invited).

**A. Camerlingo**, X. Feng, F. Poletti, G. M. Ponzo, F. Parmigiani, P. Horak, M. N. Petrovich, P. Petropoulos, W. H. Loh, D. J. Richardson. Near-zero dispersion, highly nonlinear lead silicate W-type fiber for applications at 1.55$\mu$m. *Optics Express*, Vol.18(15), pp.15747-15756, 2010.

**A. Camerlingo**, F. Parmigiani, R. Slavik, X. Feng, F. Poletti, P. Horak, W. H. Loh, P. Petropoulos, D. J. Richardson, Generation of ultra-high repetition rate pulses in a highly nonlinear dispersion-tailored compound glass fibre, *IEEE Summer Topicals* Playa del Carmen, Mexico, 19-21 Jul 2010.

F. Parmigiani, **A. Camerlingo**, X. Feng, F. Poletti, G. M. Ponzo, R. Slavik, P. Horak, M. N. Petrovich, W. H. Loh, P. Petropoulos, D. J. Richardson, Applications of highly nonlinear dispersion tailored lead silicate fibres for high speed optical communications, *International Conference on Transparent Optical Networks (ICTON)*, Munich, 27 Jun-1Jul 2010 Tu.D2.3, (Invited).

**A. Camerlingo**, F. Parmigiani, X. Feng, F. Poletti, P. Horak, W. H. Loh, P. Petropoulos, D. J. Richardson, Multichannel wavelength conversion of 40Gbit/s NRZ DPSK signals in a highly nonlinear dispersion flattened lead silicate fibre, *Nonlinear Photonics*, Karlsruhe Germany 21-24 Jun 2010, NThA3.

F. Parmigiani, R. Slavik, **A. Camerlingo**, L. Gruner-Nielsen, D. Jakobsen, S. Herstrom, R. Phelan, J. O'Gorman, S. Dasgupta, J. Kakande, S. Sygletos, A. D. Ellis, P. Petropoulos, D. J. Richardson, Generation of high repetition rate (>100 GHz) ultrastable pulse trains from a coherent optical beat-signal through non-linear compression using a high SBS-threshold fiber, *Nonlinear Photonics* Karlsruhe Germany, 21-24 Jun 2010, NThA5.

**A. Camerlingo**, F. Parmigiani, X. Feng, F. Poletti, P. Horak, W. H. Loh, D. J. Richardson, P. Petropoulos, Wavelength conversion in a short length of a solid lead-silicate fibre, *IEEE Photonics Technology Letters*, Vol.22(9), pp.628-630, 2010.

N. Vukovic, F. Parmigiani, **A. Camerlingo**, M. N. Petrovich, P. Petropoulos, N. G. R. Broderick, Experimental investigation of a parabolic pulse generation using tapered microstructured optical fibres, *SPIE Photonics Europe*, Brussels, 12-16 Apr 2010.

X. Feng, F. Poletti, **A. Camerlingo**, F. Parmigiani, P. Horak, P. Petropoulos, W. H. Loh, D. J. Richardson, Dispersion-shifted all-solid high index-contrast microstructured optical fiber for nonlinear applications at 1.55$\mu$m, *Optics Express*, Vol.17(22), pp.20249, 2009.

X. Feng, **A. Camerlingo**, F. Poletti, P. Petropoulos, F. Parmigiani, P. Horak, W. H. Loh, D. J. Richardson, A solid one-dimensional microstructured optical fiber with high nonlinearity and low dispersion at 1.55microns, *CLEO Pacific Rim*, Shanghai 30 Aug-3 Sep 2009, TuP5.

**A. Camerlingo**, F. Parmigiani, X. Feng, F. Poletti, P. Horak, W. H. Loh, D. J. Richardson, P. Petropoulos, Four-wave-mixing based wavelength conversion in a short length of a solid 1D microstructured fibre, *Proc. European Conference on Optical Communications (ECOC)* Vienna, 21-23 Sep 2009.

F. Poletti, X. Feng, **A. Camerlingo**, M. N. Petrovich, P. Horak, F. Parmigiani, P. Petropoulos, W. H. Loh, D. J. Richardson, Recent advances in highly nonlinear microstructured optical fibres, *OptoElectonics and Communication Conference, (OECC)*, Hong Kong 12-17 Jul 2009 (Invited).

X. Feng, **A. Camerlingo**, F. Poletti, P. Petropoulos, K. E. Frampton, N. M. White, C. J. Oton, W. H. Loh, D. J. Richardson, Highly nonlinear non-silica glass microstructured optical fibers with near-zero dispersion slope for 1.55micron applications, in *Conference on Lasers and Electro-Optics/Quantum electronics and Laser Science (CLEO)*, Munich 14-19 Jun 2009, CE3.4.

X. Feng, W. H. Loh, J. C. Flanagan, **A. Camerlingo**, S. Dasgupta, P. Petropoulos, P. Horak, K. E. Frampton, N. M. White, J. H. V. Price, H. N. Rutt, D. J. Richardson, Single-mode tellurite glass holey fibre with extremely large mode area for infrared nonlinear applications, *Optics Express*, Vol.16(18) pp.13651-13655, 2008.

F. Poletti, **A. Camerlingo**, P. Petropoulos, D. J. Richardson, Dispersion management in highly nonlinear carbon disulfide filled holey fibers, *IEEE Photonics Technology Letters*, Vol.20(17) pp.1449-1451, 2008.

X. Feng, W. H. Loh, **A. Camerlingo**, S. Dasgupta, J. C. Flanagan, P. Petropoulos, K. E. Frampton, N. M. White, H. N. Rutt, D. J. Richardson, Broadband supercontinuum using single-mode/dual-mode tellurite glass holey fibers with large mode area, *Conference on Lasers and Electro-Optics/Quantum electronics and Laser Science (CLEO)*, San Jose, 4-9 May 2008 CMDD7, 2008.

F. Poletti, **A. Camerlingo**, P. Petropoulos, D. J. Richardson, Dispersion management in highly nonlinear carbon disulfide filled holey fibres, *IEEE/LEOS Winter Topicals*, Sorrento 14-16 Jan 2008.